Force Fields Parametrization of Ion-Water Interactions from Density Functional Theory Based Molecular Dynamic Simulations

Doctoral thesis by

Ausias March Calvo Minguillón

Thesis advisor

Elvira Guàrdia Manuel

A thesis submitted for the degree of

Doctor of Physics

PhD program of

Computational and Applied Physics

Departament de Física

UNIVERSITAT POLITÈCNICA
DE CATALUNYA
BARCELONATECH

Barcelona, May 2021

Acknowledgements

Es un hecho ampliamente aceptado que el proceso de gestación y alumbramiento de una tesis doctoral no es fácil ni en las mejores circunstancias. Es por eso que resulta trivial deducir que, alguien que lo ha logrado, lo ha hecho gracias a mucha gente. Sin embargo, no es muy ortodoxo incluir en este tipo de publicaciones un apéndice para poder nombrar a todos ellos. Además, una inevitable omisión accidental podría interpretarse como una exclusión deliberada. Por estos motivos, limitaré este texto a puntualizar los representantes paradigmáticos de todas aquellas personas que han ayudado a que el mundo de los campos de fuerza ion-agua parametrizados mediante ajuste de fuerzas originadas en simulaciones de dinámica molecular basadas en teoría de funcionales de densidad (de ahora en adelante CFIAPMAFOSDMBTFD) avancen, con suerte, algún Angstrom. También es necesario mencionar que el orden en que se presenta a estas personas responde a un criterio meramente narrativo y en ningún lugar de relevancia.

Como no, empezaré esta antología *ab initio* (desde el principio), con mis padres. Es probable que esta historia arrancara en el asiento trasero del coche familiar, haciendo tiempo de camino a alguna extraescolar preguntando a mi padre que pasaría en el mundo si los semáforos anduvieran o por qué las grúas tenían un brazo más largo que el otro. Una pregunta me enseñó que las hay que tienen respuesta, la otra, que también las hay que, o bien no la tienen, o bien resulta inalcanzable. Estos viajes en coche desembocaron probablemente en el sesgo que me llevó a creer que *mi mamá no sabe nada*. Por suerte, mi madre era racional como acabaría siéndolo yo y nunca guardó, o por lo menos no mostró, rencor alguno y, cuando tuvo que asumir las responsabilidades que antes compartía con mi padre, no le fue problema recordarme que hasta la Física es más que Física. Si bien mis padres se encargaron de que mi línea de salida en esta carrera estuviera tan adelantada como fuera posible, fue mi hermano quién a sabiendas o *ignoriendas* me permitió arrancar con la velocidad inicial necesaria; es necesario tener a alguien delante intelectualmente para poder aspirar a más de lo que sabes.

Llegó el momento de arrancar el capítulo que cierran estas letras y, por muy obvio que pueda parecer, fueron mis dos co-directores de tesis quienes tuvieron la fe, paciencia y dedicación en aquellos momentos en los que yo las perdía. Momentos de los que, si bien la vida nunca queda exenta, el más relevante puede resumirse con "*Diligens agrícola serit arbores quarum fructus ipse numquam aspiciet*" que vendría a traducirse como "El buen agricultor planta árboles cuyos frutos nunca verá". Sin los agricultores que me plantaron, alguien tenía que recoger el testigo. Candidatos no faltaban, pero fueron Montse y Javier y Mari Carmen y Conrad quienes se aseguraron de que ningún obstáculo me impidiera continuar. Puede parecer obvio, pero no sobra mencionar que lo agradezco tanto como han hecho mis padres.

Como ya he mencionado al principio, el camino del doctorado no solo no es fácil, sino que puede hasta resultar demasiado peligroso como para tomarlo solo. Por suerte, si bien es una carrera, no es una de esas en las que para ganar tienes que pasar por delante a los demás, o, al menos, no lo es para mí. En estos casos, siempre es bueno correr del lado de quienes comparten y comprenden tu dolor y te animan a seguir adelante. Si pretendía dar ejemplos paradigmáticos, Carles Paredes es el paradigma de "el colazón del grupo". Es a la vez la cola y el pegamento. Y le agradezco sus incesantes esfuerzos para mantenernos unidos. Por otro lado, están mis amigos y jefes del trabajo, quienes no han dejado de animarme en este sprint final, más incluso de lo que les convendría a ellos y a la empresa. Y para amigos, también los hay aquellos a los que el doctorado ni les va ni les viene, pero, como anteriormente he falso-citado a mi madre: "ni la Física es solo Física". Ya lo dije en su boda y lo repito aquí: Albert y Aina me recogieron, acogieron y levantaron durante la peor caída de mi vida. Además, por motivos que se revelarán más adelante, fueron ellos los responsables de que llegara a conocer a Dolors y Magí. Es difícil cuantificar el apoyo emocional y material que han supuesto últimamente de otra manera que infinito e indispensable. Estos últimos años han sido un reto vital que difícilmente habríamos superado sin ellos.

Es posible que el lector se pregunte quienes son Magí y Dolors. Son los padres de Aina. El mismo lector puede que entonces se pregunte: ¿Y cómo han llegado a esta historia los padres de Aina? Pues porque también son los padres de mi mujer. Sobre el apoyo de Carla al mundo de los CFIAPMAFOSDMBTFD solo daré un dato: es la única persona que ha leído esta tesis, además varias veces, que no ha cobrado por hacerlo. Y como decía Salinas: "Si una persona se lee tu tesis sin necesidad, es que te quiere. Mucho". Pues yo más. Ahora, ya tan cerca de la meta, no puedo sino celebrar el poder cruzarla de su mano y, más importante, poner la vista en avanzar tanto como podamos la línea de salida de los árboles que juntos estamos plantando.

Abstract

The underlying topic of this thesis is the study of the application of the Force Matching (FM) algorithm to parameterize ion-water Force Fields using *ab initio* simulations as reference. In order to do so three different main steps have been followed. First, the results of a set of Car-Parrinello Molecular Dynamics (CPMD) simulations consistent of one ion and 96 water molecules have been analyzed and described to be used as reference for the FM algorithm and for the subsequent assessment of the obtained results. Four monovalent anions (fluoride, chloride, bromide and iodine), three monovalent cations (lithium, sodium and potassium) and two divalent cations (magnesium and calcium) have been used. For each simulation both, structural and dynamical properties, such as the ion-water Radial Distribution Functions (RDF), the coordination numbers, the residence time, the ion self-diffusion coefficient have been computed. The dynamics of the solvation shell molecules has also been analyzed. Second, to try to reduce the effects of the dimensionality reduction when moving from Density Functional Theory simulations to classical ones the use of polarization is one of the first techniques that is usually considered. In order to move a step forward in this direction the use of damping functions in conjunction with Polarizable Point Dipoles has been tested. For the chloride ion two different screening functions, Gaussian and exponential, were tested with three different values of ion polarizability: $\alpha = 2.25\text{Å}^3$, $\alpha = 4.00\text{Å}^3$ and $\alpha = 5.48\text{Å}^3$ and were then compared to the use of an undamped polarizability of $\alpha = 3.25\text{Å}^3$ and to the results from the CPMD simulations. Both damping functions performed well when compared to the CPMD results and allow a better reproduction of dynamical properties of the ion and of its solvation shell at a negligible computational cost. Last, the main part of this thesis has consisted in testing and evaluating the performance of a wide set of ion-water interaction schemes in order to validate their capacity to reproduce the *ab initio* results by means of the FM process. All the fitted force fields are of the form of a Lennard Jones potential. Three different water models have been mainly used. The well known

SPC/E and RPOL models and a set of SPC-like water models previously developed in our group using the FM process referenced in this work as SPC-FM. Two different dispersion damping functions have been used: the Tang-Toennies function and a Fermi like one. Finally, the scaling of the ion charges and the use of weights during the matching process has been tested as well. The resulting fitted potentials have been used in a series of classical Molecular Dynamics simulations of ion-water systems at the same conditions as those of the CPMD simulations. Despite having a wide range of physical properties computed from the reference CPMD simulations, to keep the comparison simple enough, the quality of the force matching potentials has been assessed by comparing the resulting ion-water forces and the ion-oxygen and ion-hydrogen RDFs of the fitted potentials to those of reference. For each ion the best combination of water model, damping, scaling and force weight has been determined.

Table of contents

List of figures

List of tables

Chapter 1

Introduction

1.1 Molecular Dynamics

Since the advent of the first civil use of computers in the mid '50s of the twentieth century [1–3], Molecular Dynamics (MD) simulations have been a powerful tool to circumvent the mathematical impossibility of reaching an analytical solution to the dynamics of an n-body system. In the beginning, the use of MD was limited to the area of statistical mechanics as a complementary tool to study abstract systems. As the power and availability of these machines grew, the original success of MD in theoretical physics soon was exported to other branches such as materials science, biochemistry or biophysics. This expansion has not stopped and nowadays, MD is commonly used in a wide amount of areas that range from the study of protein folding to the construction of nanostructures or even the analysis of geological mineral-water interfaces.

Classical MD aims to numerically solve the motion equations of a set of interacting particles. Once the movement of the particles has been determined and due to the possibility to track the trajectories of individual particles, different properties of the system can be computed, such as temperature or diffusion coefficients of the particles. There are two important approximations that must be taken in order to compute the particles trajectories. First, one must assume that the particles obey the classical Newton's equations of motion and, due to the fact that these equations are not integrable for more than two particles, some kind of numerical solution must be used to solve them. The second requirement is to be able to describe in which way particles interact between them. This interaction is modeled through a Force Field. A Force Field is composed by a functional expression and a set of parameters from which one can obtain the potential energy of the system. The functional expression should reflect the nature of the relevant

interactions present in the system, such as electrostatic forces or polarization effects and can model known properties such as bonds and dispersion forces. These functionals must be filled with adequate parameters so they faithfully represent the actual forces of the simulated system. It must be noted that while a specific combination of functional and parameters can be appropriate to study some aspects of a system, different ones can be better approached by a complete alternative choice. The origin of the parameters is usually of empirical nature. They can be chosen so the resulting potentials meet some testable experimental criteria such as melting temperature, heat of vaporization or geometrical constraints like Radial Distribution Functions. Most usual sources for these parameters include Nuclear Magnetic Resonance measurements [4], x-ray [5] and neutron [6] scattering, Ramman absorption spectroscopy measurements [7, 8], X-ray Absorption Fine Structure spectroscopic methods [9–11] or non-linear femtosecond spectroscopy [12]. Although this approach has yield a great deal of progress there is a huge lack of experimental data available for some systems such as those present in the cellular environment. It's possible to avoid the need for experimental data as a reference by adjusting the Force Fields parameters to match certain properties of high-quality *ab initio* quantum chemical data [13]. In most refined approaches of these techniques, the Force Field parameters are usually found by fitting hundreds of points on the *ab initio* Potential Energy Surface for relatively small clusters [14]. These *ab initio* calculations rely solely on highly accurate theoretical computations without any intervention from experimental sources.

When constructing the Force Field, the interaction between atoms is usually divided among separated contributions that take into account the different phenomena involved in the interaction such as the electrostatic interaction, polarization effects, bonds or dispersion forces. Each one of these phenomena can be described in several ways. For example, the potential energies due to electrostatic charges are usually described by the Coulombic potential [15–18]. The Pauli repulsion among electrons and the dispersion forces are commonly represented in classical MD by the Lennard-Jones [19] potential or the Buckingham [20] potential. For this work the Lennard-Jones potential has been used exclusively; therefore, a brief explanation of it can be found in Chapter 3. These functionals are surprisingly effective and accurate despite their mathematical simplicity and relatively small computational cost. Nevertheless, some systems require a more elaborated description [21, 22]. A common upgrade that can be added to these potentials despite being a computationally expensive one is the addition of electronic polarization effects. Again, several methods can be used to this end such as Drude Oscillators [23–25] or the Polarizable Point Dipoles method [26–29]. Being the approach used in this

thesis, in Chapter 3, the Polarizable Point Dipoles method is briefly explained. Classical Molecular Dynamics still admits further refinements such as the use of damping functions that smear point charges [30] or dipoles [31] into more spread distributions. The benefits of the latter have been more extensively studied for a solvated ion system and are explained in Chapter 5.

1.2 *Ab Initio* Molecular Dynamics

Classical Molecular Dynamics has prevailed in the condensed matter simulation area since its advent in the mid past century and probably it will continue doing so for the next imminent decades. However, a radical alternative approach to the use of modeled Force Fields is emerging since the mid eighties: the *Ab initio* Molecular Dynamics. *Ab initio* Molecular Dynamics aims to obtain the forces that drive the motion of atoms from a pure theoretical method avoiding to compromise with any external contribution like experimental data. To reach this goal this new framework uses electronic structure calculations that are achieved through the solution of the Schrödinger equation of the system. The size of this task quickly becomes impractical due to the extreme complexity of the wave function of a real system; thus, several approximations must be applied. Some of these approximations include effective potentials that render the first principle nature of the method strictly invalid. These kind of simulations become semi-empirical ones that due to ill used terminology usually keep the *ab initio* denomination. These semi-empirical methods switch the Force Field modeling and parametrization approximation for the different approximations needed to make the solution of the Schrödinger equation possible. The 1985 paper from Car and Parrinello [35] initiated the explosion in activity of the field. The revolutionary concept of the Car-Parrinello Molecular Dynamics presented in this work consisted in the introduction of the atomic electronic variables into the Lagrangian of the system as active degrees of freedom, evolving the electronic structure and the corresponding forces *on-the-fly* along with the trajectories of the atomic nuclei.

Ab initio simulations present several advantages over the classical ones besides the absence of fitted Force Fields. At each step the electronic configuration of the atoms is computed, so different properties such as the polarization can emerge naturally from it without any explicit intervention. This gives access to very relevant advantages like the ability to follow chemical reactions involving the breaking and formation of covalent bonds [36–38] or even processes where electrons are transferred [39, 40]. As it would be expected, these huge capabilities of the *ab initio* methods do not come without expense.

While classical MD can easily manage hundreds of thousands of particles and runs of even hundreds of microseconds, simulations of quantum nature are highly limited to a few hundred atoms and tens of picoseconds.

1.3 Matching Method

As it has been explained, the need of experimental reference to fit Force Fields parameters can be avoided using *ab initio* calculations. Unfortunately, these approaches have also some drawbacks. For example, the Potential Energy Surface fitting previously mentioned, although being accurate, works outside the condensed phase; thus, some points included in the fit can be physically unimportant, while at the same time some important ones can be missed. To overcome this problem a new method has been recently introduced, which is based on a least-square fitting to a series of forces and other magnitudes obtained from *ab initio* calculations of the condensed phase of interest[45–51]. This approach, called the Matching Method, is an extension of the Force Matching algorithm developed in the early nineties at the Department of Materials Science and Engineering at the University of Illinois at Urbana-Champaign. The rise in computational power and the development of Density Functional Theory calculations allow nowadays to obtain significant amounts of first principle data like interatomic forces, polarizations and even structural and dynamic properties. This huge amount of reference input can be used to train classical potentials to reproduce, within their own limitations, the results of the first principle simulations. A huge deficiency of most of the classical Force Fields used in Molecular Dynamics is their lack of transferability. Potentials that perform well under certain simulation conditions may be rendered unusable under others. With the Matching Method, data from different simulation conditions can be simultaneously used as a way to achieve, or at least get closer, to Force Field transferability.

1.4 Ion Solvation Systems

As it was stated before, both, classical MD and *ab initio* MD, are present in a vast number of fields. Due to its presence in both, biological and industrial systems, ion solvation constitutes a central topic in chemical physics and theoretical chemistry. Up to now, a huge quantity of classic Molecular Dynamics studies have been performed to look into different aspects of ion solvation. These studies include electrode processes [52], metal corrosion [53], oxidation of chemical and biochemical waste [54] or microbiology [55]. One crucial point in order to obtain good accurate MD simulations lies in the choice of

parameters of the Force Field. Due to the constraints to which experimental settings are bound, for example the imperative use of salts formed by two different elements instead of one only chemical species, ion solvation systems present great challenges for the usual methods to determine Force Field parameters based on experimental data.

1.5 This Thesis

The focus of this work is set on developing the matching method and to use it to obtain a set of Force Fields to describe the interaction between ions and water. This thesis is structured in four parts. Chapters 2 and 3 give a brief explanation of the computational methods and the different kinds of Force Fields and water models used in this thesis. Chapter 4 aims to analyze a group of Car-Parrinello simulations for a set of four anions (F^-, Cl^-, Br^-, I^-) and five cations (Li^+, Na^+, K^+, Mg^{2+}, Ca^{2+}). The result of these simulations has been used as the reference data for the matching process. Chapter 5 studies the use of polarization dampening in classical Force Fields as a way to significantly improve the agreement between the Car-Parrinello simulations and the classical ones. Finally, in Chapter 6 the matching method is applied to different combinations of Force Field functionals and water models in order to develop a consistent methodology for the matching process and to obtain the best ion water interaction Force Fields parameters possible.

References

[1] E. Fermi, J. Pasta, and S. M. Ulam. Studies of nonlinear problems, I. *LASL Report*, 5(LA-1940), 1955.

[2] B. J. Alder and T. E. Wainwright. Studies in Molecular Dynamics. I. General Method. *J. Chem. Phys.*, 31(2):459, 1959.

[3] A. Rahman. Correlations in the Motion of Atoms in Liquid Argon. *Phys. Rev.*, 136(2A):A405—-A411, oct 1964.

[4] H. Ohtaki and T. Radnai. Structure and Dynamics of Hydrated Ions. *Chemical Reviews*, 93(3):1157–1204, 1993.

[5] S. Ramos, A. C. Barnes, G. W. Neilson, and M. J. Capitan. Anomalous X-Ray Difraction Studies of Hydration Effects in Concentrated Aqueous Electrolyte Solutions. *Chemical Physics*, 258:171–180, 2000.

[6] A. K. Soper and K. Weckström. Ion Solvation and Water Structure in Potassium Halide Aqueous Solutions. *Biophysical chemistry*, 124(3):180–91, dec 2006.

[7] G. E. Walrafen. Raman Spectral Studies of the Effects of Temperature on Water and Electrolyte Solutions. *The Journal of Chemical Physics*, 44(4), 1966.

[8] G. E. Walrafen. Raman Spectral Studies of the Effects of Perchlorate Ion on Water Structure. *The Journal of Chemical Physics*, 52(8), 1970.

[9] D. M. Pfund, J. G. Darab, J. L. Fulton, and Y. Ma. An XAFS Study of Strontium Ions and Krypton in Supercritical Water. *The Journal of Physical Chemistry*, 98(50):13102–13107, 1994.

[10] Y. Marcus. Effect of Ions on the Structure of Water: Structure Making and Breaking. *Chemical Reviews*, 109:1346–1370, 2009.

[11] S. L. Wallen, B. J. Palmer, and J. L. Fulton. The Ion Pairing and Hydration Structure of Ni^{2+} in Supercritical Water at 425 °C Determined by X-Ray Absorption Fine Sstructure and Molecular Dynamics Studies. *The Journal of Chemical Physics*, 108(10), 1998.

[12] M. F. Kropman and H. J. Bakker. Dynamics of Water Nolecules in Aqueous Solvation Shells. *Science (New York, N.Y.)*, 291(5511):2118–2120, 2001.

[13] G. A. Kaminski, H. A. Stern, B. J. Berne, and R. A. Friesner. Development of an Accurate and Robust Polarizable Molecular Mechanics Force Field from ab Initio Quantum Chemistry. *Journal of Physical Chemistry A*, 108(4):621–627, 2004.

[14] D. Spångberg and K. Hermansson. Many-Body Potentials for Aqueous Li^+, Na^+, Mg^{2+}, and Al^{3+}: Comparison of Effective Three-Body Potentials and Polarizable Models. *The Journal of Chemical Physics*, 120(10), 2004.

[15] J. Priestley. Summary for Policymakers. In Intergovernmental Panel on Climate Change, editor, *Climate Change 2013 - The Physical Science Basis*, volume 1, pages 1–30. Cambridge University Press, Cambridge, 1775.

[16] C. A. Coulomb. Premier Mémoire sur l'Électricité et le Magnétisme. In *Histoire de l'Académie Royale des Sciences*, pages 569–577. De l'imprimerie royale, 1788.

[17] J Robison. *A System of Mechanical Philosophy*, volume 4. Cambridge University Press, Cambridge, 2014.

[18] J. C. Maxwel. *The Electrical Researches of the Honourable Henry Cavendish*. Cambridge University Press, Cambridge, 1879.

[19] J. E. Jones. On the Determination of Molecular Fields. II. From the Equation of State of a Gas. *Proceedings of the Royal Society A: Mathematical, Physical and Engineering Sciences*, 106(738):463–477, oct 1924.

[20] R. A. Buckingham. The Classical Equation of State of Gaseous Helium, Neon and Argon. *Proceedings of the Royal Society A: Mathematical, Physical and Engineering Sciences*, 168(933):264–283, oct 1938.

[21] D. Bucher, L. Guidoni, P. Maurer, and U. Rothlisberger. Developing Improved Charge Sets for the Modeling of the KcsA K^+ Channel Using QM/MM Electrostatic Potentials. *Journal of Chemical Theory and Computation*, 5(8):2173–2179, 2009.

[22] T. W. Allen, O. S. Andersen, and B. Roux. Ion Permeation Through a Narrow Channel: Using Gramicidin to Ascertain All-Atom Molecular Dynamics Potential of Mean Force Methodology and Biomolecular Force Fields. *Biophysical journal*, 90(10):3447–68, 2006.

[23] G. Lamoureux and B. Roux. Modeling Induced Polarization with Classical Drude Oscillators: Theory and Molecular Dynamics Simulation Algorithm. *The Journal of Chemical Physics*, 119(6):3025, 2003.

[24] G. Lamoureux, A. D. MacKerell, and B. Roux. A Simple Polarizable Model of Water Based on Classical Drude Oscillators. *The Journal of Chemical Physics*, 119(10):5185, 2003.

[25] H. Yu, T. W. Whitfield, E. Harder, G. Lamoureux, I. Vorobyov, V. M. Anisimov, A. D. MacKerell, and B. Roux. Simulating Monovalent and Divalent Ions in Aqueous Solution Using a Drude Polarizable Force Field. *Journal of Chemical Theory and Computation*, 6(3):774–786, 2010.

[26] M. Masia, M. Probst, and R. Rey. On the Performance of Molecular Polarization Methods. I. Water and Carbon Tetrachloride Close to a Point Charge. *The Journal of Chemical Physics*, 121(15):7362, 2004.

[27] M. Masia, M. Probst, and R. Rey. On the Performance of Molecular Polarization Methods. II. Water and Carbon Tetrachloride Close to a Cation. *The Journal of Chemical Physics*, 123(16):164505, 2005.

[28] J. P. Piquemal, R. Chelli, P. Procacci, and N. Gresh. Key Role of the Polarization Anisotropy of Water in Modeling Classical Polarizable Force Fields. *J. Phys. Chem. A*, 111(33):8170–8176, 2007.

[29] Pär Söderhjelm, Anders Öhrn, Ulf Ryde, and Gunnar Karlström. Accuracy of Typical Approximations in Classical Models of Intermolecular Polarization. *Journal of Chemical Physics*, 128(1), 2008.

[30] Jonàs Sala, Marco Masia, Elvira Guàrdia, and Marco Masia. The polarizable point dipoles method with electrostatic damping: Implementation on a model system. *The Journal of Chemical Physics*, 133(23):234101, 2010.

[31] E. Guàrdia, A. M. Calvo, and M. Masia. How Polarization Damping Affects Ion Solvation Dynamics. *Theoretical Chemistry Accounts*, 131(3):1152, 2012.

[32] M. P. Allen and D. J. Tildesley. *Computer Simulation of Liquids*. Oxford science publications. Oxford University Press, reprint edition, 1987.

[33] D. Frenkel, B. Smit, and M. A. Ratner. Understanding Molecular Simulation: From Algorithms to Applications. *Phys. Today*, 50(7):66, 1997.

[34] G. Ciccotti, D. Frenkel, and I.R. McDonald. *Simulation of Liquids and Solids*. North-Holland, 1987.

[35] R. Car and M. Parrinello. Unified Approach for Molecular Dynamics and Density-Functional Theory. *Physical Review Letters*, 55(22):2471–2474, 1985.

[36] J. M. Stubbs and D. Marx. Aspects of Glycosidic Bond Formation in Aqueous Solution: Chemical Bonding and the Role of Water. *Chemistry - A European Journal*, 11(9):2651–2659, 2005.

[37] N. Goldman, L. E. Fried, I. F. W. Kuo, and C. J. Mundy. Bonding in the Superionic Phase of Water. *Physical Review Letters*, 94(21):217801, 2005.

[38] A. Sillanpää and K. Laasonen. Car-Parrinello Molecular Dynamics Study of DCl Hydrate Crystals. *ChemPhysChem*, 6(9):1879–1883, 2005.

[39] H. Oberhofer and J. Blumberger. Electronic Coupling Matrix Elements from Charge Constrained Density Functional Theory Calculations Using a Plane Wave Basis Set. *Journal of Chemical Physics*, 133(24), 2010.

[40] Thomas J. Eisenmayer, Jorge A. Lasave, Adriano Monti, Huub J M De Groot, and Francesco Buda. Proton displacements coupled to primary electron transfer in the Rhodobacter sphaeroides reaction center. *Journal of Physical Chemistry B*, 117(38):11162–11168, 2013.

[41] G. Galli and M. Parrinello. *Computer Simulation in Materials Science*. Springer Netherlands, Dordrecht, 1991.

[42] G. Galli and A. Pasquarello. *Computer Simulation in Chemical Physics*. Springer Netherlands, Dordrecht, 1993.

[43] M. J. Gillan. The Virtual Matter Laboratory. *Contemporary Physics*, 38(2):115–130, 1997.

[44] M. Parrinello. From Silicon to RNA: The Coming of Age of ab Initio Molecular Dynamics. *Solid State Communications*, 102(2-3):107–120, 1997.

[45] F. Ercolessi and J. B. Adams. Interatomic Potentials from First-Principles Calculations: The Force-Matching Method. *Europhysics Letters (EPL)*, 26(8):583–588, jun 1994.

[46] X. Y. Liu, J. B. Adams, F. Ercolessi, and J. A. Moriarty. EAM Potential for Magnesium from Quantum Mechanical Forces. *Modelling and Simulation in Materials Science and Engineering*, 4(3):293–303, 1999.

[47] J. Kohanoff and J.-P. Hansen. Statistical properties of the dense hydrogen plasma: An *ab initio* molecular dynamics investigation. *Phys. Rev. E*, 54(1):768–781, jul 1996.

[48] B. Edwards, N. W. Ashcroft, and T. Lenosky. Layering Transitions and the Structure of Dense Hydrogen. *Europhysics Letters*, 34(7):519–524, 1996.

[49] T. J. Lenosky, J. D. Kress, I. Kwon, A. F. Voter, B. Edwards, D. F. Richards, S. Yang, and J. B. Adams. Highly Optimized Tight-Binding Model of Silicon. *Phys. Rev. B*, 55(3):1528–1544, 1997.

[50] S. Izvekov, M. Parrinello, C. J. Burnham, and G. A. Voth. Effective Force Fields for Condensed Phase Systems from Ab Initio Molecular Dynamics Simulation: A New Method for Force-Matching. *The Journal of Chemical Physics*, 120(23), 2004.

[51] D. Spångberg, E. Guàrdia, and M. Masia. Aqueous halide potentials from force matching of Car-Parrinello data. *Computational and Theoretical Chemistry*, 982:58–65, 2012.

[52] B. E. Conway. Individual Solvated Ion Properties and Specificity of Ion Adsorption Effects in Processes at Electrodes. *Chem. Soc. Rev.*, 21(4):253–261, 1992.

[53] R. N. Goldberg. Physical Chemistry of Aqueous Systems: Meeting the Needs of Industry. *Journal of Chemical & Engineering Data*, 42(1):225, 1997.

[54] A. Shanableh. Production of Useful Organic matter from Sludge Using Hydrothermal Treatment. *Water Research*, 34(3):945–951, 2000.

[55] F. Canganella, C. Kato, and K. Horikoshi. Effects of Micronutrients on Growth and Starch Hydrolysis of Thermococcus Guaymasensis and Thermococcus Aggregans. *Microbiological Research*, 154(4):307–312, 2000.

Chapter 2

Computational Methods

2.1 Molecular Dynamics

After setting aside the quantum nature of the electronic structure of atoms, the interaction between two atoms or molecules can be described through quite simple laws. This is due to the fact that chemical interactions are mainly governed by electrostatic interactions. Despite this simplification, the mathematical impossibility of finding an analytical solution to the motion of more than just two atoms [1] forces the use of numerical methods in order to solve the evolution of such systems. These numerical methods constitute what is known as Molecular Dynamics (MD) [2]. The target of MD is to study the dynamics and obtain experimental observables from these kind of systems. The complexity and accuracy of these results will be determined by that of the description used in the simulation.

In a classical framework an N-particle system free of any external potential will be described by a Hamiltonian comprising the sum of the potential and kinetic energy of its particles

$$H(\mathbf{p},\mathbf{r}) \equiv H(\mathbf{p}_1,\ldots,\mathbf{p}_N,\mathbf{r}_1,\ldots,\mathbf{r}_N) = \sum_{i=1}^{N} \frac{\mathbf{p}_i^2}{2m_i} + U(\mathbf{r}_1,\ldots,\mathbf{r}_N), \tag{2.1}$$

where $\mathbf{p}_1,\ldots,\mathbf{p}_N$ are the momenta of the particles and $\mathbf{r}_1,\ldots,\mathbf{r}_N$ are their positions. With a set of initial coordinates and momenta, one can use this Hamiltonian to obtain

the Newton equations of motion that describe the evolution of the system through time

$$\dot{\mathbf{r}}_i = \frac{\partial H}{\partial \mathbf{p}_i} = \frac{\mathbf{p}_i}{m_i}, \tag{2.2a}$$

$$\dot{\mathbf{p}}_i = -\frac{\partial H}{\partial \mathbf{r}_i} = -\frac{\partial U}{\partial \mathbf{r}_i} = F_i(\mathbf{r}_1, \ldots, \mathbf{r}_N). \tag{2.2b}$$

These equations of motion are Hamiltonian conservative which means that they keep the evolution of the system inside a constant energy surface in the phase space of the microcanonical ensemble of the system. This allows to connect the results from MD to those from statistical mechanics. In virtue of the *ergodic hypothesis*, those quantities from the system obtained through the averages over the Hamiltonian conservative simulation are equivalent to those obtained through averages over the microcanonical ensemble. This provides a way to connect the simulated trajectories to physical observables like diffusion coefficients, spectra or other thermodynamic properties [3–8].

2.1.1 Integrating the Equation of Motion

As there is no analytical solution to motion equations of many particle systems like those expected to study with MD, numerical methods are used in order to achieve an approximate solution. Motion equations are propagated through small but finite time steps using *finite difference methods*. Different approaches can be taken to solve the set of ordinary differential equations such as the *Verlet*, the *Velocity Verlet* or the *leap frog* algorithms [9–11]. This work relies mainly on the last one. All these methods assume that positions, velocities and accelerations of the particles can be approximated through Taylor expansion series

$$\mathbf{r}(t+\delta t) = \mathbf{r}(t) + \mathbf{v}(t)\cdot\delta t + \frac{1}{2}\mathbf{a}(t)\cdot\delta t^2 + \ldots, \tag{2.3a}$$

$$\mathbf{v}(t+\delta t) = \mathbf{v}(t) + \mathbf{a}(t)\cdot\delta t + \frac{1}{2}\mathbf{b}(t)\cdot\delta t^2 + \ldots, \tag{2.3b}$$

$$\mathbf{a}(t+\delta t) = \mathbf{a}(t) + \mathbf{b}(t)\cdot\delta t + \ldots, \tag{2.3c}$$

where $\mathbf{r}$ is their positions, $\mathbf{v}$ is their velocities (first derivative of the position with respect to time), $\mathbf{a}$ is their accelerations (second derivative of the position with respect to time), and so on. In the *leap-frog* algorithm, velocities are first calculated at a half time step

$\frac{1}{2}\delta t$. Then, these velocities are used to advance the positions a whole time step δt

$$\mathbf{r}(t+\delta t) = \mathbf{r}(t) + \mathbf{v}(t)\left(t+\tfrac{1}{2}\delta t\right)\cdot\delta t, \tag{2.4a}$$

$$\mathbf{v}(t+\tfrac{1}{2}\delta t) = \mathbf{v}\left(t-\tfrac{1}{2}\delta t\right) + \mathbf{a}(t)\cdot\delta t. \tag{2.4b}$$

A clear disadvantage of this algorithm is that positions and velocities are computed half time step apart. This problem can be solved at the expense of one last calculation

$$\mathbf{v}(t) = \frac{1}{2}\left[\mathbf{v}\left(t-\tfrac{1}{2}\delta t\right) + \mathbf{v}\left(t+\tfrac{1}{2}\delta t\right)\right]. \tag{2.5}$$

It is critical to choose an adequate size of the time step δt. On one side, larger time steps will provide a faster evolution of the system thus a lower computational cost. On the other side, a too large time step will increase energy conservation errors. Furthermore, the time step must be small enough to properly describe the fastest motion of the system.

This simulation scheme will keep constant the volume and the energy of the simulated system (within the numerical error) and the total number of particles; thus, it is appropriated to study it within the micro-canonical ensemble. However, most of the experimental conditions in condensed-phase take place within the canonical ensemble so they rely on a constant temperature more than on a constant energy. This thermalization condition can be achieved through different methods. A quite simple one and widely used is the *Berendsen thermostat* [12]. In order to achieve a constant target temperature the velocities of all the particles are rescaled at every step by a factor

$$\lambda^2 = 1 + \frac{\delta t}{\tau}\left[\frac{T_0}{T} - 1\right], \tag{2.6}$$

where T is the temperature of the system before the rescaling obtained from the instantaneous kinetic energy and τ is strength coupling parameter that determines the intensity of the rescaling. The Berendsen thermostat underestimates temperature fluctuations; thus, it does not reproduce a true canonical ensemble [13, 14]. Due to this limitation the Berendsen thermostat is usually used during the thermal equilibration of the system and the production runs are computed at constant energy.

2.1.2 Force Fields

The most expensive part in a MD simulation lays in the computation of the potential created between particles. In a usual MD simulation this effort grows quadratically as a

function of the number of particles $\mathcal{O}(n^2)$. In order to be able to simulate systems in the thousands or tens of thousands particles it is crucial to keep the computational cost of the interactions between these particles as low as possible. Again, a compromise must be made between the accuracy of these interactions and how much effort it takes to calculate them. To this end, complex inter-atomic potentials are modeled through relatively simple Force Fields (FF). These FF consist of a functional form and a set of parameters than can be adjusted to fulfill some experimental or theoretical characteristics. Chapter 3 contains a more extensive review of those FF used in this work.

2.1.3 System geometry

Although the constant growth of computational power, there is a huge limitation to the size of the simulated systems, in terms of number of particles, that can be simulated. This restriction forces a significant portion of the total amount of particles to be close to the limit of the system. Without particles outside the system, those located near the end of it will feel a very different environment than those inside the bulk. In order to avoid this boundary effects and to be able to simulate bulk systems of an infinite size, periodic boundary conditions are applied to the system [4]. The whole system is replicated around the original one so those particles near the border can interact with fictitious particles copy of those situated on the other side of the system. The simulation box can adopt different shapes as long as it tiles perfectly the whole space. The most common shape used in condensed phase simulations like in this thesis is that of a cube.

2.2 DFT Molecular Dynamics

The interaction among the atoms that constitute matter depends mainly on the properties of the electronic clouds of the atoms. Molecular Dynamics tries to reduce the massive complexity of these interactions by means of a simplified parameterized Force Field that depends only on a few parameters like the nature of the atoms, the distance between them or their polarization. This reduction leaves out the interaction effects that arise from the different electronic structure of the atoms which is the main responsible for their distinct chemical properties.

On the other side, *ab initio* Molecular Dynamics calculates the electronic structure of the atoms at each configuration in order to determine the forces that drive the evolution of the system [15, 16]. Through this explicit treatment of the electronic cloud different phenomena such as chemical reactions [17–19], polarization effects or phase

transitions [20, 21] can be directly accessed. Both, liquid water [22, 23] and aqueous solutions [24, 25] among others are growing fields for first principle Molecular Dynamics.

Ab initio calculations aim to obtain these results only through solving the Schrödinger equation avoiding any empirical patch. Unfortunately, nowadays it is not possible to eradicate all the approximations needed to solve the Schrödinger equation for fairly large systems and/or long simulations but they can be selectively chosen to achieve the accuracy allowed by the available computational resources. Some of these approximations use effective potentials to describe the nucleus and the inner electrons of the atoms leaving the strict use of the Schrödinger equation just for the valence electrons. Due to the fact that most chemical properties depend heavily on the valence electrons, this approximation allows to reduce significantly the computational cost of the simulation while maintaining a good degree of accuracy. This section explains in a roughly manner the basics of the *ab initio* and semi-empirical simulations.

2.2.1 First-principle Molecular Dynamics

The Wave Function

The basis of quantum mechanics lies in the wave function, Ψ, which is postulated to contain all the information needed to describe the state of the whole system. At any moment, the state of a system formed by a set of nuclei and their electrons can be described by its wave function $\Psi_{\mathrm{S}}(\mathbf{R}_{\mathrm{I}}, r_1, \ldots, r_n)$ which depends on the coordinates of the nuclei $\mathbf{R}_{\mathrm{I}}$ and their N electrons $r_1, \ldots, r_n$.

Observable physical properties of the system may be obtained by applying different linear quantum mechanical operators to the wave function of the system, Ψ_{S},

$$\hat{\mathrm{A}}\Psi_{\mathrm{S}} = a\Psi_{\mathrm{S}}, \tag{2.7}$$

where $\hat{\mathrm{A}}$ is any linear operator for some observable A (such as position, momentum, energy, etc.) and a is the eigenvalue of the operator and corresponds to the measured value of the observable A. More precisely, due to the probabilistic nature of quantum mechanics, one can predict the probability of finding a certain value, or range of values, and the mean value,

$$\left\langle \hat{A} \right\rangle = \int \Psi^* \hat{A} \Psi \mathrm{d}^3\mathbf{r}. \tag{2.8}$$

The Hamiltonian Operator

A most relevant observable of a system is the total energy of it, E. This observable is associated to the Hamiltonian Operator $\mathcal{H}$. When the Hamiltonian operator is used in equation 2.7,

$$\hat{\mathcal{H}}\Psi = E\Psi, \tag{2.9}$$

it is known as the Schrödinger time-independent equation. The energy of the system formed by a set of nuclei and their electrons can be described by a Hamiltonian composed by the kinetic energy of the nuclei, $\hat{\mathcal{T}}_{\mathrm{N}}$, the potential interaction among them, $\hat{\mathcal{V}}_{\mathrm{NN}}$, the kinetic energy of the electrons, $\hat{\mathcal{T}}_{\mathrm{e}}$, their potential interaction, $\hat{\mathcal{V}}_{\mathrm{ee}}$, and the interaction between the nuclei and the electrons, $\hat{\mathcal{V}}_{\mathrm{Ne}}$,

$$\hat{\mathcal{H}} = \hat{\mathcal{T}}_{\mathrm{N}} + \hat{\mathcal{V}}_{\mathrm{NN}} + \hat{\mathcal{T}}_{\mathrm{e}} + \hat{\mathcal{V}}_{\mathrm{ee}} + \hat{\mathcal{V}}_{\mathrm{Ne}}, \tag{2.10a}$$

$$\hat{\mathcal{H}} = -\sum_{k} \frac{\hbar^2}{2m_k}\nabla_k^2 + \sum_{k<l} \frac{e^2 Z_k Z_l}{r_{kl}} - \sum_{i} \frac{\hbar^2}{2m_e}\nabla_i^2 + \sum_{i<j} \frac{e^2}{r_{ij}} - \sum_{i}\sum_{k} \frac{e^2 Z_k}{r_{ik}} \tag{2.10b}$$

where i and j run over the electrons, k and l over the nuclei, $\hbar$ is the reduced Planck's constant, m_e is the mass of the electron, m_k the mass of the k-nucleus, e is the electron charge, Z_c (Z_l) is the atomic number of the k-nucleus (l-nucleus), and r_{ab} denotes the distance between two particles a and b.

The Schrödinger equation associated to this Hamiltonian and wave function is far away from what can be analytically solved; thus, a number of approximations are needed in order to work with it.

The Variational Principle

Ab initio methods arise from the variational principle [26]. Any variation, Ψ', on the ground state wave function associated to a Hamiltonian, Ψ, will result in an increase of the expectation value of the Hamiltonian,

$$E_0 = \langle\Psi|\hat{\mathcal{H}}|\Psi\rangle < \langle\Psi'|\hat{\mathcal{H}}|\Psi'\rangle. \tag{2.11}$$

This sets the lowest energy eigenvalue of the Hamiltonian as a lower limit that can be used in order to test the accuracy of the approximated wave functions. Although the exact value of the limit will rarely ever be known, one can consider that the lower the energy of the wave function the closer it will be to the exact ground state one.

2.2.2 The Born-Oppenheimer Approximation

The most fundamental and widely used approximation in *ab initio* calculations is the Born-Oppenheimer approximation [26–28]. It attempts a factorization of the whole wave function of the system into two separate contributions: the nuclei of the atoms, which will be considered fixed, and its electrons.

The Adiabatic Separation of Nuclei and Electrons

In virtue of the masses of the nuclei being much higher than those of the electrons, the movement of these will be accordingly much faster. Therefore, the electronic cloud will rapidly relax to its ground state after each variation in the position of the nuclei so it can be considered adiabatically separated from them. This separation translates into the system wave function as

$$\Psi_{\mathrm{S}}\left(\mathbf{R}_{\mathrm{N}}, \mathbf{r}_1, \ldots, \mathbf{r}_n\right) = \Psi(\mathbf{R}_{\mathrm{N}})\Psi_0(\mathbf{r}_1, \ldots, \mathbf{r}_n; \mathbf{R}_{\mathrm{N}}), \tag{2.12}$$

where $\Psi_0(\mathbf{r}_1, \ldots, \mathbf{r}_n; \mathbf{R}_{\mathrm{N}})$ is the ground state electronic wave function of the Hamiltonian $\hat{\mathcal{H}}$ at a fixed nuclear configuration $\mathbf{R}_{\mathrm{N}}$ and $\Psi(\mathbf{R}_{\mathrm{N}})$ is the nuclear part of the system wave function.

Applying the Hamiltonian from 2.10b to two wave functions decomposed as in 2.12, $\Psi_{\mathrm{S}} = \Psi \cdot \Psi_0$ and $\Psi'_{\mathrm{S}} = \Psi' \cdot \Psi_0$, results in

$$\begin{aligned}
\left\langle \Psi'_{\mathrm{S}} \middle| \hat{\mathcal{H}} \middle| \Psi_{\mathrm{S}} \right\rangle = &- \sum_k \frac{1}{2m_k} \left\langle \Psi' \middle| \nabla^2_{\mathbf{R}_{\mathrm{N}}} \middle| \Psi \right\rangle + \left\langle \Psi' \middle| \hat{\mathcal{V}}_{\mathrm{NN}} + E_0(\mathbf{R}_{\mathrm{N}}) \middle| \Psi \right\rangle && (2.13)\\
&- \sum_k \frac{1}{m_k} \left\langle \Psi' \middle| \Big(\left\langle \Psi_0 | \nabla_{\mathbf{R}_{\mathrm{N}}} \Psi_0 \right\rangle (\{\mathbf{R}\}) \Big) \middle| \nabla_{\mathbf{R}_{\mathrm{N}}} \Psi \right\rangle && (2.14)\\
&- \sum_k \frac{1}{2m_k} \left\langle \Psi' \middle| \Big(\left\langle \Psi_0 | \nabla^2_{\mathbf{R}_{\mathrm{N}}} \Psi_0 \right\rangle (\{\mathbf{R}\}) \Big) \middle| \Psi \right\rangle, && (2.15)
\end{aligned}$$

where $E_0(\hat{\mathbf{R}}_{\mathrm{N}})$ is potential energy term due to the energy of the electrons in the ground state for a given nuclear configuration

$$E_0(\mathbf{R}) = \left\langle \Psi_0 \middle| \hat{\mathcal{H}} \middle| \Psi_0 \right\rangle. \tag{2.16}$$

The last two terms (2.14 and 2.15) are the non-adiabatic coupling elements and are responsible for the breakdown of the Born-Oppenheimer approximation due to the dependence on the nuclei coordinates $\mathbf{R}_{\mathrm{N}}$ of the electronic part of the wave function Ψ_0. The third one (2.14) couples the ground state to the excited ones. To evaluate this term

we consider that

$$\left\langle \Psi_0 \middle| \nabla_{\mathbf{R}_\mathrm{N}} \middle| \Psi_0 \right\rangle = \langle \Psi_0 | \nabla_{\mathbf{R}_\mathrm{N}} \Psi_0 \rangle = \langle \nabla_{\mathbf{R}_\mathrm{N}} \Psi_0 | \Psi_0 \rangle \,, \tag{2.17}$$

and apply the chain rule to obtain

$$\nabla_{\mathbf{R}_\mathrm{N}} \langle \Psi_0 | \Psi_0 \rangle = \langle \nabla_{\mathbf{R}_\mathrm{N}} \Psi_0 | \Psi_0 \rangle + \langle \Psi_0 | \nabla_{\mathbf{R}_\mathrm{N}} \Psi_0 \rangle = 2 \left\langle \Psi_0 \middle| \nabla_{\mathbf{R}_\mathrm{N}} \middle| \Psi_0 \right\rangle. \tag{2.18}$$

As long as it can be considered that the electrons remain in the ground state, the normalization condition on Ψ_0

$$\langle \Psi_0 | \Psi_0 \rangle = 1, \forall \{\mathbf{R}\} \,, \tag{2.19}$$

applies and, being the derivative of constant, the term

$$\nabla_{\mathbf{R}_\mathrm{N}} \langle \Psi_0 | \Psi_0 \rangle = 0. \tag{2.20}$$

vanishes and so it does $\left\langle \Psi_0 \middle| \nabla_{\mathbf{R}_\mathrm{N}} \middle| \Psi_0 \right\rangle$ and $\langle \Psi_0 | \nabla_{\mathbf{R}_\mathrm{N}} \Psi_0 \rangle$ in equation 2.14.

The last term (2.15) will contribute even when restricted to the ground state but it will usually be one order of magnitude smaller and will be neglected. After removing these two terms, the effective Hamiltonian leading the evolution of the nuclei wave function under the Born-Oppenheimer, $\hat{\mathcal{H}}_\mathrm{BO}$ approximation will remain

$$\hat{\mathcal{H}}_\mathrm{BO} = \hat{\mathcal{T}}_\mathrm{N} + \hat{\mathcal{V}}_\mathrm{NN} + E_0(\hat{\mathbf{R}}_\mathrm{N}). \tag{2.21}$$

Born-Oppenheimer Molecular Dynamics

The classical motion of the nuclei arises from the energy potential surface $v_\mathrm{NN}(\mathbf{R}_\mathrm{I}) + E_0(\mathbf{R}_\mathrm{I})$. The movement of the nuclei in the classical limit will be guided by the forces obtained as the gradient of this surface through the Hellman-Feynman theorem [29]. This allows to perform a Molecular Dynamics simulation as:

1. At a time t the total energy $E_0 = E_0[\mathbf{R}(t)]$ is computed from the ionic configuration $\mathbf{R}(t)$ and the electronic state $\Psi_0(\mathbf{r}_1, \ldots, \mathbf{r}_\mathrm{N} : \mathbf{R}_\mathrm{I}(t))$.
2. Obtain the ionic forces from the Hellman-Feynman theorem.
3. Solve Newton's equations of motion and advance the ionic configuration $\mathbf{R}(t) \rightarrow \mathbf{R}(t + \delta t)$.
4. Iterate from step (1).

2.2.3 Density Function Theory

Being the electrons interacting fermions, it takes a huge effort to compute the electronic ground state of a system of just a few atoms. The Density Function Theory has become a successful method to tackle this problem. It's based on the Hohenber-Kohn theorem which states that there exists a one to one map between external potentials and the ground state electronic density [30] or

$$n^0(\mathbf{r}) \rightarrow v(\mathbf{r}). \tag{2.22}$$

An external potential $v(\mathbf{r})$ gives form to a unique ground-state wave function, as long as it is not degenerated, from which arises a unique ground state density $n^0(\mathbf{r})$. As the Hohenberg-Kohn theorem states that there is only one external potential that can give a certain electronic density, knowing that density must led to know about the external potential and the wave function; thus, all properties depending on the wave function must be representable as a functional of the electronic density.

Unfortunately, there is a great distance between knowing that there exists a unique functional of the energy an determine the exact form of it. Nowadays there is no way to achieve this, so approximated methods are used. Kohn and Sham developed the more extended method which consists in a Slater determinant like wave function of *non-interacting* electrons [31] moving in a conveniently chosen effective external potential, which reproduces the exact same ground-state density. The Kohn-Sham equations are solved through a Self Consistency process similar to that of the Hartree-Fock equations and includes an exchange-correlation potential term that remains unknown. This problem can be approached in different ways. The easiest one uses the Local Density Approximation (LDA) which assumes the electron cloud as a uniform gas introducing the electron density ρ as the only parameter of the functional [32–34]. This approach lacks the accuracy needed for chemistry purposes so the Generalized Gradient Approximation (GGA) introduces the use of both, the density and it's gradient $|\nabla\rho|$. More modern solutions known as *hybrid functionals* usually use a linear combination of the regular GGA method with a Hartree-Fock exact exchange functional. One of the most widespread of these hybrid functionals is the B3LYP [35, 36].

2.2.4 Semiepirical Methods

To keep the true *ab initio* nature of the simulation for bigger systems than a few atoms grows the cost of it to an inadmissible point. The heavier part of an *ab initio* calculation rises from the computation of the interaction between electron pairs. Although there

are ways to reduce the impact of this problem, such as avoiding the calculation of those integrals that can be considered negligible, it is common the use of semiempirical methods to simplify the problem. Such methods involve the use of pseudopotentials to substitute the integrals corresponding to the interaction with the nuclei and those from the electrons of the inner orbitals. The valence electrons, being the most relevant ones to the chemical properties, are still quantumly simulated. These pseudopotentials are constructed using empirical data losing the *ab initio* character of the method.

Carr-Parrinello Molecular Dynamics

If the Born-Oppenheimer approximation utilizes the adiabatic separation between nuclei and electrons in order to decompose the total wave-function, Car-Parrinello Molecular Dynamics (CPMD) uses it to simultaneously minimize the electrons wave-function and propagate the nuclei movement.

Extra degrees of freedom for the expansion coefficients $c_i(\mathbf{G})$ of the orbitals are introduced into the Lagrangian, which leads to the extended CPMD Lagrangian

$$\mathcal{L}^{\mathrm{CP}}(\mathbf{c},\dot{\mathbf{c}},\mathbf{R},\dot{\mathbf{R}}) = \mu\sum_{i,\mathbf{G}}\dot{c}_i^*(\mathbf{G})\dot{c}_i(\mathbf{G}) + \frac{1}{2}\sum_{\mathrm{I}} M_i\dot{\mathrm{R}}_i^2 - E(\mathbf{c},\mathbf{R}) + \sum_{i,j}\Lambda_{ij}\left[\sum_{\mathbf{G}} c_i^*(\mathbf{G})c_i(\mathbf{G}) - \delta_{ij}\right] \quad (2.23)$$

and the motion equations

$$\mu\ddot{c}_i(\mathbf{G}) = \frac{\partial E(\mathbf{c},\mathbf{R})}{\partial c_i^*(\mathbf{G})} + \sum_j \Lambda_{ij}c_j(\mathbf{G}), \quad (2.24)$$

$$M_{\mathrm{I}}\ddot{\mathbf{R}}_{\mathrm{I}} = \frac{\partial E(\mathbf{c},\mathbf{R})}{\partial \mathbf{R}_{\mathrm{I}}}. \quad (2.25)$$

As long as the fictitious mass μ of the electrons is chosen to be small enough, their dynamic will be much faster than that of the nuclei. The electrons will relax fast close to their minimum energy and it will be kept close to the Born-Oppenheimer surface.

2.2.5 The Wannier Centers

A major advantage of DFT simulations is the access to the electronic structure it gives. By means of the maximally localized Wannier functions [37–40], the electron charge, otherwise distributed along the orbitals, can be partitioned and assigned to individual

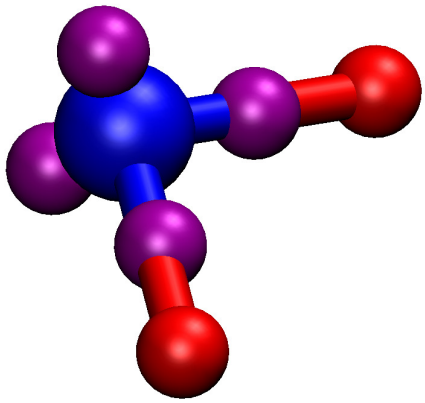

Fig. 2.1 Water molecule formed by an oxygen atom (blue) and two hydrogen atoms (red). The Wannier centers (purple) represent the location of pairs of electrons.

molecular contributions. The Wannier centers allow to perform polarization calculations of the molecules or identify where the covalent bonds take place.

2.3 The Matching Algorithm

The quality of an MD simulation is mainly determined by the quality of the Force Fields used in it. Hence the procedure to obtain these Force Fields parameters is of the utmost importance in order to obtain an accurate description of the system. Historically, the parameters used in classical Force Fields have been usually fitted so the potential is capable of reproducing certain few experimental results such as the melting point or the spectra and, more recently, of matching properties obtained through high level quantum chemical computations. In 1992, the Department of Materials Science Engineering at the University of Illinois began to develop what was called the Force Matching algorithm as an attempt to substitute these few reference quantities with massive amounts of reference forces from *ab initio* and DFT sources in order to export the higher accuracy of DFT simulations into cheaper classical FF methods. Obviously, due to the classical nature of standard MD, some of the most interesting aspects of DFT simulations are impossible to be transferred, but FM has been proven a powerful tool for improving classical potentials. This approach has been successfully used to model effective interactions for hydrogen under pressure by Kohano *et al.* [41] or to parameterize a tight-binding model for silicon by Lenosky *et al.* [42]. The Force Matching algorithm can be extended so it can include

any other magnitudes that can be obtained through these computations such as torques over molecules or polarizations. This work will refer to this extension with the more general term of Matching Algorithm. The idea behind the Matching Algorithm is to adjust through a least-squares fitting process the parameters of a classical potential (i.e. the σ and ϵ parameters from a Lennard-Jones potential [43]) so it can reproduce as accurately as possible a series of properties obtained with *ab initio* methods [44]. A clear advantage of this method is the vast number of systems over it can be used. Due to the highly detailed description that can be achieved over the reference system used to fit the potentials, it allows to access to a wide variety of properties of the system, such as forces or dipoles, that wouldn't be reachable by other means. Moreover, the amount of data that can be used as a reference greatly exceeds that of most other methods.

2.3.1 The Matching Process

The Matching process begins with the *ab initio* simulations. The positions, forces and other properties resulting from quantum calculations are stored so they can be used as reference in the fitting process. Then, a classical potential is fed with the different particles positions and is used to compute the corresponding properties one intents to match such as the forces, the torques or the polarizations. This first attempt needs some initial parameters for the classical potential that are chosen after an educated guess. The results obtained through the classical simulation are compared with the *ab initio* ones by means of a certain error function to asses a measure of how different the classical and *ab initio* simulations are. Then, the classical potential parameters are mapped and wisely modified in order to minimize the difference between the classical and the *ab initio* results. This process is iterated and stopped when the value of the error reaches a satisfactory level. Figure 2.2 shows the flowchart of the Matching algorithm. The error function, χ, used for the evaluation of the difference between *ab initio* and classical properties can be as complex as needed but, experience has shown that simplicity gives the best results. The objective error function used in this work is

$$\chi^2 = \sum_{l=1}^{L} \omega\left(F_{\mathrm{DFT}}\right) \cdot \sum_{i=1}^{N_{\mathrm{A}}} \sum_{j=1}^{3} (F_{ij}^{\mathrm{DFT}} - F_{ij}^{\mathrm{MD}})^2 \tag{2.26}$$

where l runs through all the L considered configurations, i goes over all the N_{A} particles taken into account and j stands for the three components X, Y and Z of the forces and

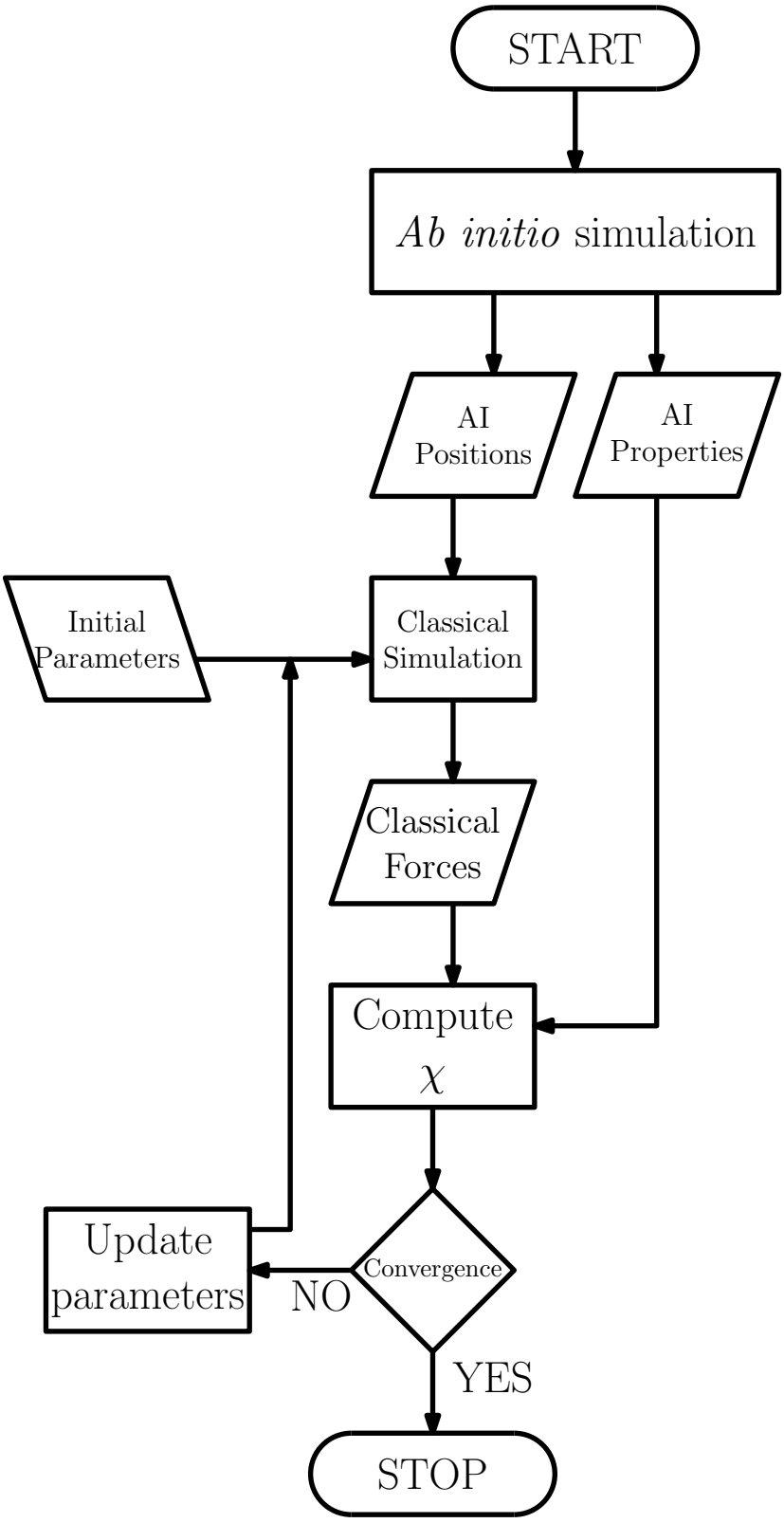

Fig. 2.2 Flowchart of the Force Matching algorithm.

$\omega\left(F_{\mathrm{DFT}}\right)$ is a weight of the form

$$\omega\left(F_{\mathrm{DFT}}\right) = \frac{1}{\left(F_x^2 + F_y^2 + F_z^2\right)^{\alpha}}, \tag{2.27}$$

that depends on the *ab initio* forces and damps the contribution of the high forces produced by unusually close atoms. The parameter α calibrates the relevance of this weight and it is manually adjusted.

2.3.2 Testing Results

Once the Force Matching process has ended and the parameters have been obtained it's necessary to test the quality of the resultant potentials. In order to do so different checks can be done.

Forces The first obvious comparison to be made is that of how similar the forces obtained with the DFT calculations and those from classical MD simulations are. A visual analysis can be done by means of a scatter plot of the DFT forces against the MD ones (figure 2.3). The resultant cloud of points must be compared to the ideal alignment over the $y = x$ line. The closer it is the cloud to the bisecting line the better the reproduced forces will be. This can be quantified performing a lest-squares fitting to a linear function $y = bx$ and comparing the value of the slope to the ideal $b = 1$.

Radial Distribution Functions Structural properties of the system can also be compared. The Radial Distribution Function (RDF), or $g(r)$, gives a measure of how density varies around a particle due to the presence of it. This information is shown as a probability of finding a particle at a set distance from the reference one relative to that expected of finding one in a random distribution of the same density. Nearby the reference particle there is a depletion zone where the probability of finding another particle is zero due to the Pauli exclusion. Each one of the peaks of the function shows the presence of a solvation shell. As the distance increases, the influence of the particle diminishes and the RDF fades to $g(r) = 1$.

The RDF between two species of the system α and β can be computed by discretizing the volume into a series spherical shells of thickness Δr centered around the particles of the species α and counting the number of particles of the species β inside the shells

$$g_{\alpha\beta}(r) = \frac{1}{N_{\mathrm{confs}}} \sum_{\mathrm{confs}} \frac{1}{N_\alpha} \sum_{\alpha} \frac{V}{N_\beta} \frac{\Delta n_\beta(r)}{4\pi r^2 \Delta r}, \tag{2.28}$$

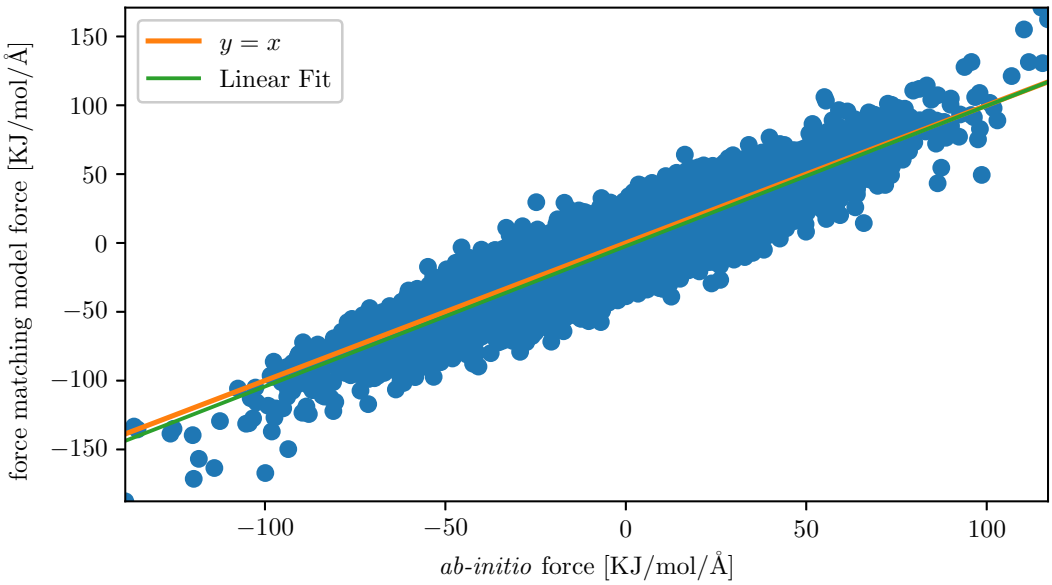

Fig. 2.3 Scatter plot of forces obtained with DFT calculations and Classical Molecular Dynamics for lithium with the SPC/E water model.

averaged over the N_α particles and the N_{confs} configurations. In equation 2.28, V stands for the volume of the simulated system, N_β is the total number of particles of the β kind and $\Delta n_\beta(r)$ is the number of particles of the β species inside a spherical shell of thickness Δr and radius r centered at the atom α.

The RDF obtained with fitted potentials can be compared to those obtained from DFT simulations (figure 2.4). A first visual analysis can give a good impression of the quality of the fitted potential but again, an objective numerical test is needed. The difference between the two functions can trivially be calculated and compared between interaction models as the root mean squared difference of the functions

$$RMSD\left[g(r)\right] = \sqrt{\int_{r=0}^{r_{\max}} \left[g^{\text{DFT}}(r) - g^{\text{MD}}(r)\right]^2 \mathrm{d}r}, \tag{2.29}$$

Other quantities can be extracted and checked from the RDF. The size and population of the coordination shells around the molecules can be obtained integrating the RDF between two consecutive minimums. Comparing the RDF of the different components of the molecules (figure 2.5) the orientation of these molecules around the central atom can also be deduced. These properties can be compared to X-ray and neutron diffraction experiments.

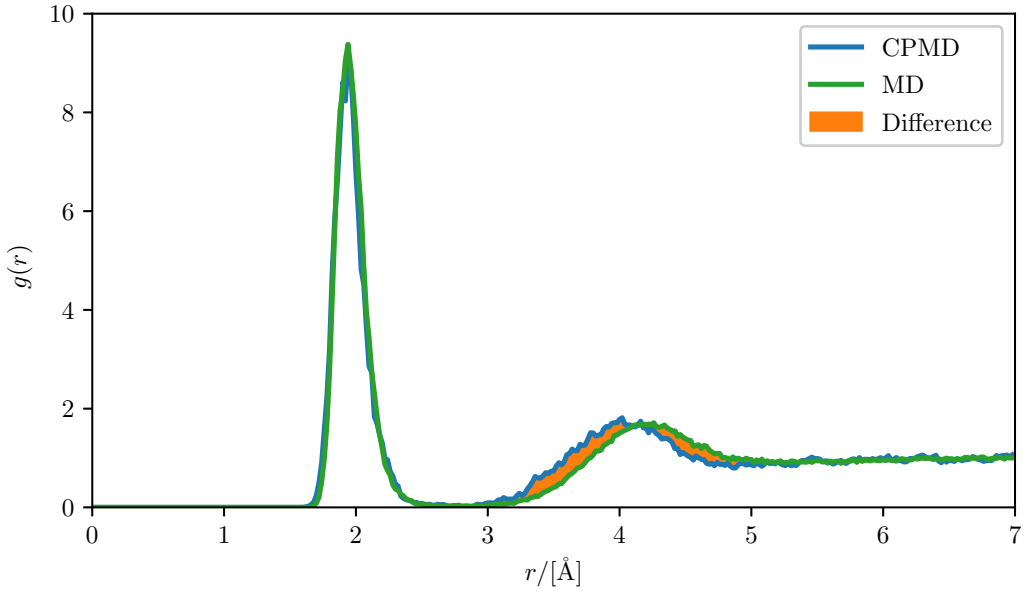

Fig. 2.4 In orange, the difference between the Radial Distribution Functions of the reference DFT simulations (blue) and the fitted classical potential simulation (green) for a lithium ion in SPCE/E water.

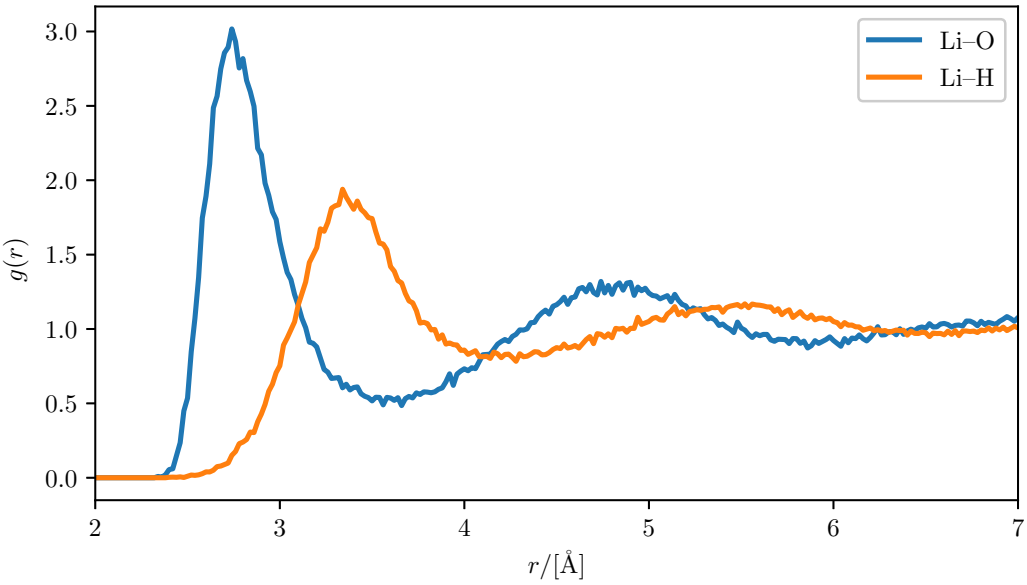

Fig. 2.5 Radial Distribution Functions for the ion-oxygen (red) and the ion-hydrogen (blue) for the potassium ion with the SPC/E water.

Self-Diffusion Coefficient The diffusion of the particles can also be studied computing the particle mean squared displacement $\langle r^2 \rangle (t)$ and velocity autocorrelation function $C_{vv}(t)$ as

$$\Delta_r(t) = \langle [\vec{r}(t) - \vec{r}(0)]^2 \rangle, \tag{2.30}$$

$$C_{vv}(t) = \frac{\langle \vec{v}(t) \cdot \vec{v}(0) \rangle}{\langle v^2(0) \rangle}. \tag{2.31}$$

the diffusion coefficient is obtained by calculating the slope of the $\Delta_r(t)$ and the integral of $C_{vv}(t)$ as

$$D_{\text{msd}} = \frac{1}{6} \lim_{t \to \infty} \frac{\mathrm{d}}{\mathrm{d}t} \Delta_r(t), \tag{2.32}$$

$$D_{\text{vacf}} = \frac{k_{\text{B}} T}{m} \int_0^\infty C_{vv}(t) \mathrm{d}t. \tag{2.33}$$

Residence Time of First Shell Particles on the first shell can escape from there and then be substituted by outer molecules. The rate of this exchange process is characteristic of each kind of atom or molecule. The mean residence time of the particles in the first shell could be evaluated from

$$n(t) = \left\langle \frac{1}{N_{1\text{st}}} \sum_{i=1}^{N_{1\text{st}}} \theta_i(t) \theta_i(0) \right\rangle, \tag{2.34}$$

where the sum runs over the $N_{1\text{st}}$ solvation molecules present in the first shell at $t = 0$, and θ_i is unity if the i^{th} molecule is in the first shell and it is zero otherwise. Given the high lability of the first hydration shell, $n(t)$ is evaluated by allowing first shell molecules to leave the first shell for a maximum period of time t^*. As in previous works [45], in this thesis a $t^* = \infty$ has been used. The resulting function can be fitted with a double exponential function $\tilde{n}(t) = A \exp(-k_1 t) + (1 - A) \exp(-k_2 t)$. The integral of this function yields the characteristic residence time:

$$\tau_{1\text{st}} = \int_0^\infty n(t) \mathrm{d}t, \tag{2.35}$$

where the integral is evaluated numerically up to $t = 5$ ps using $n(t)$ and analytically up to $t = \infty$ using $\tilde{n}(t)$.

Rotation of molecules in the first shell The study of reorientational motions has been performed by means of the time correlation function $C_2^{\mathrm{OH}}(t)$ defined as follows:

$$C_2^{\mathrm{OH}}(t) = \langle P_2 \left(\vec{u}_{\mathrm{OH}}(t) \cdot \vec{u}_{\mathrm{OH}}(0) \right) \rangle \tag{2.36}$$

where $\vec{u}_{\mathrm{OH}}$ is the unitary vector along the O–H bond of water molecules, and P_2 is the second Legendre polynomial, i.e. $P_2(\cos\theta) = \frac{1}{2}\left(3\cos^2\theta - 1\right)$. This correlation function shows a backscattering-like minimum, known as the free rotor frequency, and then decays exponentially. The long time decay can be fitted with a single exponential function $\tilde{C}_2^{\mathrm{OH}}(t) = A\exp(-kt)$. In order to interpret the $C_2^{\mathrm{OH}}(t)$ function, it is convenient to calculate its time integral, yielding the so-called reorientational correlation time

$$\tau_2^{\mathrm{OH}} = \int_0^\infty C_2^{\mathrm{OH}}(t)\mathrm{d}t, \tag{2.37}$$

which basically indicates the mean time employed by a water molecule to rotate around the O–H direction. The above integral was calculated numerically up to $t = 5$ ps using $C_2^{\mathrm{OH}}(t)$ and then analytically up to $t = \infty$ using $\tilde{C}_2^{\mathrm{OH}}(t)$.

Hydration shell rotation Analogously to the previous one, the solvation shell rotation around the ion can be characterized by computing the time correlation function $C_2^{\mathrm{OCl}}(t)$ where in Eq. 2.36 the unitary vector along O–H bond is substituted by the unitary vector joining the chloride ion to oxygen atoms $\vec{u}_{\mathrm{OCl}}$. The rotational time of the solvation shell τ_2^{OCl} was evaluated as in eq. 2.37.

References

[1] H Poincaré. Sur le Problème des Trois Corps et les Équations de la Dynamique. *Acta Math.*, 13:1–270, 1890.

[2] B. J. Alder and T. E. Wainwright. Studies in Molecular Dynamics. I. General Method. *J. Chem. Phys.*, 31(2):459, 1959.

[3] Dieter W. Heermann. *Computer Simulation Methods in Theoretical Physics*. Springer, Berlin, New York, Paris, 1990.

[4] M. P. Allen and D. J. Tildesley. *Computer Simulation of Liquids*. Oxford science publications. Oxford University Press, reprint edition, 1987.

[5] W. F. van Gunsteren and H. J. C. Berendsen. Computer Simulation of Molecular Dynamics: Methodology, Applications, and Perspectives in Chemistry. *Angew. Chemie Int. Ed. English*, 29(9):992–1023, sep 1990.

[6] D. M. Heyes. *The Liquid State: Applications of Molecular Simulations*. Wiley, Chichester, 1998.

[7] M. E. Tuckerman and G. J. Martyna. Understanding Modern Molecular Dynamics: Techniques and Applications. *J. Phys. Chem. B*, 104(2):159–178, jan 2000.

[8] D. Frenkel, B. Smit, and M. A. Ratner. Understanding Molecular Simulation: From Algorithms to Applications. *Phys. Today*, 50(7):66, 1997.

[9] A. Rahman. Correlations in the Motion of Atoms in Liquid Argon. *Phys. Rev.*, 136(2A):A405—-A411, oct 1964.

[10] L. Verlet. Computer "Experiments" on Classical Fluids. I. Thermodynamical Properties of Lennard-Jones Molecules. *Phys. Rev.*, 159(1):98–103, jul 1967.

[11] R. W. Hockney. The Potential Calculation and Some Applications. *Methods Computational Physics*, (9):136, 1970.

[12] H. J. C. Berendsen, J. P. M. Postma, W. F. van Gunsteren, A. DiNola, and J. R. Haak. Molecular Dynamics with Coupling to an External Bath. *J. Chem. Phys.*, 81(8):3684–3690, 1984.

[13] T. Morishita. Fluctuation Formulas in Molecular-Dynamics Simulations with the Weak Coupling Heat Bath. *J. Chem. Phys.*, 113(8), 2000.

[14] Philippe H. Hünenberger. Thermostat Algorithms for Molecular Dynamics Simulations. pages 105–149. jan 2005.

[15] R. Car and M. Parrinello. Unified Approach for Molecular Dynamics and Density-Functional Theory. *Physical Review Letters*, 55(22):2471–2474, 1985.

[16] D. S. Sholl and J. A. Steckel. *Density Functional Theory: A Practical Introduction*. John Wiley & Sons, Inc., Hoboken, NJ, USA, mar 2009.

[17] A. Curioni, M. Sprik, W. Andreoni, and H. Schiffer. Density Functional Theory-Based Molecular Dynamics Simulation of Acid-Catalyzed Chemical Reactions in Liquid Trioxane. *J. Am. Chem. Soc.*, III(5):7218–7229, 1997.

[18] J. Blumberger, L. Bernasconi, I. Tavernelli, R. Vuilleumier, and M. Sprik. Electronic Structure and Solvation of Copper and Silver Ions: A Theoretical Picture of a Model Aqueous Redox Reaction. *J. Am. Chem. Soc.*, 126(1):3928–3938, 2004.

[19] P. R. L. Markwick, N. L. Doltsinis, and D. Marx. Targeted Car-Parrinello Molecular Dynamics: Elucidating Double Proton Transfer in Formic Acid Dimer. *J. Chem. Phys.*, 122(5):54112, 2005.

[20] A. De Vita, G. Galli, A. Canning, and R. Car. A Microscopic Model for Surface-Induced Diamond-to-Graphite Transitions. *Nature*, 379(6565):523–526, feb 1996.

[21] C. Cavazzoni, G. L. Chiarotti, S. Scandolo, E. Tosatti, M. Bernasconi, and M. Parrinello. Superionic and Metallic States of Water and Ammonia at Giant Planet Conditions. *Science*, 283(5398):44–46, 1999.

[22] K Laasonen, M Sprik, M Parrinello, and R Car. "Ab Initio" Liquid Water. *The Journal of Chemical Physics*, 99(11):9080, 1993.

[23] I. Bakó, J. Hutter, and G. Pálinkás. Car–Parrinello Molecular Dynamics Simulation of the Hydrated Calcium Ion. *J. Chem. Phys.*, 117(21):9838, 2002.

[24] L. M. Ramaniah, M. Bernasconi, and M. Parrinello. Ab Initio Molecular-Dynamics Simulation of K^+ Solvation in Water. *J. Chem. Phys.*, 111(4):1587, 1999.

[25] J. M. Heuft and E. J. Meijer. Density Functional Theory Based Molecular-Dynamics Study of Aqueous Chloride Solvation. *The Journal of Chemical Physics*, 119(22):11788, 2003.

[26] A. J. Stone. *The Theory of Intermolecular Forces*, volume 32. 1996.

[27] M. Born and R. Oppenheimer. Zur Quantentheorie der Molekeln. *Ann. Phys.*, 20(84):457–484, 1927.

[28] E. Meerbach, E. Dittmer, I. Horenko, C. Schütte, and R. Vuilleumier. *Computer Simulations in Condensed Matter Systems: From Materials to Chemical Biology Volume 1*, volume 703. 2006.

[29] R. P. Feynman. Forces in Molecules. *Physical Review*, 56(4):340–343, 1939.

[30] P. Hohenberg and W. Kohn. The Inhomogeneous Electron Gas. *Phys. Rev.*, 136:B864, 1964.

[31] W. Kohn and L. J. Sham. Self-Consistent Equations Including Exchange and Correlation Effects. *Physical Review*, 140(4A):A 1133, 1965.

[32] S. H. Vosko, L. Wilk, and M. Nusair. Accurate Spin-Dependent Electron Liquid Correlation Energies for Local Spin-Density Calculations - a Critical Analysis. *Can. J. Phys.*, 58:1200, 1980.

[33] J. P. Perdew and A. Zunger. Self-Interaction Correction to Density-Functional Approximations for Many-Electron Systems. *Phys. Rev. B*, 23(10):5048–5079, 1981.

[34] J. P. Perdew and Y. Wang. Accurate and Simple Analytic Representation of the Electron-gas Correlation Energy. *Phys. Rev. B*, 45(23):13244–13249, jun 1992.

[35] C. Lee, W. Yang, and R. G. Parr. Development of the Colle-Salvetti Correlation-Energy Formula into a Functional of the Electron Density. *Physical Review B*, 37(2):785–789, jan 1988.

[36] A. D. Becke. A New Mixing of Hartree–Fock and Local Density-Functional Theories. *J. Chem. Phys.*, 98(2):1372, 1993.

[37] Nicola Marzari and David Vanderbilt. Maximally-localized generalized Wannier functions for composite energy bands. *Physical Review B*, 56(20):22, nov 1997.

[38] N. Marzari, A. A. Mostofi, J. R. Yates, I. Souza, and D. Vanderbilt. Maximally Localized Wannier Functions: Theory and Applications. *Reviews of Modern Physics*, 84(4):1419–1475, 2012.

[39] P. L. Silvestrelli and M. Parrinello. Structural, Electronic, and Bonding Properties of Liquid Water from First Principles. *Journal of Chemical Physics*, 111(8):3572–3580, 1999.

[40] Elvira Guàrdia, Ioannis Skarmoutsos, and Marco Masia. On ion and molecular polarization of halides in water. *Journal of Chemical Theory and Computation*, 5(6):1449–1453, 2009.

[41] J. Kohanoff and J.-P. Hansen. Statistical properties of the dense hydrogen plasma: An *ab initio* molecular dynamics investigation. *Phys. Rev. E*, 54(1):768–781, jul 1996.

[42] T. J. Lenosky, J. D. Kress, I. Kwon, A. F. Voter, B. Edwards, D. F. Richards, S. Yang, and J. B. Adams. Highly Optimized Tight-Binding Model of Silicon. *Phys. Rev. B*, 55(3):1528–1544, 1997.

[43] J. E. Lennard-Jones. On the Forces Between Atoms and Ions. *Proc. R. Soc. A Math. Phys. Eng. Sci.*, 109(752):584–597, dec 1925.

[44] F. Ercolessi and J. B. Adams. Interatomic Potentials from First-Principles Calculations: The Force-Matching Method. *Europhysics Letters (EPL)*, 26(8):583–588, jun 1994.

[45] E. Guàrdia, D. Laria, and J. Martí. Reorientational Dynamics of Water in Aqueous Ionic Solutions at Supercritical Conditions: A Computer Simulation Study. *Journal of Molecular Liquids*, 125(2-3):107–114, apr 2006.

Chapter 3

Force Fields and Water Models

Classical Molecular Dynamics attempts to simplify the huge complexity of the electronic structure of the atoms and thus, that of the interaction between them. This simplification must balance the needs to keep a reasonable computational cost and maintain a good level of accuracy. The potential energy of the simulated system, U_{tot}, can be decomposed as a sum of *intermolecular*, U_{inter}, and *intramolecular*, U_{intra}, terms [1]

$$U_{\text{tot}} = U_{\text{inter}} + U_{\text{intra}}, \tag{3.1a}$$

$$U_{\text{inter}} = \sum_{\text{LJ}} 4\epsilon_{ij} \left[\left(\frac{\sigma_{ij}}{r_{ij}} \right)^{12} - \left(\frac{\sigma_{ij}}{r_{ij}} \right)^{6} \right] + \sum_{\text{elec}} \frac{q_i q_j}{r_{ij}}, \tag{3.1b}$$

$$U_{\text{intra}} = \sum_{\text{bonds}} \frac{1}{2} k_r (r - r_0)^2 + \sum_{\text{angles}} \frac{1}{2} k_\theta (\theta - \theta_0)^2. \tag{3.1c}$$

Equation 3.1b describes the interaction between different molecules. r_{ij} is the distance between two interacting particles and q_i and q_j are the charges of those particles. The first term of 3.1b accounts for the short range forces due to the fluctuations in electronic structure of the atoms and it takes the form the *12-6 Lennard Jones* potential [2]. The second term describes the usual Couloumb interaction between electrical charges. The value of these charges is set as the parameters of the Force Field (FF). The Lennard-Jones potential is an attractive potential composed by a very step potential wall that acconts for the Pauli repulsion among electrons and an attractive term that models the Van der Waals interactions. σ_{ij} and ϵ_{ij} are the Lennard-Jones potential parameters that determine the strength and range of the interaction. The LJ potential is usually

implemented in computer simulations through the alternative expression

$$V_{\mathrm{LJ}} = \frac{A}{r^{12}} - \frac{C}{r^6} \tag{3.2}$$

where the parameters A and C translate as

$$A = 4\epsilon\sigma^{12}, \tag{3.3a}$$

$$B = 4\epsilon\sigma^{6}. \tag{3.3b}$$

When the interaction takes place between atoms of different species the parameters from both particles must be combined following one of a large variety of merging rules. For the LJ potential the simple Lorentz-Berthelot rule

$$\sigma_{ij} = \frac{\sigma_{ii} + \sigma_{jj}}{2}, \tag{3.4a}$$

$$\epsilon_{ij} = \sqrt{\epsilon_{ii}\epsilon_{jj}}, \tag{3.4b}$$

is widely used.

Interactions like the Lennard Jones potential are short ranged, i.e. they decay faster than the volume grows when the inter particle distance increases. This means that a cut-off can be set so only those particles within a certain distance from each other will interact. This cut-off avoids an infinite calculation of the energy over all the particles from the infinite replicated simulation cells. Of course leaving out the contribution of those particles outside the cut-off will introduce a certain amount of error into the simulation but it will be manageable as long as the cut-off is set to a high enough value. Usually a minimum image convention is applied so each particle interacts only once with the rest of the particles of the system. For each particle, only the closer version is selected whether it is the original one or one of its periodic replicas.

While the Lennard Jones potential decays as r^{-6} and can be neglected, this is not the case for the electrostatic interaction which decays as r^{-1}. Fortunately, the infinite summation can still be avoided. The *Ewald* method [3] utilizes the periodic structure of the replicated simulation cell to move the calculation of the long-range summation from the real space to a Fourier space. The original long-range interaction is divided into two contributions,

$$U_{\mathrm{el}} = U_{\mathrm{el}}^{\mathrm{real}} + U_{\mathrm{el}}^{\mathrm{recip}}, \tag{3.5}$$

a short range one that can be computed in the real space and a long-range one that can be calculated over the reciprocal space through a Fourier transform. This method

increases the convergence speed of the energy calculation so it can be used to a high level of accuracy. This speed and precision makes the Ewald summation the usual method of choice to tackle the calculation of long-range interactions.

Equation 3.1c describes the potential energy between the inner parts that conforms a molecule. The interactions between same molecule atoms are usually decomposed as a stretching movement around an equilibrium point r_0 and as a bending movement around an equilibrium angle θ_0. These forces are commonly described with harmonic functions defined by the strengths of the harmonic potentials k_r and k_θ and their respective equilibrium points.

Astonishingly simple interaction models like the Lennard-Jones potential are capable of achieving remarkable good results while keeping low computational costs. To reproduce the behaviour of specific molecules different models can be used. This models can incorporate different approximations such as the use of rigid or flexible molecules, limit the number of interaction points of the molecule or introduce the polarization of the molecule.

Several water models have been used in the search of the best agreement with the CPMD results [4]. These models include the widely used SPC and SPC/E models, the polarizable model RPOL and a variation of the SPC model.

3.1 Semi-epirical Force Fields

3.1.1 SPC and SPC/E models

In the case of the water molecules the SPC (Simple Point Charge) and SPC/E models are an option widely used in computational chemistry [5]. The SPC water model is a rigid model composed of three electrostatic interaction points, one at each one of the atoms of the molecule, and a Lennard-Jones potential at the oxygen site. The separation between the oxygen and each of the hydrogen atoms is fixed at $r(\mathrm{OH}) = 1\text{Å}$, and the overture of the molecule is set at 109.47°.

The SPC/E water model is a slight variation of the SPC model. It adds a correction that accounts for an effective average constant polarization of the water molecule of 2.351 D. Since the position and charge of the interacting sites of the water molecule are constant the resulting dipole is also constant and generates an effective increase in the total energy of 1.25 kcal/mol.

3.2 Polarizable Point Dipole Models

Both previous Force Fields rely on set of fixed charges in order to reproduce the electrostatic interaction between atoms, thus dismissing any explicit description of the electronic polarization. These fixed charges can be adjusted in order to attempt to minimize the effects that arise from the polarization absence. While this approximation is usually enough for a wide set of systems it is fundamentally wrong [6, 7] and sometimes an explicit treatment of the polarization must be implemented [8–10]. The implicit account of polarization in the SPC/E water model can't take into account the dynamic effects of the dipoles distribution. This takes special relevance when highly polarizability species are involved. Many efforts have been done in order to introduce polarization explicitly into different fields such as liquid-air interfaces [10, 11], liquid water [12, 13], water-salt solutions [8, 9, 12, 14–17], among others [18–20]. These efforts can be classified into one of three classes: polarizable point dipole models (PPDM), charge fluctuating models and classical Drude oscillator models [21–29]. In this work, the polarizable point dipole induction model will be used when an explicit use of polarization is needed.

Working inside the PPDM framework, while point charges are usually kept constant, new sites with induced three-dimensional point dipoles are added. These point dipoles respond and adjust to the changes in the electric field as the simulation advances. These dipoles will contribute to the total energy of the system as

$$u_i^{\mathrm{pol}} = -\vec{\mu}_i \cdot \vec{E}_i^{\mathrm{q}} - \vec{\mu}_i \cdot \vec{E}_i^{\mu} + \frac{1}{2}\vec{\mu}_i \cdot \hat{\alpha}_i^{-1} \cdot \vec{\mu}_i, \tag{3.6}$$

where $\vec{\mu}_i$ and $\hat{\alpha}_i$ are the induced dipole moment and the polarizability tensor for the dipole site i. The first two terms accounts for the interaction between the dipole and the point charges and the dipole and the other dipoles. The last term is the polarization term and gives a sense of the energy needed for the formation of the dipole. If the polarizability can be considered isotropic, the non-diagonal elements of the tensor are zero and the diagonal ones are equal to each other; thus, $\hat{\alpha}_i$ can be treated as an scalar quantity.

3.2.1 RPOL

Due to the highly polar character of the water molecule it pays off to increase the level of detail of the electronic structure and account for the polarization of the molecule at expense of a higher computational effort. The RPOL water model introduces an explicit dipole moment into the SPC/E model adding polarizable sites at the oxygen

and hydrogen locations with a polarizability value of $\alpha_{\mathrm{O}} = 0.528\text{Å}^3$ and $\alpha_{\mathrm{H}} = 0.170\text{Å}^3$ respectively. The partial electrostatic charges of these sits are also altered as $q_{\mathrm{O}} = -0.730$ C and $q_{\mathrm{H}} = +0.365$ C.

3.3 Force Matching Force Fields

Following the same Force Matching scheme of these work, a set of variations of the original SPC model with re-adjusted parameters have been recently obtained [30]. These potentials use different damping functions to correct the attraction term of the Lennard-Jones potential. These damping functions are explained with more detail later in section 3.3.1. For each ion-water interaction potential fitted, the corresponding one of these potentials has been used to model the solvating water. In this work these potentials will be referenced as SPC-FM.

3.3.1 Damping

Electrostatic damping

The use of electrostatic damping functions has revealed itself as a powerful tool since it's introduction by Thole in 1981 [31]. In an attempt to tackle the *polarization catastrophe* Thole discarded the point charge approximation at short ranges and diluted the charge distribution through the use of a damping function. This damping function is only relevant at short distance so at long range the point charge behavior is conserved. The damping of the static charges is introduced in the Couloumb interaction energy function between two charges as

$$u_{ij}^{\mathrm{qq}} = q_i q_j \int\int \frac{\rho_i^N(\vec{r}_i)\rho_j^N(\vec{r}_j)}{|\vec{r}_i - \vec{r}_j|} \mathrm{d}\vec{r}_i \mathrm{d}\vec{r}_j, \tag{3.7}$$

where q_i and q_j are the value of the damped charges, $\vec{r}_i$ and $\vec{r}_j$ their positions and $\rho_i^N(\vec{r}_i)$ and $\rho_j^N(\vec{r}_j)$ are normalized distributions.

Dispersion Damping

Many damping functions are available such as linear, exponential and gaussian functions. Because of previous positive results, two functions, the Tang-Toennies dispersion damping and a Fermi like function, have been used in combination with the different interaction models.

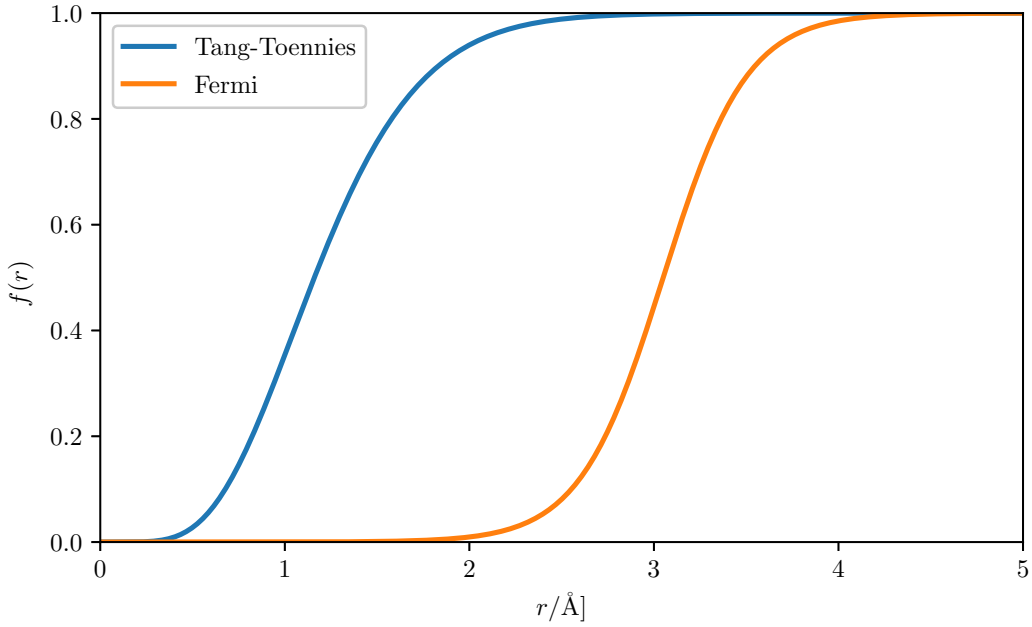

Fig. 3.1 Tang-Toennies damping with $d_{\mathrm{TT}} = 5.78\,\text{Å}^{-1}$ and Fermi damping with $d_{\mathrm{FE}} = 13.38\,\text{Å}^{-1}$ and $R_{\mathrm{FE}} = 3.05\,\text{Å}$.

Tang-Toennies Damping The first screening function used in the present work is the Tang-Toennies dispersion damping function [32] which takes the form

$$f_{\mathrm{TT}}(r) = 1 - \exp(-d_{\mathrm{TT}} r) \sum_{k=0}^{6} \frac{(d_{\mathrm{TT}} r)^k}{k!}, \tag{3.8}$$

where d_{TT} is the parameter that determines the length of the short range interaction. Figure 3.1 contains an example of the Tang-Toennies damping profile.

Fermi Damping The second damping function used is a Fermi like function [33] as

$$f_{\mathrm{FE}}(r) = \frac{1}{1 + \exp\left[-d_{\mathrm{FE}}\left(\frac{r}{R_{\mathrm{FE}}} - 1\right)\right]}, \tag{3.9}$$

where R_{FE} gives a sense of the size of the atoms, and d_{FE} is an adjustable parameter. Figure 3.1 contains an example of the Fermi damping profile.

	SPC/E	RPOL	SPC-FM No damping	SPC-FM Tang-Toennies	SPC-FM Fermi
r_{OH} [Å]	1.0	1.0	0.995	0.995	0.995
HÔH angle [deg]	109.47	109.47	105.6	105.6	105.6
$A \cdot 10^{-3}$ [kcalÅ^{12}/mol]	629.4	726.9	377.743	533.722	478.881
C [kcalÅ^{6}/mol]	625.5	682.1	−1319.455	287.224	493.883
q_{O} [C]	−0.8476	−0.730	−0.884	−0.881	−0.878
q_{H} [C]	+0.4238	+0.365	0.442	0.4405	0.439
α_{O} [Å^{3}]	-	0.528	-	-	-
α_{H} [Å^{3}]	-	0.170	-	-	-
d [Å^{-1}]	-	-	-	0.762	33.1
R_{FE} [Å]	-	-	-	-	2.75

Table 3.1 Parameters for the SPC/E, RPOL and SPC-FM water models.

References

[1] A. D. MacKerell. Empirical Force Fields. In Jie Xu, Ying, Xu, Dong, Liang, editor, *Computational Methods for Protein Structure Prediction and Modeling*, chapter 2. Springer, New York, 2007.

[2] J. E. Lennard-Jones. On the Forces Between Atoms and Ions. *Proc. R. Soc. A Math. Phys. Eng. Sci.*, 109(752):584–597, dec 1925.

[3] D. C. Rapaport. *The Art of Molecular Dynamics Simulation*. Cambridge University Press, 2004.

[4] B. Guillot. A reappraisal of what we have learnt during three decades of computer simulations on water. *Journal of Molecular Liquids*, 101(1-3):219–260, nov 2002.

[5] H. J. C. Berendsen, J. P. M. Postma, W. F. van Gunsteren, and J. Hermans. Interaction Models for Water in Relation to Protein Hydration. In *Intermolecular Forces*, pages 331–342. Springer Netherlands, 1981.

[6] Anthony J. Stone. Intermolecular Potentials. *Science (New York, N.Y.)*, 321(5890):787–789, 2008.

[7] William L. Jorgensen. Special Issue on Polarization. *Journal of Chemical Theory and Computation*, 3(6):1877, 2007.

[8] Elvira Guàrdia, Ioannis Skarmoutsos, and Marco Masia. On ion and molecular polarization of halides in water. *Journal of Chemical Theory and Computation*, 5(6):1449–1453, 2009.

[9] Marco Masia and Rossend Rey. Diffusion Coefficient of Ionic Solvation Shell Molecules. *Journal of Chemical Physics*, 122(9), 2005.

[10] P. Jungwirth, B. J. Finlayson-Pitts, and D. J. Tobias. Introduction: Structure and Chemistry at Aqueous Interfaces. *Chemical Reviews*, 106(4):1137–1139, 2006.

[11] I-Feng W. Kuo and Christopher J Mundy. An ab Initio Molecular Dynamics Study of the Aqueous Liquid-Vapor Interface. *Science*, 303(5658):658–660, jan 2004.

[12] M. Salanne, R. Vuilleumier, P. A. Madden, C. Simon, P. Turq, and B. Guillot. Polarizabilities of Individual Molecules and Ions in Liquids from First principles. *Journal of Physics: Condensed Matter*, 20(49):494207, 2008.

[13] F. Paesani and G. A. Voth. Quantum Effects Strongly Influence the Surface Premelting of Ice. *The Journal of Physical Chemistry C*, 112(2):324–327, 2008.

[14] D. Bucher and S. Kuyucak. Polarization of Water in the First Hydration Shell of K^+ and Ca^{2+} Ions. *The journal of physical chemistry. B*, 112(35):10786–90, 2008.

[15] C. D. Wick and S. S. Xantheas. Computational Investigation of the first Solvation Shell Structure of Interfacial and Bulk Aqueous Chloride and Iodide Ions. *J. Phys. Chem. B*, 113(13):4141–4145, 2009.

[16] M. Souaille, H. Loirat, D. Borgis, and M. P. Gaigeot. MDVRY: a Polarizable Classical Molecular Dynamics Package for Biomolecules. *Comput. Phys. Commun.*, 180(2):276–301, 2009.

[17] Collin D. Wick. Electrostatic dampening dampens the anion propensity for the air-water interface. *J. Chem. Phys.*, 131(8):84715, 2009.

[18] B. Qiao, C. Krekeler, R. Berger, L. Delle Site, and C. Holm. Effect of Anions on Static Orientational Correlations, Hydrogen Bonds, and Dynamics in Ionic Liquids: A Simulational Study. *Journal of Physical Chemistry B*, 112(6):1743–1751, 2008.

[19] Edward Harder, Alexander D. MacKerell, and Benoît Roux. Many-body polarization effects and the membrane dipole potential. *Journal of the American Chemical Society*, 131(8):2760–2761, 2009.

[20] Vicente Bitrián and Joaquim Trullàs. Molecular Dynamics Study of Polarization Effects on AgI. *The journal of physical chemistry. B*, 112(6):1718–1728, 2008.

[21] L. Perera and M. L. Berkowitz. Many-Body Effects in Molecular Dynamics Simulations of $Na^+(H_2O)$n and $Cl^-(H_2O)$n Clusters. *The Journal of Chemical Physics*, 95(3):1954, 1991.

[22] L. X. Dang, J. E. Rice, J. Caldwell, and P. A. Kollman. Ion Solvation in Polarizable Water: Molecular Dynamics Simulations. *Journal of the American Chemical Society*, 113(7):2481–2486, mar 1991.

[23] S. J. Stuart and B. J. Berne. Effects of Polarizability on the Hydration of the Chloride Ion. *Journal of Physical Chemistry*, 100(29):11934–11943, 1996.

[24] H. A. Stern, G. A. Kaminski, J. Banks, R. Zhou, B. J. Berne, and R. A. Friesner. Fluctuating Charge, Polarizable Dipole, and Combined Models: Parameterization from ab Initio Quantum Chemistry. *The Journal of Physical Chemistry B*, 103(22):4730–4737, 1999.

[25] S. W. Rick and S. J. Stuart. Potentials and Algorithms for Incorporating Polarizability in Computer Simulations. In *Reviews in computational chemistry*, volume 18, chapter 3, page 89. Wiley1999, 2002.

[26] H. Yu and W. F. van Gunsteren. Accounting for Polarization in Molecular Simulation. *Computer Physics Communications*, 172(2):69–85, nov 2005.

[27] M. Masia, M. Probst, and R. Rey. On the Performance of Molecular Polarization Methods. I. Water and Carbon Tetrachloride Close to a Point Charge. *The Journal of Chemical Physics*, 121(15):7362, 2004.

[28] Pedro E. M. Lopes, Benoit Roux, and Alexander D. MacKerell. Molecular Modeling and Dynamics Studies with Explicit Inclusion of Electronic Polarizability: Theory and Applications. *Theoretical Chemistry Accounts*, 124(1-2):11–28, sep 2009.

[29] P. Cieplak, F. Dupradeau, Y. Duan, and J. Wang. Polarization Effects in Molecular Mechanical Force Fields. *Journal of Physics: Condensed Matter*, 21(33):333102, aug 2009.

[30] Paolo Nicolini, Elvira Guàrdia, and Marco Masia. Shortcomings of the Standard Lennard–Jones Dispersion term in Water Models, Studied with Force Matching. *The Journal of Chemical Physics*, 139(18):184111, 2013.

[31] B.T. T Thole. Molecular Polarizabilities Calculated with a Modified Dipole Interaction, 1981.

[32] K. T. Tang and J. Peter Toennies. An Improved Simple Model for the van der Waals Potential Based on Universal Damping Functions for the Dispersion Coefficients. *The Journal of Chemical Physics*, 80(8):3726, apr 1984.

[33] Q. Wu and W. Yang. Empirical Correction to Density Functional Theory for van der Waals Interactions. *The Journal of Chemical Physics*, 116(2):515, 2002.

Chapter 4

Ion Water Carr-Parrinelo Simulations

4.1 Computational details

The aim of this thesis is to characterize the interaction between a certain set of ions (F^-, Cl^-, Br^-, I^-, Li^+, Na^+, K^+, Mg^{2+}, Ca^{2+}) and water through the Force Matching algorithm. In order to do so, a set of Car-Parrinello Molecular Dynamics [1] (CPMD) where performed with the package `CPMD` [2] to be used as reference for the matching process. The BLYP density functional [3, 4] was used for the electronic structure calculations. The cutoff for the wavefunction was set to 80 Ry, the time step was set to 4 a.u. and the fictitious mass for the orbital was chosen to be 400 a.m.u. In the present study we have used dispersion–corrected atom–centered pseudopotentials (DCACPs) [5] in the Troullier–Martins [6] format for oxygen and hydrogen. Production runs of 15 ps in the microcanonical ensemble followed by an NVT equilibration run of 3 ps. The initial configuration was taken from classical molecular dynamics simulations. For some of the ions (Ca^{2+}, Cl^-, K^+, Li^+, Mg^{2+} and Na^+) ionic and molecular dipole moments where computed using the Wannier center [7, 8] analysis as explained in Refs. [9, 10]. The temperature of the simulations was set to $T = 330\,\mathrm{K}$ and the size of the simulation box was fixed to achieve a density of $\rho = 1\,\mathrm{g/cm^3}$.

Following the procedures previously explained in section 2.3.2, several structural and dynamical properties have been calculated from the data obtained from these CPMD simulations in order to be used as a test reference for the matching process. In order to analyse the effects due to the presence of the ion, when possible, the study of these properties has taken into account the differences that arise from the water molecules belonging to the first solvation shell, the second one or the bulk.

4.2 Structural properties

4.2.1 Radial Distribution Function

Particles inside a liquid tend to self arrange between them forming bonds that causes the molecules to adopt a determinate distance from one to another and forming certain angles between them. When a different kind of particle is introduced among liquid water it alters the original organization among the molecules. Due to the polar nature of the water molecule, showing the oxygen atoms an excess of negative charge and the hydrogen atoms a lack of one, when an ion is solvated among water molecules, a fairly strong couloumbic interaction appears between the water molecules and the charged atoms. These forces determine in great measure how the solvation structure of water molecules around the central ion is formed. The Radial Distribution Function (RDF) is a measure of how two kinds of particles (A and B) are arranged around each others. The density of B particles at a given distance of the A particle is averaged and rated against the average density of B particles for the whole system.

Usually, a RDF presents a depletion zone for the lowest values of r where no particles are present. This zone accounts for the Pauli repulsion among particles that prevents them from collapsing on each other. Other particles take advantage of this void and get located at the end of it, what translates into a well pronounced first peak. As each of these opportunist particles has its own exclusion zone, a more or less defined depletion zone follows this first peak. A succession of peaks and valleys keep alternating getting attenuated until it fades away as the function tends to $g(r) \to 1$ which is the average probability of finding a particle in a random position of the liquid. Each one of these peaks between their limiting valleys can be considered as, and are in fact called, shells. When the particles that are accounted for are from a solvent, the more precise term solvation shell is usually used. As the solvent in this works is constituted by water, the term hydration shell is indistinctly used with the other two. Figures 4.1 and 4.2 show the computed RDFs ($g(r)$) for each one of the anions and the cations respectively. Ion-oxygen and ion-hydrogen RDFs are plotted in blue and orange lines respectively. The corresponding Coordination Functions ($N(r)$) are also represented with dashed lines. The asymmetric charge distribution of the water molecules causes that their orientation varies whether if the central ion has a positive or negative net charge. This behaviour causes that the first peak of the plot corresponds to the oxygen distribution in the case of the anions and to the hydrogen distribution in the case of the cations.

As should be expected the distance at which the first hydration shell is situated grows with the size of the central ion and decreases with the value of its net charge. Table

4.1 gathers the positions of the first peaks and valleys for both the ion-oxygen and ion-hydrogen RDFs. Ions of smaller size tend to have a more defined shell structure while bigger ions usually have a rather unstructured and diffuse limit between shells. Most ions have a significant presence of water molecules between the first two water layers. The calcium ion presents a deep minimum and only the lithium and the magnesium ions show a complete oxygen depletion range between the first and the second shells. The lack of shell definition gets enhanced by the limited statistics of the simulations and grows to the point where the distinction between the first and the second shell may disappear. This fuzziness between shells take the most relevance in the case of the potassium ion and especially for the iodide ion. The impossibility to determine a clear limit between each one of the shells and the bulk affects to all the analysis aimed to determine the the influence of the ion into the water medium. Higher charges also contribute strongly to the presence of sharper peaks and deeper valleys. Divalent ions tend to show higher structured water shells than monovalent ions of comparable size. Tables 4.2 and 4.3 also contain reference data of diverse nature (MD simulations, CPMD simulations and experimental results) for the positions and values of the first two peaks and valleys of the ion-oxygen RDFs. These tables are quite sparse due to the wide scope of the study, making hard to find works that comprehend all of the nine studied ions. From the agreement among the different references it can be seen that the position of the oxygen peaks has been consensually determined within a couple of tenths of an Angstrom for all the ions. This consensus fades slightly in regard to the position of the valleys. This may be a consequence of the already mentioned blurred nature of the limits between different hydration shells. The maximum value of the different RDF first peaks show huge differences depending on the nature of the source consulted. MD results tend to present significantly higher values than CPMD simulations. Unfortunately, the spread of results within each method is significant. Due to the fact that experimental data regarding this question is hard to come by, these discrepancies are difficult to solve. On the other side, the few available RDF values for the second peak and both minima is quite consistent. Again, the lack of references prevents from considering this question as settled, especially in the absence of experimental results.

4.2.2 Coordination numbers

Figures 4.3 and 4.4 show the population distribution of the first and second anionic and cationic coordination shells respectively. The limit between the first and the second shells and the bulk have been defined through the position of the local minima of the RDF computed for the water molecules centres of mass. This criterion has been used through

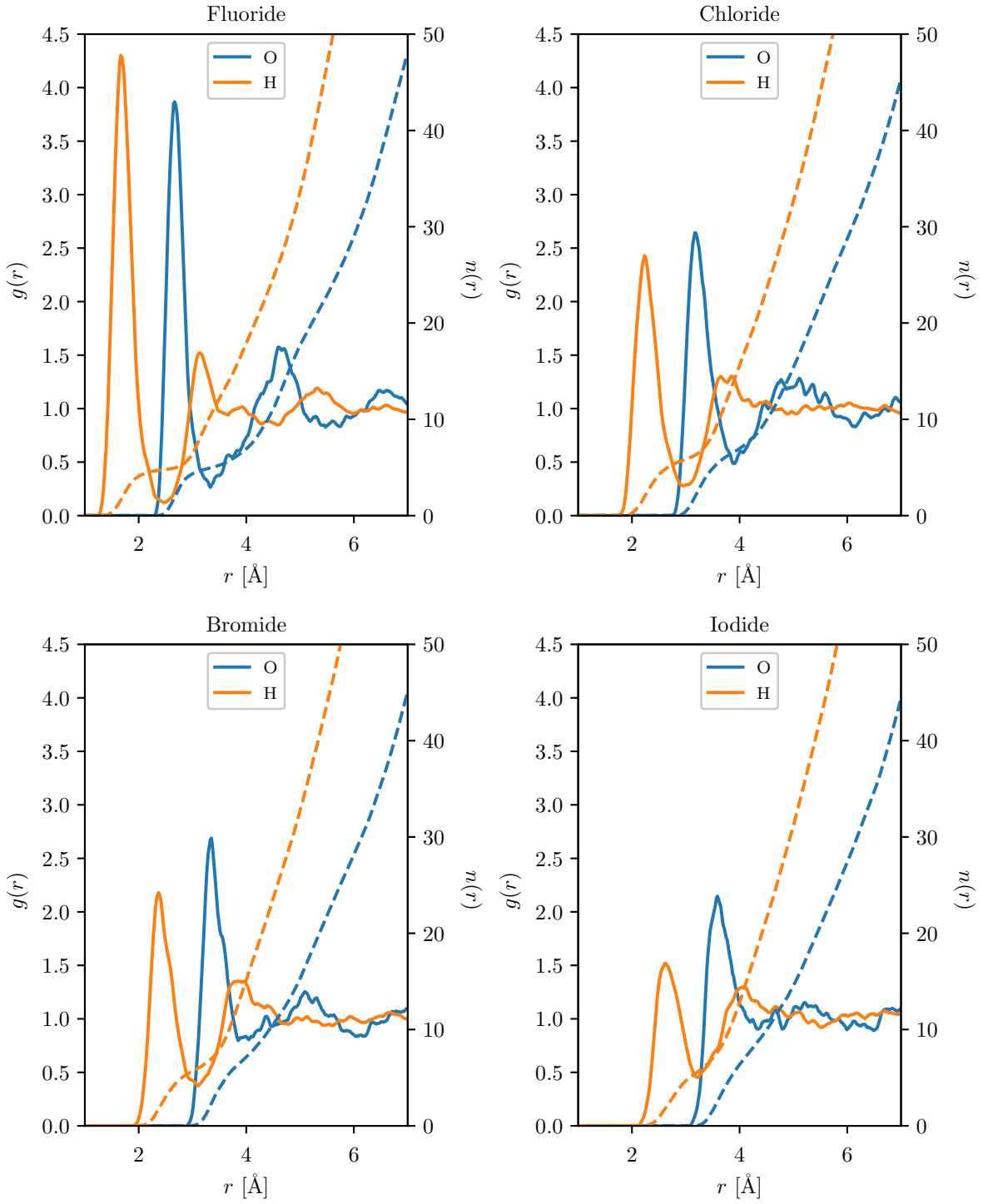

Fig. 4.1 Ion-oxygen and ion-hydrogen RDFs and coordination numbers for the anions.

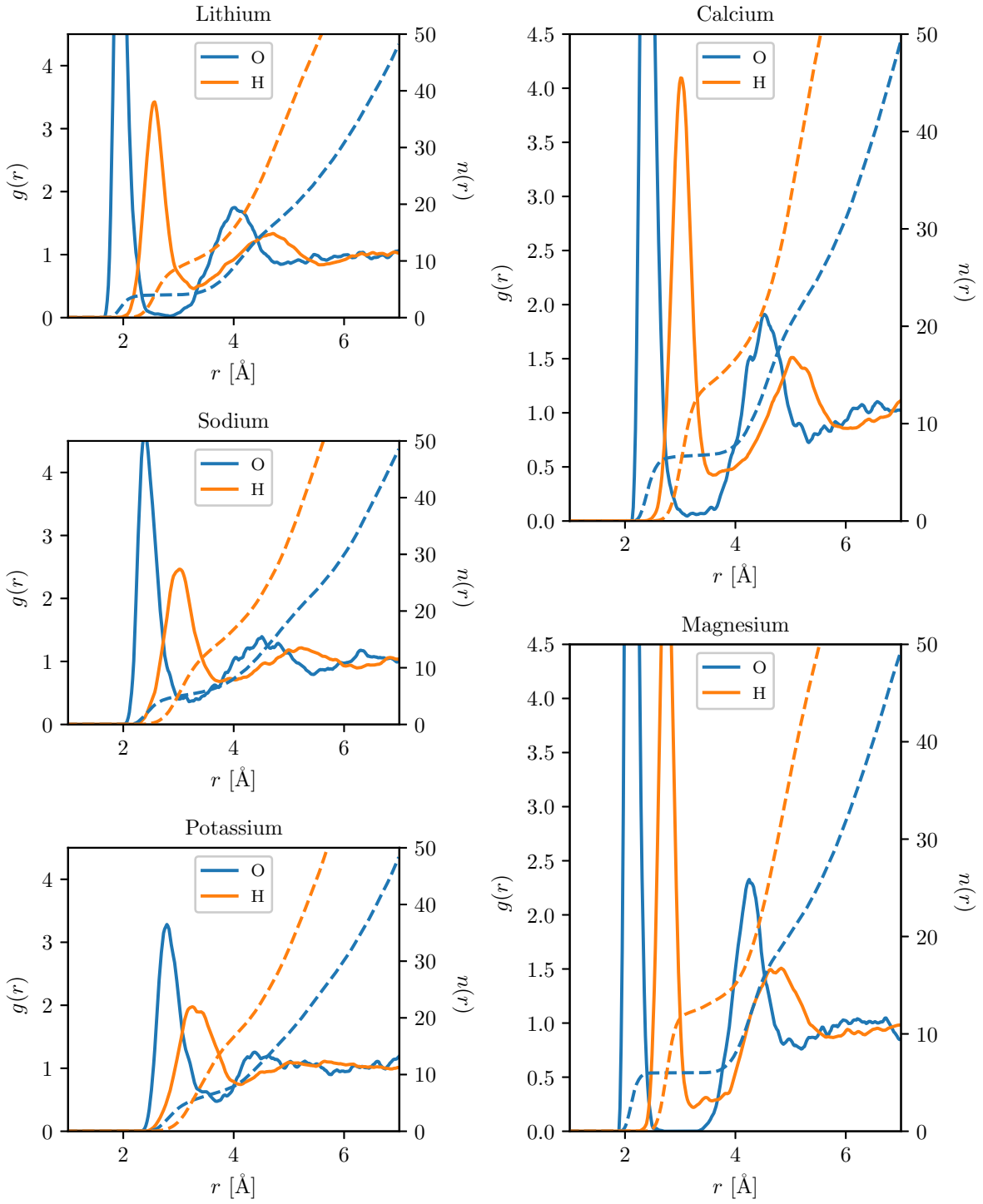

Fig. 4.2 Ion-oxygen and ion-hydrogen RDFs and coordination numbers for the cations.

all this work to compare the properties between the water molecules belonging to the different hydration shells and the bulk. The effects of the previous mentioned blurring of the boundaries between the first and the second shell also affects to the population distributions of the hydration shells. Smaller ions show narrower distributions and lower coordination numbers. Again, also higher charged atoms present narrower distributions than monovalent ions. Table 4.4 contains average coordination numbers of the first, $< N_c^{1st} >$, and second, $< N_c^{2nd} >$, hydration shells. As it was previously warned, the coordination numbers of both the potassium and iodide ions differ greatly from those found in the literature. The coordination number of the second hydration shell found for the potassium ion, $N_c^{K^+} = 39.3$, is considerably higher that those of the other ions and falls far from the more consistent value found in the literature of $N_c^{K^+} = 19.4$ [11]. As explained before this is probably caused by the wide shell considered due to the difficulty to assess it's limits.

Tongraar [12, 13] concluded that MD simulations tend to give higher coordination numbers due to the neglected many body interactions. It can be seen in table 4.4 how this trend seems to fit quite nice for the cations, where both the DFT and classical results are above the experimental ones. Note how those form Yu *et al.* [14], classical MD simulations that include a Drude polarizable force field, fall between the CPMD and the non-polarizable MD values. Soper's [15] experiments of neutron diffraction with hydrogen isotope substitution on anion solutions showed how the coordination number didn't increase with the size of the ion but kept a stable value around $N_c = 7$ despite the size increase of the hydration shell. This steadiness in the coordination number doesn't appear neither in this work nor in the other CPMD or classical MD references. Soper explains this result with the overlapping between the first two hydration shells. A discrepancy between the number of oxygen and hydrogen atoms present in the first layer leads to believe that not all the water molecules present in the first hydration shell bound directly to the central atom. A collection by Varma [16] of different neutron diffraction experiments doesn't support the sustained coordination number for small cations. On the other hand, through a series of theoretical *ab initio* studies, Varma agrees that only an exact number of four water molecules are directly linked to the cation while an increasing number of additional molecules occupy positions at distances that overlaps with first hydration shell as the size of the ion grows.

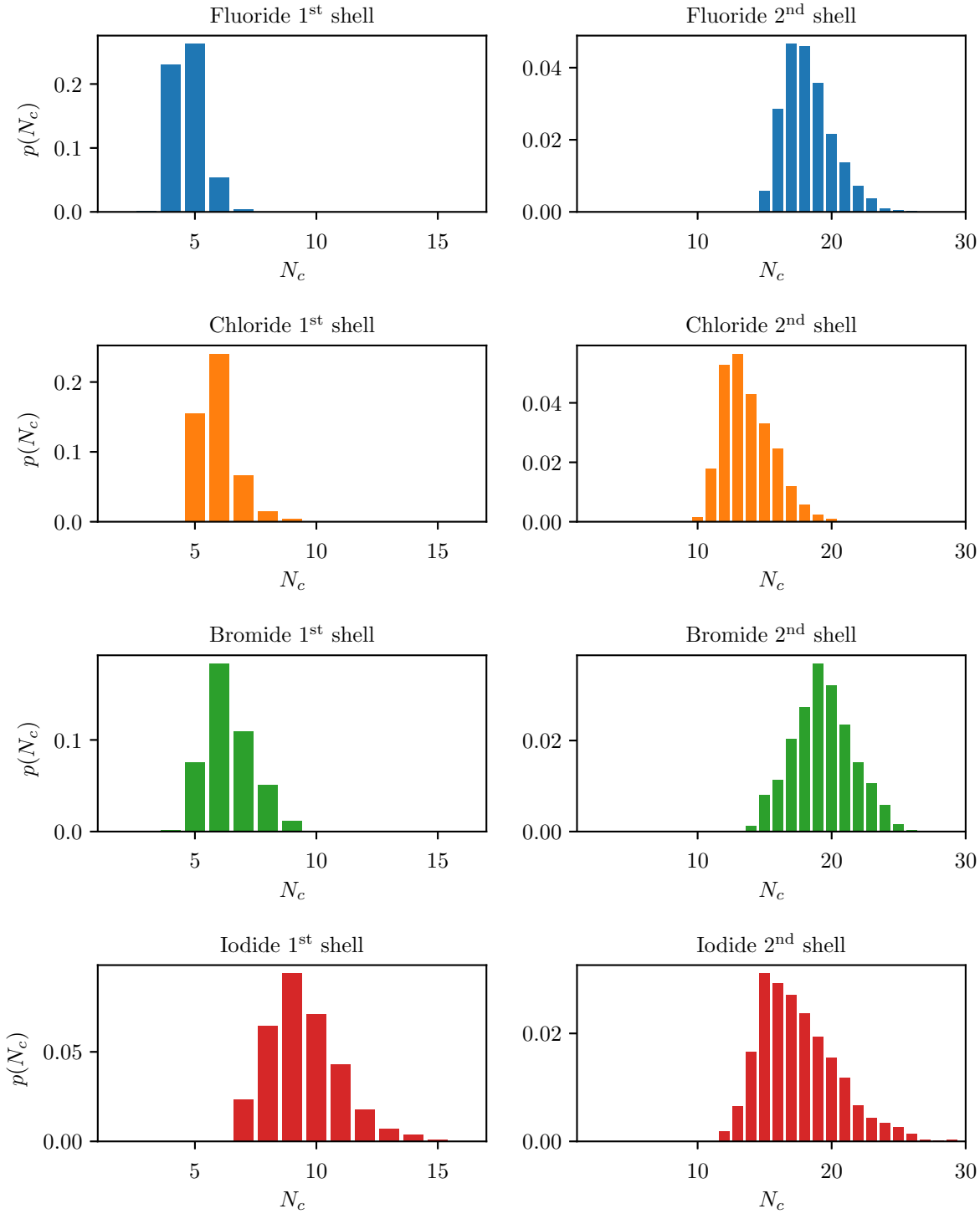

Fig. 4.3 Frequency distribution of the hydration number of the first and second hydration shells for the anions.

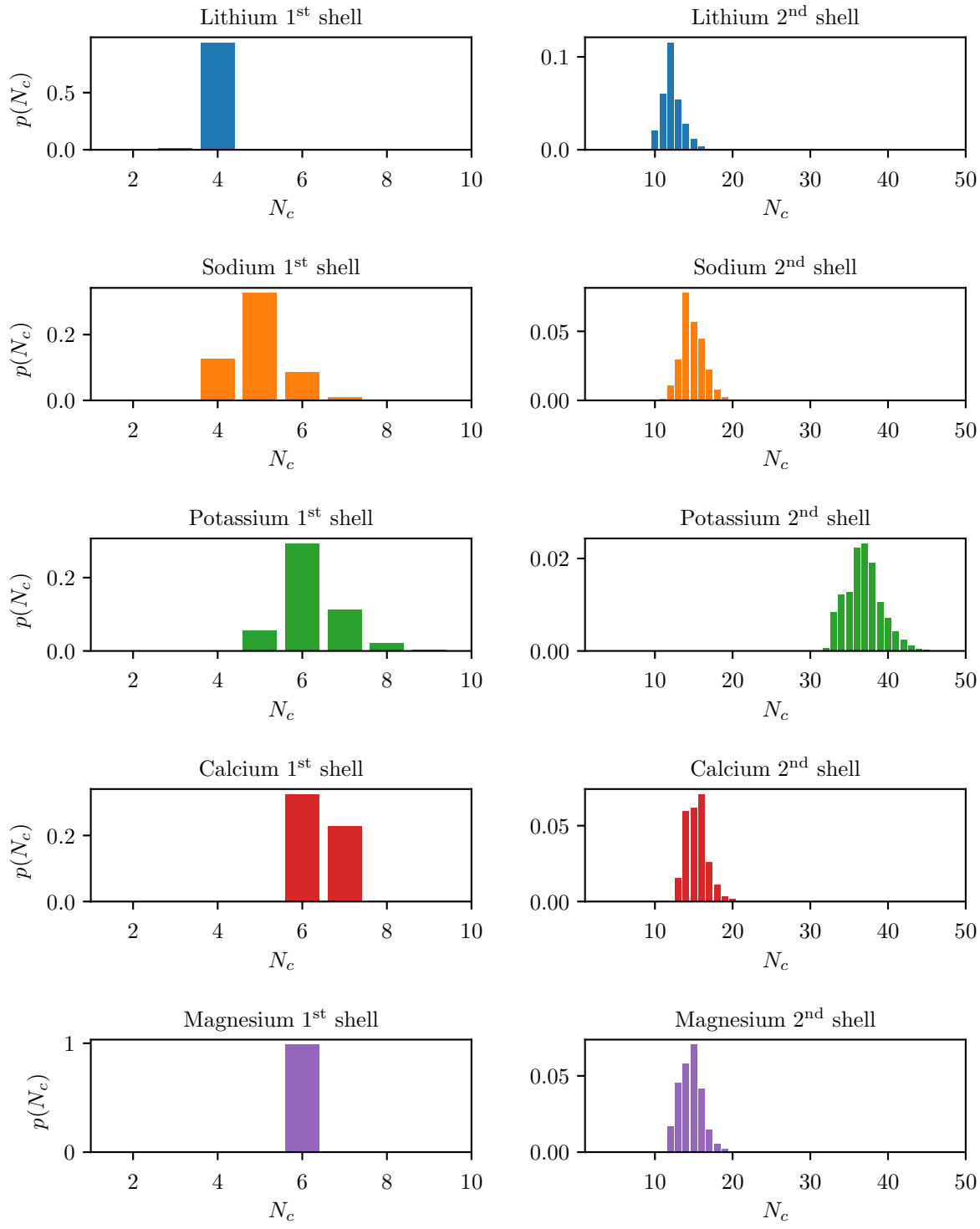

Fig. 4.4 Frequency distribution of the hydration number of the first and second hydration shells for the cations.

Ion	$< N_c^{1st} >$	$< N_c^{2nd} >$	$r_O^{max}(r)$ [Å]	$r_O^{min}(r)$ [Å]	$r_H^{max}(r)$ [Å]	$r_H^{min}(r)$ [Å]
Fluoride	5.0	19.9	2.66	3.40	1.68	2.47
Chlorine	6.4	15.3	3.19	3.90	2.23	3.00
Bromide	7.0	21.3	3.33	4.00	2.38	3.11
Iodide	10.6	20.1	3.59	4.60	2.62	3.23
Lithium	4.0	13.2	1.95	2.79	2.55	3.25
Sodium	5.3	16.0	2.40	3.25	3.02	3.88
Potassium	6.7	39.3	2.77	3.70	3.28	3.14
Magnesium	6.0	15.7	2.12	2.65	2.74	3.45
Calcium	6.7	16.5	2.39	3.20	3.03	3.65

Table 4.1 Coordination number of the first and second hydration shells, position of the ion-oxygen and the ion-hydrogen RDF maxima and minima for the different ions.

Ion	r_{O1}^{max} (Å)							$g_{O1}^{max}(r)$			
		MD		CPMD		Exp			MD		CPMD
	This work	ref. [11]	ref. [14]	ref. [17]	ref. [18–20]	ref. [15]	ref. [21]	This work	ref. [11]	ref. [14]	ref. [17]
Fluoride	2.66	2.6	2.72		2.66	2.54		3.94	7.92	4.77	
Chlorine	3.19	3.2	3.16		3.2	3.14		2.72	4.05	3.15	
Bromide	3.34	3.3	3.28			3.32		2.69	3.46	2.7	
Iodide	3.59	3.6	3.50		3.55	3.63		2.19	2.68	2.28	
Lithium	1.94	1.95	2.02	2.0			1.96	9.17	14	12.5	8.3
Sodium	2.40	2.45	2.38	2.4			2.4	4.86	7.21	7.42	5.8
Potassium	2.79	2.8	2.74	2.8		2.65		3.35	4.57	4.8	2.5
Magnesium	2.11		2.06					14.12		19	
Calcium	2.40	2.45	2.28					9.31	14.45	16.9	

Ion	r_{O1}^{min} (Å^3)						$g_{O1}^{min}(r)$			
		MD		CPMD		Exp		MD		CPMD
	This work	ref. [11]	ref. [14]	ref. [17]	ref. [18–20]	ref. [15]	This work	ref. [11]	ref. [14]	ref. [17]
Fluoride	3.34	3.2	3.34			3.27	0.25	0.17	0.37	
Chlorine	3.96	3.8	3.78		3.76	3.77	0.49	0.49	0.72	
Bromide	3.96	3.85	3.96			3.9	0.76	0.52	0.75	
Iodide	4.50	4.3	4.16		4.15	4.1*	0.87	0.72	0.9	
Lithium	2.87	2.65	2.56	2.8			0.02	0.02	0.0	0.0
Sodium	3.23	3.25	3.24	3.2			0.33	0.16	0.2	0.2
Potassium	3.72	3.65	3.56	3.7		3.45	0.49	0.47	0.45	0.7
Magnesium	2.67-3.29		2.72				0.00		0.0	
Calcium	3.12	3.39	2.76				0.04	0.01	0.0	

Table 4.2 Positions and values of the first maximum and minimum of the ion-oxygen RDF obtained from different literature sources.

Ion	r_{O2}^{max} (Å)				$g_{O2}^{max}(r)$		
	This work	MD ref. [11]	CPMD ref. [17]	Exp ref. [15]	This work	MD ref. [11]	CPMD ref. [17]
Fluoride	4.67	4.45		4.49	1.59	1.45	
Chlorine	5.02	5		4.99	1.21	1.28	
Bromide	5.16	5.05		5.1	1.20	1.23	
Iodide	5.24	5.05			1.11	1.25	
Lithium	4.04	4.10	4.1		1.73	1.69	1.6
Sodium	4.55	4.5	4.5		1.36	1.42	1.5
Potassium	4.81	4.75	4.8	4.85	1.22	1.15	1.2
Magnesium	4.25	4.46			2.33		
Calcium	4.53				1.87	1.96	

Ion	r_{O2}^{min} (Å)				$g_{O2}^{min}(r)$		
	This work	MD ref. [11]	CPMD ref. [17]	Exp ref. [15]	This work	MD ref. [11]	CPMD ref. [17]
Fluoride	5.58	5.5		5.54	0.86	0.9	
Chlorine	6.14	6.05		6.19	0.88	0.79	
Bromide	6.07	6.15		6.2	0.84	0.89	
Iodide	6.29	6.65		5.9	0.90	0.88	
Lithium	4.96	5.25	5.1		0.84	0.85	0.75
Sodium	5.51	5.40	5.5		0.80	0.89	0.8
Potassium	5.87	5.8		6	0.88	0.84	
Magnesium	5.15				0.77	0.9	
Calcium	5.38	5.43			0.75	0.79	

Table 4.3 Positions and values of the second maximum and minimum of the ion-oxygen RDF obtained from different literature sources.

Ion	$< N_c^{1st} >$								$< N_c^{2nd} >$	
	MD			CPMD	Exp				MD	
	This work	ref. [11]	ref. [14]	ref. [17]	ref. [15]	ref. [22]	ref. [21]	ref. [16]	This work	ref. [11]
Fluoride	5.0	6.3	5.5		6.9				19.9	19.4
Chlorine	6.4	7.2	6.5		7.1				15.3	
Bromide	7.0	7.5	6.8		6.7				21.3	26.5
Iodide	10.6	7.9	7.1		6.7*				20.1	29.5
Lithium	4.0	4.1	4.0	4.0			4	4	13.2	17.4
Sodium	5.3	5.8	5.6	5.13			4.9	5	16.0	18.3
Potassium	6.7	7.1	6.9	6.55	6.4		5.3	6	39.3	19.4
Magnesium	6.0		6.0						15.7	
Calcium	6.7	7.9	6.0			6.8			16.5	17.6

Table 4.4 Coordination numbers of the first and second hydration shells obtained from different literature sources.

(a) Definition of the θ_1 and θ_2 angles.

(b) Non coplanarity contribution to θ_1 and θ_2.

Fig. 4.5 Orientation of a water molecule in the first hydration shell of a cation. The oxygen atom has a higher electronegativity, so it shows a slightly negative charge; thus, it will be attracted by the cation and it will get closer to it than the positive hydrogen atoms. Both hydrogen atoms get oriented symmetrically away from the ion so the angles formed by the cation-oxygen vector and the oxygen-hydrogen vectors of both hydrogen atoms will be similar (subfigure 4.5a). The plane that contains the water molecule is tilted with respect to the the ion-oxygen vector (subfigure 4.5b).

4.2.3 Orientation

Cations

Due to the polar nature of the water molecule, those present in the first hydration shell take radically different orientations with respect to the central ion whether the net charge of it is negative or positive. The negative excess charge of the water molecule is located on the oxygen side of the molecule. In the presence of a positive cation, the oxygen atom is attracted to the cation while the hydrogen atoms tend to shy away from it. The water molecule ends adopting a trigonal pyramidal like formation where the plane formed by the water molecule is not aligned with the cation-oxygen vector but tilted in some degree. This structure can be seen in figure 4.5a. This figure also explains the definition of the angles θ_1 and θ_2 between the cation-oxygen and both oxygen-hydrogen vectors, angles that are useful in order to study the orientation of the water molecules.

Figure 4.6 contains the θ_1 and θ_2 angles distribution (as defined in reference [15]) for each one of the cations. The different contributions from the first and the second hydration layer, and the bulk have been considerated separately. It can be seen how the θ_1 and θ_2 angles of the water molecules from the first hydration shell are arranged around a single peak centered close to $\theta \simeq 60°$. The fact that only a single peak is present

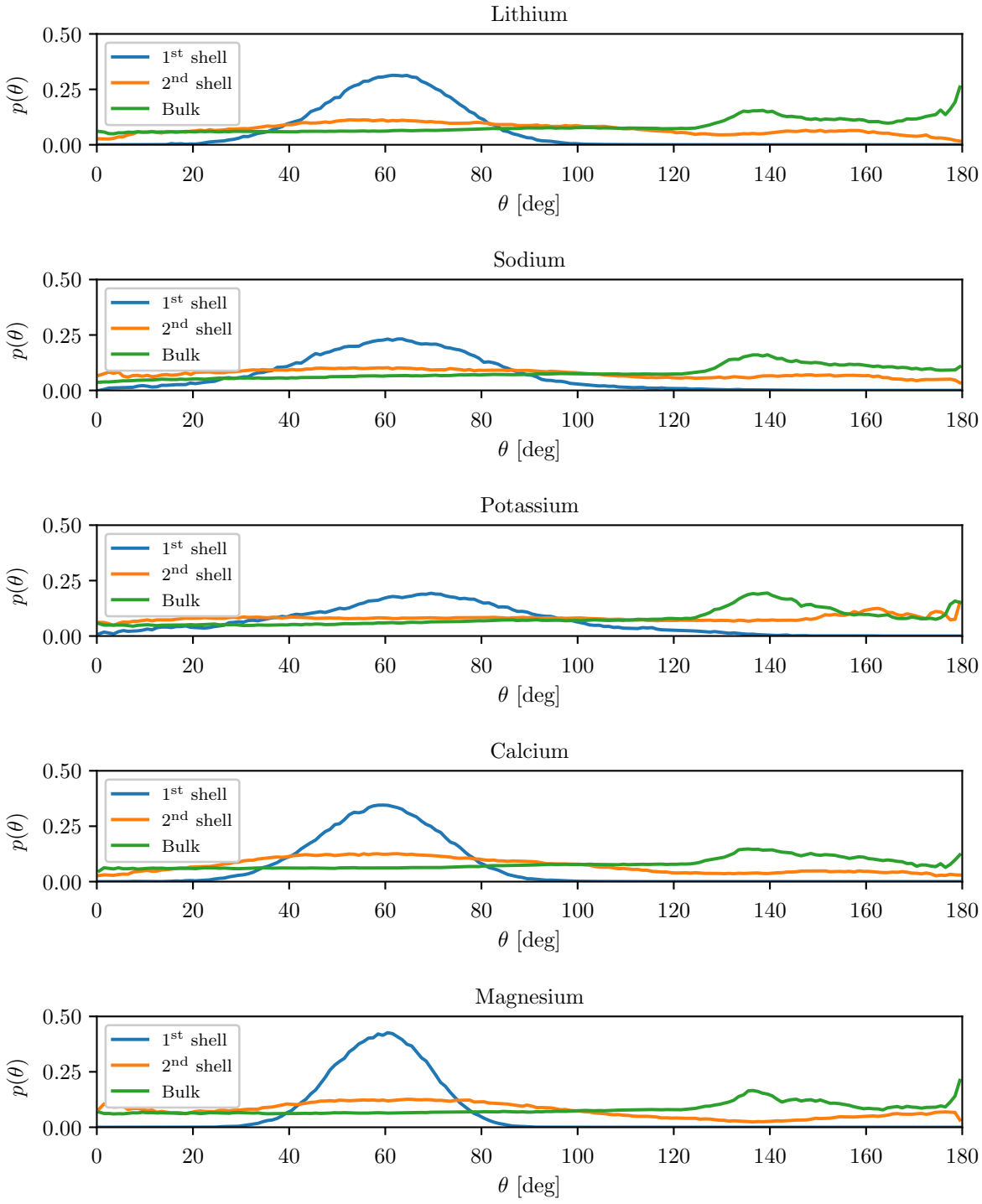

Fig. 4.6 Density of oxygen-hydrogen bonds orientation respect the ion-oxygen vector for the water molecules of the second hydration shell.

indicates that the two hydrogen atoms are positioned symmetrically with respect to the cation-oxygen vector. If the water molecules where coplanar to the central vector $\vec{r}_{IO}$ the average value of the θ angle would be around the semiangle formed by the hydrogen-oxygen bonds of the water molecule $\theta \simeq 104/2 = 52°$. The inclination of the water molecule plane adds a contribution to the total angle that shifts the peak to higher values of angle θ. In figure 4.6 it can be observed how the cation growth goes along with a slight increase on the shifting. A more intense consequence of the ion radius increment is the widening of the θ distribution peak. Both effects can be explained in terms of the weakening of the electric field around the ion as it grows in size. It can be seen how the divalent cations, in spite of having a comparable size to their immediate periodic table neighbors, have less shifted and more pronounced peaks than them. Further away from the first water layer, the effects of the cation fade away, leaving a mostly plain distribution with a mild bump where the peak used to be. For the water molecules in the bulk a small peak appears around $\theta \simeq 140°$ which is probably caused by finite size effects.

Figure 4.7 contains a representation of a typical configuration of the lithium ion and its first hydration layer formed by four water molecules. It can be seen how the water molecules adopt the previously explained trigonal pyramidal orientation with the oxygen atoms facing the cation. Also it can be appreciated how the water molecules get arranged around the ion in a tetrahedral geometry.

Anions

Although the negative excess charge in the water molecule is concentrated at one location, the positive one is distributed between the two hydrogen atoms. Due to this asymmetrical distribution of the positive excess charge in the water molecules, the orientation that they will adopt in the presence of a negative net charged ion will not just be a specular image of the one in the presence of a positive ion. When a cation is present the oxygen atom is pulled away from it while the hydrogen atoms move closer. While in the case of the cations the distance between the ion and both the hydrogen atoms tends to be the same, with the anions, the position of the hydrogen atoms loses that symmetry. The attraction of one of the hydrogen atoms dominates over the other one and forces the second one to adopt a position further away. Figure 4.8 is an schematic of how a water molecule gets oriented near a negative ion. Again, the angle formed by the central vector between the ion and the oxygen and the oxygen-hydrogen vectors is useful to study the orientation of the water molecules. Figure 4.9 shows the different θ angle distributions of the first and second hydration shells and the bulk for each of the anions.

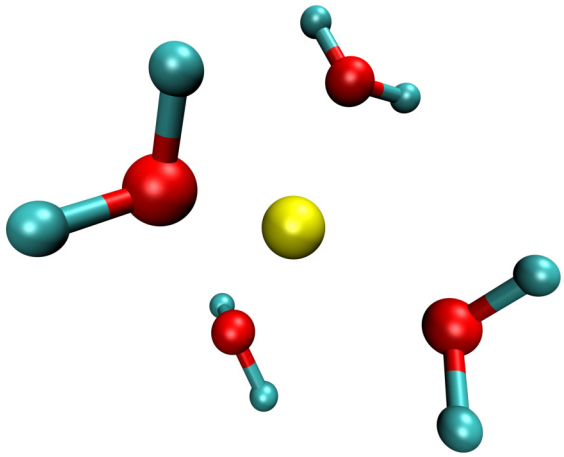

Fig. 4.7 The lithium ion (yellow) surrounded by its first hydration shell. Oxygen atoms are represented in red and hydrogen atoms in cyan.

It can be seen how, unlike with the cations, the distribution of the first layers shows two differentiated peaks, one around the perpendicular plane at $\theta_1 \simeq 70^\circ$ and one close to anti-parallel alignment near the $\theta_2 \simeq 180^\circ$ angle. This angle distribution translates into a water molecule orientation where a hydrogen atom is facing the anion close to the IO line which corresponds to the peak situated around the $\theta_2 \simeq 180^\circ$ angle. The symmetry around the ion-oxygen axis over which the angle is defined along with the constrained water molecule geometry allows two possible positions for the second hydrogen atom, one beyond the $\theta = 90^\circ$ angle and one before it. The surprise arises from the fact that the second hydrogen atom is not situated between the first one and the oxygen atom but further away giving place to the second peak in the distribution around the $\theta_1 \simeq 70^\circ$ angle. Again, the plane formed by water molecule is not aligned to the IO vector. This inclination adds a contribution to the total θ angle, even though it is smaller than that from the anions.

Figure 4.10 contains a representation of a typical configuration of the chloride ion and its first hydration layer formed by six water molecules. It can be seen how the water molecules get oriented with one of the hydrogen atoms facing the ion and the other one facing outwards.

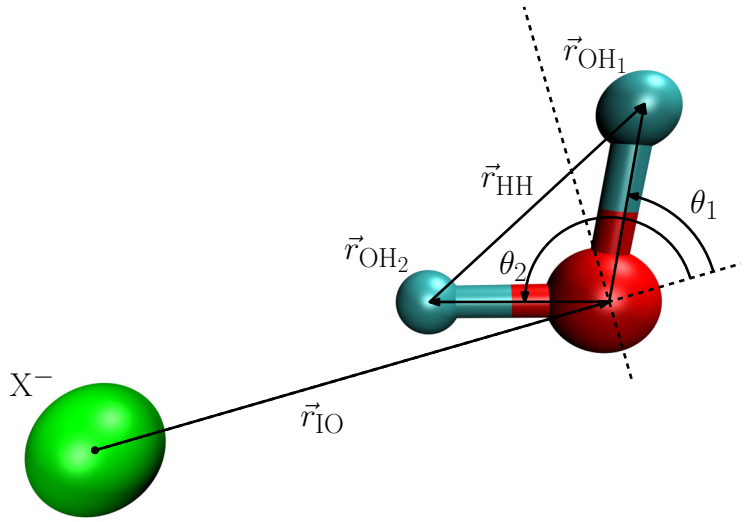

Fig. 4.8 Orientation of a water molecule in the first hydration shell of an anion. The hydrogen atoms have a lower electro-negativity, so it shows a slightly positive charge; thus, they will both be attracted by the cation. As the oxygen atom shows a negative charge the anion will repeal it and it will move away from the anion. This movement will force one of the hydrogen atoms to also move away form the central ion. This arrangement of the atoms will translate into two widely different angles between the cation-oxygen vector and the oxygen-hydrogen vectors of each hydrogen atoms.

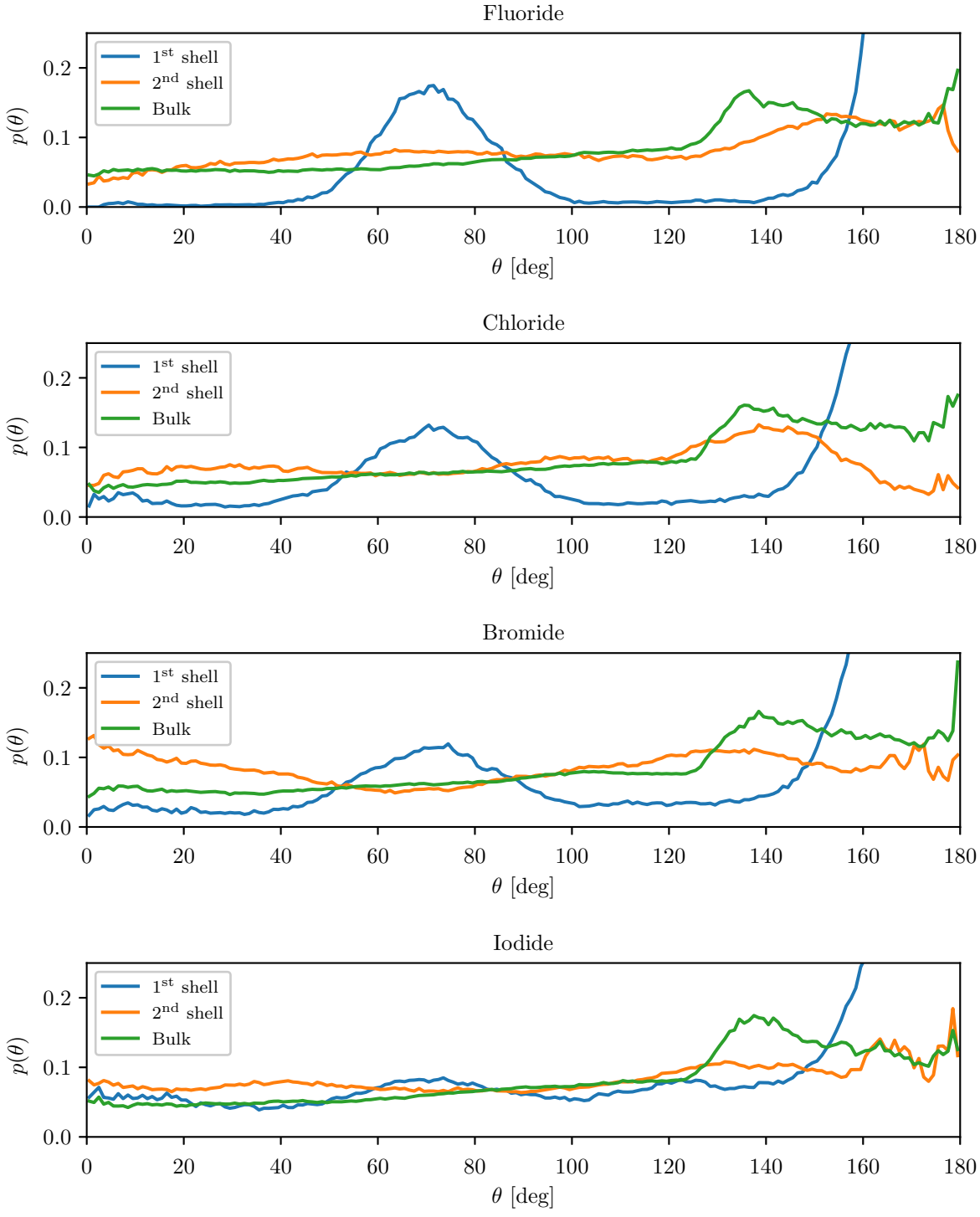

Fig. 4.9 Density of oxygen-hydrogen bonds orientation respect the ion-oxygen vector for the water molecules of the first hydration shell.

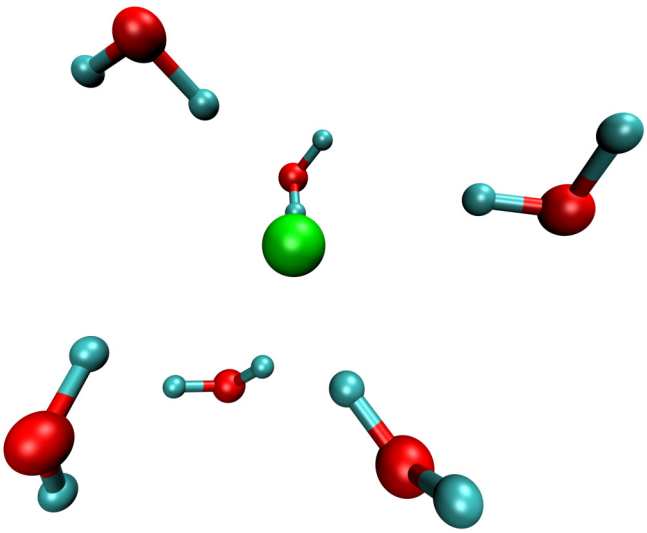

Fig. 4.10 The chloride ion (green) sourrounded by its first hydration shell. Oxygen atoms are represented in red and hydrogen atoms in cyan.

4.3 Dynamical properties

4.3.1 Residence time

The nature of the structures formed around the ions is usually very dynamical; water molecules may, for example, continuously enter and leave the hydration shells. The rate at which this happens varies greatly from one ion to another and can alter in grand manner the propagation of the surrounding water molecules, the ion itself and other properties of the solution. As explained in section 2.3.2, residence functions, $n(t)$, have been computed for the molecules in the first and second hydration shells of each ion. In figures 4.11 and 4.12 we can see the residence functions for the anions and the cations respectively. There are no substantial layout differences between the residence functions of anions and cations. The first obvious conclusion comes from the fact that water molecules in the second hydration shell are more weakly bound to it and have a higher chance to leave it than those in the first layer. Again, also the size and net charge of the central ion affects how tied the water molecules are to the ion. With closer water molecules to the ion and higher net charges, the interaction between them becomes stronger which translates in higher levels of residence. This effect is specially relevant for the lithium ion, the calcium ion and the magnesium ion. As an example of how stable the hydration shell can be, for the magnesium ion, not a single water molecule leaved or entered the first hydration shell for the whole simulation run. The decay of the residence time function can be fitted to a double exponential function so it can be integrated up to infinity in order to obtain the characteristic residence time τ_{1st}. Table 4.5 shows the computed characteristic residence time for the water molecules in the first hydration shell for each one of the simulated ions and some reference values for comparison. Due to the absence of any exchange of water molecules between the first and second hydration shells of the magnesium ion, its characteristic residence time can't be calculated so it has been omitted.

Exploring and comparing the values for τ_{1st} in table 4.5 it can be seen that there is quite a disagreement among the different sources. Moreover, the lack of consistency in the variations among values from different sources, forces to question the reliability of these numbers. In the case of this work, this inconsistency can probably be attributed to the poor statistical sample size. Several studies [20, 25–27] blame the high sensitivity of the residence time to variations in the ion concentration as another possible source of discrepancy.

Despite these variances some general trends can be concluded from this numbers. It seems clear, especially from the MD results of Joung *et al.* in 2009 [28] and the

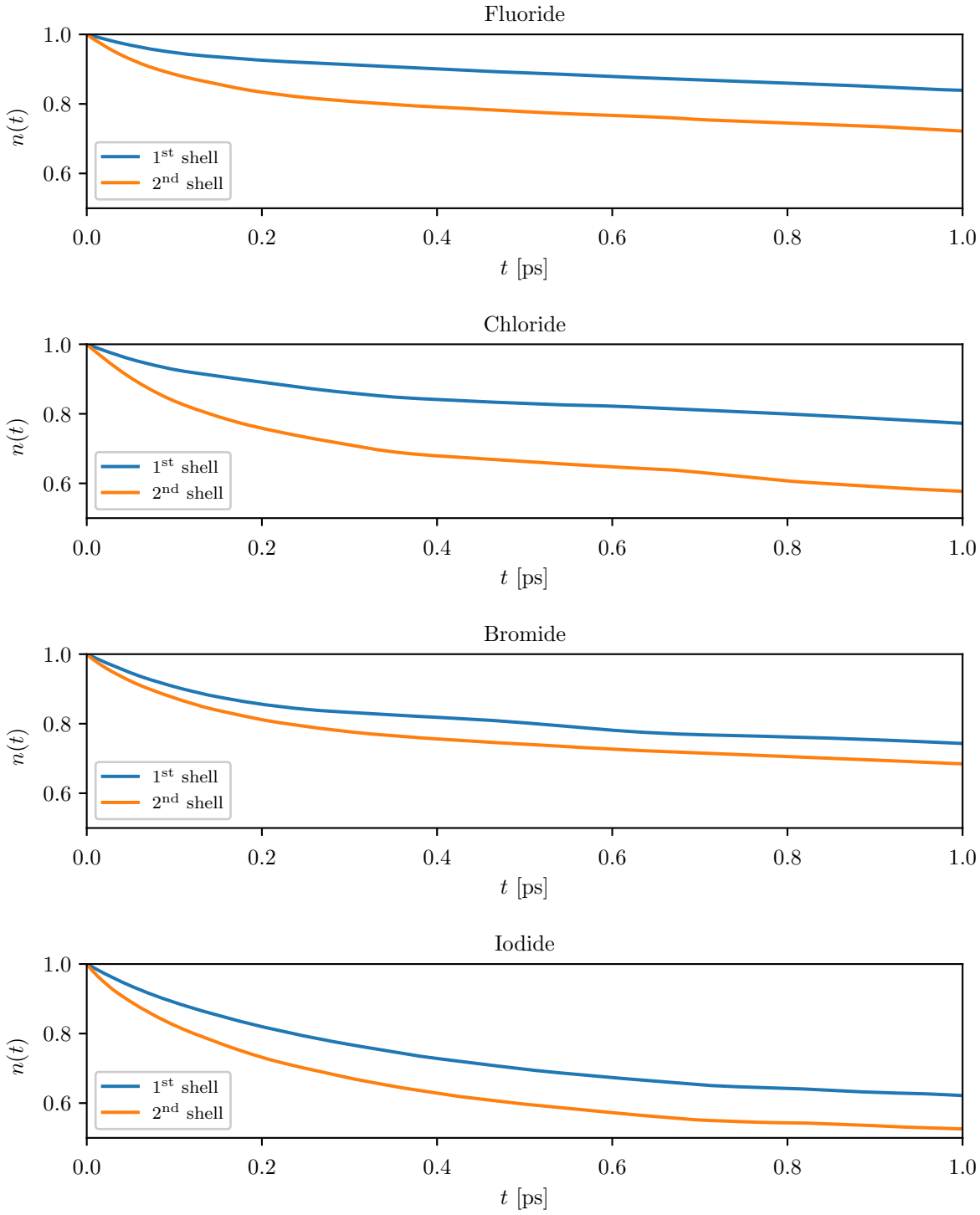

Fig. 4.11 Residence time correlation functions for the anions.

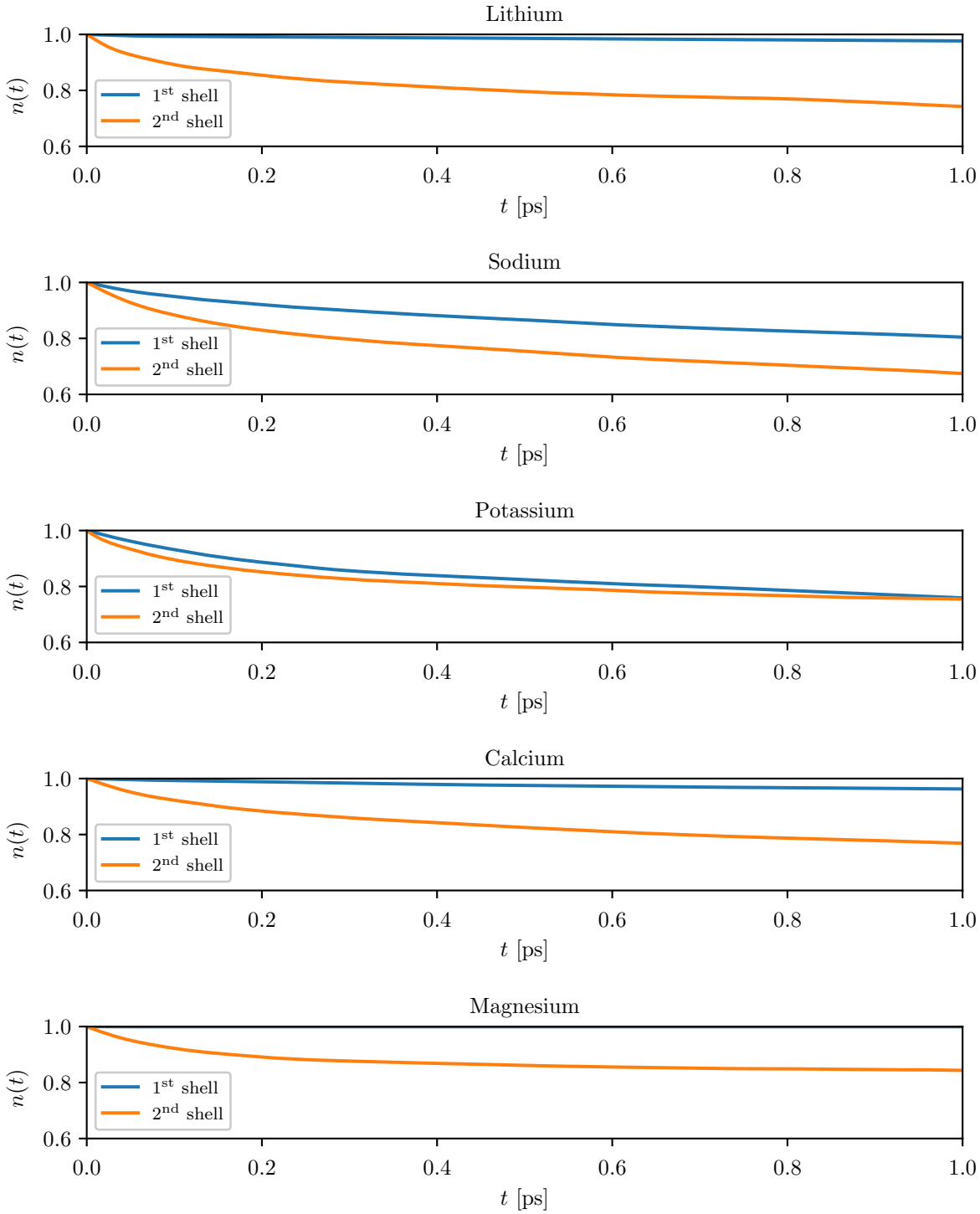

Fig. 4.12 Residence time correlation functions for the cations.

	τ_{1st} [ps]			
	CPMD	MD		Exp
	This work	ref. [23]	ref. [11]	ref. [24]
Fluoride	11.6	17.6	25.5	
Chloride	7.5	8.3	17.5	15
Bromide	5.5	7.3	13.6	10
Iodide	5.6	6.0	14.9	5
Lithium	43.1	29.0	50.6	39
Sodium	5.6	19.6	22.8	27
Potassium	8.1	7.2	15.1	15
Magnesium	-			90
Calcium	110.0		699	60

Table 4.5 Residence times for each of the ions compared to those obtained from different literature sources.

experimental ones of Baker in 2008 [24] that, as with previous properties, the intensity of the electric field nearby the ions plays a fundamental role in the persistence of the water molecules in the first hydration shell. The smaller and more charged the central ion is, the higher it is the stability of the water layer which will raise to higher values of the characteristic residence time. Despite this is a reasonable explanation Kropman and Bakker proposed in 2001 [25] that the reluctance of a water molecule to leave the hydration shell comes more from the energy cost of breaking the water shell structure than from the ion-water interaction itself. The bulk should be able to make up for this energy variation more easily than the ion environment; thus, the residence time near the ion would be higher than far from it.

At any rate the dynamical nature of the hydration shells can be related to the level of structure found when studying the RDFs. Ions with more dynamical layers have also less structured water shells and more diffuse limits between them. A lower characteristic residence times means that there is a rather constant exchange of water molecules among shells. This flow of molecules involves the, at least, temporary presence of water molecules between shells thus smoothing the curves between the RDFs peaks. For example, the RDFs from the lithium, magnesium and calcium ions display a highly pronounced valley between the first two shells, indicating that water molecules do not have a great chance be located at those positions and consequently the exchange of molecules between shells is inhibited.

4.3.2 Mean Squared Displacement

The Mean Square Displacement (MSD) is a measure of how far the particles move through liquid due to their Brownian movement. From the MSD measurements, the self-diffusion coefficient, D, can be easily calculated [29]. Table 4.6 contains the self-diffusion coefficient of the water molecules in the first and the second hydration shells. As a measure for comparison the self-diffusion coefficient of the water molecules in an analogous pure water simulation is $D_{H_2O} = 1.91 \times 10^{-9}\,m^2\,s^{-1}$. The usual behaviour when comparing the MDS from the different hydration layers is that those molecules situated in the shells tend to move slower than those present in the bulk. Unfortunately, probably due to the short run time of the simulations, this trend can't be appreciated.

The MSD of the ions can also be calculated. Figures 4.15 and 4.16 show the MSD functions for the anions and the cations respectively. Its clear in these figures that due to the fact of being just one particle for each simulation, the statistics for these calculations is very poor and any conclusion extracted from them should be taken carefully. Even so, some qualitative behaviours can be noticed. For example, it seems clear that those ions with more stable hydration shells like the lithium ion, the magnesium ion and the calcium ion, also have lower self-diffusion coefficients. This correlation can be easily explained considering the ion and its first hydration shell as a whole effectively heavier entity that moves through the liquid [23]. Those ions with less difficulty to leave water molecules behind can move through them with ease while those stuck to their solvation shells need to drag them across. A comparison between the mobilities of ions and neutralized versions of themselves by Konesan *et al.* [11] supports this explanation. The self-diffusion coefficients, D_{Ion}, for each of the ions are gathered next to some reference values in table 4.7. As expected, the computed values of D_{Ion} are hard to reconcile with the literature values. But, at least, it can be seen that the correlation between the stability of the hydration shell of the ion and its ability to move through the water its more than a coincidental trend. Comparison between experimental and simulated diffusion should be taken carefully as most experimental data in the literature is obtained from conductivity measurements of salts [30] that need further assumptions instead of from individual ionic species. Yu *et al.* [14] states that a comparison with neutral salts simulation would be a more suited method.

4.3.3 Velocity Autocorrelation Functions

The velocity of the ions can also be autocorrelated to obtain the Velocity Autocorrelation Function C_{vv} (VACF). Usually, this function can also be used to calculate the self-

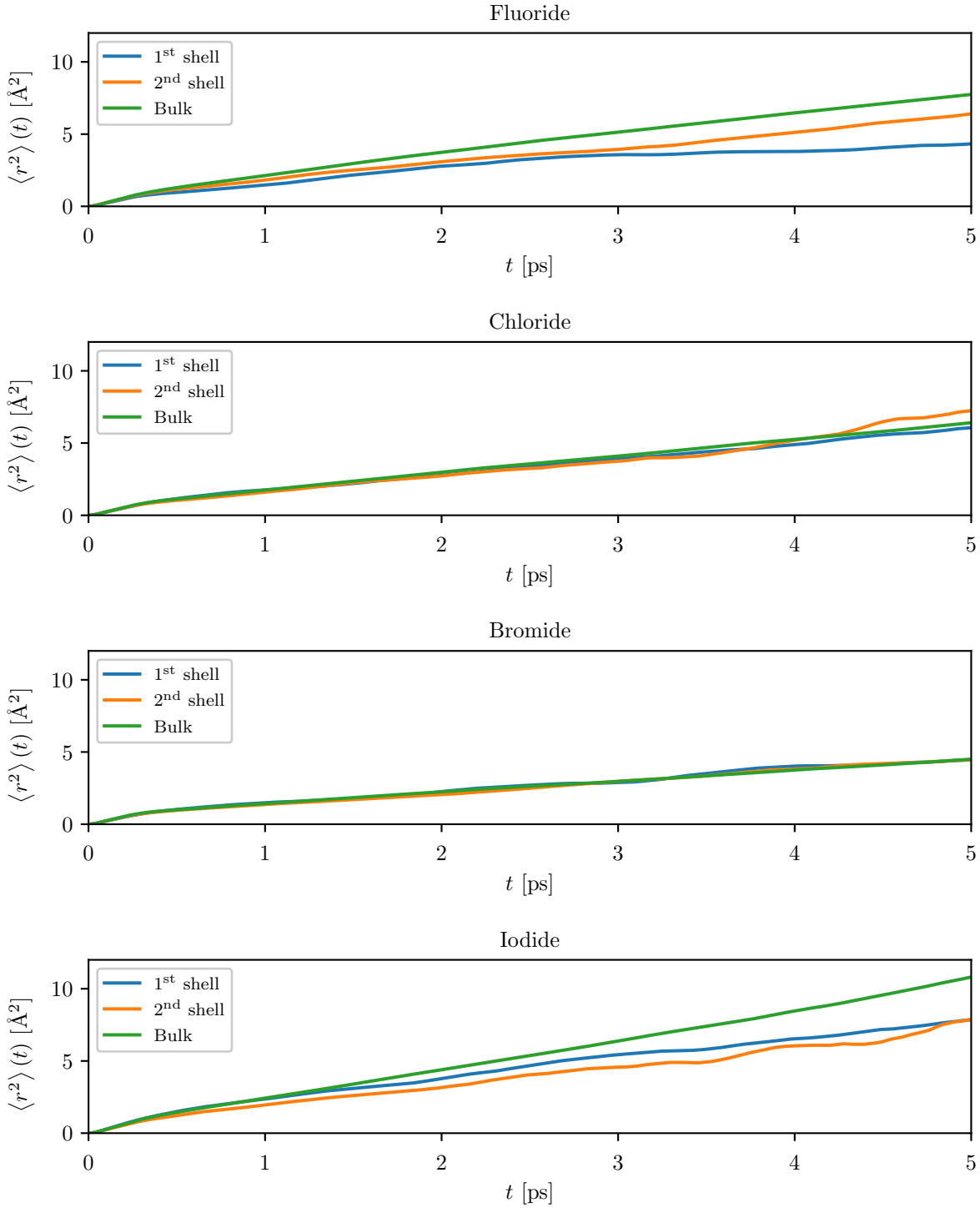

Fig. 4.13 Mean Square Displacement of the water molecules of the solvation shells of the anions.

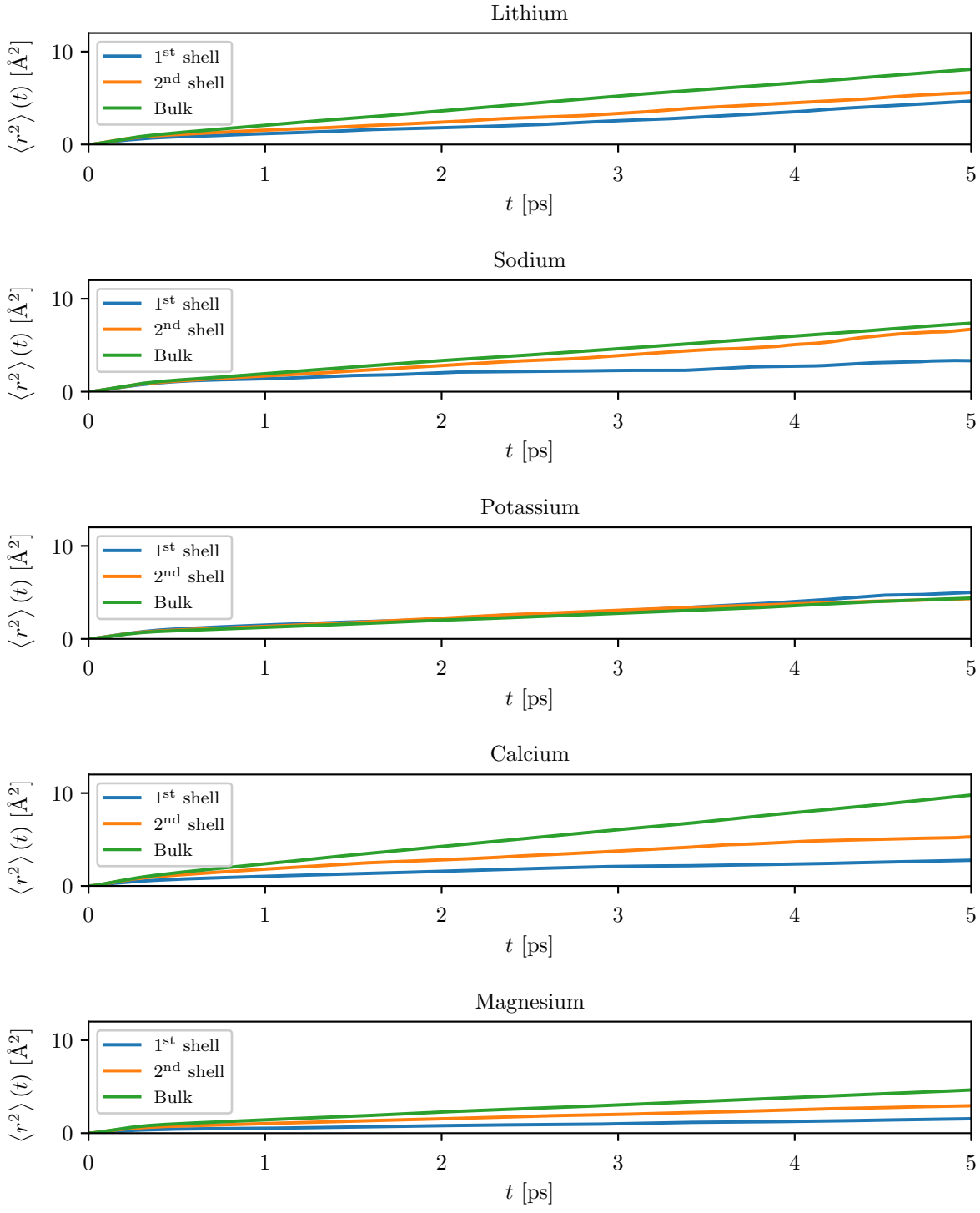

Fig. 4.14 Mean Square Displacement of the water molecules of the solvation shells of the cations.

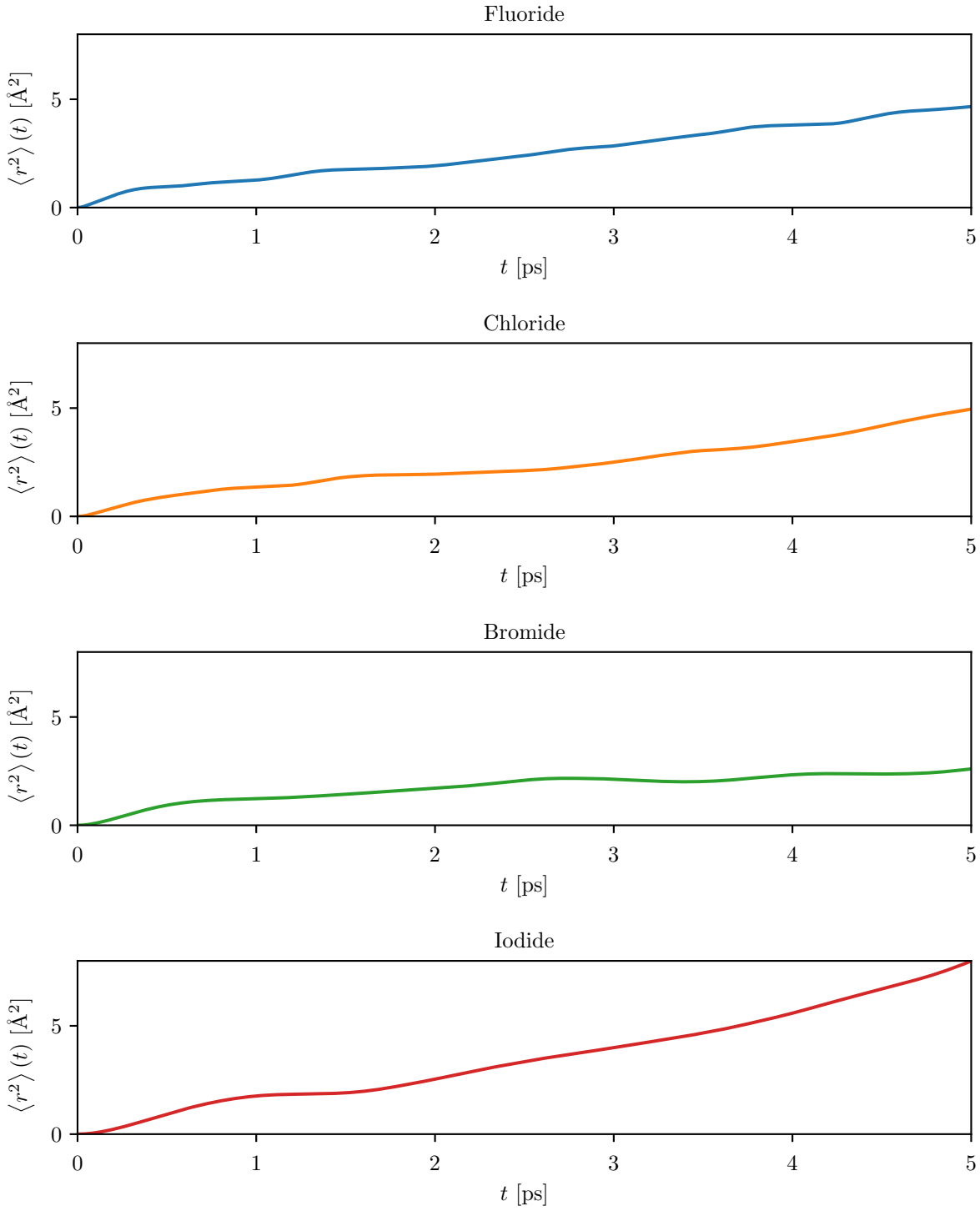

Fig. 4.15 Mean Square Displacement for the anions.

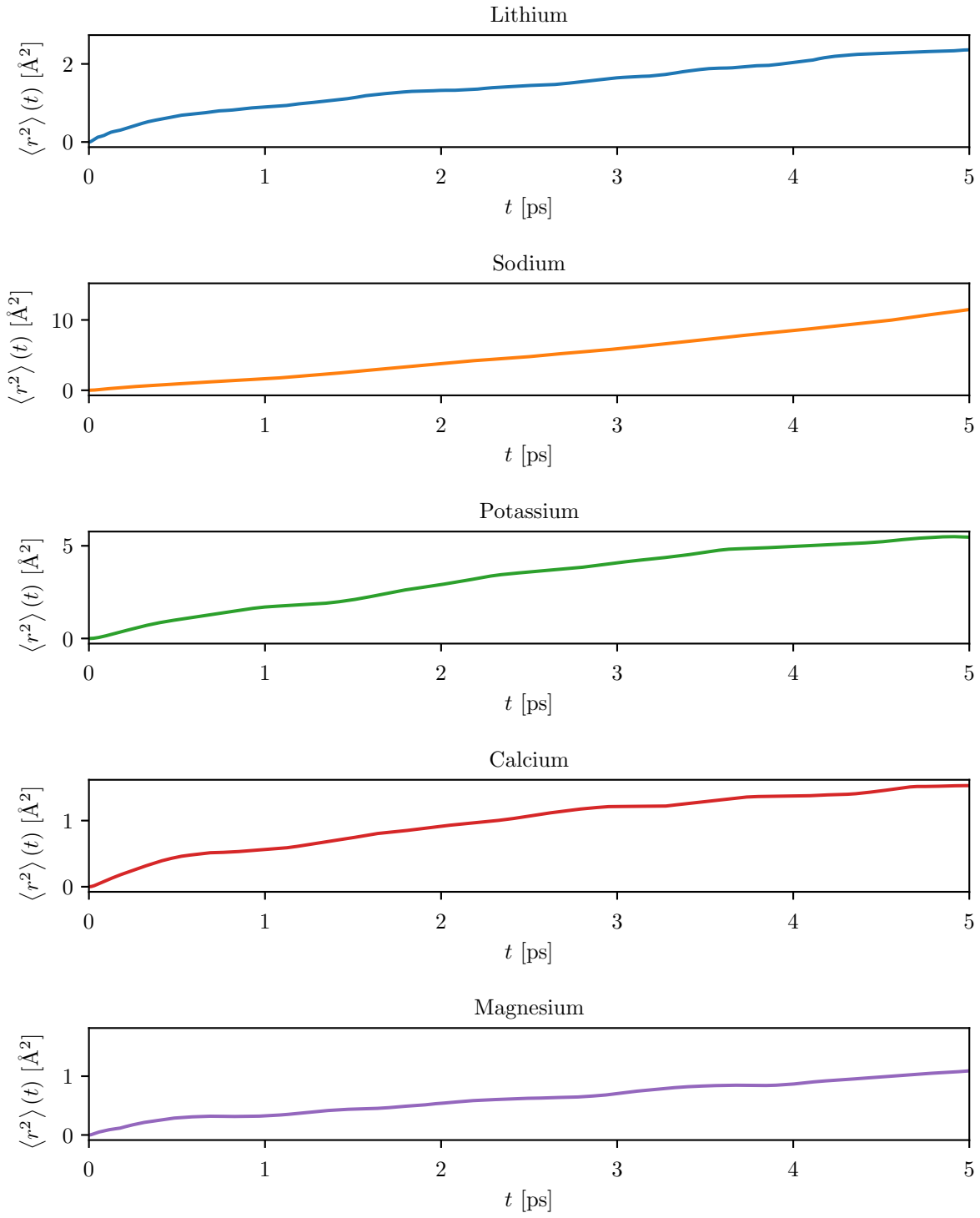

Fig. 4.16 Mean Square Displacement for the cations.

	D_{1st} $[10^{-9}\,m^2\,s^{-1}]$	D_{2nd} $[10^{-9}\,m^2\,s^{-1}]$	τ_{1st}^{HH} [ps]	τ_{1st}^{IO} [ps]
Fluoride	1.30	1.69	5.4	5.9
Chloride	1.79	1.78	6.1	6.2
Bromide	1.40	1.40	4.2	6.8
Iodide	2.36	2.17	1.2	3.6
Lithium	1.26	1.66	2.2	3.4
Sodium	0.65	1.86	2.1	2.6
Potassium	1.39	1.38	2.8	3.3
Magnesium	0.41	0.80	3.8	49.9
Calcium	0.75	1.59	1.8	14.3

Table 4.6 Diffusion coefficients of the water molecules in the first and second hydration shells and reorientational times of the HH and the IO vectors of the first hydration shell and of the different anions and cations.

	D_{Ion} $[10^{-9}\,m^2\,s^{-1}]$				
	CPMD		MD		Exp
	This work	ref. [14]	ref. [23]	ref. [11]	ref. [30]
Fluoride	1.42	1.33	1.09	1.04	1.48
Chloride	1.08	1.82	1.66	1.77	2.03
Bromide	0.57	1.85	1.78	1.85	2.08
Iodide	2.23	2.02	1.81	1.60	2.05
Lithium	0.60	1.3	1.3	1.22	1.03
Sodium	3.79	1.58	1.34	1.28	1.33
Potassium	1.99	2.2	1.89	1.83	1.98
Magnesium	0.31	0.82			0.71
Calcium	0.46	0.96		0.53	0.79

Table 4.7 Ion diffusion coefficients compared to those obtained from different literature sources.

diffusion coefficients of the ions but the lack of statistics prevents the function to steadily go to zero and doesn't allow to achieve a reliable value. Figures 4.17 and 4.18 contain the VACFs for the anions and the cations respectively. Ionic VACFs start with a fast decline to which an oscillatory decay follows. For a given charge, the life span of this initial drop increases when increasing the ion size.

From the VACF of the particles and by means of the Fourier Transform it can be obtained the power spectrum associated with the different bonds. Although the lack of statistics does not allow a deep analysis, there are still some effects that can be appreciated. Figures 4.19 and 4.20 show a partial spectrum of the movement of the hydrogen and oxygen atoms in the first hydration layer of the chlorine, fluoride, magnesium and calcium ions and, as a comparison, those from a pure water simulation.

It can be observed how the two peaks around the $\omega \simeq 3300\,\mathrm{cm}^{-1}$ corresponding to the symmetric and the asymmetric stretching of the covalent HO bond that are indistinguishable in the case of the pure water splits in two separate ones about $\Delta\omega \simeq 100\,\mathrm{cm}^{-1}$ apart due to the strong hydrogen bond between the water molecule and the anion.

4.3.4 Reorientation

Another important property in the characterization of the solvation shell dynamics is the reorientational movement of the water molecules that forms it. As also explained in section 2.3.2, this movement is studied by means of different time autocorrelation functions. There are two different movements of the water molecule to be studied: the rotation of the water molecule around itself and the rotation around the central ion. The first one is calculated upon the unitary vectors that join the two hydrogen atoms of the water molecules, $\hat{u}_{\mathrm{HH}}$ (see figures 4.5 and 4.8). Figures 4.21 and 4.22 show the autocorrelation function of the second Legendre polynomial of these angles, C_2^{HH}, for the first and the second hydration shells for anions and cations respectively. It can be observed that, as expected, in most of the cases the structure of the second hydration shell is of a more spurious nature than that of the first shell or with no appreciable difference between them. This trend gets smaller as the size of the ion increases and it even gets inverted for the biggest anions as the bromide ion and specially the iodide ion. This result can be explained by the large amount of water molecules present in the second hydration shell due to the diffuse nature of it. The initial short-time decay is a result of librational motion that ends in a minimum known as the free rotor frequency. After that, there is the long-time decay that arises from the structural changes. This long-time decay can be fitted to a single exponential function that can be used to complete

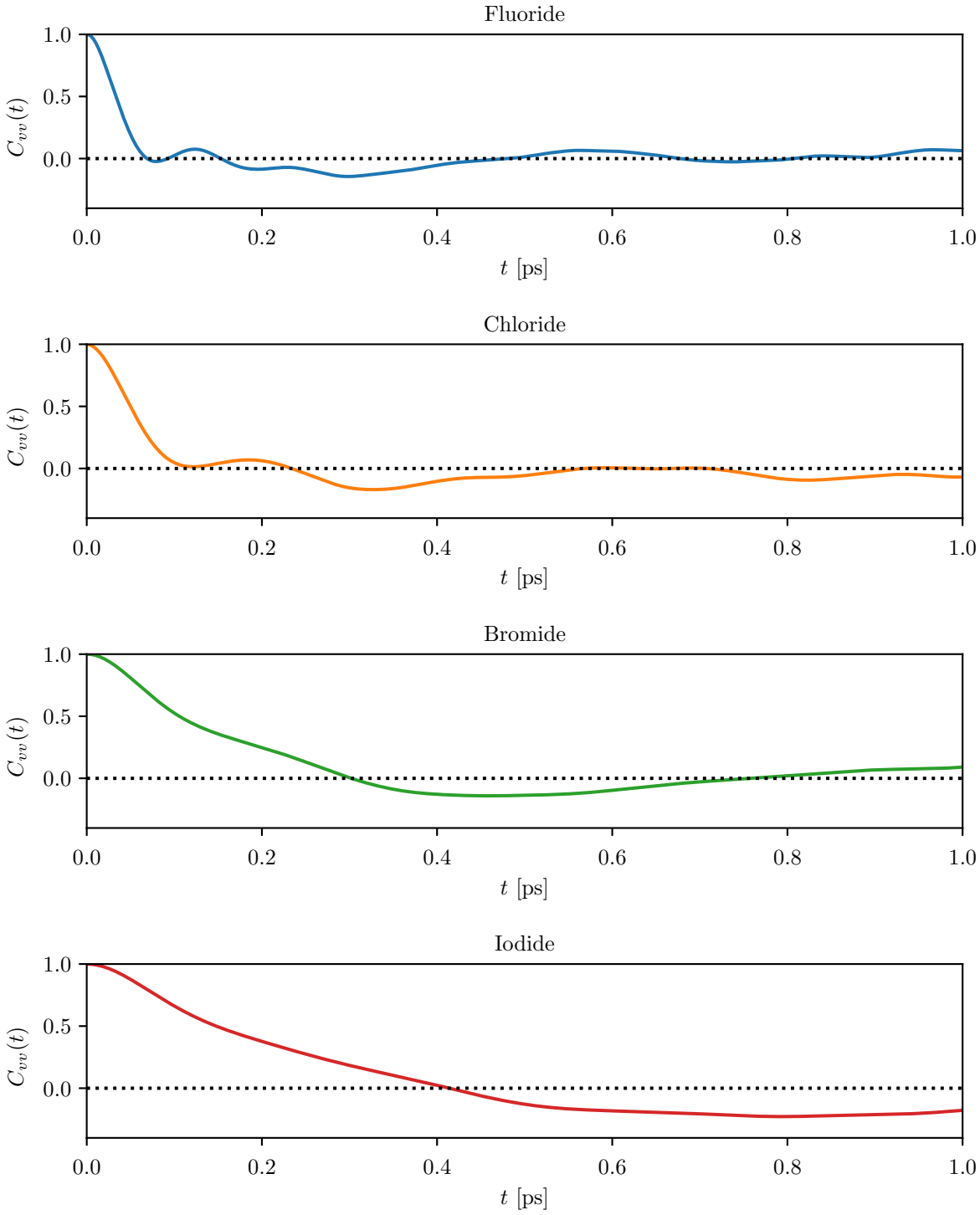

Fig. 4.17 Velocity Autocorrelation Functions for the anions.

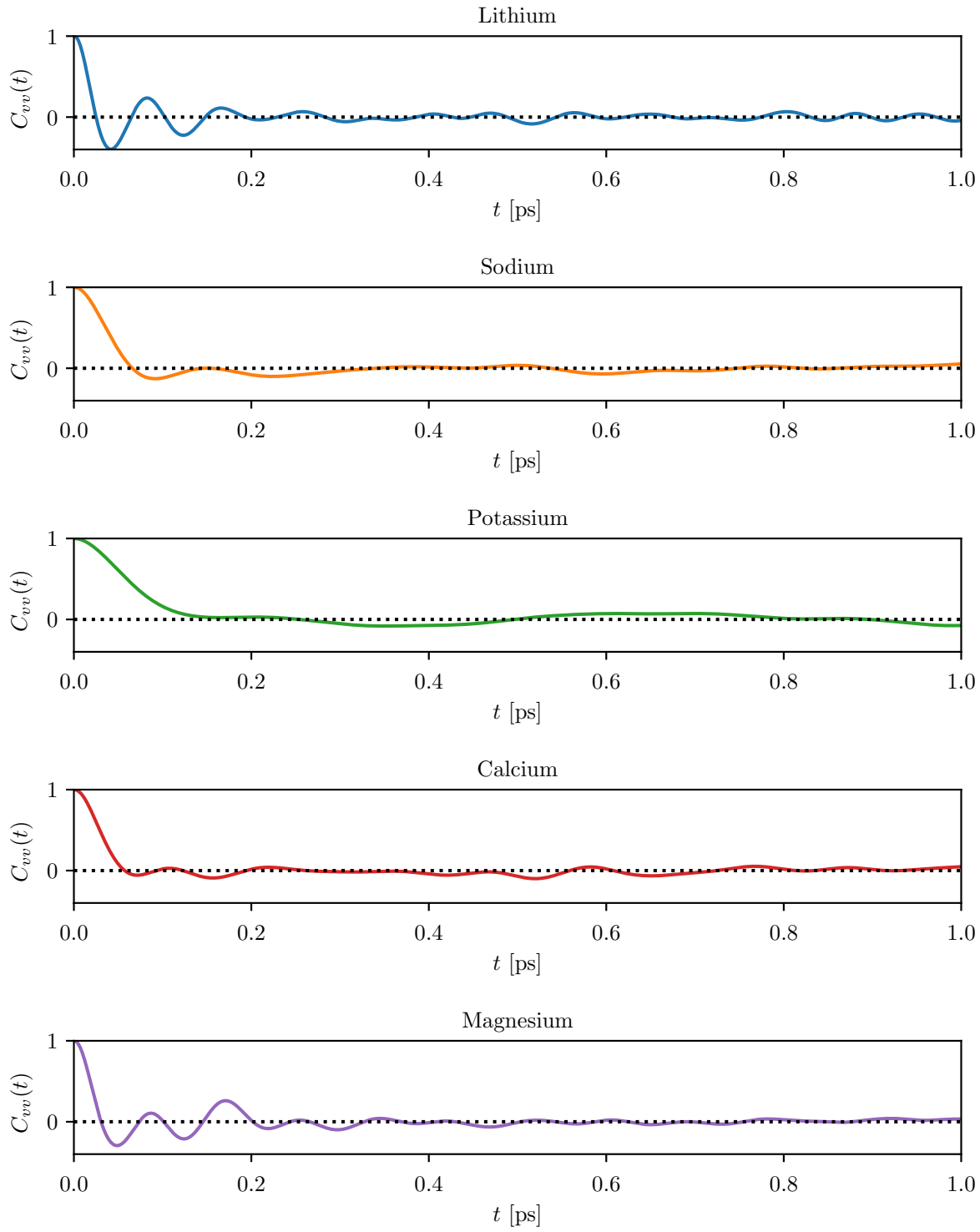

Fig. 4.18 Velocity Autocorrelation Functions for the cations.

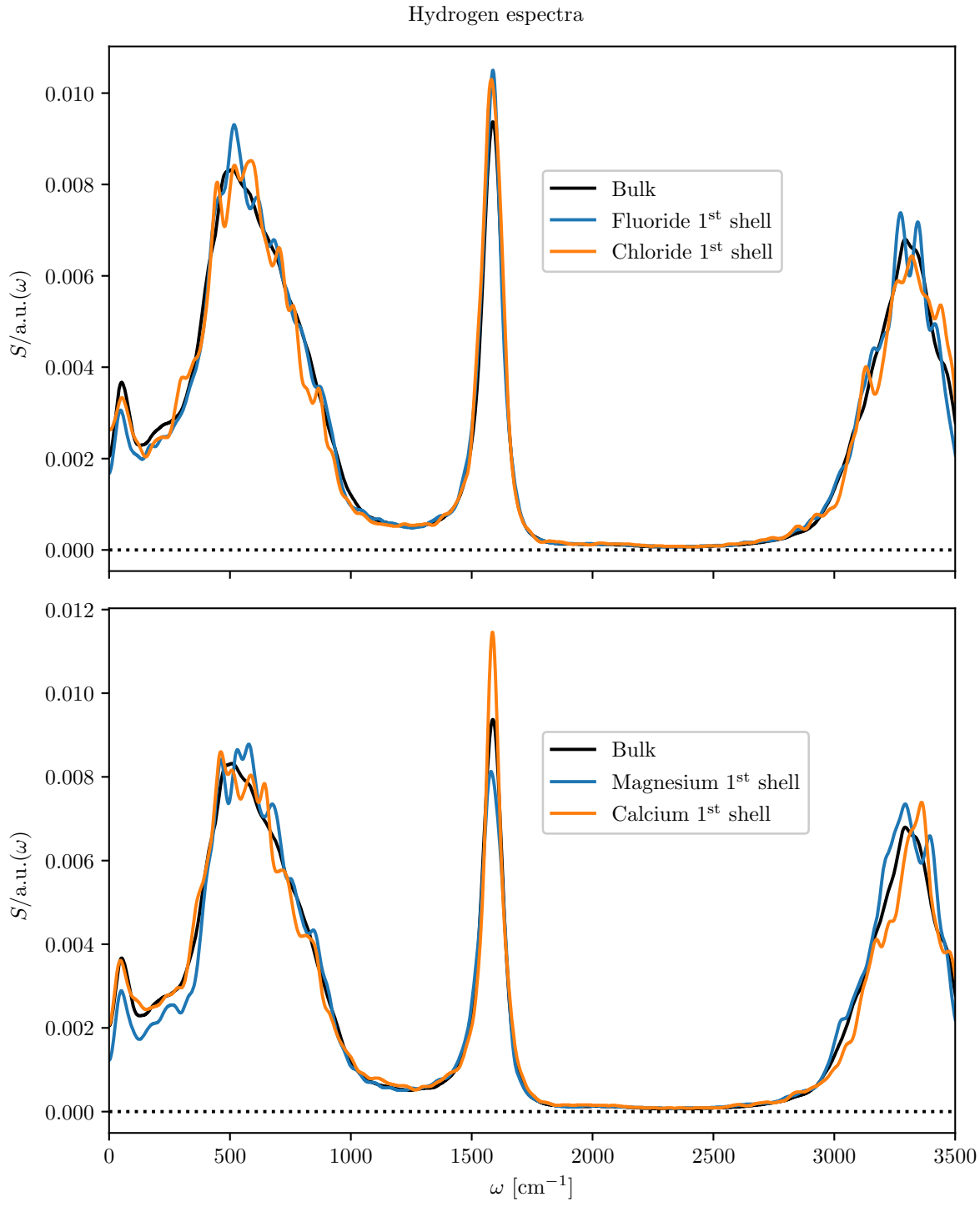

Fig. 4.19 Power espectra for the hydrogen atoms of the first hydration shell (Cl^- and F^- in the upper figure, Ca^{2+} and F^{2+} espectra in the lower figure) compared to that of the bulk water.

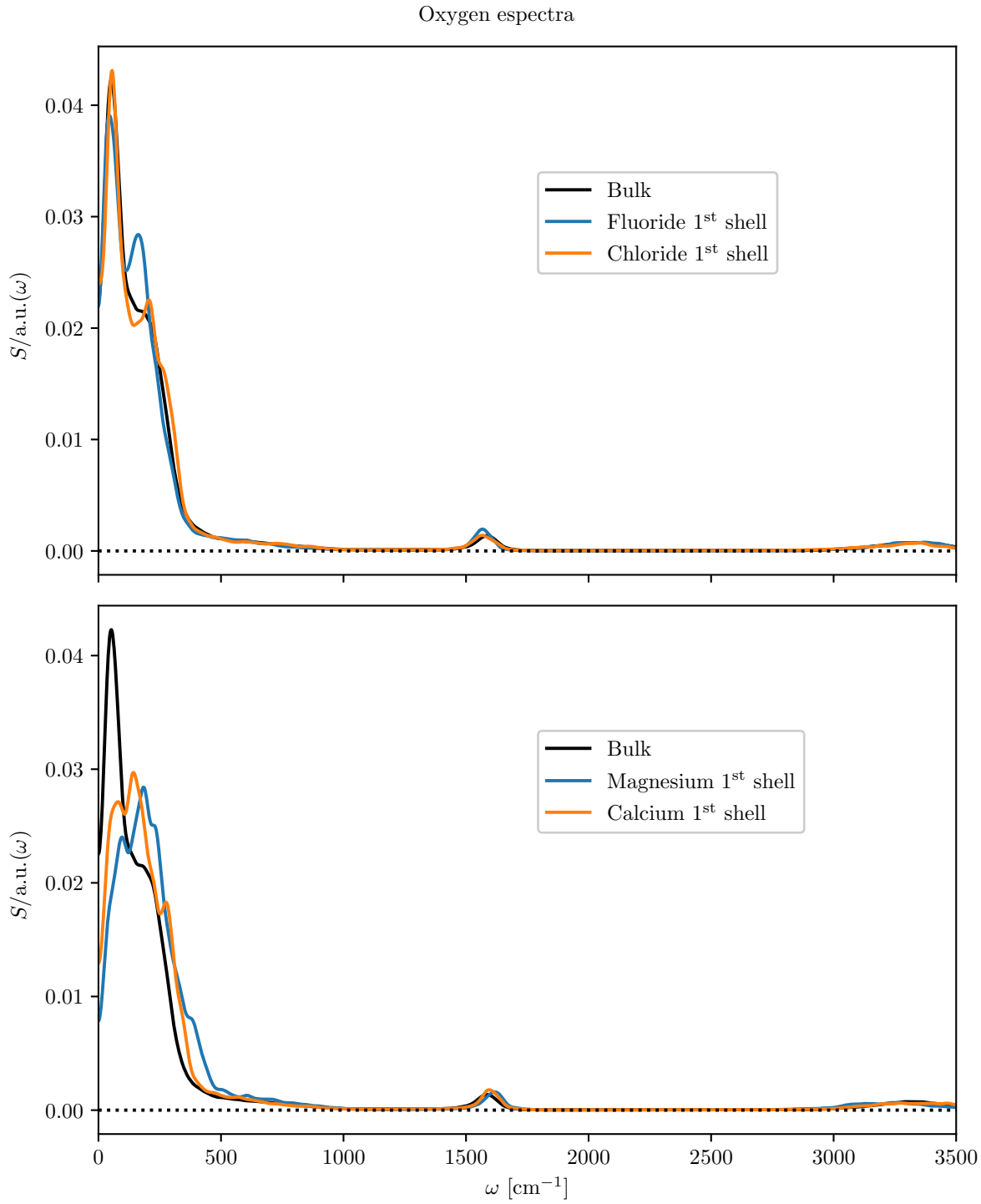

Fig. 4.20 Power espectra for the oxygen atoms of the first hydration shell (Cl^- and F^- in the upper figure, Ca^{2+} and F^{2+} espectra in the lower figure) compared to that of the bulk water.

the numeric integration of the autocorrelation function and obtain the reorientational correlation time τ_2^{HH}. Table 4.6 contains the different values of the hydrogen-hydrogen reorientational correlation time of the first shell for each one of the ions.

By autocorrelating the angle formed by the unitary vector along the ion-oxygen atoms, $\hat{u}_{\mathrm{IO}}$, the movement of the hydration shell as a whole around the ion can also be studied. The corresponding autocorrelation functions are collected for the anions in figure 4.23 and for the cations in figure 4.24. Like with the $\hat{u}_{\mathrm{HH}}$ reorientational movement, the reorientation correlation times of these functions, τ_2^{IO}, can be obtained by fitting them to an exponential function and integrating both the numerical and the analytical domains. The different values of the characteristic ion-oxygen reorientational time for each ion can be found in table 4.6. Once again, it can be seen how smaller ions and higher charges maintain the orientation correlation for longer times. It can be appreciated how, in this case, the first hydration shell molecules lose their angular position around the central ion faster than those in the second shell. This should not surprise as being the second shell water molecules significantly further away than those in the first one, they need to travel longer distances in order to alter their angular position in the same amount.

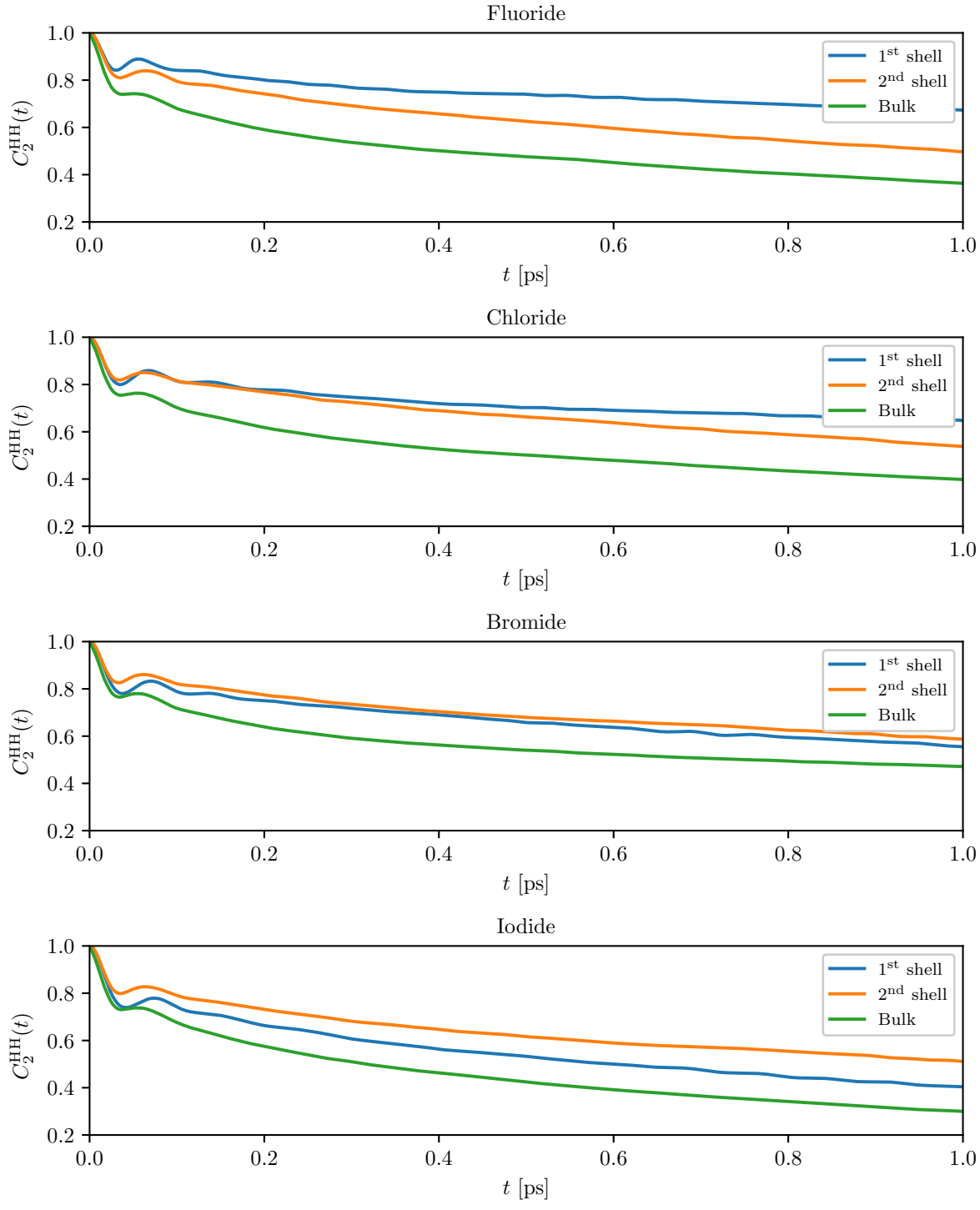

Fig. 4.21 Reorientational Correlation Function of the hydrogen-hydrogen vector for the anions.

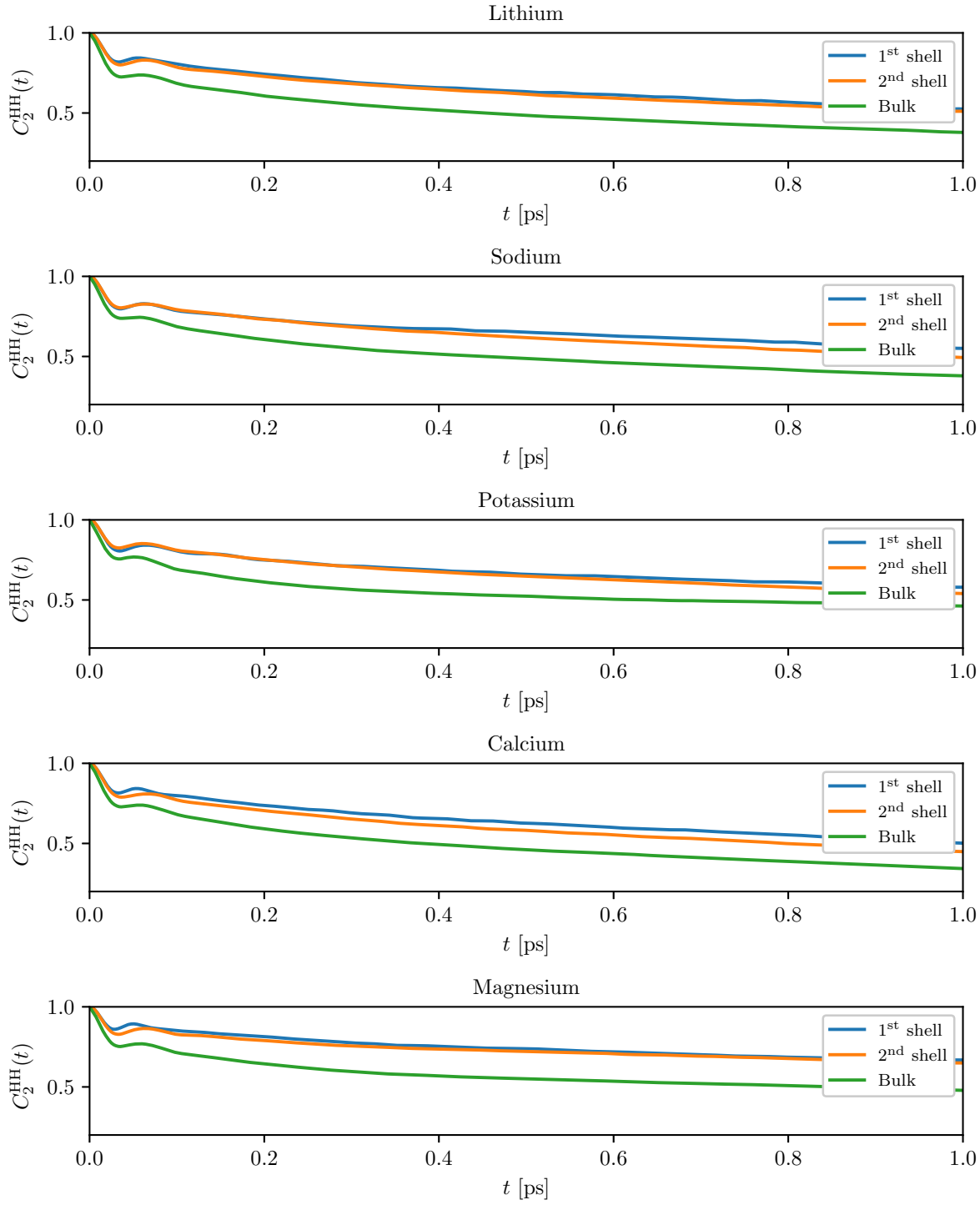

Fig. 4.22 Reorientational Correlation Function of the hydrogen-hydrogen vector for the cations.

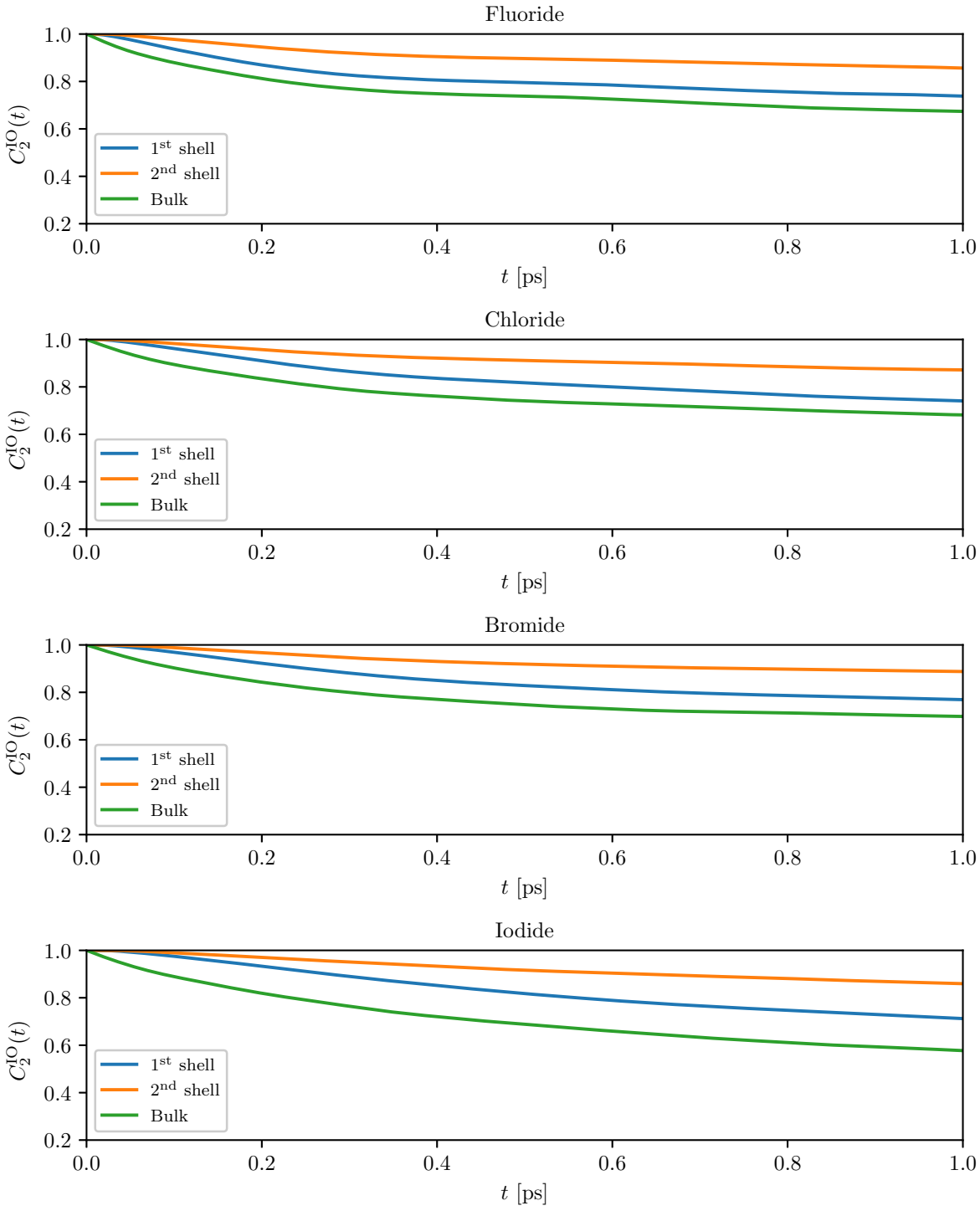

Fig. 4.23 Reorientational Correlation Function of the ion-oxygen vector for the anions.

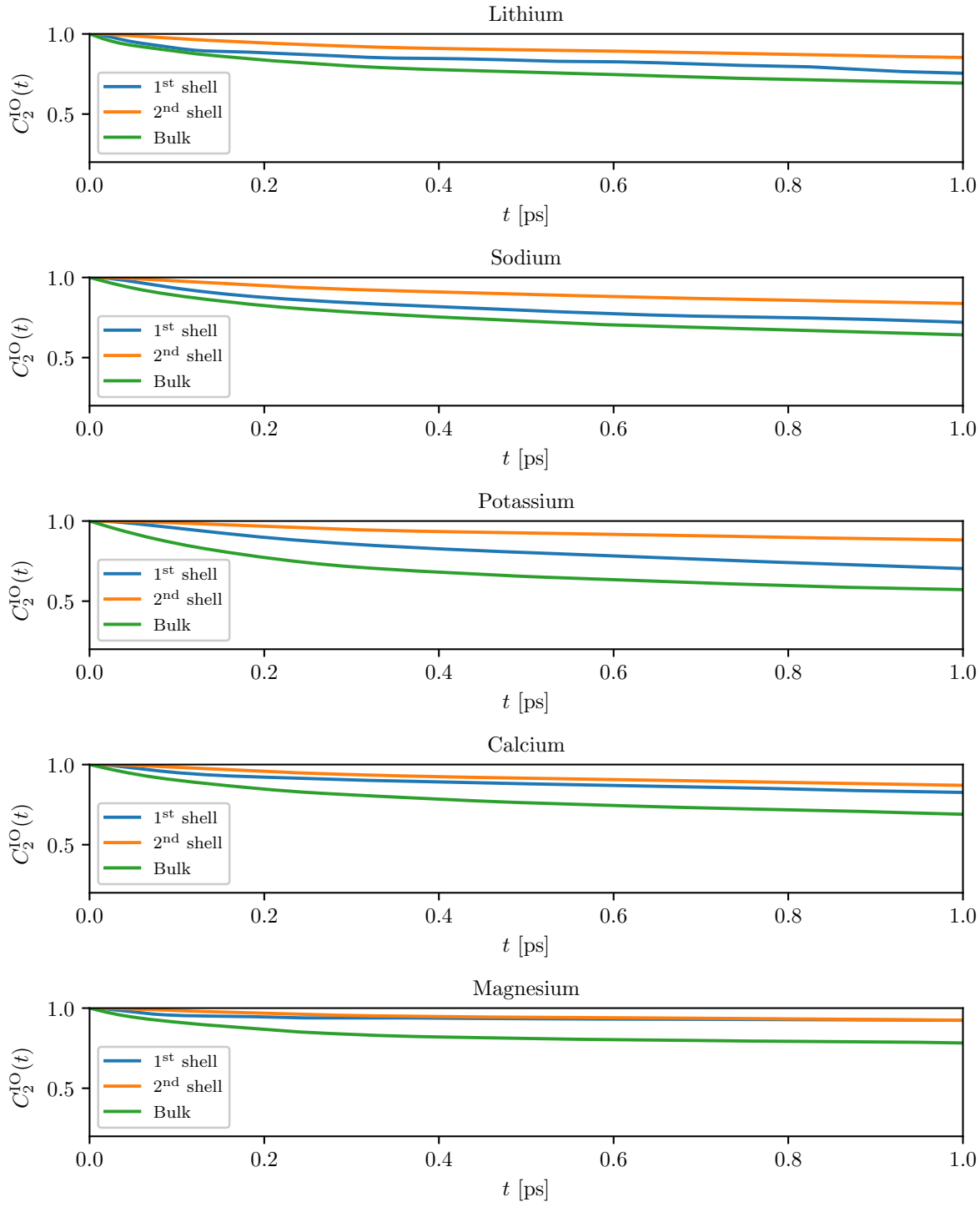

Fig. 4.24 Reorientational Correlation Function of the ion-oxygen vector for the cations.

References

[1] R. Car and M. Parrinello. Unified Approach for Molecular Dynamics and Density-Functional Theory. *Physical Review Letters*, 55(22):2471–2474, 1985.

[2] Copyright MPI P I P I P I für Festkörperforschung Stuttgart 1997-2001 Copyright IBM Corp 1990-2008. CPMD.

[3] Axel D. Becke. Density-Functional Exchange-Energy Approximation with Correct Asymptotic Behavior. *Physical Review A*, 38(6):3098–3100, 1988.

[4] C. Lee, W. Yang, and R. G. Parr. Development of the Colle-Salvetti Correlation-Energy Formula into a Functional of the Electron Density. *Physical Review B*, 37(2):785–789, jan 1988.

[5] I-Chun C. Lin, Ari P. Seitsonen, Maurício D. Coutinho-Neto, Ivano Tavernelli, and Ursula Rothlisberger. Importance of van der Waals Interactions in Liquid Water. *The journal of physical chemistry. B*, 113(4):1127–1131, jan 2009.

[6] N. Troullier and J. L. Martins. Efficient Pseudopotentials for Plane-Wave Calculations. II. Operators for Fast Iterative Diagonalization. *Physical Review B*, 43(11):8861–8869, apr 1991.

[7] Nicola Marzari and David Vanderbilt. Maximally-localized generalized Wannier functions for composite energy bands. *Physical Review B*, 56(20):22, nov 1997.

[8] P. L. Silvestrelli and M. Parrinello. Structural, Electronic, and Bonding Properties of Liquid Water from First Principles. *Journal of Chemical Physics*, 111(8):3572–3580, 1999.

[9] M. Masia. *Ab initio* Based Polarizable Force Field Parametrization. *Journal of Chemical Physics*, 128(18):184107, 2008.

[10] Elvira Guàrdia, Ioannis Skarmoutsos, and Marco Masia. On ion and molecular polarization of halides in water. *Journal of Chemical Theory and Computation*, 5(6):1449–1453, 2009.

[11] S. Koneshan, J. C. Rasaiah, R. M. Lynden-Bell, and S. H. Lee. Solvent Structure, Dynamics, and Ion Mobility in Aqueous Solutions at 25 °C. *The Journal of Physical Chemistry B*, 102(98):4193–4204, 1998.

[12] A Tongraar, K. R. Liedl, and B. M. Rode. Born-Oppenheimer ab Initio QM/MM Dynamics Simulations of Na^+ and K^+ in Water: From Structure Making to Structure Breaking Effects. *The Journal of Physical Chemistry A*, 102(50):10340–10347, 1998.

[13] Y. Marcus. Effect of Ions on the Structure of Water: Structure Making and Breaking. *Chemical Reviews*, 109:1346–1370, 2009.

[14] H. Yu, T. W. Whitfield, E. Harder, G. Lamoureux, I. Vorobyov, V. M. Anisimov, A. D. MacKerell, and B. Roux. Simulating Monovalent and Divalent Ions in Aqueous Solution Using a Drude Polarizable Force Field. *Journal of Chemical Theory and Computation*, 6(3):774–786, 2010.

[15] A. K. Soper and K. Weckström. Ion Solvation and Water Structure in Potassium Halide Aqueous Solutions. *Biophysical chemistry*, 124(3):180–91, dec 2006.

[16] S. Varma and S. B. Rempe. Coordination Numbers of Alkali Metal Ions in Aqueous Solutions. *Biophysical Chemistry*, 124(3):192–199, 2006.

[17] T. Ikeda and M. Boero. Role of van der Waals Corrections in First Principles Simulations of Alkali Metal Ions in Aqueous Solutions. *The Journal of Chemical Physics*, 143(19):194510, 2015.

[18] J. M. Heuft and E. J. Meijer. Density Functional Theory Based Molecular-Dynamics Study of Aqueous Chloride Solvation. *The Journal of Chemical Physics*, 119(22):11788, 2003.

[19] J. M. Heuft and E. J. Meijer. Density Functional Theory Based Molecular-Dynamics Study of Aqueous Fluoride Solvation. *The Journal of chemical physics*, 122(9):094501, 2005.

[20] J. M. Heuft and E. J. Meijer. Density Functional Theory Based Molecular-Dynamics Study of Aqueous Iodide Solvation. *Journal of Chemical Physics*, 123(9):12–17, 2005.

[21] S. Ansell, A. C. Barnes, P. E. Mason, G. W. Neilson, and S. Ramos. X-ray and Neutron Scattering Studies of the Hydration Structure of Alkali Ions in Concentrated Aqueous Solutions. *Biophysical chemistry*, 124(3):171–9, 2006.

[22] J. L. Fulton, S. M. Heald, Y. S. Badyal, and J. M. Simonson. Understanding the Effects of Concentration on the Solvation Structure of Ca^{2+} in Aqueous Solution. I:

The Perspective on Local Structure from EXAFS and XANES. *J. Phys. Chem. A*, 107(23):4688–4696, 2003.

[23] I. S. Joung and T. E. Cheatham, III. Molecular Dynamics Simulations of the Dynamic and Energetic Properties of Alkali and Halide Ions Using Water-Model-Specific Ion Parameters. *The Journal of Physical Chemistry B*, 113(40):13279–13290, oct 2009.

[24] H. J. Bakker. Structural Dynamics of Aqueous Salt Solutions, 2008.

[25] M. F. Kropman and H. J. Bakker. Dynamics of Water Nolecules in Aqueous Solvation Shells. *Science (New York, N.Y.)*, 291(5511):2118–2120, 2001.

[26] M. F. Kropman and H. J. Bakker. Femtosecond Mid-Infrared Spectroscopy of Aqueous Solvation Shells. *Journal of Chemical Physics*, 115(19):8942–8948, 2001.

[27] M. F. Kropman, H. K. Nienhuys, and H. J. Bakker. Real-Time Measurement of the Orientational Dynamics of Aqueous Solvation Shells in Bulk Liquid Water. *Physical review letters*, 88(7):077601, 2002.

[28] I. S. Joung and T. E. Cheatham, III. Supporting Information: Molecular Dynamics Simulations of the Dynamic and Energetic Properties of Alkali and Halide Ions Using Water-Model Specific Ion Parameters. pages 1–52, 2009.

[29] Albert Einstein. On the Motion of Small Particles Suspended in a Stationary Liquid, as Required by the Molecular Kinetic Theory of Heat. *Annalen der Physik*, 322(8):549–560, 1905.

[30] David R Lide, W M Mickey Haynes, Grace Baysinger, Lev I Berger, Henry V Kehiaian, Dana L Roth, Daniel Zwillinger, Michael Frenkel, and Robert N Goldberg. *CRC Handbook of Chemistry and Physics*. 90 edition, 2010.

Chapter 5

How Polarization Damping Affects Ion Solvation Dynamics

5.1 Introduction

It is widely accepted that the inclusion of polarization effects in force field Molecular Dynamics (MD) simulations is of high importance for studying both homogeneous and inhomogeneous systems [1–6]. The contribution of many body terms to the total interaction potential (neglected in non-polarizable empirical potentials) is known to vary with the systems, and it is not straightforward to assess it *a priori* [7]. It is certain, though, that a proper description of polarizable interactions represents the next milestone in force field development. In fact, even though dipolar interactions decay faster than Coulomb ones, they are responsible of interesting and non-negligible physical chemical properties; as an example, the anion surface propensity in water/air interfaces could be explained only by using polarizable force fields [8–11]. The same applies to solvation of highly charged cations: for lanthanides in water it has been found that EXAFS and XANES spectra could be reproduced only by adding polarizability [12]. Besides these applications, strictly related to ions in water, the study of many different systems might be faced with polarizable force fields, e.g. molten salts [13, 14], ionic liquids [15] and biosystems [16].

The most widespread methods to deal with polarization in MD simulations are the Drude oscillator model (or charge on spring), the fluctuating charge model and the Polarizable Point Dipoles method [5, 17, 18]. The latter has been applied in this work; it should be stressed, though, that the conclusions of this study are of general validity and that they could be easily ported to any of the above mentioned methods. The main

focus of this research is to ascertain which features a polarizable force field should have in order to accurately describe the intermolecular potential. These aspects are important for developing the next generation of force fields, that might be used to study, *inter alia*, heterogeneous systems in presence of high electric fields.

Recently, many authors [19–24] have pointed out that one of the largest limitations of standard molecular-mechanics polarizable force fields lies in the fact that the transferability of gas phase derived potentials to condensed phase is hindered by the absence of polarization exchange-coupling in classical models (since it is due to short range electron cloud repulsion, it is also known as *Pauli effect* [25]). In 1981 Thole [26] published a seminal paper on the use of damping functions for hindering the so-called *intramolecular polarization catastrophe*, i.e. the divergence of dipole moments causing the dynamics to breakdown. Although his results could be extended also to *intermolecular interactions*, only recently this approach has been used in Molecular Dynamics simulations [27, 28]. This perspective guided the pursue of a method to develop polarizable models which could faithfully reproduce the electrostatic properties of simple systems such as ion-molecule (either water or carbon tetrachloride) dimers [17, 21–23]. The method was then extended to bulk systems [28], where the impact of damping short range electrostatic interactions on static properties was assessed. A model system, namely a chloride ion in water, was studied by comparing force field and Car-Parrinello Molecular Dynamics. It was found that, while the structure (radial distribution function) is already well reproduced by using a low value for the polarizability ($\alpha_{\mathrm{Cl}} = 3.2$ Å^3) without damping, electrostatic properties are not. In particular, it was proved that, with such systems, the ion dipole moment is overestimated (broad dipole moment distribution, shifted to high values), and that the ion is characterized by a high polarization anisotropy. Finally, it was showed that all these quantities are well reproduced if gas phase polarizability is used ($\alpha_{\mathrm{Cl}} = 5.48$ Å^3), together with damping functions. Recently, it has been pointed out that including short range damping allows to reproduce thermodynamical properties of halide ions at interfaces [10]. It must be noticed that many authors suggest the use of low polarizabilities for halide in water, thus introducing implicitly the interaction with the electron density of surrounding molecules. With their approach, the polarizability at condensed phase would be smaller than that at gas phase. One weak point of this approach is that the polarization at intermediate distances is lower than expected, as highlighted by high level quantum chemical calculations on a simple ion-water dimer [22]. On the other hand, this work's approach is based on the assumption that the ionic polarizability is the same as that at gas phase, and that, using suitable

damping functions, it accounts for the dynamical response of the anion to the electron density of the environment

In this work the impact of using short range damping functions on the dynamical properties of the systems is investigated. This is of particular interest mainly for people studying ion solvation dynamics. Indeed, these features are the focus of many experimental and theoretical studies such as in references [8, 9, 29–33], to cite just the most outstanding ones. In particular the properties which are mostly observed/simulated are related to the ion (diffusion coefficients), and to its environment (rotational relaxation, exchange times and mechanism, etc). Since in the bulk, ionic and molecular polarization influences solvation shell dynamics [21, 32–35], this work focuses on ion diffusion, characteristic exchange times of first shell water molecules and rotational dynamics.

5.2 Computational Details

5.2.1 Electrostatic Damping

The total electrostatic energy of a system of charges and dipoles can be partitioned into different contributions arising from charge-charge, charge-dipole and dipole-dipole interactions plus the dipole polarization term:

$$\begin{aligned} U_{\mathrm{el}} &= U_{qq} + U_{q\mu} + U_{\mu\mu} + U_{\mathrm{dip}}^{\mathrm{pol}} = \\ &= \sum_i \sum_{j>i} \left(q_i \hat{T}_{ij} q_j + \mu_i^{\alpha} \hat{T}_{ij}^{\alpha} q_j - q_i \hat{T}_{ij}^{\alpha} \mu_j^{\alpha} - \mu_i^{\alpha} \hat{T}_{ij}^{\alpha\beta} \mu_j^{\beta} \right) \qquad (5.1) \\ &\quad + \frac{1}{2} \sum_{i=1}^{N_\mu} \vec{\mu}_i \cdot \hat{\alpha}_i^{-1} \cdot \vec{\mu}_i, \qquad (5.2) \end{aligned}$$

where $\hat{\alpha}_i$ is the i^{th} atom polarizability tensor; in the following discussion it will be considered to be isotropic, thus substituting the tensor with a scalar. In the above equation it has been introduced the *electrostatic interaction tensors* $\hat{T}_{ij}$, $\hat{T}_{ij}^{\alpha}$ and $\hat{T}_{ij}^{\alpha\beta}$, that are useful for calculating, energies, forces and electric fields. Their functional form [28,

36] is given by:

$$\hat{T}_{ij} = [s_0(r)]\,\frac{1}{r} \tag{5.3}$$

$$\hat{T}^{\alpha}_{ij} = \nabla_\alpha \hat{T}_{ij} = -\,[s_1(r)]\,\frac{r_\alpha}{r^3} \tag{5.4}$$

$$\hat{T}^{\alpha\beta}_{ij} = \nabla_\alpha \hat{T}^{\beta}_{ij} = [s_2(r)]\,\frac{3r_\alpha r_\beta}{r^5} - [s_1(r)]\,\frac{\delta_{\alpha\beta}}{r^3} \tag{5.5}$$

$$\hat{T}^{\alpha\beta\gamma}_{ij} = \nabla_\alpha \hat{T}^{\beta\gamma}_{ij} = -\,[s_3(r)]\,\frac{15}{r^7} r_\alpha r_\beta r_\gamma + \tag{5.6}$$

$$[s_2(r)]\,\frac{3}{r^5}\left(r_\alpha \delta_{\beta\gamma} + r_\beta \delta_{\alpha\gamma} + r_\gamma \delta_{\alpha\beta}\right), \tag{5.7}$$

where r_α, r_β and r_γ are the cartesian components of the vector $\vec{r} = \vec{r}_i - \vec{r}_j$ defining the distance (which norm is $r = |\vec{r}|$) between particles i and j, and the Kronecker delta function $\delta_{\alpha\beta}$ returns 1 if $\alpha = \beta$ and 0 otherwise. The appropriate screening functions $s_n(r)$ describe the kind of interacting charges' distributions. In traditional point charge schemes the charge distribution is a delta function centered in $\vec{r}_i$ ($s_n(r) = 1$); some applications deal with smeared charges and the screening functions are not unit, but rather a nonlinear function of the distance. It can be easily shown that, knowing $s_0(r)$, higher order screening functions are recursively obtained applying

$$s_k(r) = s_{k-1}(r) - \frac{r}{2k-1}\frac{\partial}{\partial r} s_{k-1}(r). \tag{5.8}$$

The use of screening function is well established both for the Ewald summation method (accounting for the periodic boundary conditions) and for electrostatic damping schemes. The latter arise naturally if one considers that the charges or dipoles are not points, but rather distributed according to same *a priori* assumed distribution. This is indeed a realistic situation when molecules come "close enough". In the case of halide ions it has been shown that "close enough" means ca. 4 Å [22, 23]. In this work it has been studied both, the exponential and the Gaussian charge distributions, which have been shown to be the most promising; furthermore, they are easy to implement and they imply a negligible computational overhead (see Ref. [28] for further details).

It should be stressed that, although the Polarizable Point Dipole scheme allows for more flexibility, the method could be easily extended to other schemes accounting for polarizability. In fact, the overall effect of damping functions is to screen the electric field for short range interactions. Therefore, given that both in Drude oscillators and in fluctuating charges methods there are no dipoles, but only charges, it suffices to consider the damping of the tensors accounting for charge-charge interactions. Recently,

Model	Charge Distribution	$\hat{\alpha}$ [Å^3]
A3.2-none	none	3.25
A3.2-gau	Gaussian	3.25
A4.0-gau	Gaussian	4.00
A5.5-gau	Gaussian	5.48
A3.2-exp	exponential	3.25
A4.0-exp	exponential	4.00
A5.5-exp	exponential	5.48

Table 5.1 List of names and main features of the studied models (see Ref. [28] for further details).

the method has been implemented in CHARMM force field [37, 38], together with Drude oscillators.

5.2.2 Classical MD

Classical MD simulations were performed with an in-house program. The system is composed of 96 water molecules and one chloride anion. The size of system was chosen in order to compare with Car-Parrinello Molecular Dynamics simulations; in fact, although the Ewald summation technique allows to deal with charged systems, according to our calculations, static and dynamical properties are slightly affected by the size of the simulation box.

The Polarizable Point Dipole method has been used for accounting for polarization. For water it has been implemented the RPOL model [39]: the charges associated to each atom reproduce the water dipole moment at gas phase. On top of that, site polarizabilities are associated to each atom, that allow to obtain a dipole moment distribution at condensed phase peaked at ca. 2.6 D. The force fields parameters are divided into seven models, differing among them for the value of chloride polarizability and for the type of the assumed charge distribution; the main features of these models are resumed in table 5.1. The entire set of parameters for the force fields used are given in tables I and II of Ref. [28].

In order to accelerate the computational time the ASPC scheme [40] has been implemented. After having equilibrated the system at 298 K for 500 ps, we have run six NVE 1 ns simulations, starting from different initial configurations.

Model	D_{msd} $[10^{-9}\,\mathrm{m^2\,s^{-1}}]$	D_{vacf} $[10^{-9}\,\mathrm{m^2\,s^{-1}}]$	T [K]
A3.2-none	0.67 (0.09)	0.72 (0.12)	299.1 (2.4)
A3.2-exp	0.78 (0.17)	0.86 (0.15)	297.0 (5.3)
A3.2-gau	0.83 (0.12)	0.74 (0.11)	307.0 (5.1)
A4.0-exp	1.11 (0.12)	1.10 (0.12)	305.4 (2.5)
A4.0-gau	0.87 (0.14)	0.93 (0.10)	298.6 (2.7)
A5.5-exp	1.12 (0.10)	1.22 (0.09)	295.2 (3.9)
A5.5-gau	0.78 (0.17)	0.85 (0.16)	291.5 (4.9)
CPMD	1.07	–	300.0

Table 5.2 Diffusion coefficients for the chloride ion obtained from the mean square displacement (D_{msd}) and from the velocity autocorrelation function (D_{vacf}). Values for classical MD are averaged over six NVE simulations (mean standard deviations in parenthesis). The average temperatures are also reported.

5.2.3 Car-Parrinello MD

The results of the CPMD simulations for the chloride ion, explained in Chapters 2 and 4, have been used to compare ion diffusion, water molecules residence times, reorientational motions of water molecules and the hydration shell as a whole.

Comparing the above dynamical properties to experimental data would require the description of zero point energy contributions with path integral techniques [41, 42]. Nevertheless, since the focus of the present contribution is on the capabilities of classical force field to reproduce dynamical properties of density functional based simulations, neither our classical nor Car-Parrinello MD simulations account for nuclear quantum effects.

5.3 Results and Discussion

The diffusion of a solute is connected to its interaction with the solvent, particularly with the first shell molecules. For ions in water, it has been shown that there exist a tight coupling between equilibrium and non-equilibrium effects of hydration shell exchange and ion diffusion [43]. Furthermore, in case of halide anions, a proper modeling of the interaction potential is of high importance for reproducing the hydrogen bonds, as the first hydration shell seems to be critically dependent on them. In figure 5.1 the mean square displacement (MSD) of the ion from CP and classical MD simulations are shown. For sake of clarity, the results are shown in three panels, each containing the MSD of

potential models with a fixed value of anion polarizability (the same approach is used also for the following figures). It can be noticed that the MSD obtained in CPMD simulations is not as straight as the one computed in classical simulations. This is due to the shortness of CPMD trajectories which do not allow to gather enough statistics for the MSD. A similar effect was found for the velocity autocorrelation functions (not shown here). Nevertheless, a general trend could be appreciated in the graphs: for low values of the anion polarizability the diffusion is slower than in the case of high polarizability. In table 5.2 the values for the diffusion coefficients are shown. It can be noticed that the difference between exponential and Gaussian damping functions correlates well with the difference in temperatures. Nonetheless, the potential with exponential damping seems to perform slightly better than the ones with Gaussian damping.

The lower ion mobility can be explained by considering that the interaction of ion and water dipole moments is badly described when a low polarizability value is taken as reference. In the case of undamped potentials, the induced dipole moment on the ion is much higher than in *ab initio* calculations. Therefore, high dipolar interactions render the system more viscous. In the case of damped potentials, the dipole moment is lower than the *ab initio* one at all distances. Hence the Coulomb interaction prevails upon the dipolar one, causing the hydrogen bond to be stronger and to slower the system dynamics. This is confirmed by the inspection of hydration shell exchange and rotational dynamics in figures 5.2, 5.3 and 5.4, and in table 5.3. The residence time correlation function of first shell molecules decays much faster for high polarizability rather than for low polarizability. In the case of the exponential damping with high anion polarizability, the correlations function overlaps almost completely with CPMD results. A similar trend is observed in the rotational times of first shell molecules around the O-H bond. This measure is intimately connected to the hydrogen bond dynamics of first shell molecules with the anion. It can be seen that the correlation functions (figure 5.3) resemble the CPMD results better for high values of the polarizability.

As mentioned in the introduction, in a previous article it was shown that a higher polarization anisotropy of the first solvation shell is associated with a low anion polarizability. This has a direct consequence on the collective motion of first shell molecules. The rotational correlation function of the Cl-O bond (figure 5.4) conveys a picture of how fast the whole solvation shell rotates around the ion. Again, only at high values of the anion polarizability, we recover the dynamical behavior of *ab initio* simulations.

From the above results it is learned that the ion solvation dynamics is well reproduced by a system with high anion polarizability. Using a low polarizability seems to dampen the dynamics and to render it slower, at least for the motions studied here. Moreover,

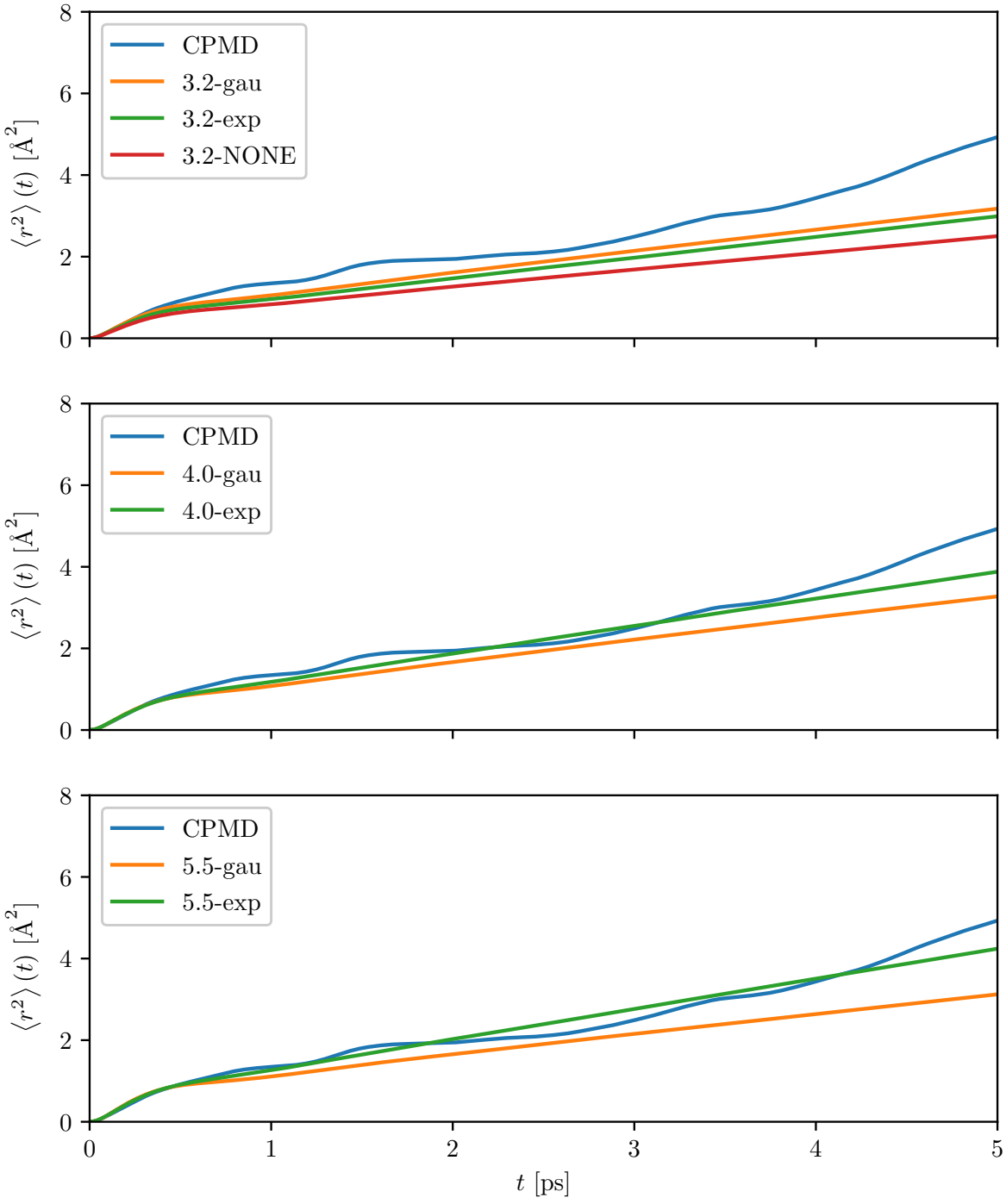

Fig. 5.1 Chloride mean square displacement of all models compared to Car-Parrinello results (key in the legend of each panel).

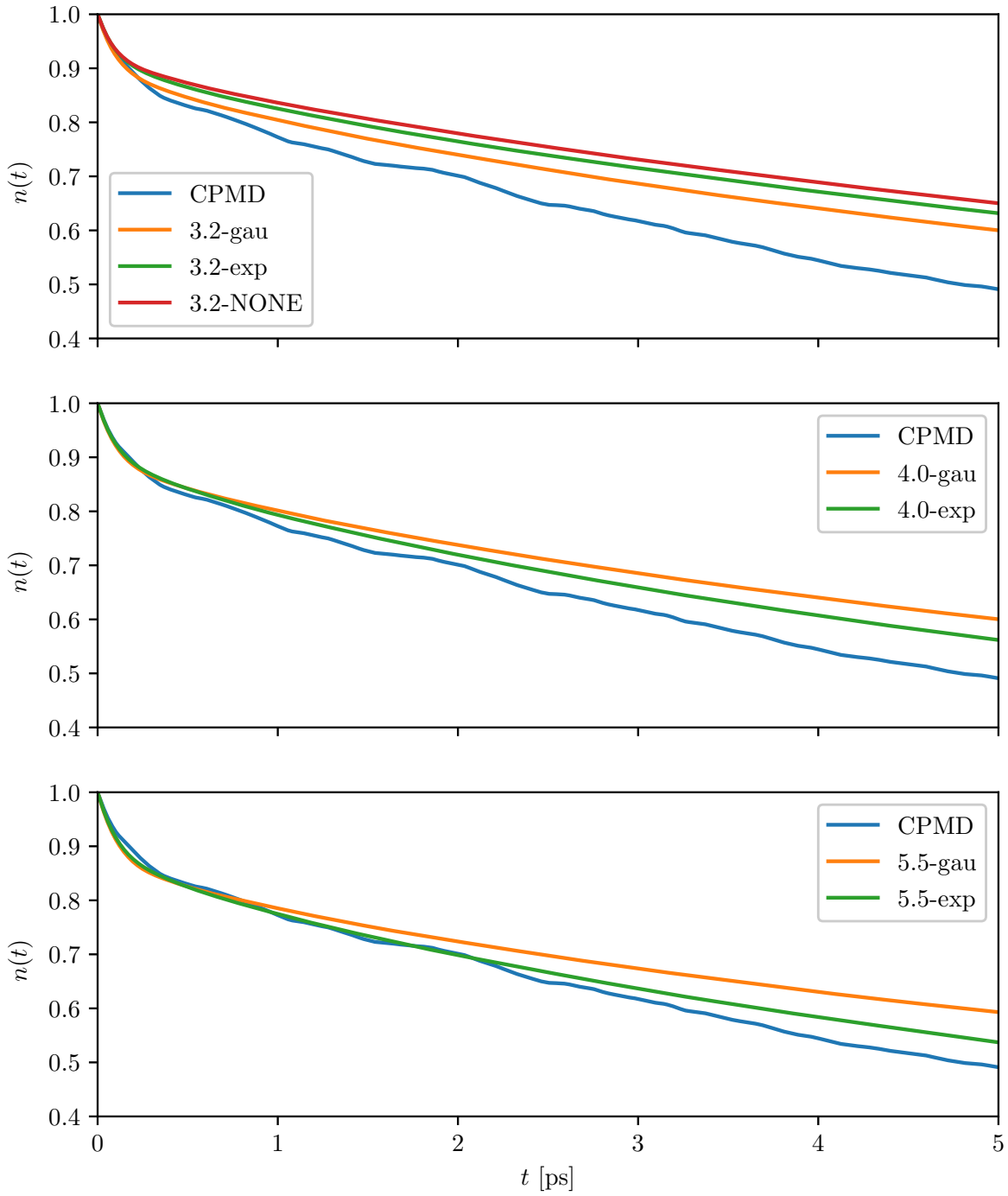

Fig. 5.2 First shell residence correlation function of all models compared to Car-Parrinello results (key in the legend of each panel).

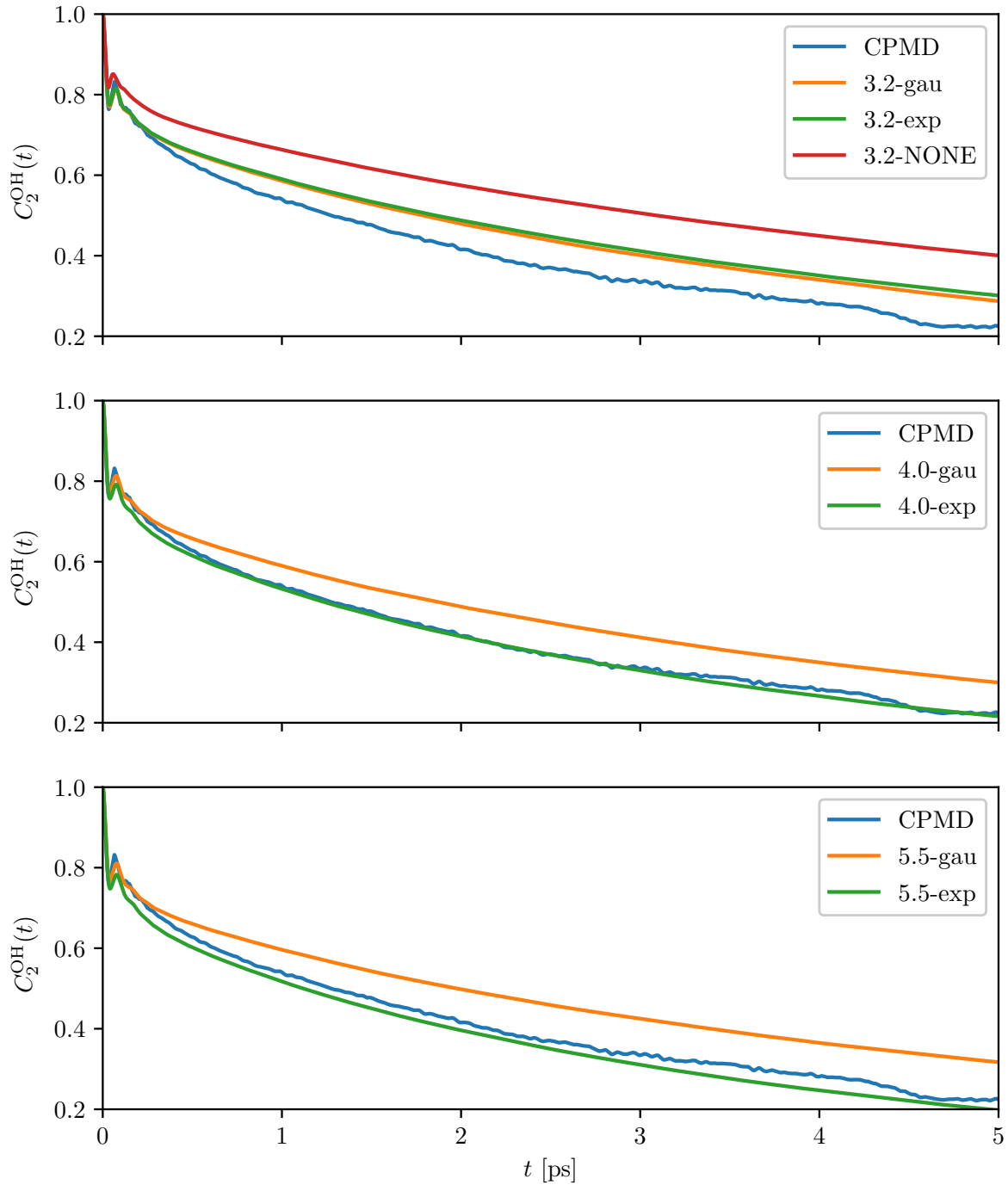

Fig. 5.3 O-H reorientational correlation functions for the first shell water molecules. Results for second Legendre polynomial are shown for all models, compared to Car-Parrinello results (key in the legend of each panel).

Model	τ_{1st} [ps]	τ_2^{OH} [ps]	τ_2^{ClO} [ps]
A3.2-none	14.0 (1.3)	6.2 (0.5)	11.3 (0.9)
A3.2-exp	13.2 (2.0)	4.4 (0.9)	9.5 (1.7)
A3.2-gau	11.6 (0.7)	4.1 (0.5)	8.6 (0.9)
A4.0-exp	9.9 (1.3)	3.0 (0.3)	6.8 (0.9)
A4.0-gau	11.8 (1.4)	4.3 (0.5)	8.8 (1.2)
A5.5-exp	9.1 (0.5)	2.8 (0.2)	6.4 (0.4)
A5.5-gau	11.9 (1.8)	4.6 (0.7)	9.4 (1.5)
CPMD	7.5	3.0	6.0

Table 5.3 Residence time, and O-H and O-Cl reorientational correlation times of the first shell molecules. Values for classical MD are averaged over six NVE simulations (mean standard deviations in parenthesis).

it seems that the exponential damping performs slightly better than the Gaussian one. Nonetheless, it needs to be remarked that the damping parameters were not optimized for condensed phase simulations. Thus, it is not correct to conclude that, *always*, the exponential damping performs better than the Gaussian one; in fact, it is only in the case of our parameter set. Finally, it can be seen that the results obtained for polarizability values equal to 4 Å^3 and 5.48 Å^3 do not differ very much, the main difference lying in the decay of the exchange correlation function. From this result it would be tempting to use the anion polarizability equal to 4 Å^3; it must be highlighted, though, that statical properties are not as well reproduced for A4.0-gau and A4.0-exp model potentials (see Ref. [28]). Therefore, since it is highly important to reproduce faithfully both static and dynamical properties, we suggest the use of A5.5-gau and A5.5-exp force fields, or similar (optimized) ones with the value of the anion polarizability equal to 5.48 Å^3.

In the above discussion it has never been mentioned the role played by water polarizability. The water model is certainly important when considering the solvation shell dynamics. Although a better force field for water is needed, it should be observed that the anion shows higher fluctuations in the dipole moment (from almost 0 to 2 Debye), which are relevant in driving the system dynamics.

5.4 Conclusions and Perspectives

The use of damping functions for the simulation of polarizable systems has been introduced in 1981 [26]. The main reason to include *intra-molecular* damping has been the need to hinder the polarization catastrophe for simulations with the Polarizable Point

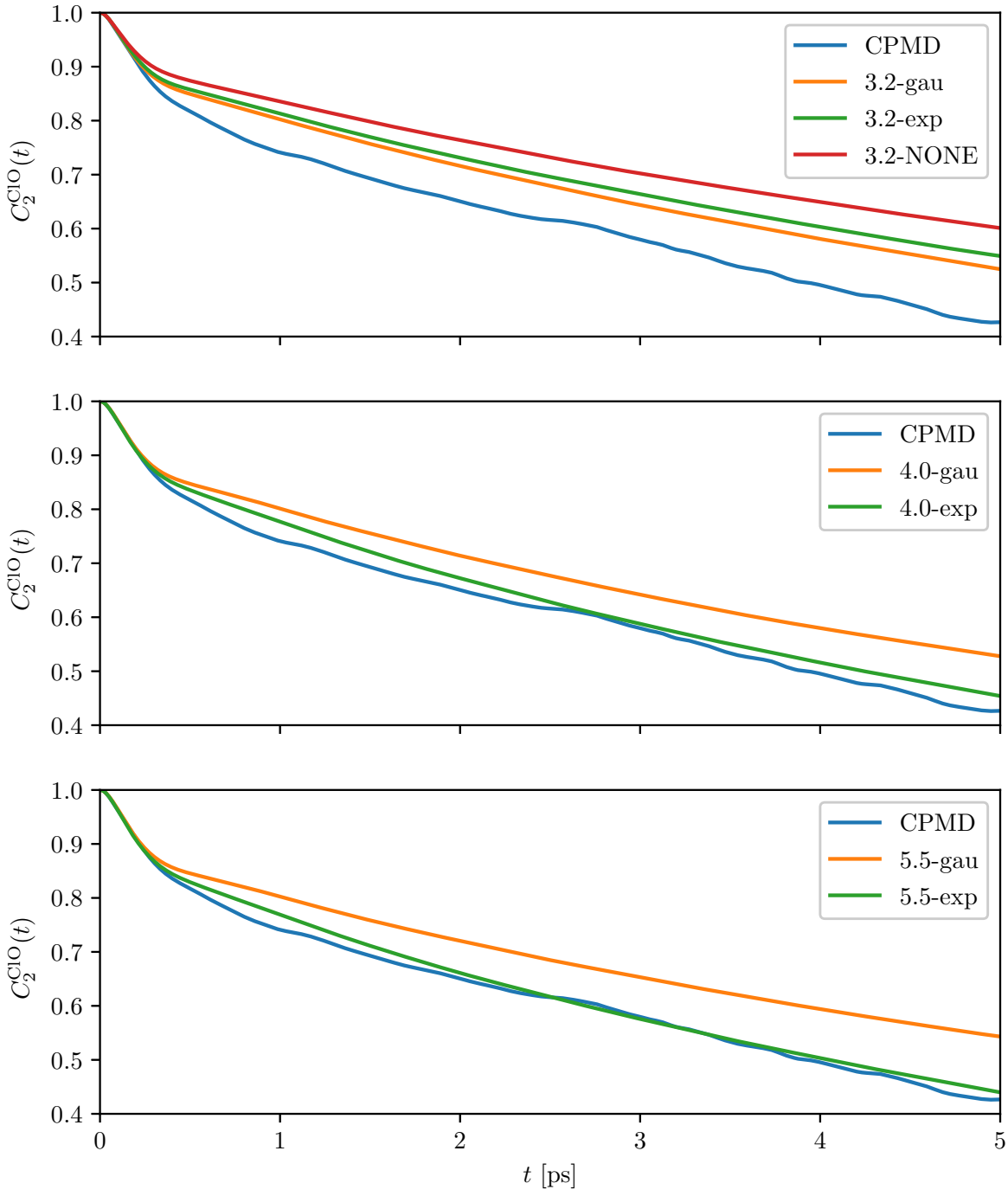

Fig. 5.4 O-Cl reorientational correlation functions for the first shell water molecules. Results for second Legendre polynomial are shown for all models, compared to Car-Parrinello results (key in the legend of each panel).

Dipoles method. Though, until a few years ago, electrostatic damping was not used to treat also *inter-molecular* interactions; probably this delay was due to the fact that the electric fields in most of the studied systems were not high enough to cause any appreciable divergence of the dipoles. In 2005, by studying a simple ion-water dimer, it was found that the damping of inter-molecular electrostatic interactions was needed to reproduce short range effects of interacting electron densities [21]. In the case of highly polarizable ions, such as halides, it was remarked that, to reproduce both long and short range polarization, the damping functions should be used on top of force field where the halide had its gas phase polarizability [22].

Recently it was shown that the latter conclusion holds also for the case of chloride in bulk water; *ab initio* results on the static properties of this system were nicely reproduced using the same polarizability and damping functions optimized for gas phase calculations [28].

In this work, it has been shown that the same force field allows to reproduce better also dynamical properties of the ion and of its solvation shell. It seems that, in absence of damping functions, the dynamics of chloride and of first shell molecules is slower. Therefore, the introduction of damping functions is highly important when studying dynamical properties. Both, exponential and Gaussian charge distributions yield good results, the former performing slightly better that the latter. It must be stressed that the force field was not parameterized using the above properties as target in any optimization procedure. Thus, it seems that the results have a broad range of validity and that the force field parameters used are portable from gas to condensed phase.

The calculation of damping functions implies a negligible computational overhead and it can be easily ported also to other methods to include polarizability. In fact, it suffices to use the appropriate screening functions in the electrostatic interaction tensors (Eqs. 5.1). The application to shell models at gas and condensed phase could be found in Refs. [21, 37, 38].

Finally, a subtle issue arising from the above conclusions needs to be addressed. On the one hand, it has been shown that using gas phase polarizability with the appropriate damping functions allows to reproduce many static and dynamical properties compared to *ab initio* results. On the other hand, the use of gas phase polarizability at condensed phase could seem nonsense; in fact it is usually assumed that, in the bulk, the polarizability is lower than at gas phase. Whether the polarizability is an intrinsic property or not is still to be answered but, merely from the operative point of view, considering it an intrinsic property allows for a better description of structural and dynamical properties.

References

[1] William L. Jorgensen. Special Issue on Polarization. *Journal of Chemical Theory and Computation*, 3(6):1877, 2007.

[2] S. Iuchi, S. Izvekov, and G. A. Voth. Are Many-Body Electronic Polarization Effects Important in Liquid Water? *J. Chem. Phys.*, 126(12):124505, 2007.

[3] Jean Philip Piquemal, Lalith Perera, G. Andrés Cisneros, Pengyu Ren, Lee G. Pedersen, and Thomas A. Darden. Towards Accurate Solvation Dynamics of Divalent Cations in Water Using the Polarizable Amoeba Force Field: From Energetics to Structure. *Journal of Chemical Physics*, 125(5), 2006.

[4] D. Jiao, C. King, A. Grossfield, T. A. Darden, and P. Ren. Simulation of Ca^{2+} and Mg^{2+} Solvation Using Polarizable Atomic Multipole Potential. *J. Phys. Chem. B*, 110(37):18553–18559, 2006.

[5] S. W. Rick and S. J. Stuart. Potentials and Algorithms for Incorporating Polarizability in Computer Simulations. In *Reviews in computational chemistry*, volume 18, chapter 3, page 89. Wiley1999, 2002.

[6] C.J. J. Burnham, J. Li, S.S. S. Xantheas, and Maurice Leslie. The Parametrization of a Thole-Type All-Atom Polarizable Water Model from First Principles and its Application to the Study of Water Clusters (n= 2–21) and the Phonon Spectrum of Ice Ih. *The Journal of chemical physics*, 110(9):4566, 1999.

[7] Anthony J. Stone. Intermolecular Potentials. *Science (New York, N.Y.)*, 321(5890):787–789, 2008.

[8] P. Jungwirth and D. J. Tobias. Specific Ion Effects at the Air/Water Interface. *Chem. Rev.*, 106(4):1259–1281, 2006.

[9] I-Feng W. Kuo and Christopher J Mundy. An ab Initio Molecular Dynamics Study of the Aqueous Liquid-Vapor Interface. *Science*, 303(5658):658–660, jan 2004.

[10] C. D. Wick and S. S. Xantheas. Computational Investigation of the first Solvation Shell Structure of Interfacial and Bulk Aqueous Chloride and Iodide Ions. *J. Phys. Chem. B*, 113(13):4141–4145, 2009.

[11] Collin D. Wick. Electrostatic dampening dampens the anion propensity for the air-water interface. *J. Chem. Phys.*, 131(8):84715, 2009.

[12] Magali Duvail, Pierre Vitorge, and Riccardo Spezia. Building a Polarizable Pair Interaction Potential for Lanthanoids(III) in Liquid Water: A Molecular Dynamics Study of Structure and Dynamics of the Whole Series. *Journal of Chemical Physics*, 130(10), 2009.

[13] S Hull, D A Keen, P A Madden, and M Wilson. Ionic Diffusion Within the α^* and β Phases of Ag_3SI. *Journal of Physics: Condensed Matter*, 19(40):406214, oct 2007.

[14] Vicente Bitrián and Joaquim Trullàs. Molecular Dynamics Study of Polarization Effects on AgI. *The journal of physical chemistry. B*, 112(6):1718–1728, 2008.

[15] C. Krekeler, F. Dommert, J. Schmidt, Y. Y. Zhao, C. Holm, R. Berger, and L. Delle Site. Electrostatic Properties of Liquid 1,3-dimethylimidazolium Chloride: Role of Local Polarization and Effect of the Bulk. *Phys. Chem. Chem. Phys.*, 12(8):1817–1821, 2010.

[16] Edward Harder, Alexander D. MacKerell, and Benoît Roux. Many-body polarization effects and the membrane dipole potential. *Journal of the American Chemical Society*, 131(8):2760–2761, 2009.

[17] M. Masia, M. Probst, and R. Rey. On the Performance of Molecular Polarization Methods. I. Water and Carbon Tetrachloride Close to a Point Charge. *The Journal of Chemical Physics*, 121(15):7362, 2004.

[18] Pedro E. M. Lopes, Benoit Roux, and Alexander D. MacKerell. Molecular Modeling and Dynamics Studies with Explicit Inclusion of Electronic Polarizability: Theory and Applications. *Theoretical Chemistry Accounts*, 124(1-2):11–28, sep 2009.

[19] G. A. Kaminski, H. A. Stern, B. J. Berne, and R. A. Friesner. Development of an Accurate and Robust Polarizable Molecular Mechanics Force Field from ab Initio Quantum Chemistry. *Journal of Physical Chemistry A*, 108(4):621–627, 2004.

[20] T. J. Giese and D. M. York. Improvement of Semiempirical Response Properties with Charge-Dependent Response Density. *Journal of Chemical Physics*, 123(16), 2005.

[21] Marco Masia and Rossend Rey. Diffusion Coefficient of Ionic Solvation Shell Molecules. *Journal of Chemical Physics*, 122(9), 2005.

[22] M. Masia, M. Probst, and R. Rey. Polarization Damping in Halide-Water Dimers. *Chem. Phys. Lett.*, 420(1-3):267–270, 2006.

[23] M. Masia. *Ab initio* Based Polarizable Force Field Parametrization. *Journal of Chemical Physics*, 128(18):184107, 2008.

[24] J. P. Piquemal, R. Chelli, P. Procacci, and N. Gresh. Key Role of the Polarization Anisotropy of Water in Modeling Classical Polarizable Force Fields. *J. Phys. Chem. A*, 111(33):8170–8176, 2007.

[25] Pär Söderhjelm, Anders Öhrn, Ulf Ryde, and Gunnar Karlström. Accuracy of Typical Approximations in Classical Models of Intermolecular Polarization. *Journal of Chemical Physics*, 128(1), 2008.

[26] B.T. T Thole. Molecular Polarizabilities Calculated with a Modified Dipole Interaction, 1981.

[27] M. Souaille, H. Loirat, D. Borgis, and M. P. Gaigeot. MDVRY: a Polarizable Classical Molecular Dynamics Package for Biomolecules. *Comput. Phys. Commun.*, 180(2):276–301, 2009.

[28] Jonàs Sala, Marco Masia, Elvira Guàrdia, and Marco Masia. The polarizable point dipoles method with electrostatic damping: Implementation on a model system. *The Journal of Chemical Physics*, 133(23):234101, 2010.

[29] J. D. Smith, R. J. Saykally, and P. L. Geissler. The Effects of Dissolved Halide Anions on Hydrogen Bonding in Liquid Water. *J. Am. Chem. Soc.*, 129(45):13847–13856, 2007.

[30] H. J. Bakker. Structural Dynamics of Aqueous Salt Solutions, 2008.

[31] B. S. Mallik, A. Semparithi, and A. Chandra. A First Principles Theoretical Study of Vibrational Spectral Diffusion and Hydrogen Bond Ddynamics in Aqueous Ionic Solutions: D_2O in Hydration Shells of Cl^- Ions. *J. Chem. Phys.*, 129(19), 2008.

[32] A. W. Omta, M. F. Kropman, S. Woutersen, and H. J. Bakker. Negligible Effect of Ions on the Hydrogen-Bond Structure in Liquid Water. *Science (New York, N.Y.)*, 301(5631):347–349, 2003.

[33] D. Laage and J. T. Hynes. Reorientional Dynamics of Water Molecules in Anionic Hydration Shells. *Proc. Natl. Acad. Sci.*, 104(27):11167–11172, jul 2007.

[34] M. F. Kropman, H. K. Nienhuys, and H. J. Bakker. Real-Time Measurement of the Orientational Dynamics of Aqueous Solvation Shells in Bulk Liquid Water. *Physical review letters*, 88(7):077601, 2002.

[35] M. F. Kropman and H. J. Bakker. Dynamics of Water Nolecules in Aqueous Solvation Shells. *Science (New York, N.Y.)*, 291(5511):2118–2120, 2001.

[36] A. J. Stone. *The Theory of Intermolecular Forces*, volume 32. 1996.

[37] G. Lamoureux and B. Roux. Absolute Hydration Free Energy Scale for Alkali and Halide Ions Established from Simulations with a Polarizable Force Field. *Journal of Physical Chemistry B*, 110(7):3308–3322, 2006.

[38] E. Harder, V. M. Anisimov, T. W. Whitfield, A. D. MacKerell, and B. Roux. Understanding the Dielectric Properties of Liquid Amides from a Polarizable Force Field. *J. Phys. Chem. B*, 112(11):3509–3521, 2008.

[39] L. X. Dang. The Nonadditive Intermolecular Potential for Water Revised. *J. Chem. Phys.*, 97(4):2659, 1992.

[40] J. Kolafa. Time-Reversible Always Stable Predictor-Corrector Method for Molecular Dynamics of Polarizable Molecules. *J. Comput. Chem.*, 25(3):335–342, 2004.

[41] Francesco Paesani, Satoru Iuchi, and Gregory A. Voth. Quantum Effects in Liquid Water from an ab Initio-Based Polarizable Force Field. *Journal of Chemical Physics*, 127(7), 2007.

[42] F. Paesani, S. Yoo, H. J. Bakker, and S. S. Xantheas. Nuclear Quantum Effects in the Reorientation of Water. *J. Phys. Chem. Lett.*, 1(15):2316–2321, 2010.

[43] Klaus B. Møller, Rossend Rey, Marco Masia, and James T. Hynes. On the Coupling Between Molecular Diffusion and Solvation Shell Exchange. *Journal of Chemical Physics*, 122(11), 2005.

Chapter 6

Ion Water Force Matching

6.1 Introduction

The main objective of this work is to lay insight on how the Force Matching algorithm can be used to obtain interaction potentials using as the point of reference *ab initio* simulations, which are getting more accessible every day, instead of hard to get experimental values.

As it was explained in section 2.3 the force field parameters are fit to minimize a differential functional between the classic and *ab initio* forces. In this work, the minimization process has been carried by a quadratic polynomial interpolation line-search with the line-search vectors found by means of the Broyden-Fletcher-Goldfatb-Shanno (BFGS) formula [1]. The gradient of the objective function has been numerically evaluated using central differences. A critical factor in the computational cost of the matching process is the number of parameters of the classical potential to be fitted. Each new parameter increases greatly both, the length of the fitted process and the number of evaluations needed in order to find the minimization path, taking the process between a few hours and a couple of days of 8 CPUs usage. Figures 6.1 and 6.2 show how the fitted parameters travel across the phase space from the initial guess to the final minimized ones for a two and a three parameter fits respectively. When only the LJ parameters are fitted the surface that holds χ value is quite simple and takes a shape close to an elliptic paraboloid, making the journey from the inital parameters to the optimized ones quite straightforward. When more parameters are introduced the shape of the phase space becomes far from trivial allowing for the parameters to tour it greatly before reaching the minimum. In this work, after a study of convergence, a value of $L = 300$ configurations spanned through the total 30000 has been chosen. The use of a

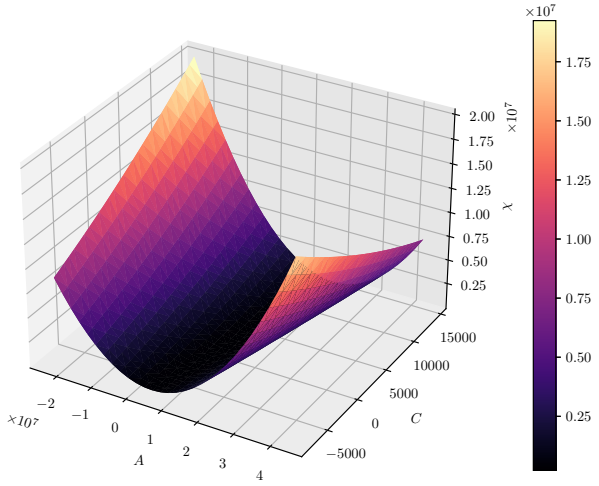

Fig. 6.1 Minimization path of the error function $\chi = \chi(A, C)$ for a two parameter Lennard-Jones potential.

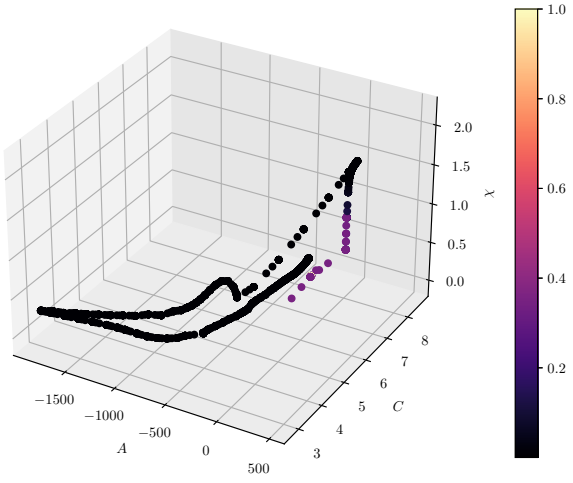

Fig. 6.2 Minimization path of the error function $\chi = \chi(A, C, \alpha)$ for a three parameter model, a Lennard-Jones potential with ion polarizability α.

higher number of configurations doesn't improve the quality of the obtained parameters and notably increases the computational cost of the process.

A huge range of ions, water models, temperatures, charges, polarizations, and damping functions have been tested. This makes it hard, if not impossible, to come up with a comprehensive and clarifying simultaneous comparison between all of them. To simplify this, the results have been gathered among different topics to reduce the dimensionality of the comparison to manageable levels.

A wide variety of different water models have been tested in the Force Matching process such as, the SPC, SPC/E or RPOL models, but for the sake of consistency, a family of Force Matching variations (one for each dispersion damping) of the original SPC model [2] has predominantly been used. In this work, these models will be called SPC-FM. Also three different damping functions applied to the dispersion term of the Lennard-Jones potential between the ions and the water molecules have been combined with each one of these water models. These damping functions are the unit function, which means that no effective damping is applied, the Tang-Toennies damping and a Fermi like damping function. Each one of these combinations has also been tested with and without a Polarizable Point Dipole Model that has added polarization to the ion. Although it would be possible to use all the SPC-FM water models in conjunction with any damping function they have been kept paired within the same damping function.

6.2 Force matching with the SPC/E water model

The first model tested for the Force Matching algorithm has been the renowned SPC/E. Table 6.1 contains the obtained fitted parameters and the quality metrics obtained for the SPC/E water model at a temperature of $T = 300\,\mathrm{K}$ when used with the three damping solutions previously explained. It has to be kept in mind that the temperature used does not match that of the reference simulations. This temperature was used to match that of the original parametrization of the SPC/E model and it will lead to a slightly unfair comparative.

We can see how the SPC/E model performs fairly well for all ions without the use of a dampening function. In fact, when a dampening function is used it results in consistently worse results.

When going over the fitted Lennard-Jones parameters obtained it can be seen that they range widely. It draws special attention the recurrent appearance of negative values for the C parameter. This behavior is due to the fact that this parameter accounts for all the interactions that form the dispersion forces but also some of the corrections needed

Ion	A [kcalÅ^{12}/mol]	C [kcalÅ^{6}/mol]	$RMSD_{\mathrm{F}}$	$RMSD_{\mathrm{O}}$	$RMSD_{\mathrm{H}}$	b_{scatt}
F^-	251201.61	−2126.4	20.97	0.29	0.55	1.19
Cl^-	2281999.96	−2188.78	15.75	0.04	0.04	1.18
Br^-	4312367.7	−1294.14	17.3	0.08	0.06	1.22
I^-	9947477.19	939.8	15.58	0.11	0.11	1.15
Li^+	1128.87	−459.62	15.23	0.26	0.27	1.04
Na^+	34287.93	−897.11	9.6	0.09	0.08	1.04
K^+	188209.05	−1476.81	9.13	0.14	0.14	1.02
Mg^{2+}	2289.12	−1249.7	45.23	0.31	0.46	0.79
Ca^{2+}	41179.2	−2154.41	21.67	0.29	0.37	0.99

Table 6.1 For each ion: the value of the fitted LJ fitted parameters and the quality metrics $RMSD_{\mathrm{F}}$, $RMSD_{\mathrm{O}}$, $RMSD_{\mathrm{H}}$ and b_{scatt} for simulations with the SPC/E water model at $T = 300\,\mathrm{K}$.

to accommodate a too simplistic reality to a way more complex reality. For example, if the electrostatic attraction between the ion and the water molecule is overestimated in comparison to that of the CPMD one, the Force Matching algorithm will have to overrely on this component in order to compensate, turning its contribution into a repulsive one. Although some techniques have been tried, this negative values have been proven extremely resilient and hard to eliminate.

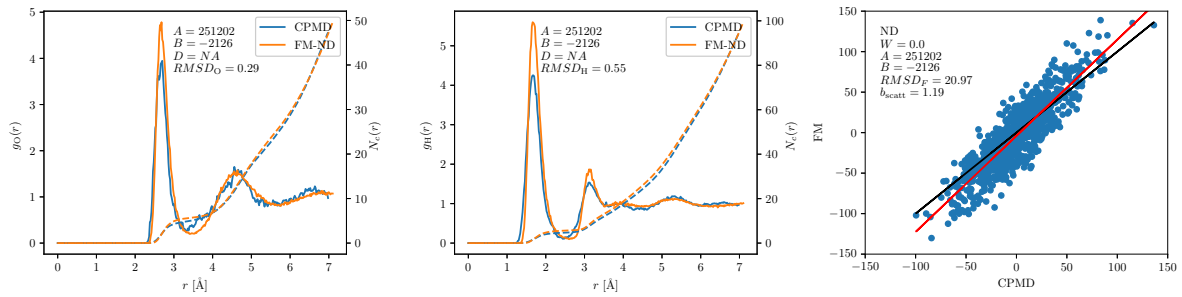

Fig. 6.3 For the fluoride ion: comparison between the ion-oxygen (left) and ion-hydrogen (center) RDFs and the forces (right) for the SPC/E water model at temperature $T = 300\,\mathrm{K}$ against the CPMD reference.

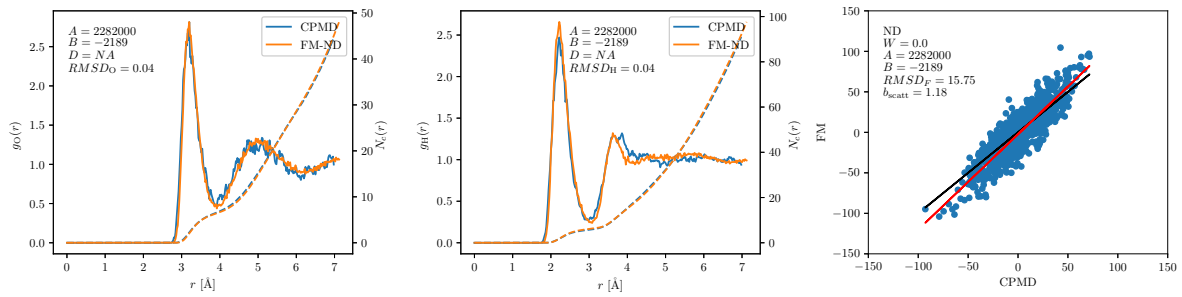

Fig. 6.4 For the chloride ion: comparison between the ion-oxygen (left) and ion-hydrogen (center) RDFs and the forces (right) for the SPC/E water model at temperature $T = 300\,\mathrm{K}$ against the CPMD reference.

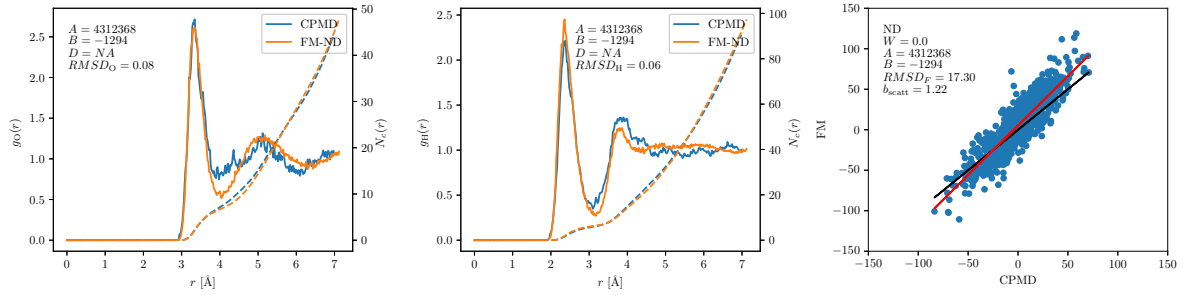

Fig. 6.5 For the bromide ion: comparison between the ion-oxygen (left) and ion-hydrogen (center) RDFs and the forces (right) for the SPC/E water model at temperature $T = 300\,\mathrm{K}$ against the CPMD reference.

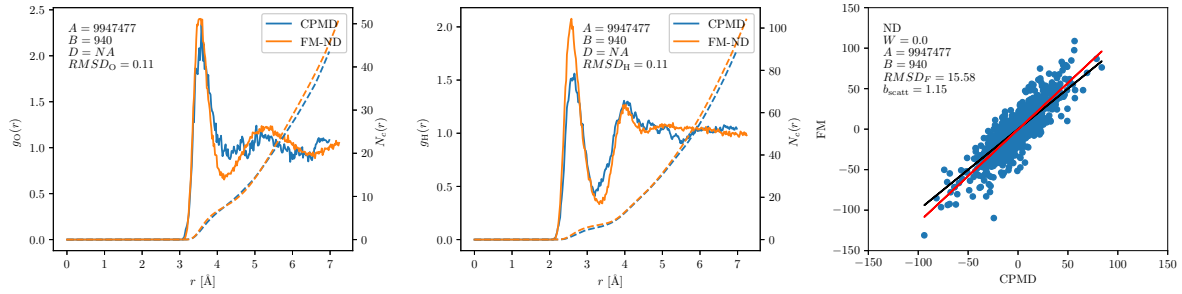

Fig. 6.6 For the iodide ion: comparison between the ion-oxygen (left) and ion-hydrogen (center) RDFs and the forces (right) for the SPC/E water model at temperature $T = 300\,\mathrm{K}$ against the CPMD reference.

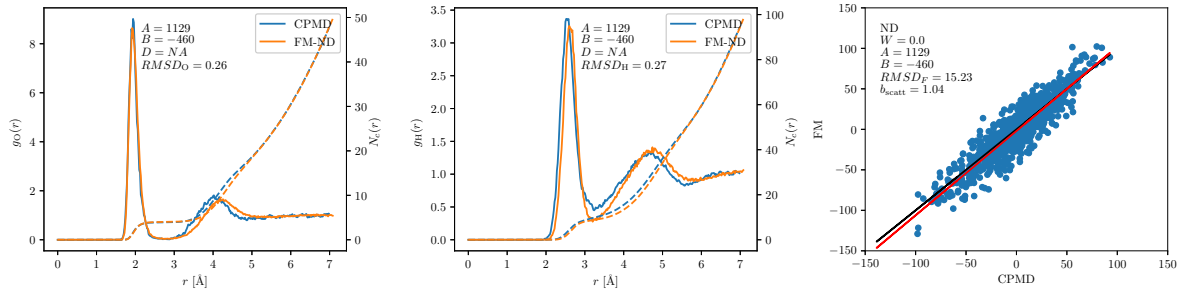

Fig. 6.7 For the lithium ion: comparison between the ion-oxygen (left) and ion-hydrogen (center) RDFs and the forces (right) for the SPC/E water model at temperature $T = 300\,\mathrm{K}$ against the CPMD reference.

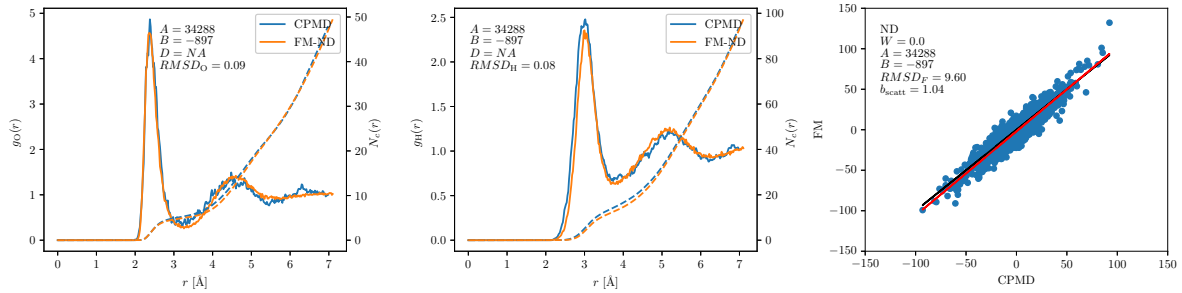

Fig. 6.8 For the sodium ion: comparison between the ion-oxygen (left) and ion-hydrogen (center) RDFs and the forces (right) for the SPC/E water model at temperature $T = 300\,\mathrm{K}$ against the CPMD reference.

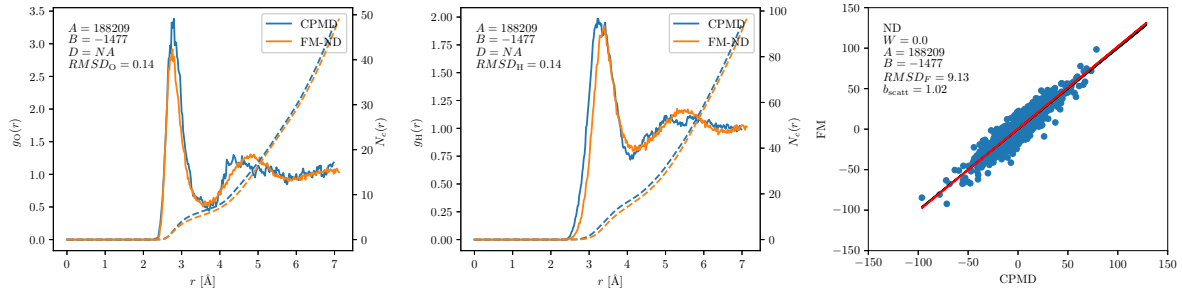

Fig. 6.9 For the potassium ion: comparison between the ion-oxygen (left) and ion-hydrogen (center) RDFs and the forces (right) for the SPC/E water model at temperature $T = 300\,\mathrm{K}$ against the CPMD reference.

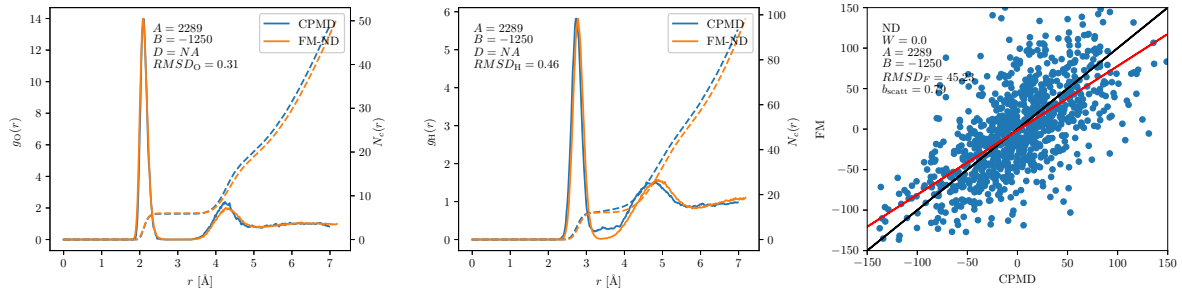

Fig. 6.10 For the magnesium ion: comparison between the ion-oxygen (left) and ion-hydrogen (center) RDFs and the forces (right) for the SPC/E water model at temperature $T = 300\,\mathrm{K}$ against the CPMD reference.

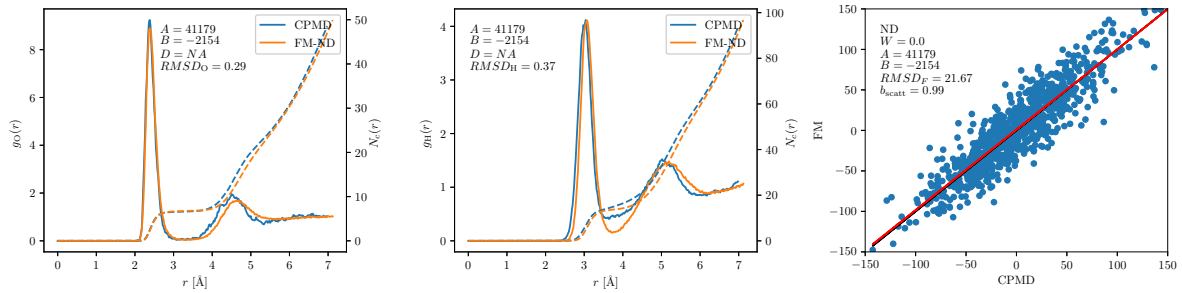

Fig. 6.11 For the calcium ion: comparison between the ion-oxygen (left) and ion-hydrogen (center) RDFs and the forces (right) for the SPC/E water model at temperature $T = 300\,\mathrm{K}$ against the CPMD reference.

Ion	A [kcalÅ^{12}/mol]	C [kcalÅ^{6}/mol]	α [Å]	$RMSD_{\mathrm{F}}$	$RMSD_{\mathrm{O}}$	$RMSD_{\mathrm{H}}$	b_{scatt}
Cl^-	2403610.73	−1123.28	1.0	12.67	0.23	0.33	1.11
Br^-	4190748.28	−632.99	1.0	14.01	0.25	0.26	1.13

Table 6.2 For the chloride and bromide ions: the value of the fitted LJ fitted parameters and the quality metrics $RMSD_{\mathrm{F}}$, $RMSD_{\mathrm{O}}$, $RMSD_{\mathrm{H}}$ and b_{scatt} for simulations with the RPOL water model at $T = 300\,\mathrm{K}$.

6.3 Force matching with the RPOL water model

As it has just been explained, one of the reasons why negative values of the C parameter are obtained is due to simplifications, for example those related to the polarizability of the atoms. In an attempt to reduce these effects, the RPOL water model was tested under the same conditions that the SPC/E model and adding a polarizable site to the ion with a fitted polarizability.

The introduction of the polarization certainly allows a better description of the forces involved. It can be seen how the b_{scatt} values in table 6.2 are closer to the unit and lower values of the $RMSD_{\mathrm{F}}$ quality parameter, which represents a perfect match between classical and *ab initio* forces, than those in the SPC/E table 6.1. Moreover, in some instances the introduction of the polarization allows to reduce the negativity of the C values but it does not manage to fully dispose of them. However, it introduces instabilities in the Force Matching process that lead to extreme fitted polarizability values next to either $\alpha = 0$ or $\alpha = 1$ and even to prevent the convergence of the fit. This limitation next to the huge increase in fitting time that supposes the addition of a new fitting parameter calls for alternative methods to tackle this problem.

6.4 Force matching with the SPC-FM water models

As explained in Chapter 3, water models that were developed in our group by means of the FM algorithm have also been used. These family of models, referenced in this work as SPC-FM, were derived using pure water at a temperature of $T = 330\,\mathrm{K}$, i.e. the same as in the CPMD reference simulations. For this reason, the quality of the ion-water FM potentials has been assessed with classical MD simulations at same temperature of $T = 330\,\mathrm{K}$. For the sake of completeness, as the SPC/E and RPOL models where

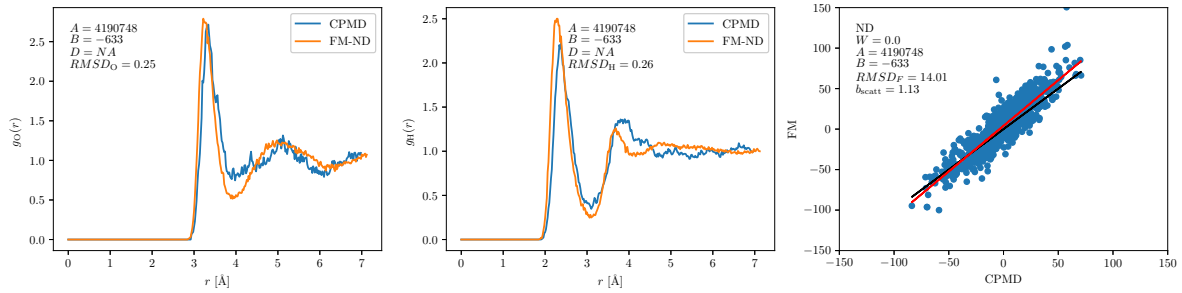

Fig. 6.12 Comparison between the ion-oxygen (left) and ion-hydrogen (center) radial distribution functions and the forces (right) with the RPOL water model at temperature $T = 300\,\mathrm{K}$ against the CPMD reference for the bromide ion.

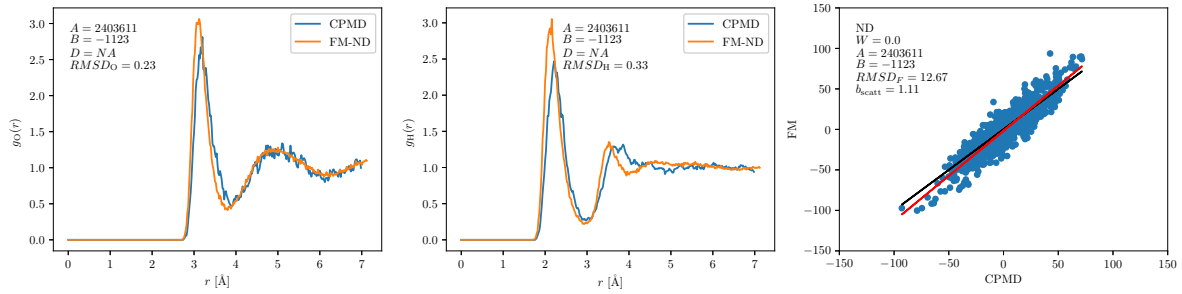

Fig. 6.13 Comparison between the ion-oxygen (left) and ion-hydrogen (center) radial distribution functions and the forces (right) with the RPOL water model at temperature $T = 300\,\mathrm{K}$ against the CPMD reference for the chloride ion.

tested at a temperature of $T = 300\,\mathrm{K}$, we repeated the procedure for the SPC-FM water models a $T = 300\,\mathrm{K}$. These results can be found in Appendix A.

6.4.1 Influence of the force weight

It has been stated in section 6.2 that one contribution to the negativity of the C values comes from the over-estimation of the electrostatic forces. It seems then reasonable to try to avoid this limiting the contribution of these forces, more precisely those of higher intensity. This can be achieved by including a weight factor to each force contribution during the Force Matching process as it is explained in section 2.3.

Table 6.3 gathers the comparative results of simulations with the SPC-FM model at a temperature of $T = 330\,\mathrm{K}$ without damping for weights values of $W = 0$ and $W = 1$. Although higher values of the weight W have been tested they do not outperform those shown here. As obvious result of this weight, the indicators of forces similarity worsen. Like with the RPOL water model the values of C tend to get less negative, although with exceptions. On the one hand, for the bromide and iodine ions the resulting potentials obtain better results with the weighted forces than with the unweighted ones. On the other hand, for the rest of the ions the values get worse as the weight increases. This inconsistent behavior is maintained when different damping functions are used.

6.4.2 Influence of the charge scaling

Ions are, like water, mostly modeled through a LJ potential and a point charge both located at the same site. Usually, the value of the point charge is set to that of the individual ion in gas-like state. The parameters of the LJ potentials are then established so it reproduces certain thermodynamic properties when it is used jointly with a given water model like the ones described before.

Like with the water model this description provides a great combination of simplicity and accuracy but it still has deficiencies. One of these deficiencies arises from the neglect of the ion polarizability.

While this polarizability can be introduced into the model by different means such as point dipoles, variable charges or Drude oscilators, these explicit methods increase the computational cost of the simulations. Recent works from Leontyev and Stuchebrukhov [3–8] indicate that a more realistic description can also be achieved by adding a phenomenological electric continuum effect to the ion interaction model.

Leontyev and Stuchebrukhov argue that the lack of polarization and the consequential incomplete electronic contribution to the dielectric constant can explain, in some

Ion	Weigth	A [kcalÅ^{12}/mol]	C [kcalÅ^{6}/mol]	$RMSD_{\mathrm{F}}$	$RMSD_{\mathrm{O}}$	$RMSD_{\mathrm{H}}$	b_{scatt}
F^-	0.0	193 215.98	−2851.51	20.57	0.27	0.46	1.16
	1.0	244 452.35	−2676.86	21.01	0.44	0.71	1.26
Cl^-	0.0	2 208 317.68	−2437.44	16.04	0.24	0.34	1.18
	1.0	3 101 860.56	−931.61	17.38	0.30	0.36	1.38
Br^-	0.0	5 185 935.65	923.90	20.30	0.73	0.77	1.32
	1.0	5 756 408.64	−854.07	23.27	0.14	0.14	1.63
I^-	0.0	11 352 578.28	3203.42	16.67	0.70	0.66	1.18
	1.0	13 604 996.19	2789.58	19.05	0.32	0.30	1.49
Li^+	0.0	1965.53	−430.64	17.99	0.49	0.43	1.06
	1.0	6346.27	−240.49	21.57	0.79	0.41	1.36
Na^+	0.0	38 553.42	−867.62	9.99	0.11	0.06	1.06
	1.0	54 059.44	−749.79	10.96	0.11	0.08	1.19
K^+	0.0	178 595.53	−1759.62	8.18	0.07	0.08	1.06
	1.0	233 600.46	−1578.10	8.58	0.06	0.09	1.15
Mg^{2+}	0.0	19 588.38	−820.91	35.51	0.94	1.62	1.10
	1.0	48 372.35	185.60	39.12	9.11	0.80	1.33
Ca^{2+}	0.0	47 683.14	−2158.37	20.81	0.48	0.43	1.04
	1.0	13 559.38	−2632.13	21.73	0.28	0.52	0.93

Table 6.3 For each ion and force weights $W = 0$ and $W = 1$: the value of the fitted LJ fitted parameters and the quality metrics $RMSD_{\mathrm{F}}$, $RMSD_{\mathrm{O}}$, $RMSD_{\mathrm{H}}$ and b_{scatt} for simulations with the SPC-FM water models without damping at $T = 330\,\mathrm{K}$.

T [K]	Damping	T_{sim} [K]	ϵ_{sim}	ϵ_0	$\epsilon_{\text{el}}^{-1/2}$
300	ND	292.56	113.09	80.30	1.19
300	FE	295.04	109.33	79.40	1.17
300	TT	291.40	103.64	80.73	1.13
330	ND	341.98	89.72	64.15	1.18
330	FE	343.37	90.26	63.74	1.19
330	TT	323.80	92.19	69.67	1.15

Table 6.4 Simulated ϵ_{sim} and experimental ϵ_0 dielectric constants and resulting scaling factors $\epsilon_{\text{el}}^{-1/2}$ for the SPC-FM water models at different temperatures.

measure, why non-polarizable water model simulations yield lower values for the dielectric like SPC/E, $\epsilon_0 = 71$, and TIP4P, $\epsilon_0 = 52$ compared to that of the experimental one, $\epsilon_0 = 78.4$.

This electronic continuum contribution can be included simply by scaling the charges of the ions according to

$$q_{eff} = q/\sqrt{\epsilon_{el}} \tag{6.1}$$

in which ϵ_{el} is the electronic part of the relative permittivity and is generally related to the experimental high-frequency dielectric constant. This method, called Molecular Dynamics in the Electronic Continuum (MDEC), has already been successfully used for different electrolyte solutions [9–13].

Kann and Skinner [11] proposed to apply this method to different water models by using $\epsilon_{el} = \epsilon_0/\epsilon_{\text{sim}}$, where ϵ_0 is the experimental value and ϵ_{sim} the one for the water model, to determine the scaling factor. They argued that as the electrostatic energy between two charges q separated by distance r inside a medium of dielectric constant ϵ_0 is $q^2/\epsilon_0 r$ while for a model without explicit polarization contribution it would be $q_{eff}^2/\epsilon_{\text{sim}} r$. This, jointly with equation 6.1, leads to $\epsilon_{sim}\epsilon_{el} = \epsilon_0$; thus, making $\epsilon_{el} = \epsilon_0/\epsilon_{\text{sim}}$.

To set the value of the charge scaling for the SPC-FM water models, a series of classical MD simulations of pure water were performed in order to compute the simulation dielectric constant ϵ_{sim} for each case. Experimental values obtained from reference [14] and interpolated according to the polynomial approximation in expression 5 of the same work where used to evaluate the reference dielectric constant of water ϵ_0. Table 6.4 contains the results for each environment where the ϵ_{sim} where taken averaging the dielectric constant along the corresponding simulation (figures 6.14 and 6.15). For the sake of simplicity, a unique compromised scale has been chosen for each damping as $\epsilon_{\text{el,ND}}^{-1/2} = 1.19$, $\epsilon_{\text{el,TT}}^{-1/2} = 1.15$ and $\epsilon_{\text{el,FE}}^{-1/2} = 1.19$.

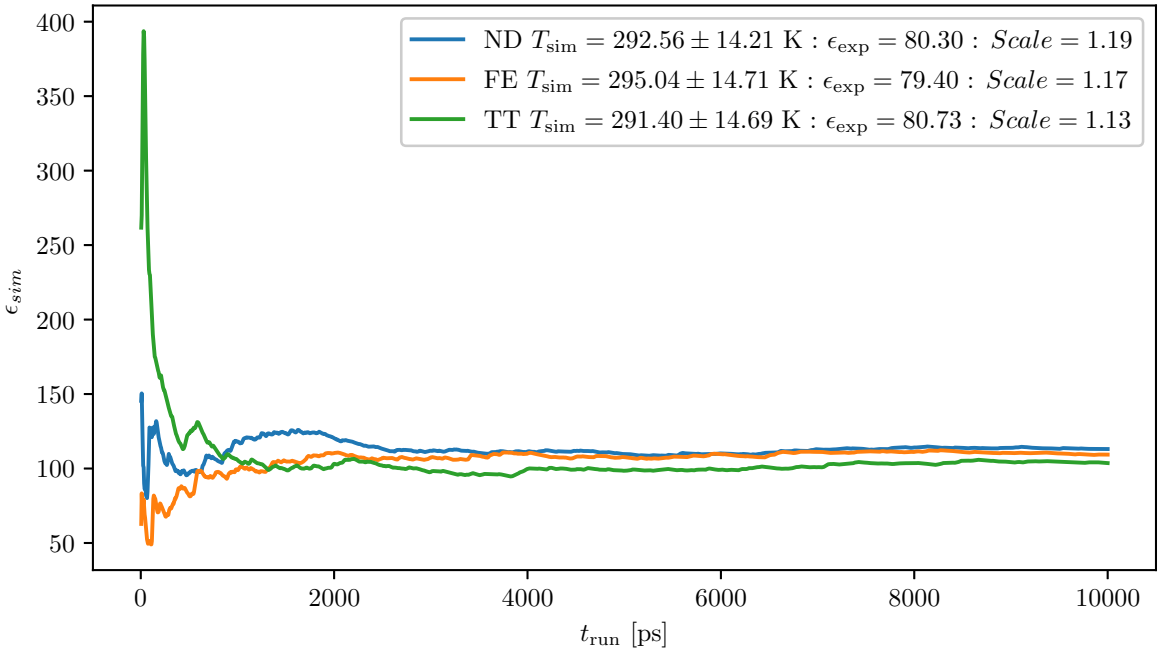

Fig. 6.14 Convergence of the simulated dielectric constant for the SPC-FM models at temperature $T = 300\,\mathrm{K}$.

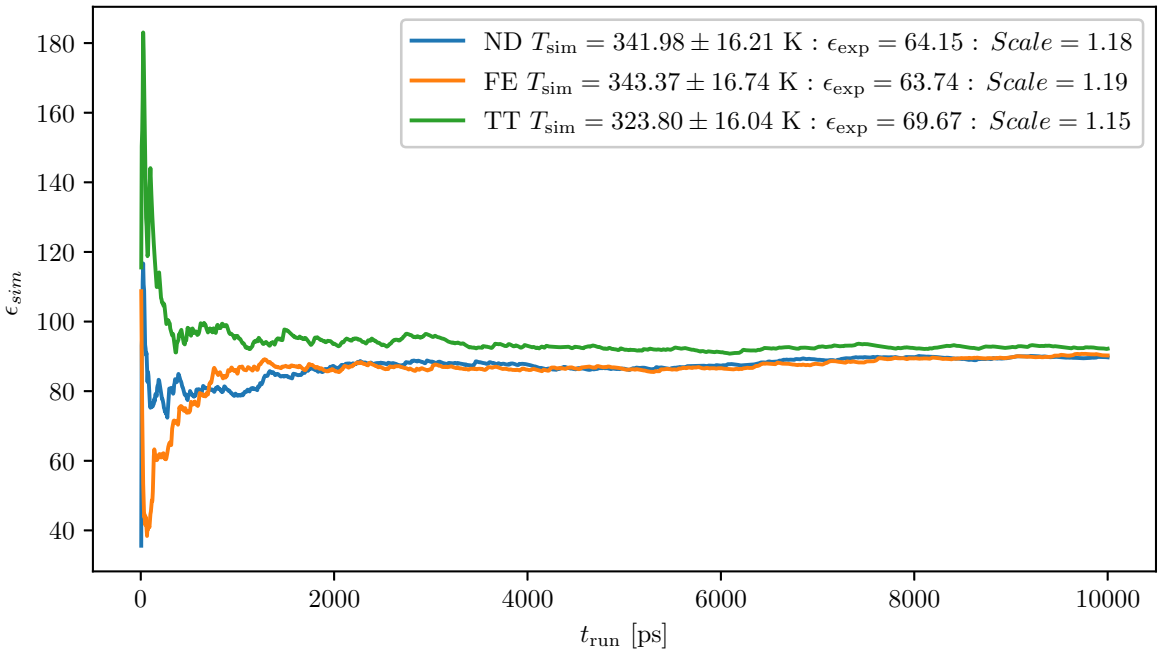

Fig. 6.15 Convergence of the simulated dielectric constant for the SPC-FM models at temperature $T = 330\,\mathrm{K}$.

Ion	Damping	$\epsilon_{\text{el}}^{-1/2}$	A [kcalÅ^{12}/mol]	C [kcalÅ^{6}/mol]	d [Å^{-1}]	R_{FE} [Å]	$RMSD_{\text{F}}$	$RMSD_{\text{O}}$	$RMSD_{\text{H}}$	b_{scatt}
F^-	ND	1.0	193 215.98	−2851.51	-	-	20.57	0.27	0.46	1.16
	TT	1.0	491 199.16	562.19	0.16	-	24.46	1.98	3.42	1.32
	FE	1.0	490 048.93	1168.04	9.49	1.65	24.34	1.36	2.24	1.31
Cl^-	ND	1.0	2 208 317.68	−2437.44	-	-	16.04	0.24	0.34	1.18
	TT	1.0	2 208 711.53	−2417.27	15.07	-	15.96	0.06	0.05	1.18
	FE	1.0	2 972 815.78	620.75	32.45	2.05	16.57	0.27	0.28	1.23
Br^-	ND	1.0	5 185 935.65	923.90	-	-	20.30	0.73	0.77	1.32
	TT	1.0	5 177 860.47	927.67	11.33	-	20.20	0.34	0.31	1.32
	FE	1.0	5 276 826.79	19 853.55	5.11	2.10	19.90	1.03	0.87	1.32
I^-	ND	1.0	11 352 578.28	3203.42	-	-	16.67	0.70	0.66	1.18
	TT	1.0	11 338 691.60	3204.27	11.80	-	16.59	0.30	0.28	1.18
	FE	1.0	9 170 486.13	−49 911.40	11.86	2.22	15.84	0.17	0.18	1.14
Li^+	ND	1.0	1965.53	−430.64	-	-	17.99	0.49	0.43	1.06
	TT	1.0	2170.95	−424.99	8.38	-	17.91	0.14	0.32	1.06
	FE	1.0	8256.31	−4690.75	49.68	2.63	21.81	4.29	0.22	1.21
Na^+	ND	1.0	38 553.42	−867.62	-	-	9.99	0.11	0.06	1.06
	TT	1.0	83 492.88	4 103 318.16	0.38	-	12.39	1.59	0.10	1.14
	FE	1.0	83 679.44	12 360.18	20.45	2.77	12.27	1.30	0.13	1.14
K^+	ND	1.0	178 595.53	−1759.62	-	-	8.18	0.07	0.08	1.06
	TT	1.0	409 693.23	11 011 932.56	0.32	-	10.03	0.20	0.02	1.14
	FE	1.0	170 232.04	−2239.50	−2.22	3.02	8.07	0.61	0.16	1.06
Mg^{2+}	ND	1.0	19 588.38	−820.91	-	-	35.51	0.94	1.62	1.10
	TT	1.0	37 841.27	383 612.97	0.87	-	35.85	48.89	1.32	1.16
	FE	1.0	38 052.10	27 161.64	31.14	2.42	35.59	25.17	0.34	1.14
Ca^{2+}	ND	1.0	47 683.14	−2158.37	-	-	20.81	0.48	0.43	1.04
	TT	1.0	155 479.55	11 372 950.41	0.40	-	26.43	17.59	0.82	1.16
	FE	1.0	155 972.42	12 010.55	34.02	2.78	26.35	14.39	0.62	1.15

Table 6.5 For each ion and damping dispersion: the charge scaling factor $\epsilon_{\text{el}}^{-1/2} = 1$ (without scaling), the resulting fitted LJ parameters and damping parameters (when they apply) and the quality metrics $RMSD_{\text{F}}$, $RMSD_{\text{O}}$, $RMSD_{\text{H}}$ and b_{scatt} for simulations with the SPC-FM water models at $T = 330\,\text{K}$.

Tables 6.5 and 6.6 show the fitted parameters and quality results for each combination of ion and damping simulation with SPC-FM water model, at temperature $T = 330\,\text{K}$ without and with scaled ion charges respectively. It can be seen how the charge scaling is way more stable and less expensive process than the introduction of the polarization which accomplishes in some instances to reduce the negative values, but at a cost of increasing considerably the discrepancies between the reference CPMD and the classical simulations for both the forces and radial distribution functions. Figures for the charge scaled fitted potentials at a temperature $T = 330\,\text{K}$ can be found in Appendix B.

Ion	Damping	$\epsilon_{\text{el}}^{-1/2}$	A [kcalÅ^{12}/mol]	C [kcalÅ^{6}/mol]	d [Å^{-1}]	R_{FE} [Å]	$RMSD_{\text{F}}$	$RMSD_{\text{O}}$	$RMSD_{\text{H}}$	b_{scatt}
F^-	ND	1.18	158 877.31	−3768.46	-	-	25.71	0.47	0.77	1.27
	TT	1.15	542 571.38	641.12	0.17	-	29.99	3.68	6.58	1.45
	FE	1.18	551 444.41	3359.55	9.57	1.65	30.97	3.05	5.55	1.47
Cl^-	ND	1.18	2 187 424.25	−3507.19	-	-	20.34	0.44	0.67	1.29
	TT	1.15	2 224 332.40	−3286.92	4.94	-	19.51	0.10	0.11	1.27
	FE	1.18	3 290 682.91	−486.39	402.74	2.05	21.23	0.85	0.98	1.36
Br^-	ND	1.18	5 614 107.76	723.61	-	-	25.87	1.25	1.40	1.47
	TT	1.15	5 533 450.15	761.31	11.43	-	24.80	0.58	0.63	1.44
	FE	1.18	5 828 958.01	21 983.20	5.11	2.10	25.41	1.24	1.32	1.47
I^-	ND	1.18	12 089 393.17	3158.54	-	-	20.85	1.35	1.34	1.28
	TT	1.15	11 950 616.83	3167.00	12.00	-	20.05	0.63	0.63	1.26
	FE	1.18	9 878 133.74	−59 845.46	12.23	2.22	19.70	0.52	0.54	1.23
Li^+	ND	1.18	672.56	−580.11	-	-	22.12	0.43	0.53	1.14
	TT	1.15	1153.48	−548.14	8.37	-	21.30	0.57	0.52	1.13
	FE	1.18	9152.50	−5796.91	50.46	2.63	27.70	13.94	0.66	1.34
Na^+	ND	1.18	30 732.29	−1177.12	-	-	12.78	0.35	0.15	1.14
	TT	1.15	90 627.28	218 149.10	0.62	-	15.54	3.65	0.28	1.24
	FE	1.18	92 006.86	16 536.55	19.35	2.77	16.06	3.63	0.26	1.25
K^+	ND	1.18	144 064.92	−2357.28	-	-	10.55	0.18	0.15	1.17
	TT	1.15	447 561.49	202 088.14	0.53	-	12.60	0.74	0.06	1.24
	FE	1.18	132 860.58	−2998.19	−2.23	3.02	10.40	0.35	0.21	1.16
Mg^{2+}	ND	1.18	14 365.54	−1204.82	-	-	43.49	1.46	1.50	1.18
	TT	1.15	40 698.73	555 117.34	0.83	-	43.24	78.18	2.92	1.25
	FE	1.18	41 546.14	35 229.68	29.95	2.42	44.22	62.94	1.17	1.25
Ca^{2+}	ND	1.18	28 417.41	−2873.55	-	-	25.70	0.86	1.12	1.12
	TT	1.15	169 522.66	232 757.30	0.57	-	32.60	16.60	0.98	1.25
	FE	1.18	172 669.82	16 850.58	28.03	2.78	33.57	24.92	1.23	1.27

Table 6.6 For each ion and damping dispersion: the charge scaling factor, the resulting fitted LJ parameters and damping parameters (when they apply) and the quality metrics $RMSD_{\text{F}}$, $RMSD_{\text{O}}$, $RMSD_{\text{H}}$ and b_{scatt} for simulations with the SPC-FM water models at $T = 330\,\text{K}$.

6.4.3 Influence of the dispersion damping

Finally, the performance of the two different dampening functions can be compared against the undamped results. The Tang-Toennies and Fermi functions have been used as explained in section 3.3.1. When using the Fermi damping the value of the r_0 parameter in equation 3.9 has been set to the sum of the equilibrium van Deer Waals radii of the involved atoms [15] obtained from Table 9. of reference [16].

Figures from 6.16 through 6.24 contain a comparison of each damping solution for each ion. For the sake of consistency, as both, the original SCP-FM potentials and the reference CPMD simulations, where realized at a temperature of 330K, the same temperature was used for the test simulations. Comparing with the previous table 6.5 it can be seen how the performance of the damping functions is not consistent across ions. For example, for the fluoride, sodium, potassium, magnesium and calcium ions, the undamped results are better than any of the obtained with both damping functions. This is especially notable for the divalent cations where the usage of the damping functions lead to huge differences in the ion-oxygen radial functions while obtaining reasonable results for the ion-hydrogen one. Figures 6.23 and 6.24 evince how these huge differences come from the combined effect of a slight deviation in the position of the first peak and a large overestimation of its height. When using squared differences between functions with large slopes, small shifts in the position generate massive aggregated differences.

On the other hand, for the chloride, bromide and lithium ions the Tang-Toennies damping performs significantly better than the absence of damping. It can be seen in figure 6.17 how the radial distribution functions of the classical and the *ab initio* simulations fit almost perfectly for both the first and second peaks, especially in the case of the ion-oxygen, while the undamped results overestimate significantly the height of both first peaks.

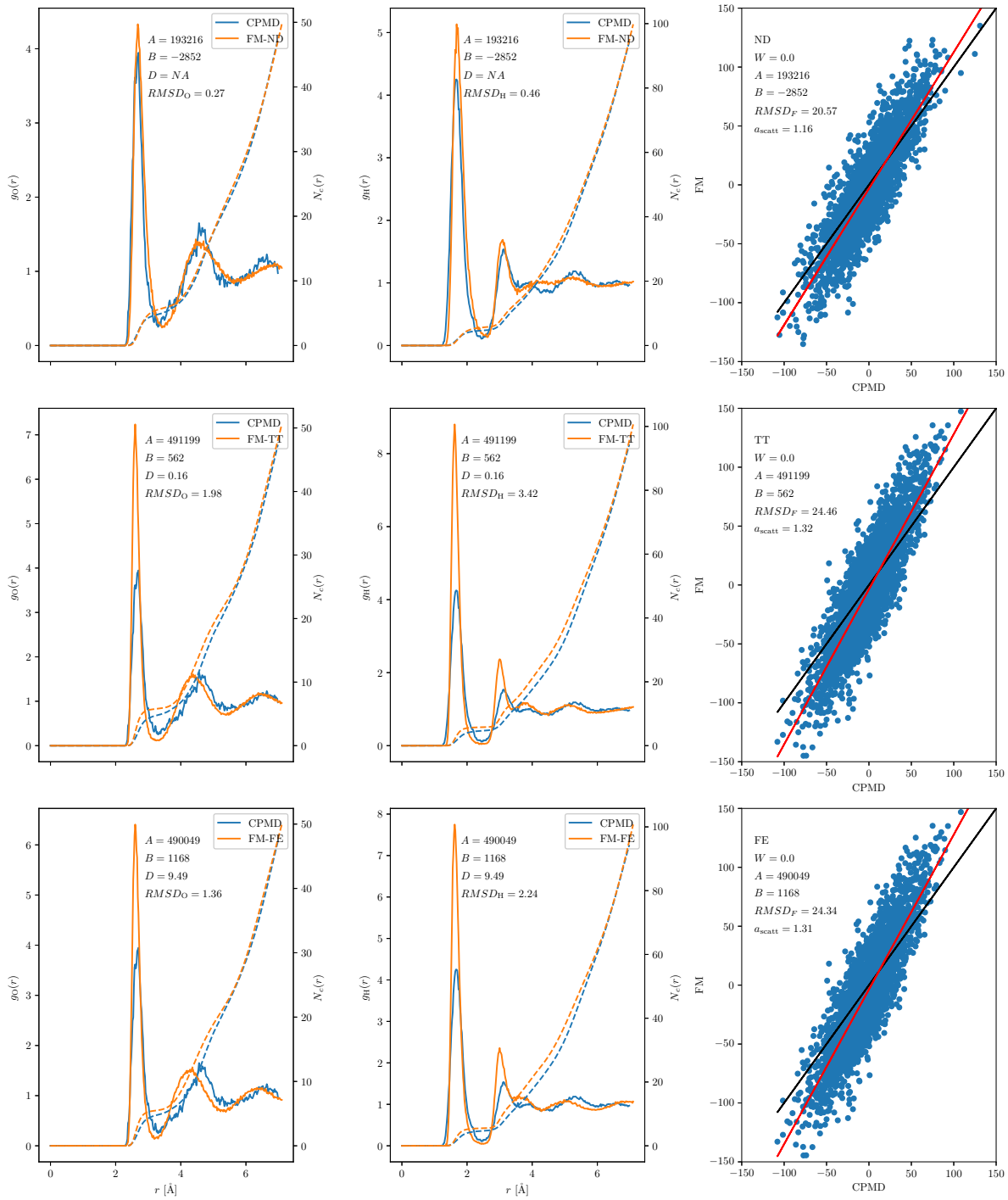

Fig. 6.16 Comparison between the ion-oxygen (left) and ion-hydrogen (center) radial distribution functions and the forces (right) for the undamped (top), Tang-Toennies (middle) and Fermi (bottom) dampings of the SPC-FM water model at temperature $T = 330\,\mathrm{K}$ with unscaled charges and weight $W = 0$ against the CPMD reference for the fluoride ion.

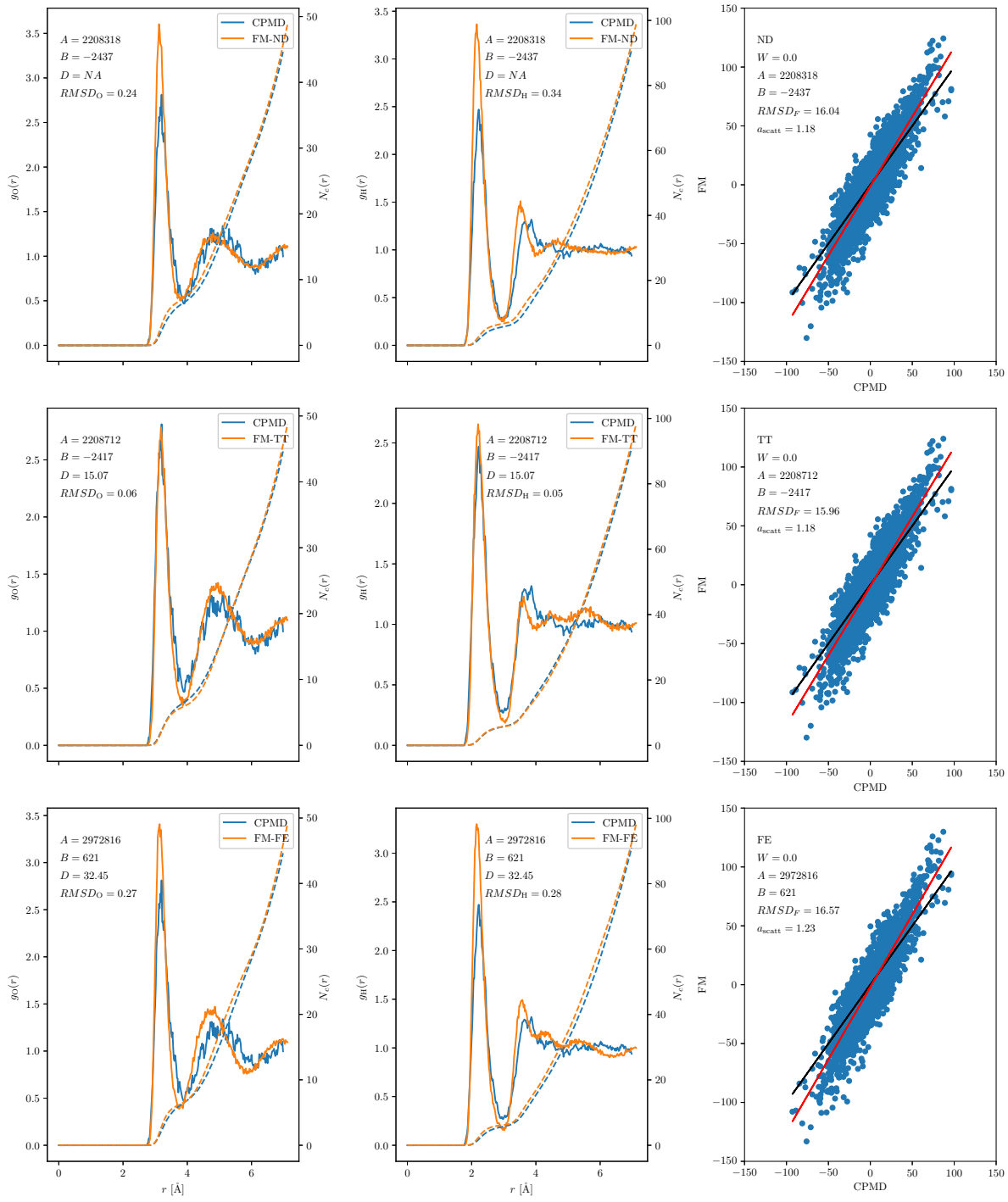

Fig. 6.17 Comparison between the ion-oxygen (left) and ion-hydrogen (center) radial distribution functions and the forces (right) for the undamped (top), Tang-Toennies (middle) and Fermi (bottom) dampings of the SPC-FM water model at temperature $T = 330\,\mathrm{K}$ with unscaled charges and weight $W = 0$ against the CPMD reference for the chloride ion.

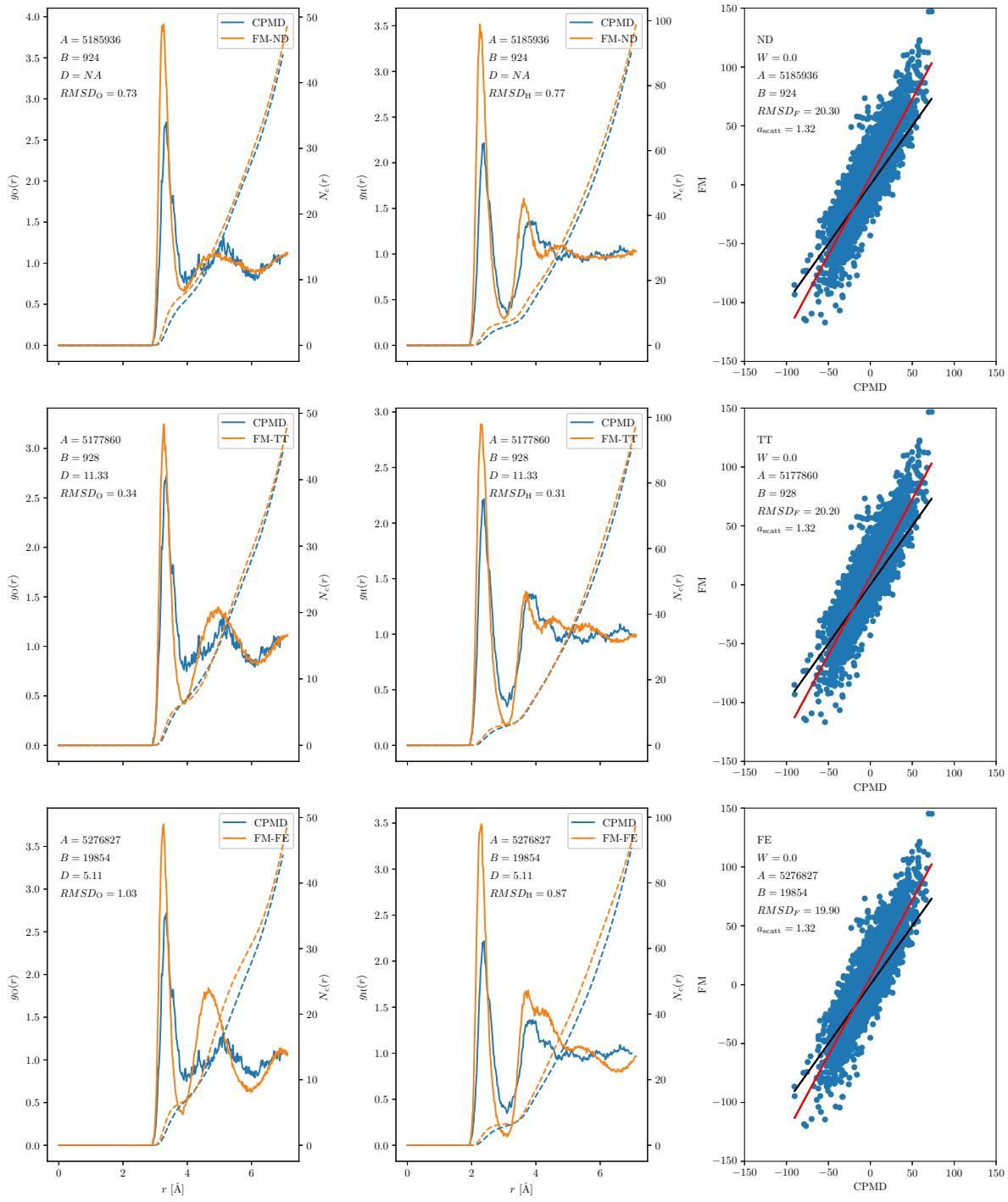

Fig. 6.18 Comparison between the ion-oxygen (left) and ion-hydrogen (center) radial distribution functions and the forces (right) for the undamped (top), Tang-Toennies (middle) and Fermi (bottom) dampings of the SPC-FM water model at temperature $T = 330\,\mathrm{K}$ with unscaled charges and weight $W = 0$ against the CPMD reference for the bromide ion.

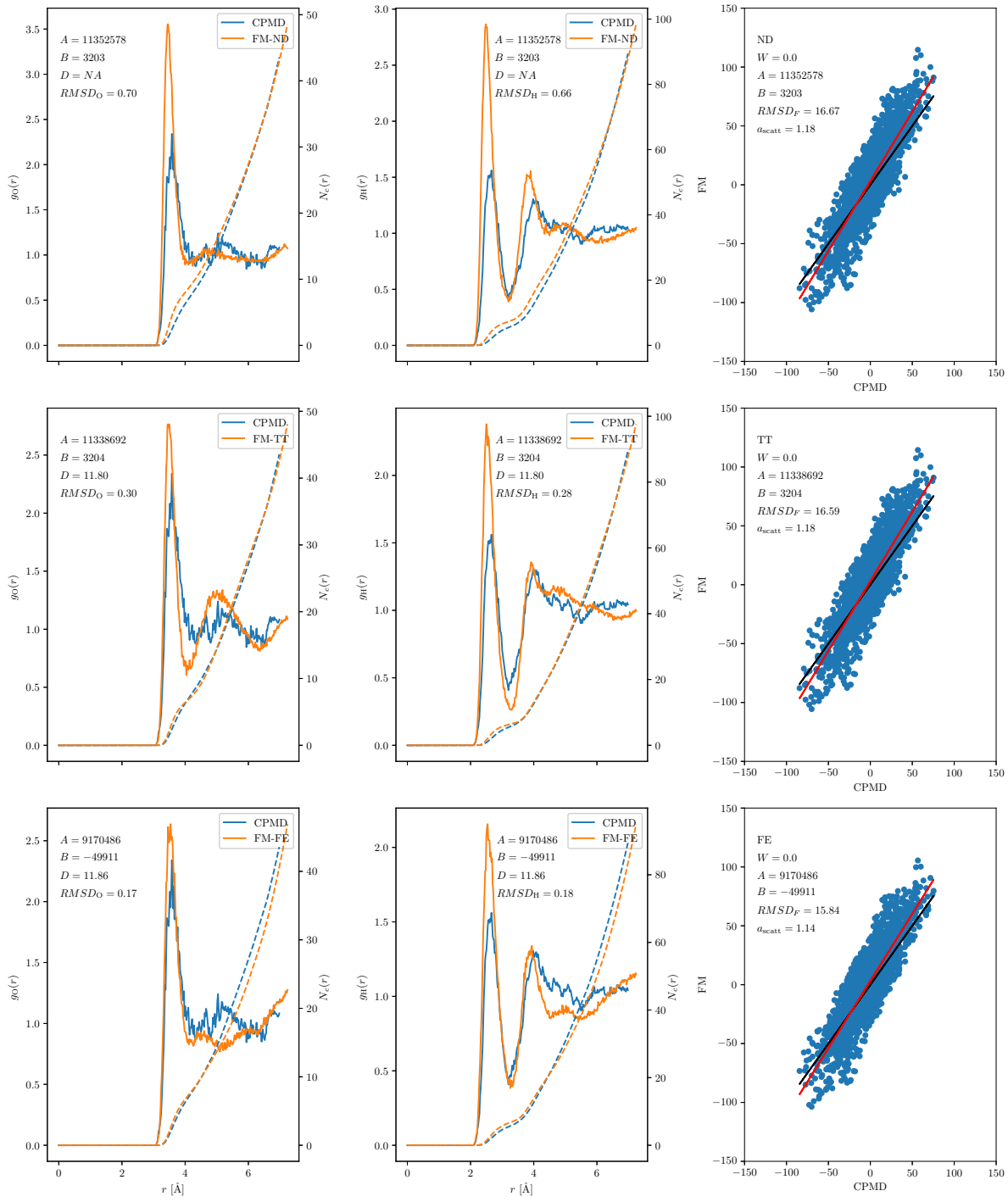

Fig. 6.19 Comparison between the ion-oxygen (left) and ion-hydrogen (center) radial distribution functions and the forces (right) for the undamped (top), Tang-Toennies (middle) and Fermi (bottom) dampings of the SPC-FM water model at temperature $T = 330\,\mathrm{K}$ with unscaled charges and weight $W = 0$ against the CPMD reference for the iodide ion.

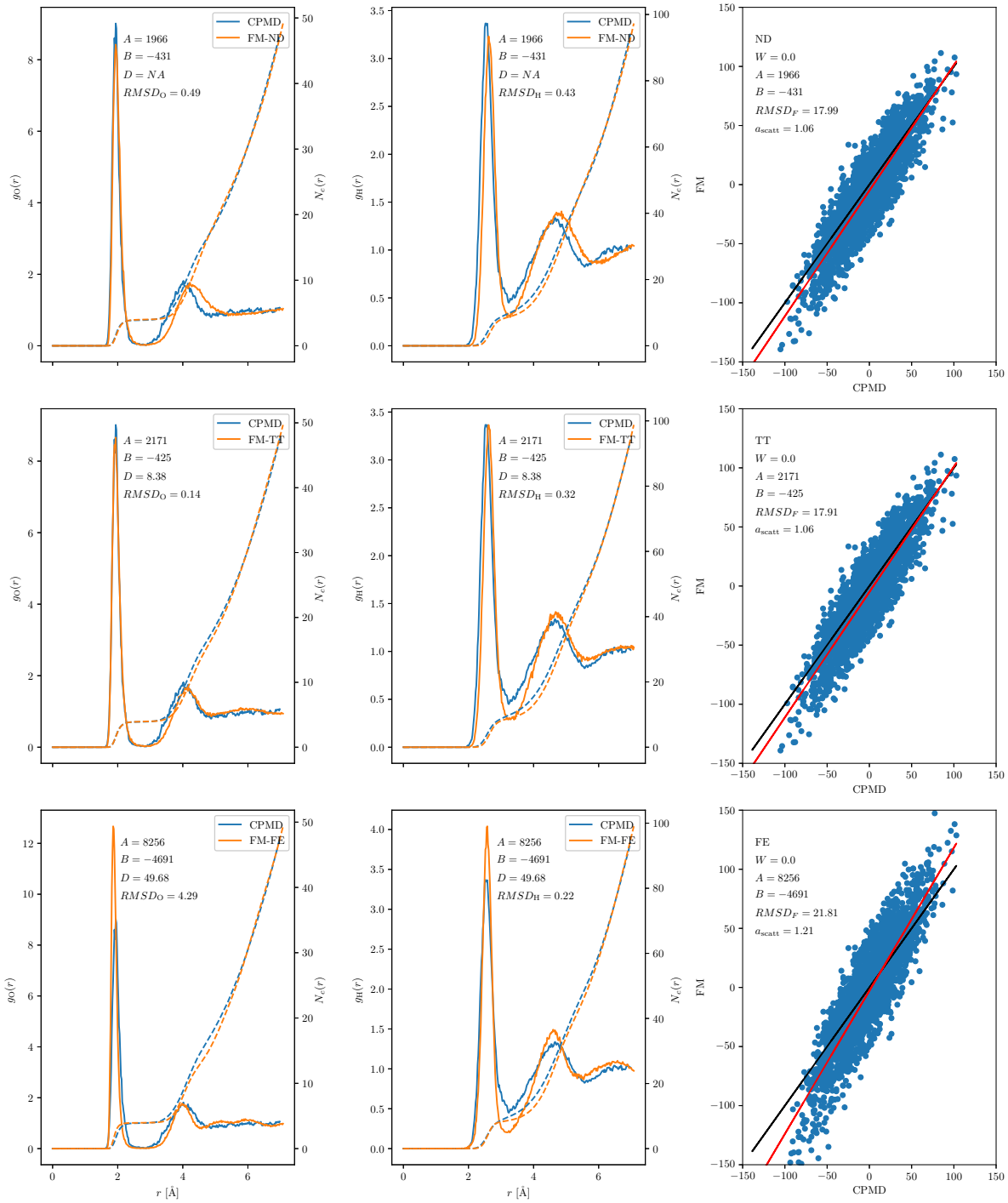

Fig. 6.20 Comparison between the ion-oxygen (left) and ion-hydrogen (center) radial distribution functions and the forces (right) for the undamped (top), Tang-Toennies (middle) and Fermi (bottom) dampings of the SPC-FM water model at temperature $T = 330\,\mathrm{K}$ with unscaled charges and weight $W = 0$ against the CPMD reference for the lithium ion.

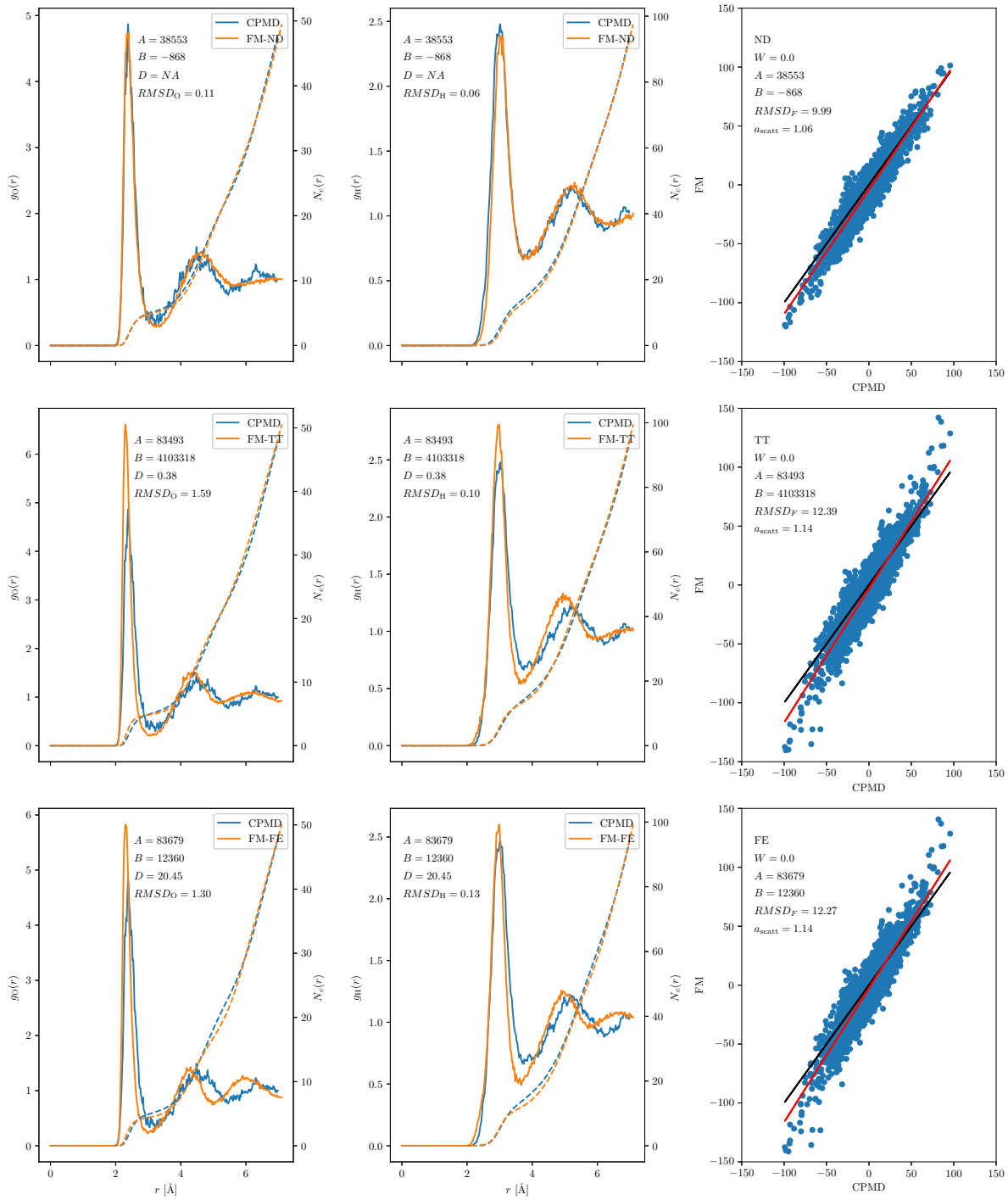

Fig. 6.21 Comparison between the ion-oxygen (left) and ion-hydrogen (center) radial distribution functions and the forces (right) for the undamped (top), Tang-Toennies (middle) and Fermi (bottom) dampings of the SPC-FM water model at temperature $T = 330\,\mathrm{K}$ with unscaled charges and weight $W = 0$ against the CPMD reference for the sodium ion.

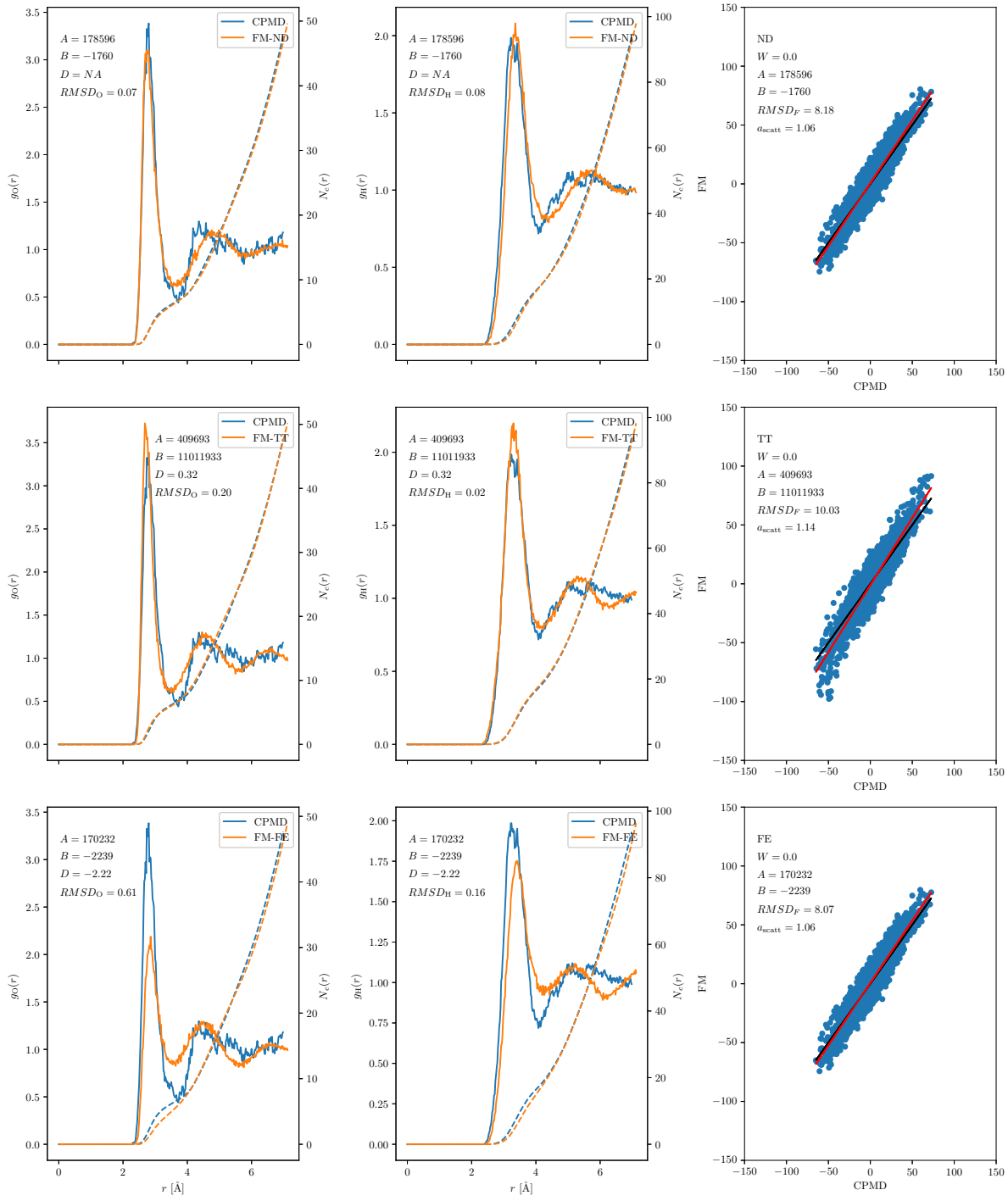

Fig. 6.22 Comparison between the ion-oxygen (left) and ion-hydrogen (center) radial distribution functions and the forces (right) for the undamped (top), Tang-Toennies (middle) and Fermi (bottom) dampings of the SPC-FM water model at temperature $T = 330\,\mathrm{K}$ with unscaled charges and weight $W = 0$ against the CPMD reference for the potassium ion.

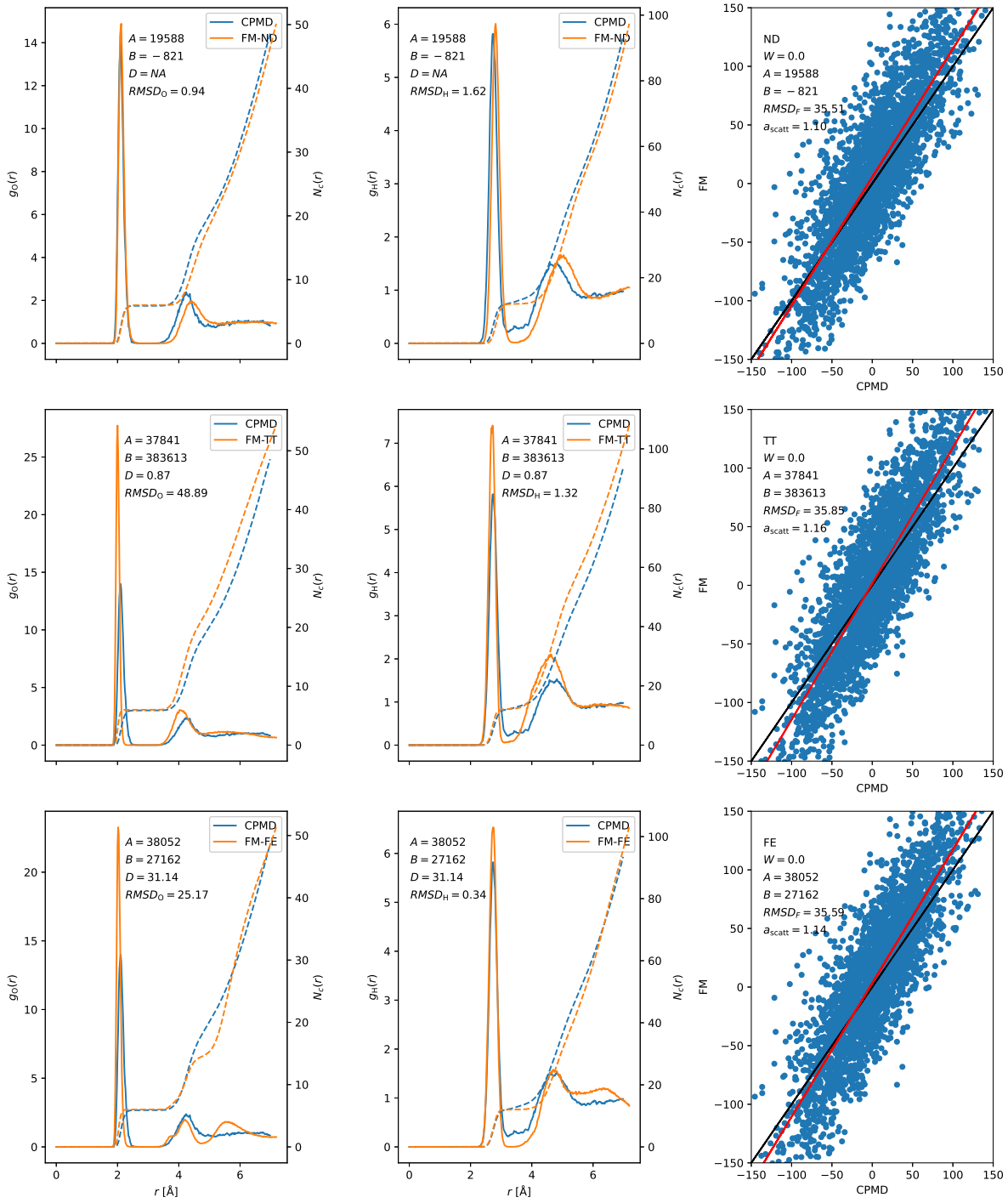

Fig. 6.23 Comparison between the ion-oxygen (left) and ion-hydrogen (center) radial distribution functions and the forces (right) for the undamped (top), Tang-Toennies (middle) and Fermi (bottom) dampings of the SPC-FM water model at temperature $T = 330\,\mathrm{K}$ with unscaled charges and weight $W = 0$ against the CPMD reference for the magnesium ion.

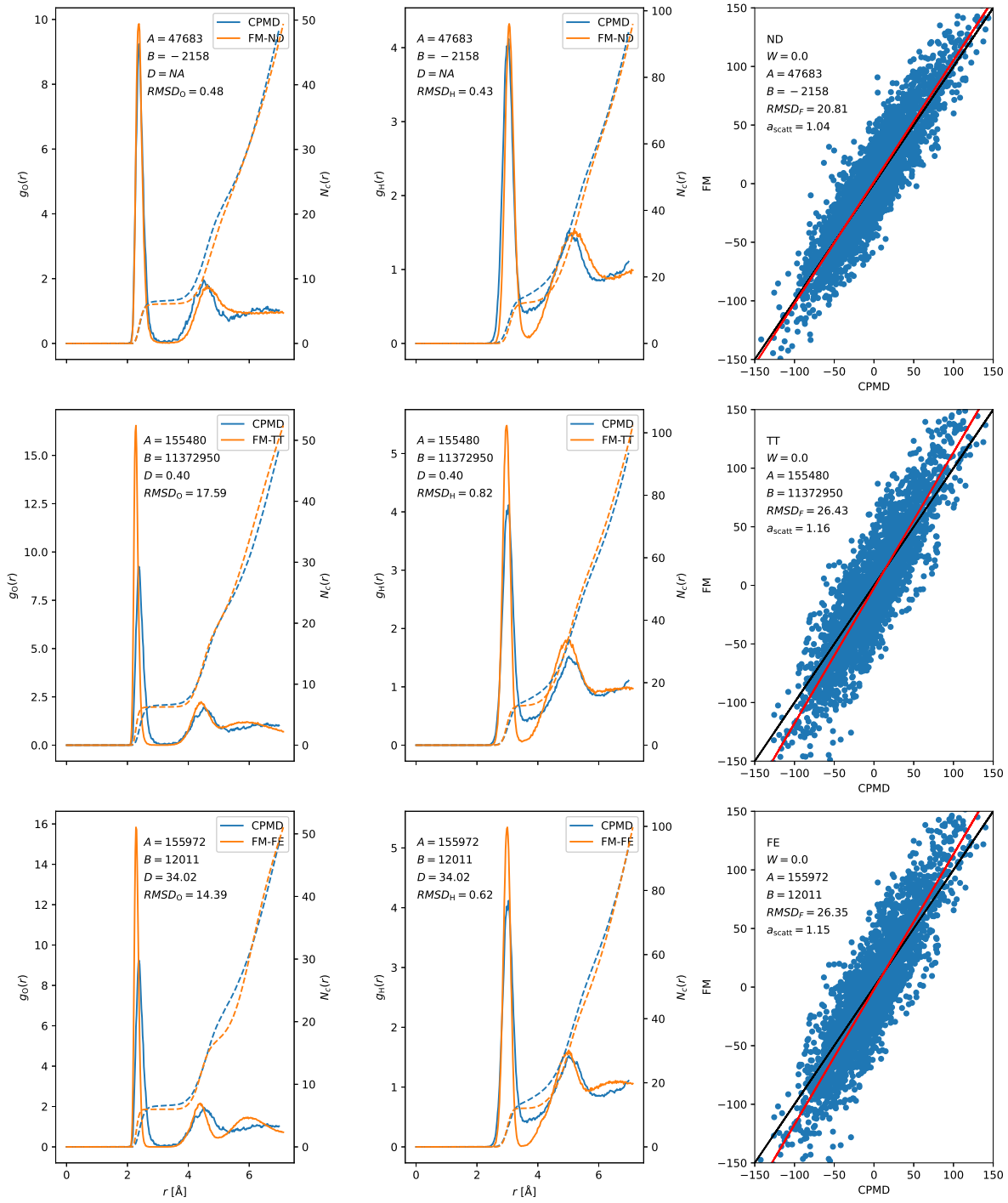

Fig. 6.24 Comparison between the ion-oxygen (left) and ion-hydrogen (center) radial distribution functions and the forces (right) for the undamped (top), Tang-Toennies (middle) and Fermi (bottom) dampings of the SPC-FM water model at temperature $T = 330\,\mathrm{K}$ with unscaled charges and weight $W = 0$ against the CPMD reference for the calcium ion.

References

[1] J. Nocedal and S. J. Wright. *Numerical Optimization*, volume 43. 1999.

[2] Paolo Nicolini, Elvira Guàrdia, and Marco Masia. Shortcomings of the Standard Lennard–Jones Dispersion term in Water Models, Studied with Force Matching. *The Journal of Chemical Physics*, 139(18):184111, 2013.

[3] I. V. Leontyev and A. A. Stuchebrukhov. Electronic continuum model for molecular dynamics simulations. *Journal of Chemical Physics*, 130(8), 2009.

[4] I. V. Leontyev and A. Stuchebrukhov. Electronic Polarizability and the Effective Pair Potentials of Water. *Journal of Chemical Theory and Computation*, 6(10):3153–3161, oct 2010.

[5] I. V. Leontyev and A. A. Stuchebrukhov. Electronic continuum model for molecular dynamics simulations of biological molecules. *Journal of Chemical Theory and Computation*, 6(5):1498–1508, 2010.

[6] Igor V. Leontyev and Alexei Stuchebrukhov. Accounting for Electronic Polarization in non-Polarizable Force Fields. *Physical chemistry chemical physics : PCCP*, 13(7):2613–2626, feb 2011.

[7] Igor V. Leontyev and Alexei A. Stuchebrukhov. Polarizable mean-field model of water for biological simulations with AMBER and CHARMM force fields. *Journal of Chemical Theory and Computation*, 8(9):3207–3216, 2012.

[8] Igor V. Leontyev and Alexei A. Stuchebrukhov. Polarizable molecular interactions in condensed phase and their equivalent nonpolarizable models. *Journal of Chemical Physics*, 141(1), 2014.

[9] Luís Pegado, Ondrej Marsalek, Pavel Jungwirth, and Erik Wernersson. Solvation and ion-pairing properties of the aqueous sulfate anion: Explicit versus effective electronic polarization. *Physical Chemistry Chemical Physics*, 14(29):10248–10257, 2012.

[10] Philip E. Mason, Erik Wernersson, and Pavel Jungwirth. Accurate description of aqueous carbonate ions: An effective polarization model verified by neutron scattering. *Journal of Physical Chemistry B*, 116(28):8145–8153, 2012.

[11] Z. R. Kann and J. L. Skinner. A scaled-ionic-charge simulation model that reproduces enhanced and suppressed water diffusion in aqueous salt solutions. *Journal of Chemical Physics*, 141(10), 2014.

[12] I. M. Zeron, J. L.F. Abascal, and C. Vega. A force field of Li+, Na+, K+, Mg2+, Ca2+, Cl-, and S O 4 2 - In aqueous solution based on the TIP4P/2005 water model and scaled charges for the ions. *Journal of Chemical Physics*, 151(13), 2019.

[13] S. Blazquez, I. M. Zeron, M. M. Conde, J. L.F. Abascal, and C. Vega. Scaled charges at work: Salting out and interfacial tension of methane with electrolyte solutions from computer simulations. *Fluid Phase Equilibria*, 513:112548, 2020.

[14] C.G. Malmberg and A.A. Maryott. Dielectric constant of water from 0 to 100 C. *Journal of Research of the National Bureau of Standards*, 56(1):1, 1956.

[15] Q. Wu and W. Yang. Empirical Correction to Density Functional Theory for van der Waals Interactions. *The Journal of Chemical Physics*, 116(2):515, 2002.

[16] S. S. Batsanov. Van der Waals Radii of Elements. *Inorganic Materials*, 37(9):871–885, 2001.

Chapter 7

Summary and Conclusions

7.1 On ion water Carr-Parrinelo simulations

- The aim of this thesis is to characterize the interaction between a certain set of ions (F^-, Cl^-, Br^-, I^-, Li^+, Na^+, K^+, Mg^{2+}, Ca^{2+}) and water through the Force Matching algorithm. In order to do so, a set of ion-water Car-Parrinello Molecular Dynamics (CPMD) simulations where performed to be used as a reference for the matching process.

- A wide range of properties from these *ab initio* simulations like the ion-water Radial Distribution Functions (RDF), the coordination numbers, the residence time, the ion self-diffusion coefficient have been computed and then compared to those of experimental sources.

- The degree of agreement between the experimental values and the simulated ones provides a high enough level of confidence to allow their use as reference in the Force Matching process.

7.2 On polarization damping and Ion solvation dynamics

- In previous works it was shown the value of using a screening function when computing the short range electrostatic interaction between molecules, both the short

and long range polarizations of highly polarizable ions and the chlorine ion in bulk water. In this work this relevance has been extended to the dynamical properties of the ion and of its solvation shell. This relevance comes from the fact that water molecules in the first hydration shell of the chlorine atom behave faster (closer to the *ab initio* reference) with dampened electrostatic interactions than without them.

- While both, the exponential and Gaussian distributions, perform well, they suppose practically no extra computational cost and they have been ported to different polarizability methods such as shell models at gas and condensed phase.

- These results show that the use of appropriate damping functions in conjunction with gas phase polarizability leads to a good statics and dynamics results comparing to those of CPMD reference. This conclusion can not be translated into the assumption that the polarizability is constant between phases but just that it is convenient from an operational point of view to use it as such.

7.3 On the Force Matching algorithm

- The Force Matching algorithm has been applied to parametrize the water-ion Lennard-Jones electrostatic potentials for a wide selection of anions and cations in conjunction with a widespread of water models: SPC/E, RPOL and SPC-FM.

- The optimization process has been led by the minimization of the RMSD between the potential forces and those of reference obtained from CPMD simulations. Once the potentials where obtained, their quality was assessed in terms of the RMSD of the Radial Distribution Functions and the slopes of the force-force correlations between the classical and the *ab initio* results.

- The first obvious conclusion that can be drawn from the results obtained in this work referring the Force Matching process is that there is no one-fits-all approach when it comes to choosing a combination of water model, dispersion damping, polarization and Force Matching parameters to model the interaction between ions and water.

- When going over the results it can be easily seen that they display a wide range of values for the fitted parameters. It might be especially uncomfortable the presence of negative values of the C parameter of the Lennard-Jones potential. Different

attempts of preventing this parameter to go negative like the use of polarization, force weights or charge scaling, have been unsuccessfully tried.

- **On the influence of the polarization** Polarization has been introduced by means of the RPOL water model and using a Polarizable Point Dipole site at the center of the ion with a fitted polarizability value. While the polarizations helps getting a better reproduction of the forces it does introduce big instabilities in the matching process that have prevented from obtaining results for most of the ions. Also, as an extra parameter needs to be fitted, the computational cost of the matching process gets increased greatly.

- **On the influence of the force weight** Adding a weight proportional to the force intensity during the force matching process is computationally cheap and should prevent the overestimation of forces leading to better performing LJ potentials. While this was true for some of the ions such as bromide and iodine, it does not provide a universal improvement. In this thesis only integer values of the weight where tested; it might be interesting in future works to explore the effects of using real values.

- **On the influence of the charge scaling** A relatively recent method to account in some degree for polarization effects within classical MD simulations consists on adding an electric continuum effect to the ion. This method has been found to be way more stable and less computationally demanding than explicitly introducing a polarization description.

  Different scaling factors where computed for each SPC-FM and dispersion damping pair.

  While the introduction of the charge scaling has a moderate positive effect on the negative values of the C parameter of the fitted Lennard-Jones potentials, the resulting Radial Distribution Functions consistently move away from the reference ones.

  It is worth to keep in mind that in this work only structural properties have been used to measure the quality of the potential. Due to the previous success of this method for reproducing dynamic properties of water around ions, it might be worthwhile in the future to compute those properties for the fitted potentials and include them in the comparison.

- **On the influence of the dispersion damping** Two different dispersion damping functions, the Tang-Toennies and the Fermi damping functions, have been tested and compared to the absence of damping.

  Once again, none of the three performs better than the other across all the nine tested ions. On the one hand, unitary damping function works best in the case of the fluoride, sodium, potassium, magnesium and calcium ions. On the other hand, the Tang-Toennies function generated better potentials for the chloride, bromide and lithium ions. Only for the iodine ion the Fermi dispersion damping performed better than the other two functions. It is notable how in the case of both divalent ions, both dampening functions obtain a reasonable success reproducing the ion-hydrogen Radial Distribution function while completely missing the ion-oxygen one.

- Although it is unknown how to predict when a certain combination of dampening function, force weight, charge scale, etc., will obtain better results than the others, the Force Matching process remains as powerful as a tool to obtain reliable Lennard-Jones potentials, especially for systems where the access to experimental data to fit the potentials is hard to obtain.

Appendix A

Force matching for the SPC-FM water models at T=300 K

Ion	Damping	$\epsilon_{\mathrm{el}}^{-1/2}$	A [kcalÅ^{12}/mol]	C [kcalÅ^{6}/mol]	d [Å^{-1}]	R_{FE} [Å]	$RMSD_{\mathrm{F}}$	$RMSD_{\mathrm{O}}$	$RMSD_{\mathrm{H}}$	b_{scatt}
F^-	ND	1.0	193 215.98	−2851.51	-	-	20.57	0.40	0.67	1.16
	TT	1.0	491 198.72	559.61	0.16	-	24.46	2.09	3.67	1.32
	FE	1.0	490 048.93	1168.04	9.49	1.65	24.34	1.39	2.32	1.31
Cl^-	ND	1.0	2 208 317.57	−2437.44	-	-	16.04	0.33	0.46	1.18
	TT	1.0	2 231 623.92	−2404.18	4.97	-	15.96	0.17	0.10	1.18
	FE	1.0	2 972 815.77	620.76	32.45	2.05	16.57	0.21	0.21	1.23
Br^-	ND	1.0	5 185 935.93	923.90	-	-	20.30	0.86	0.93	1.32
	TT	1.0	5 177 860.47	927.67	11.33	-	20.20	0.50	0.45	1.32
	FE	1.0	5 276 826.79	19 853.55	5.11	2.10	19.90	0.84	0.86	1.32
I^-	ND	1.0	11 352 578.28	3203.42	-	-	16.67	0.80	0.79	1.18
	TT	1.0	11 338 691.60	3204.27	11.80	-	16.59	0.41	0.37	1.18
	FE	1.0	9 170 486.29	−49 911.41	11.86	2.22	15.84	0.20	0.21	1.14
Li^+	ND	1.0	1965.53	−430.64	-	-	17.99	0.60	0.55	1.06
	TT	1.0	2170.95	−424.99	8.38	-	17.91	0.17	0.40	1.06
	FE	1.0	8256.31	−4690.75	49.68	2.63	21.81	4.34	0.31	1.21
Na^+	ND	1.0	38 553.42	−867.62	-	-	9.99	0.13	0.08	1.06
	TT	1.0	83 674.10	244 465.74	0.59	-	12.40	1.79	0.15	1.14
	FE	1.0	83 679.44	12 360.18	20.45	2.77	12.27	1.25	0.17	1.14
K^+	ND	1.0	178 595.53	−1759.62	-	-	8.18	0.06	0.09	1.06
	TT	1.0	410 485.21	216 089.51	0.53	-	10.05	0.23	0.03	1.14
	FE	1.0	170 232.04	−2239.50	−2.22	3.02	8.07	0.67	0.20	1.06
Mg^{2+}	ND	1.0	19 588.38	−820.91	-	-	35.51	1.44	2.01	1.10
	TT	1.0	37 956.24	245 217.01	0.94	-	35.87	54.23	1.69	1.16
	FE	1.0	38 052.10	27 161.64	31.14	2.42	35.59	26.64	0.35	1.14
Ca^{2+}	ND	1.0	47 683.14	−2158.37	-	-	20.81	0.86	0.50	1.04
	TT	1.0	155 690.98	223 173.48	0.59	-	26.58	17.96	0.85	1.16
	FE	1.0	155 972.42	12 010.55	34.02	2.78	26.35	14.32	0.88	1.15

Table A.1 For each ion and damping dispersion: the charge scaling factor, the resulting fitted LJ parameters and damping parameters (when they apply) and the quality metrics $RMSD_{\mathrm{F}}$, $RMSD_{\mathrm{O}}$, $RMSD_{\mathrm{H}}$ and b_{scatt} for simulations with the SPC-FM water models at $T = 300\,\mathrm{K}$.

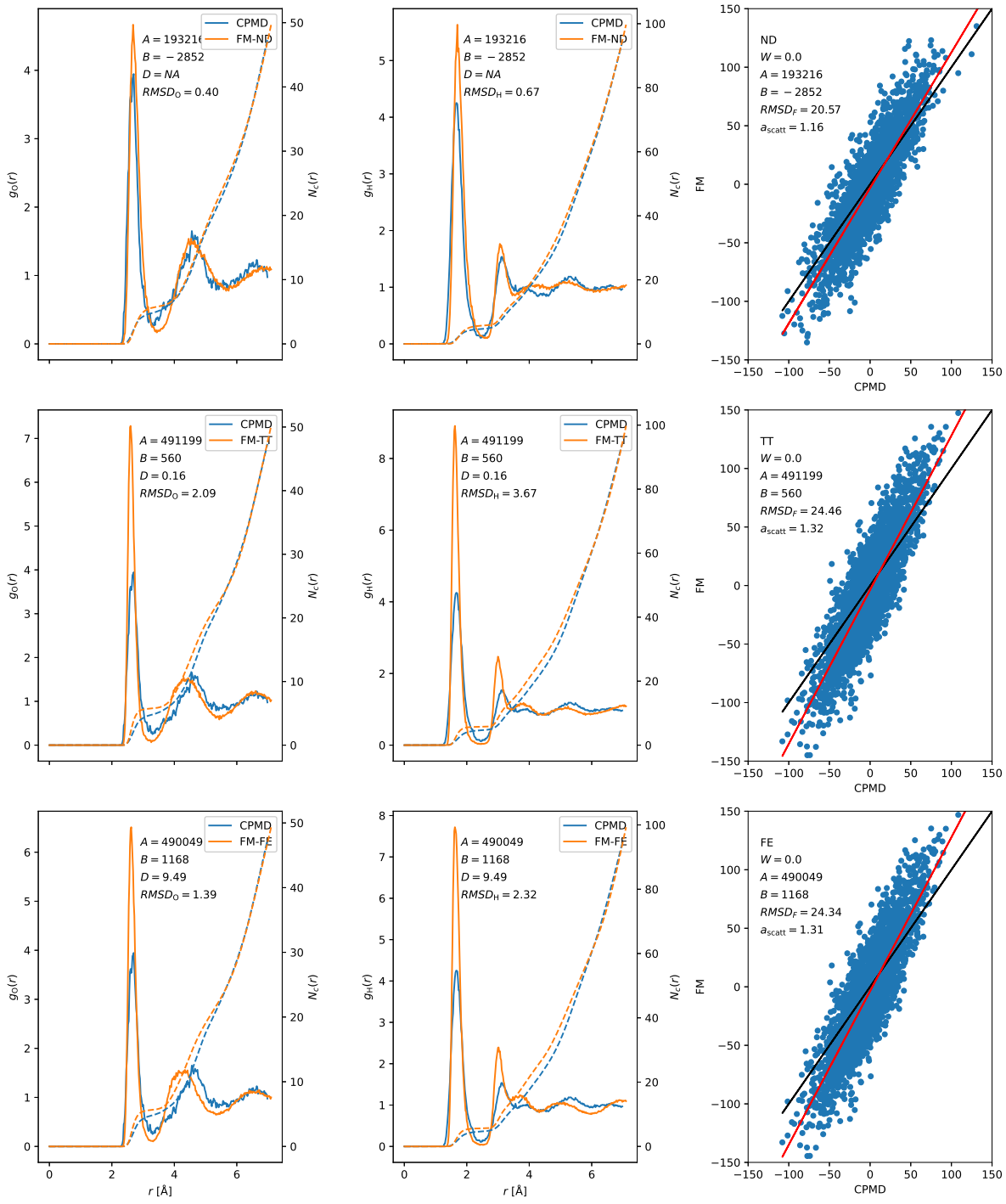

Fig. A.1 Comparison between the ion-oxygen (left) and ion-hydrogen (center) RDFs and the forces (right) for the undamped (top), Tang-Toennies (middle) and Fermi (bottom) dampings of the SPC-FM water models at temperature $T = 300\,\mathrm{K}$ with unscaled charges and weight $W = 0$ against the CPMD reference for the fluoride ion.

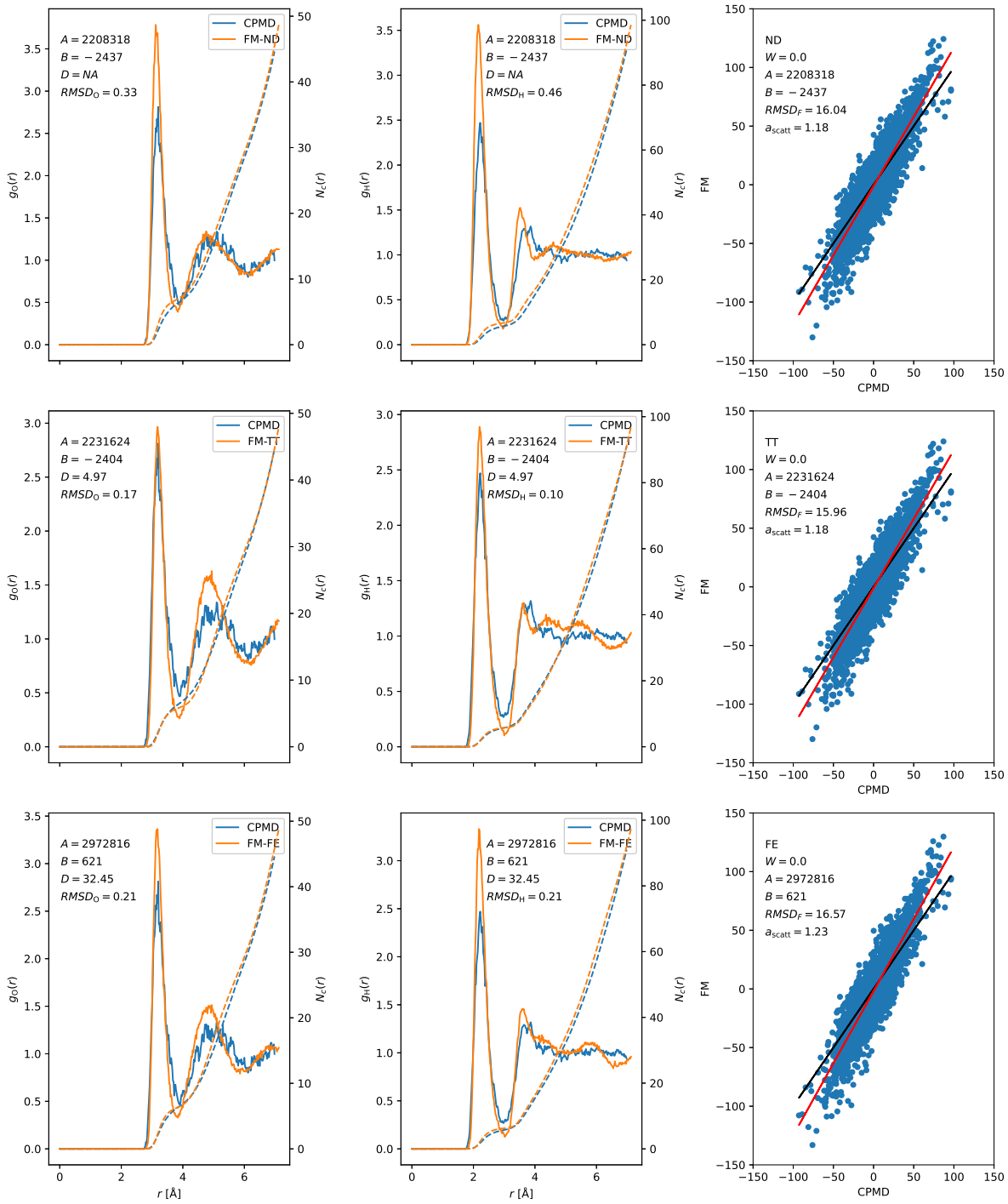

Fig. A.2 Comparison between the ion-oxygen (left) and ion-hydrogen (center) RDFs and the forces (right) for the undamped (top), Tang-Toennies (middle) and Fermi (bottom) dampings of the SPC-FM water models at temperature $T = 300\,\mathrm{K}$ with unscaled charges and weight $W = 0$ against the CPMD reference for the chloride ion.

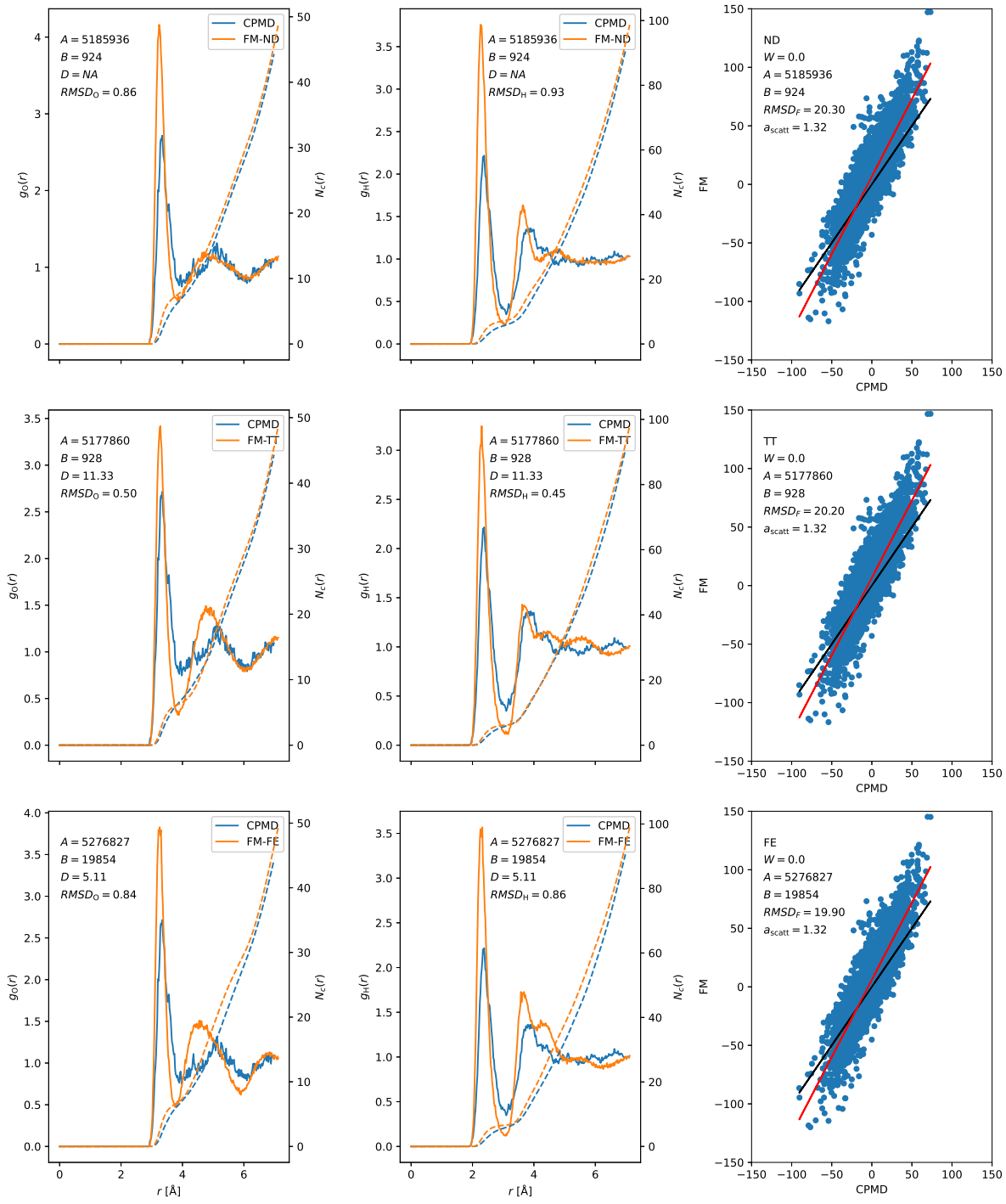

Fig. A.3 Comparison between the ion-oxygen (left) and ion-hydrogen (center) RDFs and the forces (right) for the undamped (top), Tang-Toennies (middle) and Fermi (bottom) dampings of the SPC-FM water models at temperature $T = 300\,\mathrm{K}$ with unscaled charges and weight $W = 0$ against the CPMD reference for the bromide ion.

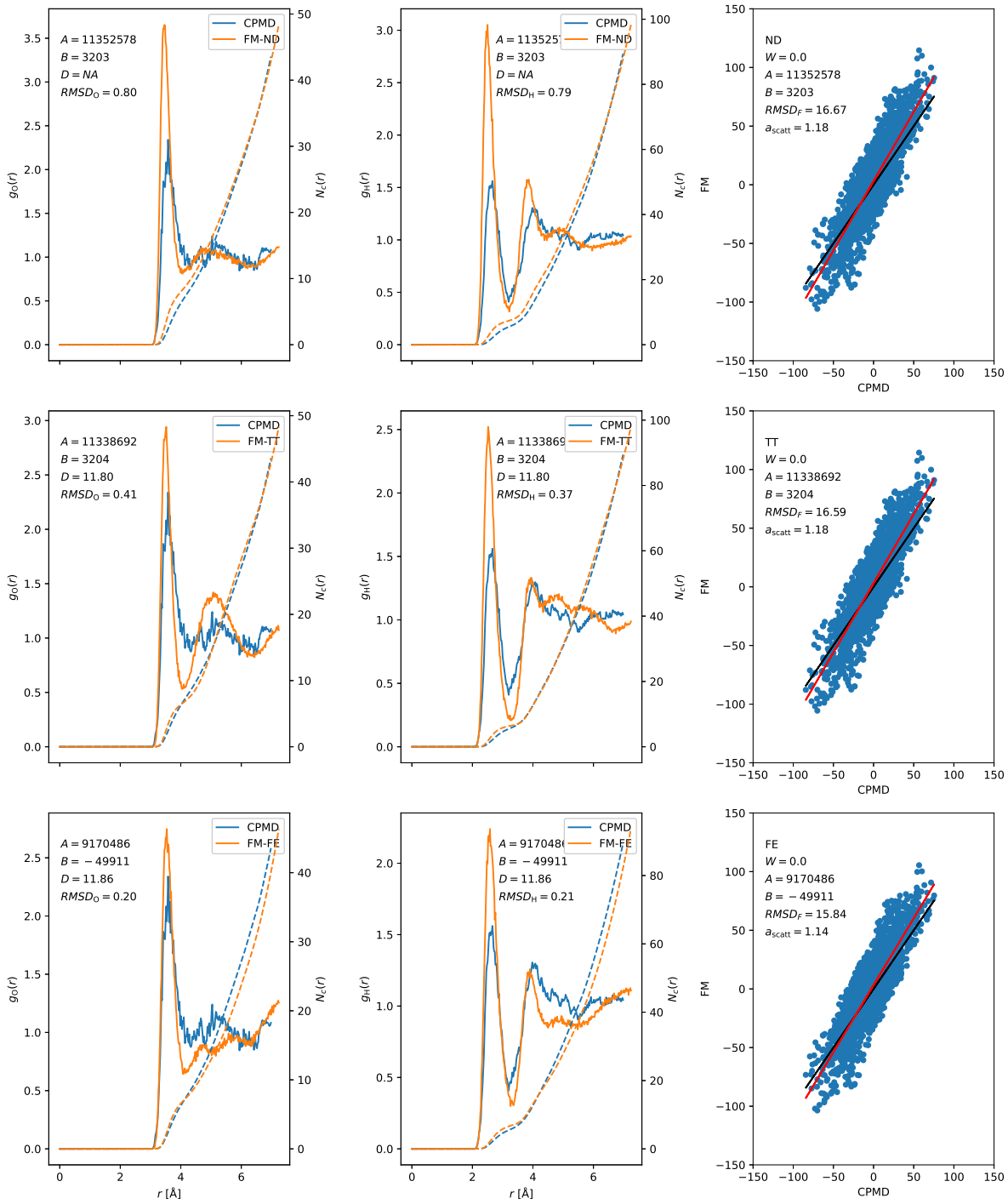

Fig. A.4 Comparison between the ion-oxygen (left) and ion-hydrogen (center) RDFs and the forces (right) for the undamped (top), Tang-Toennies (middle) and Fermi (bottom) dampings of the SPC-FM water models at temperature $T = 300\,\mathrm{K}$ with unscaled charges and weight $W = 0$ against the CPMD reference for the iodide ion.

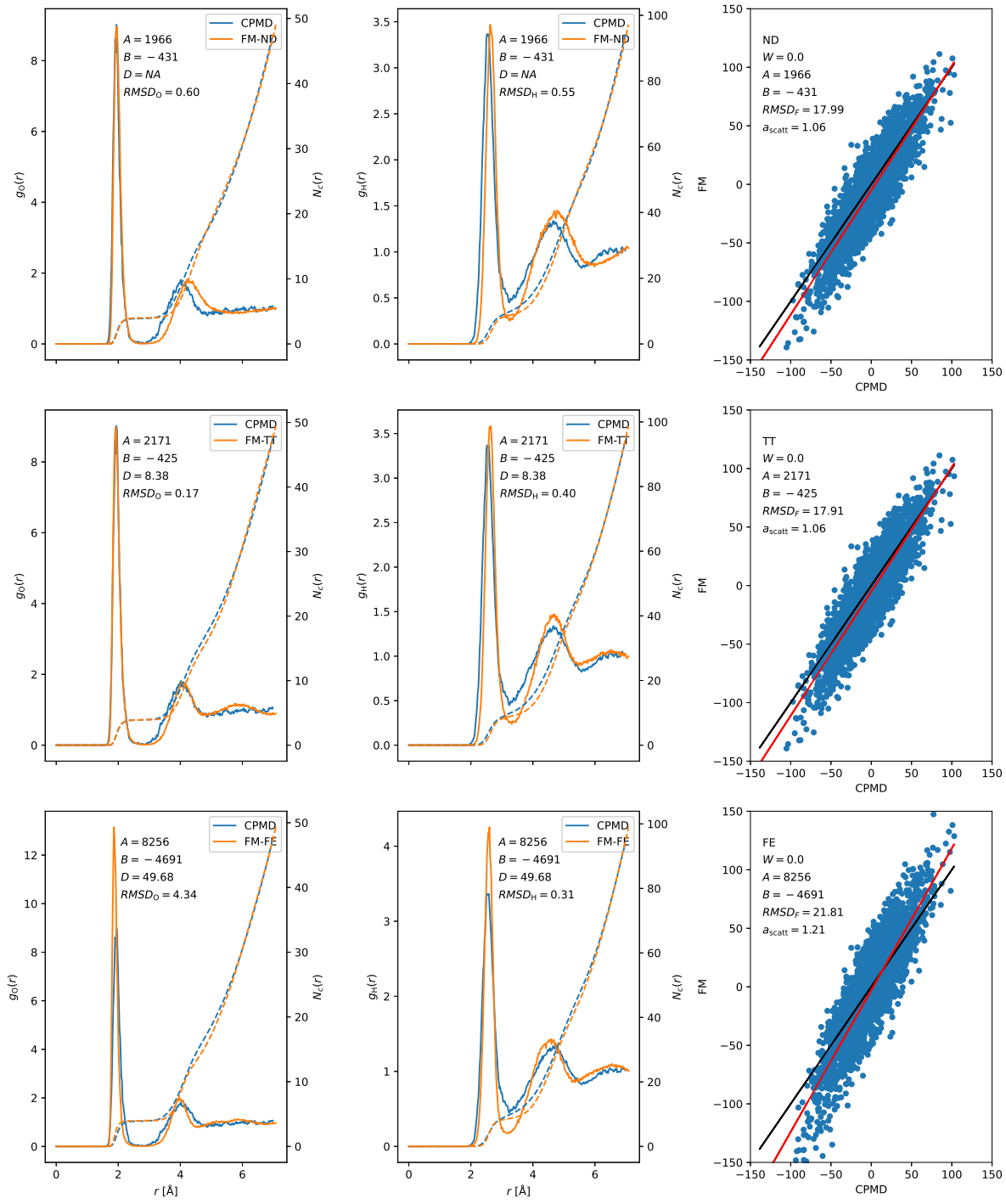

Fig. A.5 Comparison between the ion-oxygen (left) and ion-hydrogen (center) RDFs and the forces (right) for the undamped (top), Tang-Toennies (middle) and Fermi (bottom) dampings of the SPC-FM water models at temperature $T = 300\,\mathrm{K}$ with unscaled charges and weight $W = 0$ against the CPMD reference for the lithium ion.

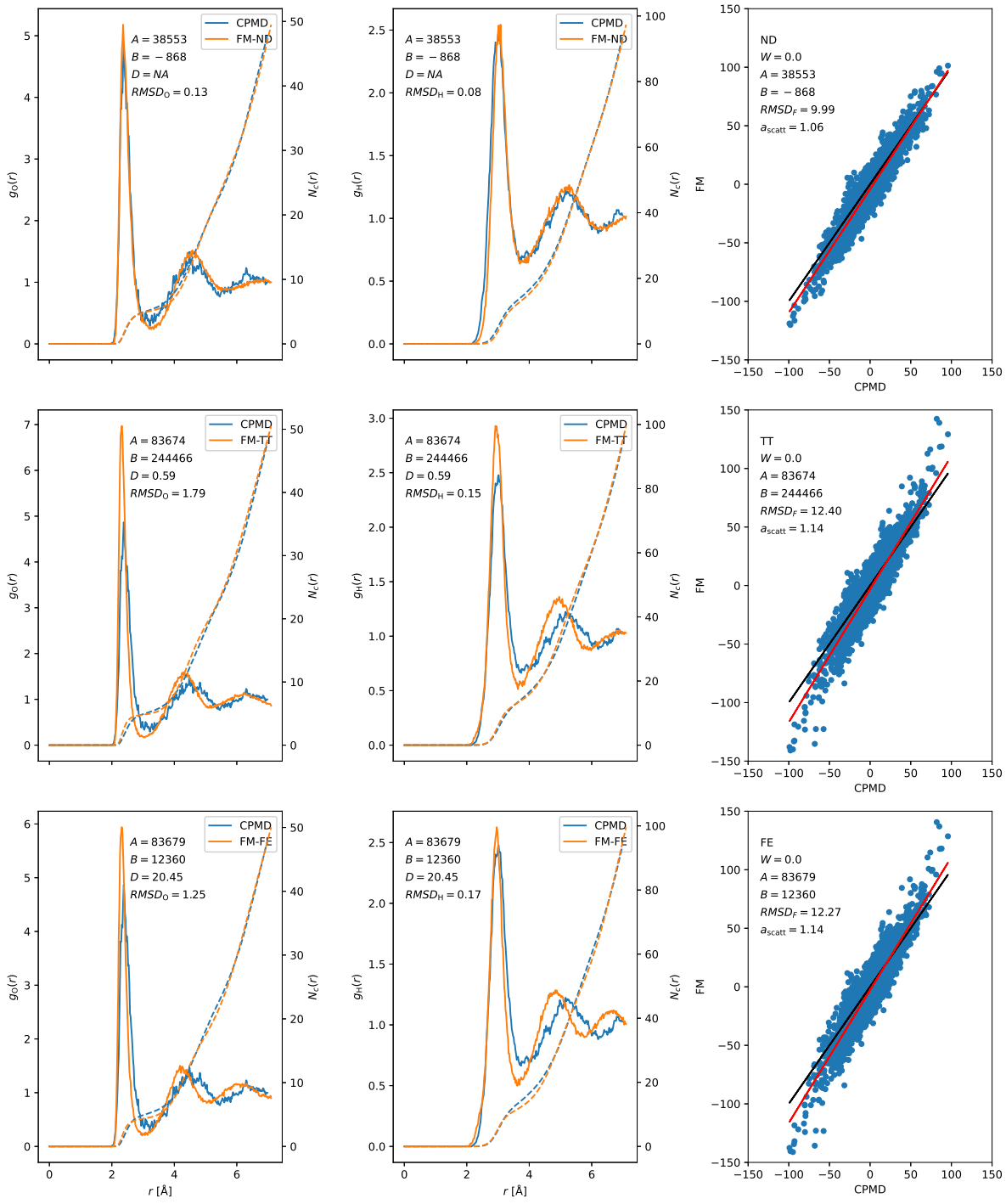

Fig. A.6 Comparison between the ion-oxygen (left) and ion-hydrogen (center) RDFs and the forces (right) for the undamped (top), Tang-Toennies (middle) and Fermi (bottom) dampings of the SPC-FM water models at temperature $T = 300\,\mathrm{K}$ with unscaled charges and weight $W = 0$ against the CPMD reference for the sodium ion.

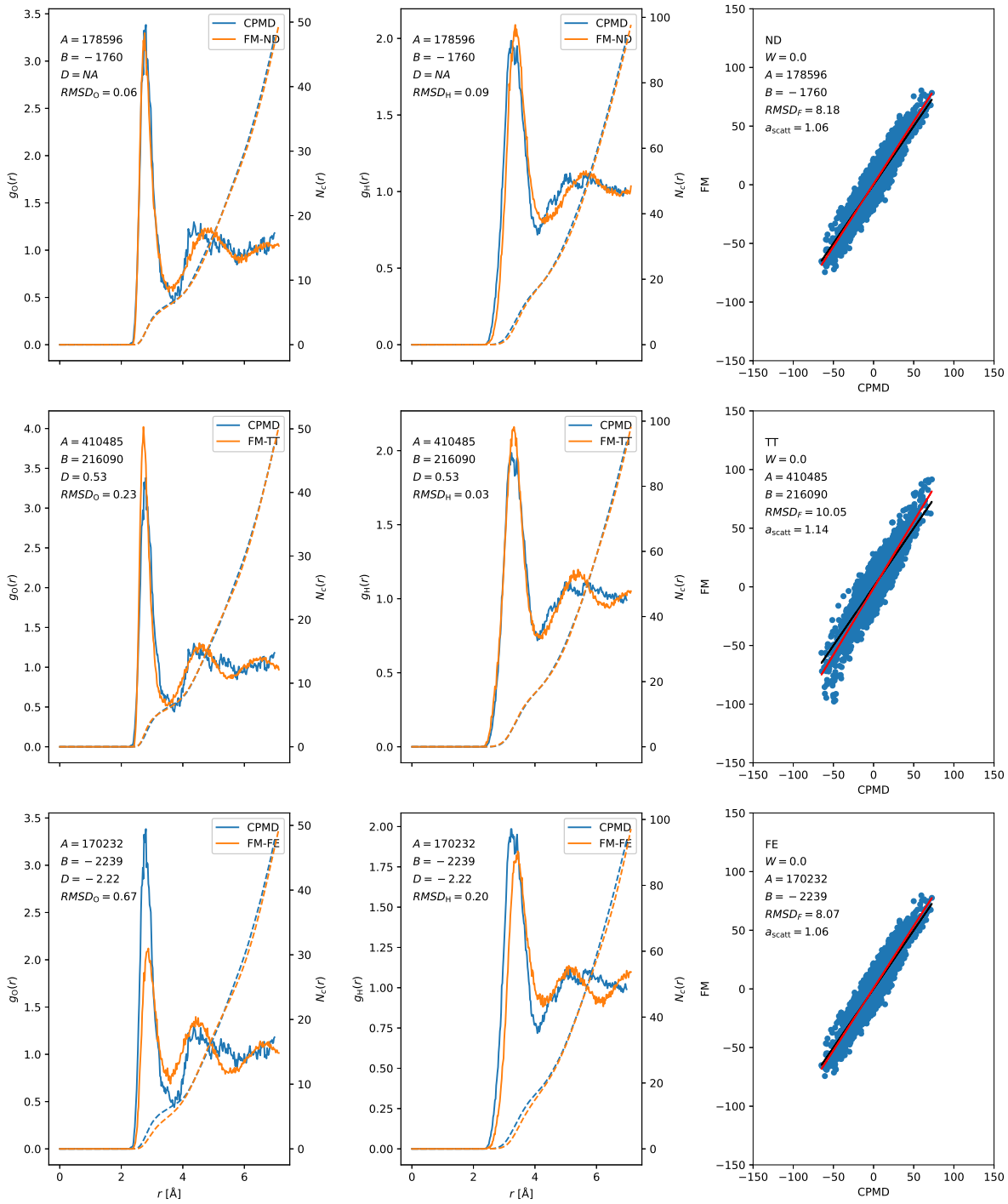

Fig. A.7 Comparison between the ion-oxygen (left) and ion-hydrogen (center) RDFs and the forces (right) for the undamped (top), Tang-Toennies (middle) and Fermi (bottom) dampings of the SPC-FM water models at temperature $T = 300\,\mathrm{K}$ with unscaled charges and weight $W = 0$ against the CPMD reference for the potassium ion.

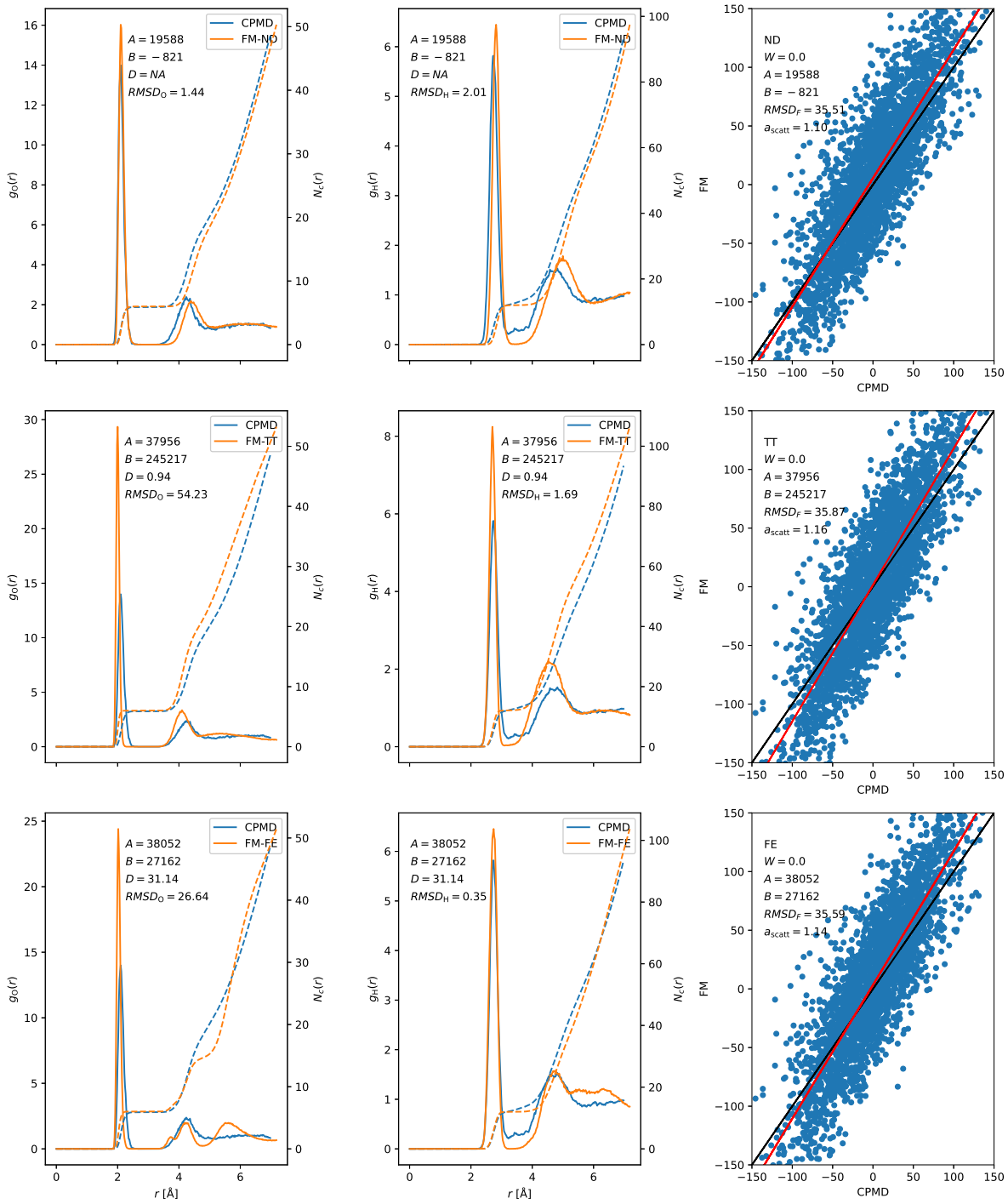

Fig. A.8 Comparison between the ion-oxygen (left) and ion-hydrogen (center) RDFs and the forces (right) for the undamped (top), Tang-Toennies (middle) and Fermi (bottom) dampings of the SPC-FM water models at temperature $T = 300\,\mathrm{K}$ with unscaled charges and weight $W = 0$ against the CPMD reference for the magnesium ion.

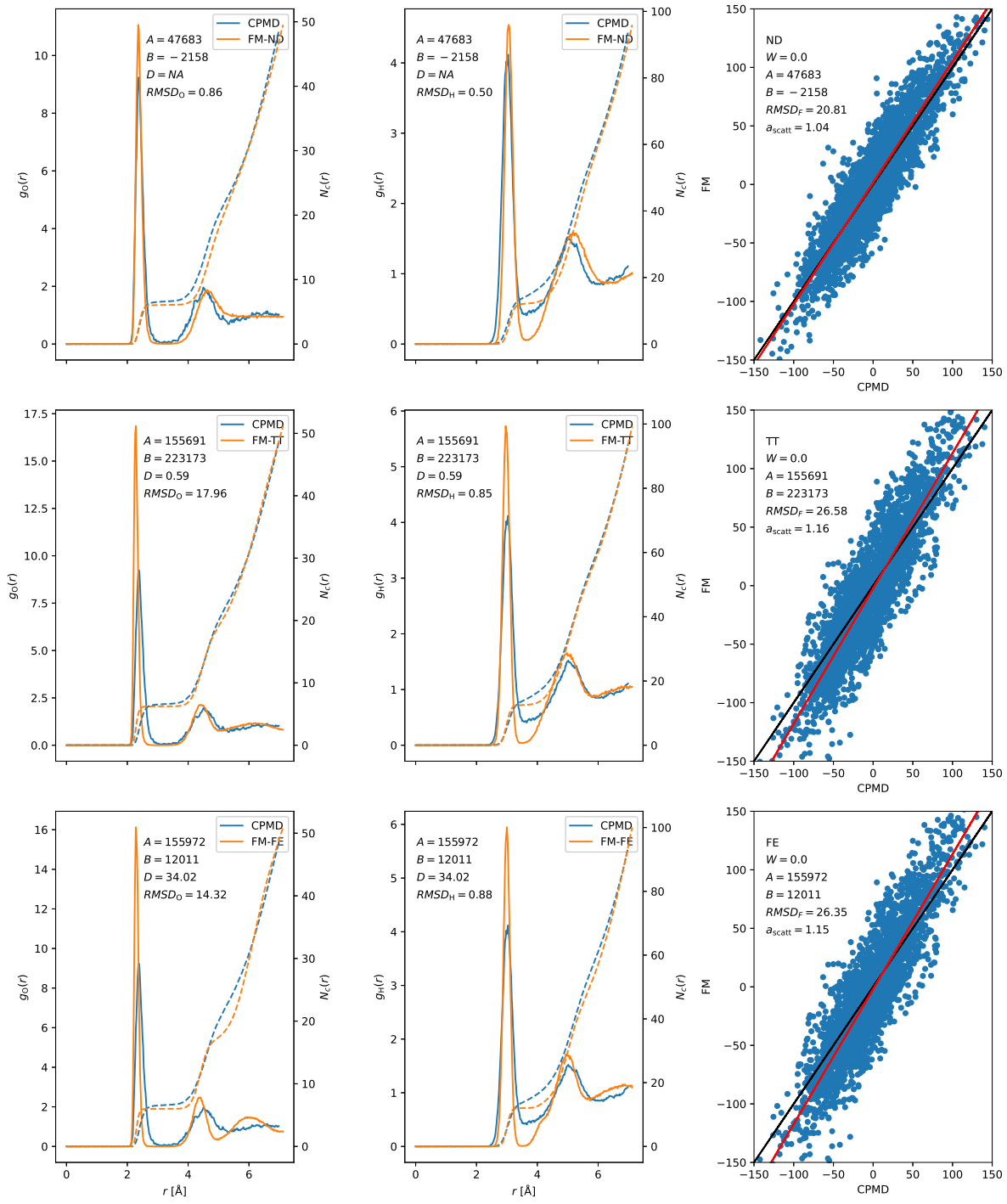

Fig. A.9 Comparison between the ion-oxygen (left) and ion-hydrogen (center) RDFs and the forces (right) for the undamped (top), Tang-Toennies (middle) and Fermi (bottom) dampings of the SPC-FM water models at temperature $T = 300\,\mathrm{K}$ with unscaled charges and weight $W = 0$ against the CPMD reference for the calcium ion.

Ion	Damping	$\epsilon_{\mathrm{el}}^{-1/2}$	A [kcalÅ^{12}/mol]	C [kcalÅ^{6}/mol]	d [Å^{-1}]	R_{FE} [Å]	$RMSD_{\mathrm{F}}$	$RMSD_{\mathrm{O}}$	$RMSD_{\mathrm{H}}$	b_{scatt}
F^-	ND	1.18	158 877.31	−3768.46	-	-	25.71	0.60	1.03	1.27
	TT	1.15	542 571.38	641.12	0.17	-	29.99	4.34	7.70	1.45
	FE	1.18	551 444.41	3359.55	9.57	1.65	30.97	3.54	5.82	1.47
Cl^-	ND	1.18	2 187 424.15	−3507.19	-	-	20.34	0.54	0.80	1.29
	TT	1.15	2 224 332.40	−3286.92	4.94	-	19.51	0.24	0.22	1.27
	FE	1.18	3 290 682.91	−486.39	402.74	2.05	21.23	0.74	0.88	1.36
Br^-	ND	1.18	5 614 103.15	723.60	-	-	25.87	1.49	1.69	1.47
	TT	1.15	5 533 450.15	761.31	11.43	-	24.80	0.72	0.77	1.44
	FE	1.18	5 828 958.01	21 983.20	5.11	2.10	25.41	1.68	1.80	1.47
I^-	ND	1.18	12 089 394.15	3158.54	-	-	20.85	1.58	1.60	1.28
	TT	1.15	11 950 616.83	3167.00	12.00	-	20.05	0.85	0.82	1.26
	FE	1.18	9 878 133.74	−59 845.46	12.23	2.22	19.70	0.52	0.55	1.23
Li^+	ND	1.18	672.55	−580.11	-	-	22.12	0.59	0.63	1.14
	TT	1.15	1153.48	−548.14	8.37	-	21.30	0.71	0.59	1.13
	FE	1.18	9152.50	−5796.91	50.46	2.63	27.70	14.37	0.83	1.34
Na^+	ND	1.18	30 732.29	−1177.12	-	-	12.78	0.49	0.23	1.14
	TT	1.15	89 907.03	109 098 410.42	0.26	-	15.50	3.81	0.33	1.23
	FE	1.18	92 006.86	16 536.55	19.35	2.77	16.06	5.39	0.49	1.25
K^+	ND	1.18	144 064.92	−2357.28	-	-	10.55	0.23	0.18	1.17
	TT	1.15	446 700.00	10 306 495.25	0.33	-	12.58	0.88	0.13	1.24
	FE	1.18	446 503.23	−26 277.73	11.39	3.02	13.01	0.50	0.12	1.25
Mg^{2+}	ND	1.18	14 365.54	−1204.82	-	-	43.49	1.84	1.68	1.18
	TT	1.15	40 698.73	555 117.34	0.83	-	43.24	81.91	3.01	1.25
	FE	1.18	41 546.14	35 229.68	29.95	2.42	44.22	65.59	1.17	1.25
Ca^{2+}	ND	1.18	28 417.53	−2873.55	-	-	25.70	0.65	1.12	1.12
	TT	1.15	169 272.82	11 870 622.37	0.40	-	32.45	20.77	1.52	1.26
	FE	1.18	172 669.86	16 850.58	28.03	2.78	33.57	22.80	1.24	1.27

Table A.2 For each ion and damping dispersion: the charge scaling factor, the resulting fitted LJ parameters and damping parameters (when they apply) and the quality metrics $RMSD_{\mathrm{F}}$, $RMSD_{\mathrm{O}}$, $RMSD_{\mathrm{H}}$ and b_{scatt} for simulations with the SPC-FM water models at $T = 300\,\mathrm{K}$.

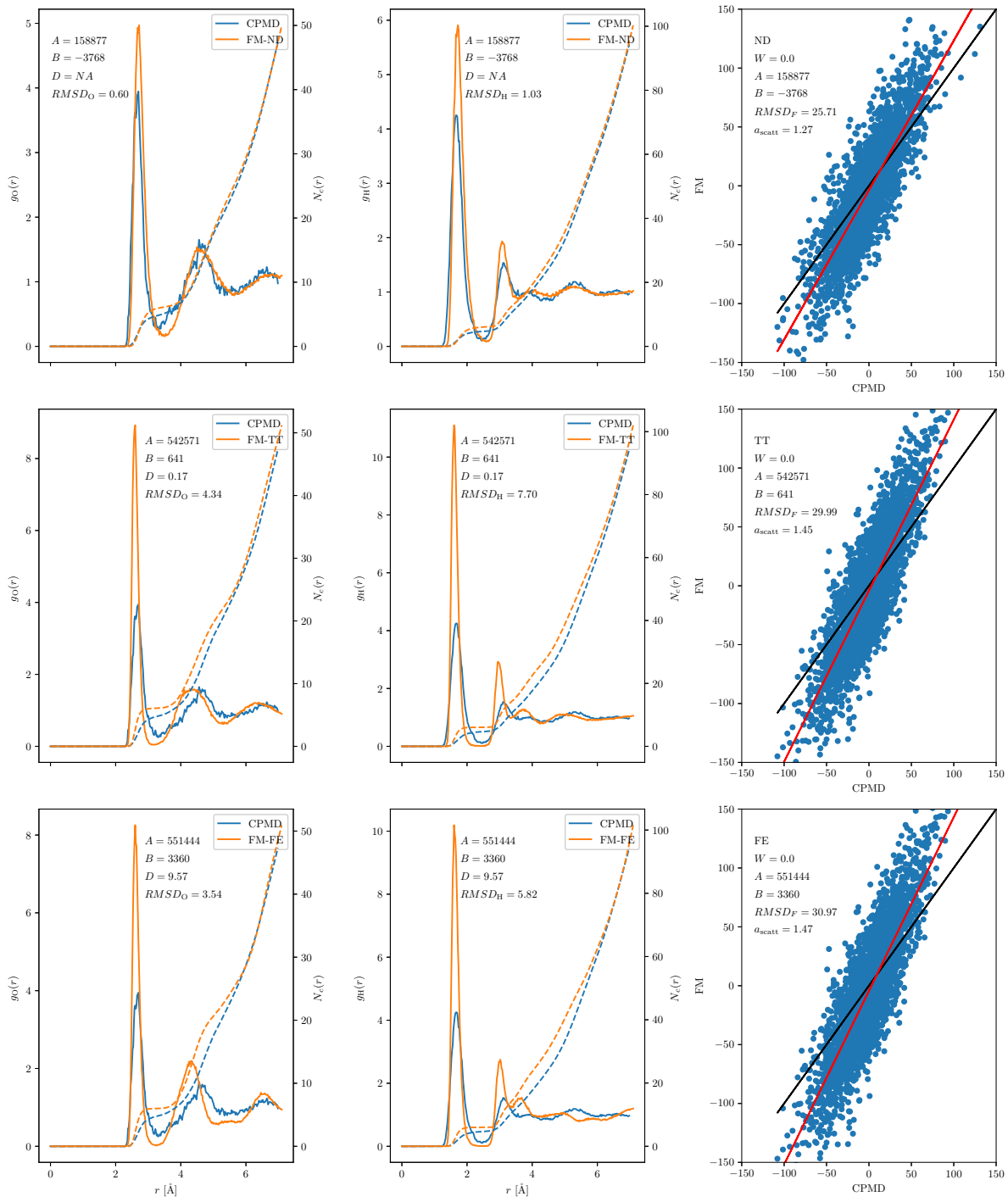

Fig. A.10 Comparison between the ion-oxygen (left) and ion-hydrogen (center) RDFs and the forces (right) for the undamped (top), Tang-Toennies (middle) and Fermi (bottom) dampings of the SPC-FM water models at temperature $T = 300\,\mathrm{K}$ with scaled charges and weight $W = 0$ against the CPMD reference for the fluoride ion.

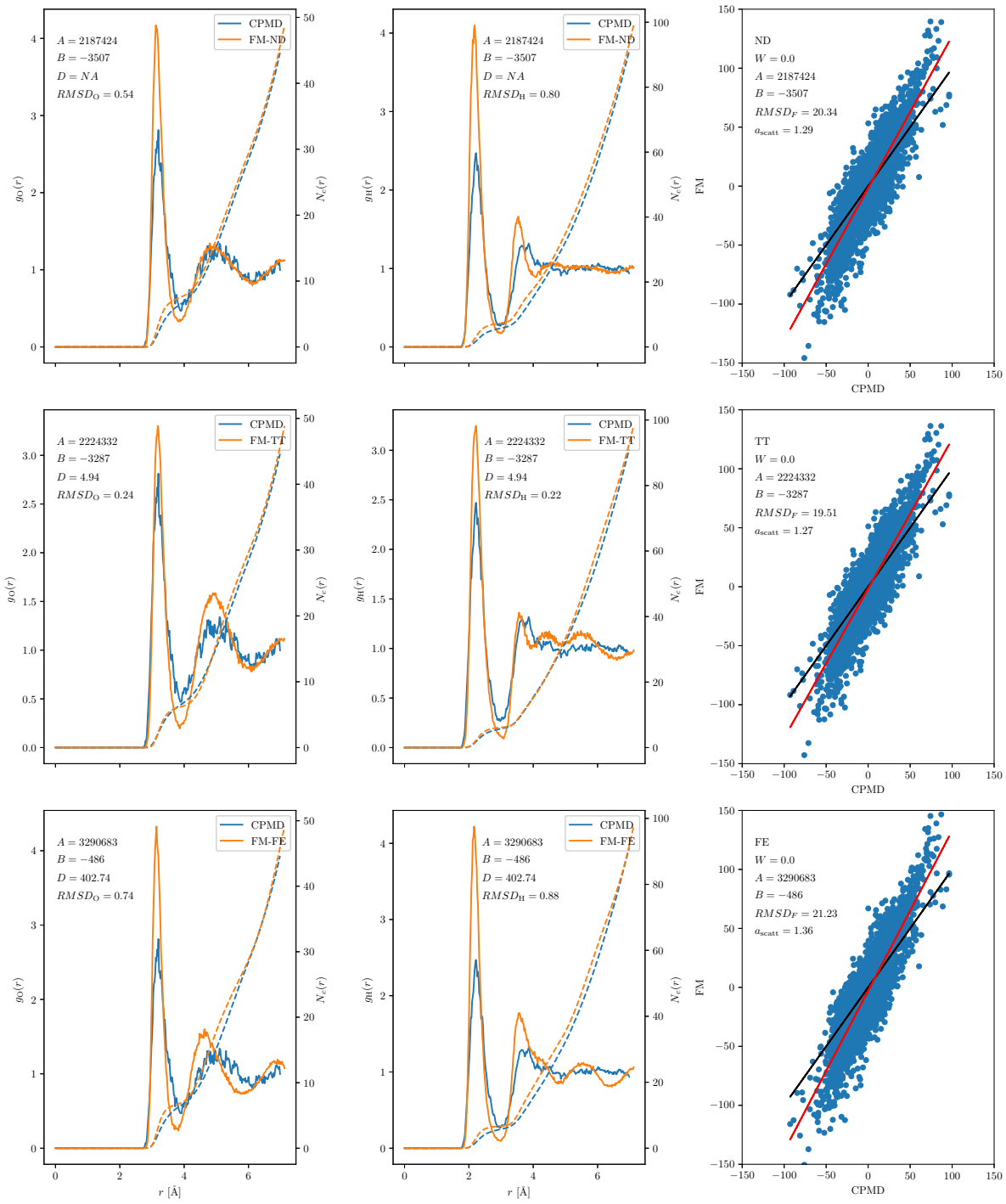

Fig. A.11 Comparison between the ion-oxygen (left) and ion-hydrogen (center) RDFs and the forces (right) for the undamped (top), Tang-Toennies (middle) and Fermi (bottom) dampings of the SPC-FM water models at temperature $T = 300\,\mathrm{K}$ with scaled charges and weight $W = 0$ against the CPMD reference for the chloride ion.

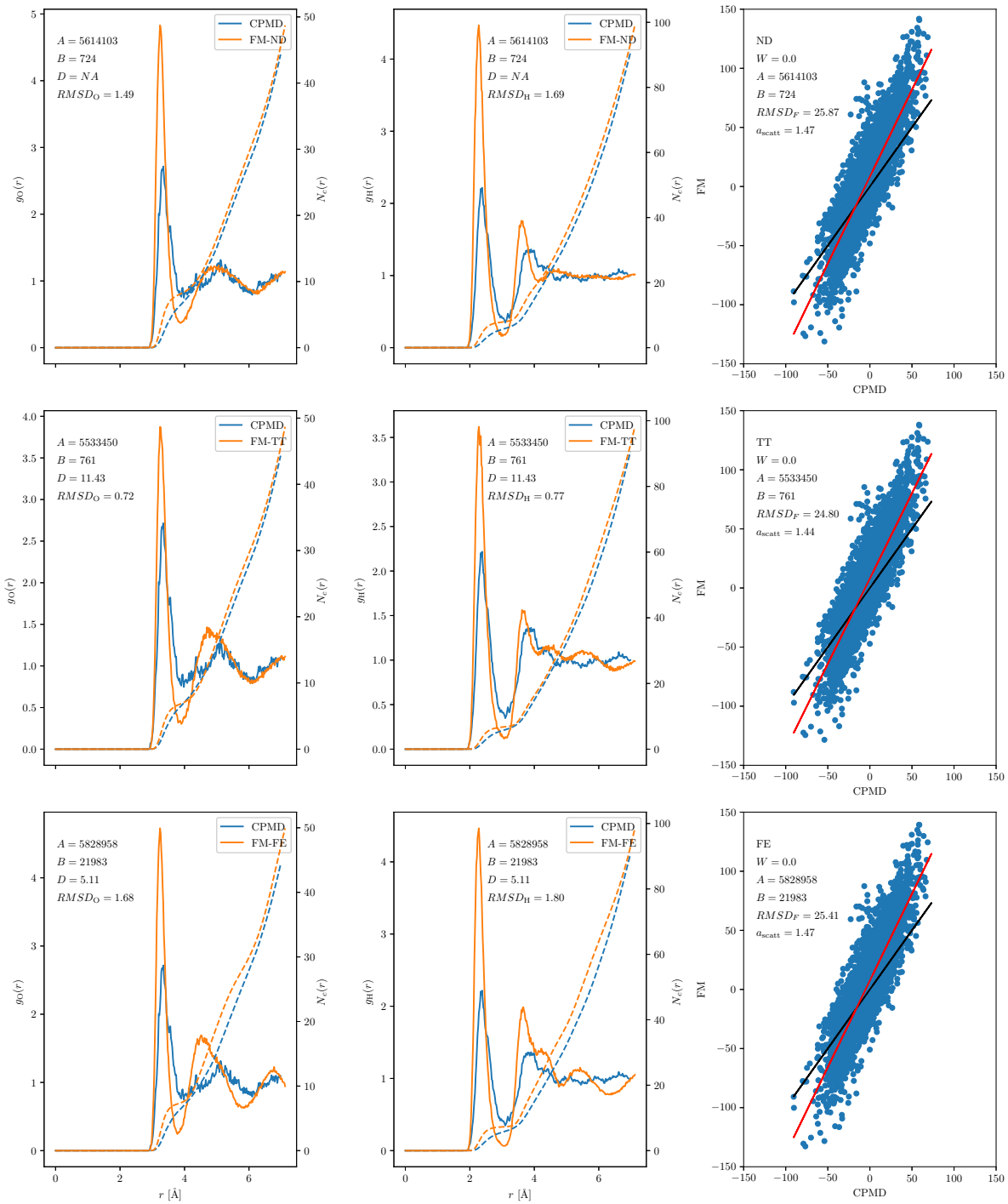

Fig. A.12 Comparison between the ion-oxygen (left) and ion-hydrogen (center) RDFs and the forces (right) for the undamped (top), Tang-Toennies (middle) and Fermi (bottom) dampings of the SPC-FM water models at temperature $T = 300\,\mathrm{K}$ with scaled charges and weight $W = 0$ against the CPMD reference for the bromide ion.

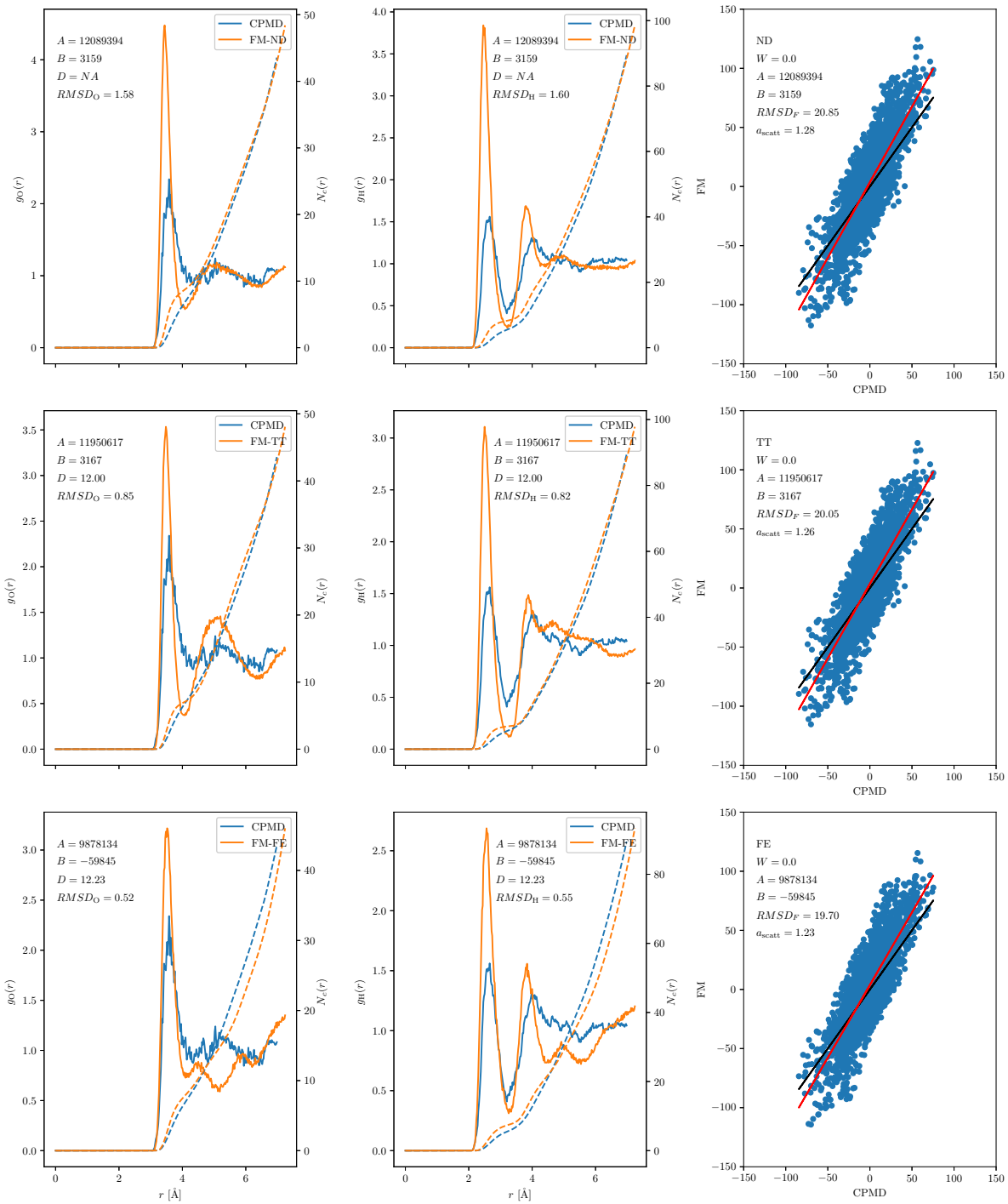

Fig. A.13 Comparison between the ion-oxygen (left) and ion-hydrogen (center) RDFs and the forces (right) for the undamped (top), Tang-Toennies (middle) and Fermi (bottom) dampings of the SPC-FM water models at temperature $T = 300\,\mathrm{K}$ with scaled charges and weight $W = 0$ against the CPMD reference for the iodide ion.

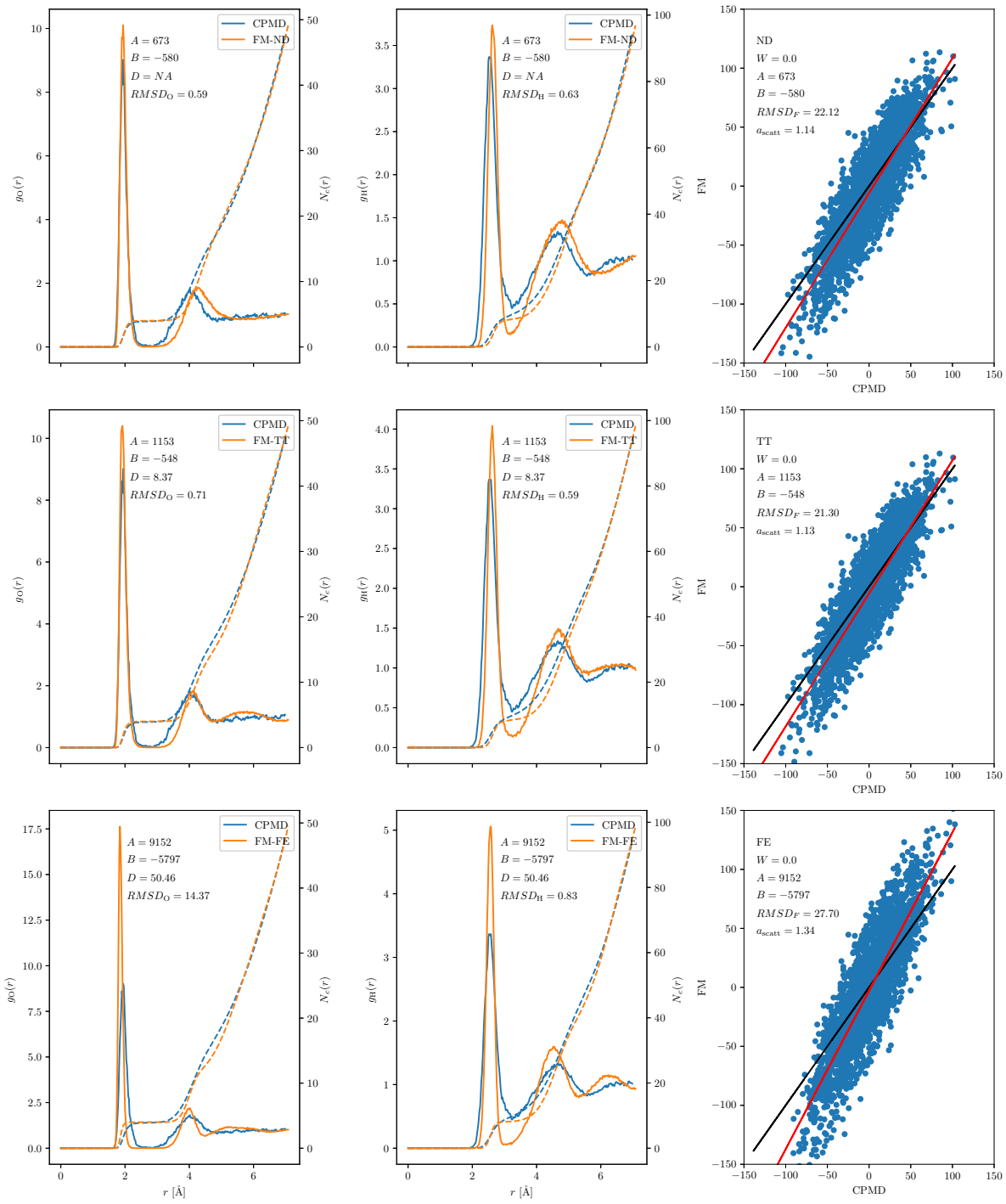

Fig. A.14 Comparison between the ion-oxygen (left) and ion-hydrogen (center) RDFs and the forces (right) for the undamped (top), Tang-Toennies (middle) and Fermi (bottom) dampings of the SPC-FM water models at temperature $T = 300\,\mathrm{K}$ with scaled charges and weight $W = 0$ against the CPMD reference for the lithium ion.

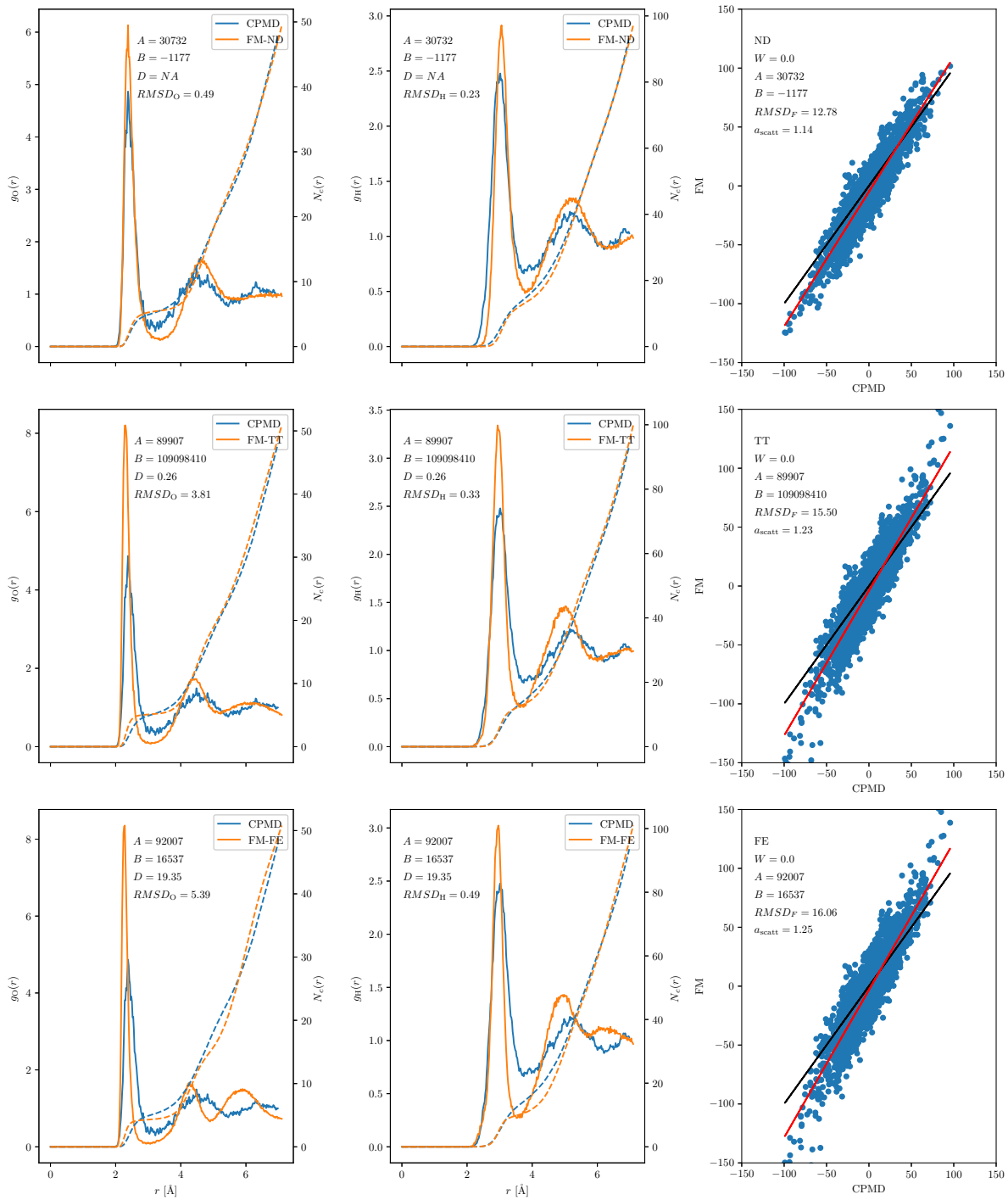

Fig. A.15 Comparison between the ion-oxygen (left) and ion-hydrogen (center) RDFs and the forces (right) for the undamped (top), Tang-Toennies (middle) and Fermi (bottom) dampings of the SPC-FM water models at temperature $T = 300\,\mathrm{K}$ with scaled charges and weight $W = 0$ against the CPMD reference for the sodium ion.

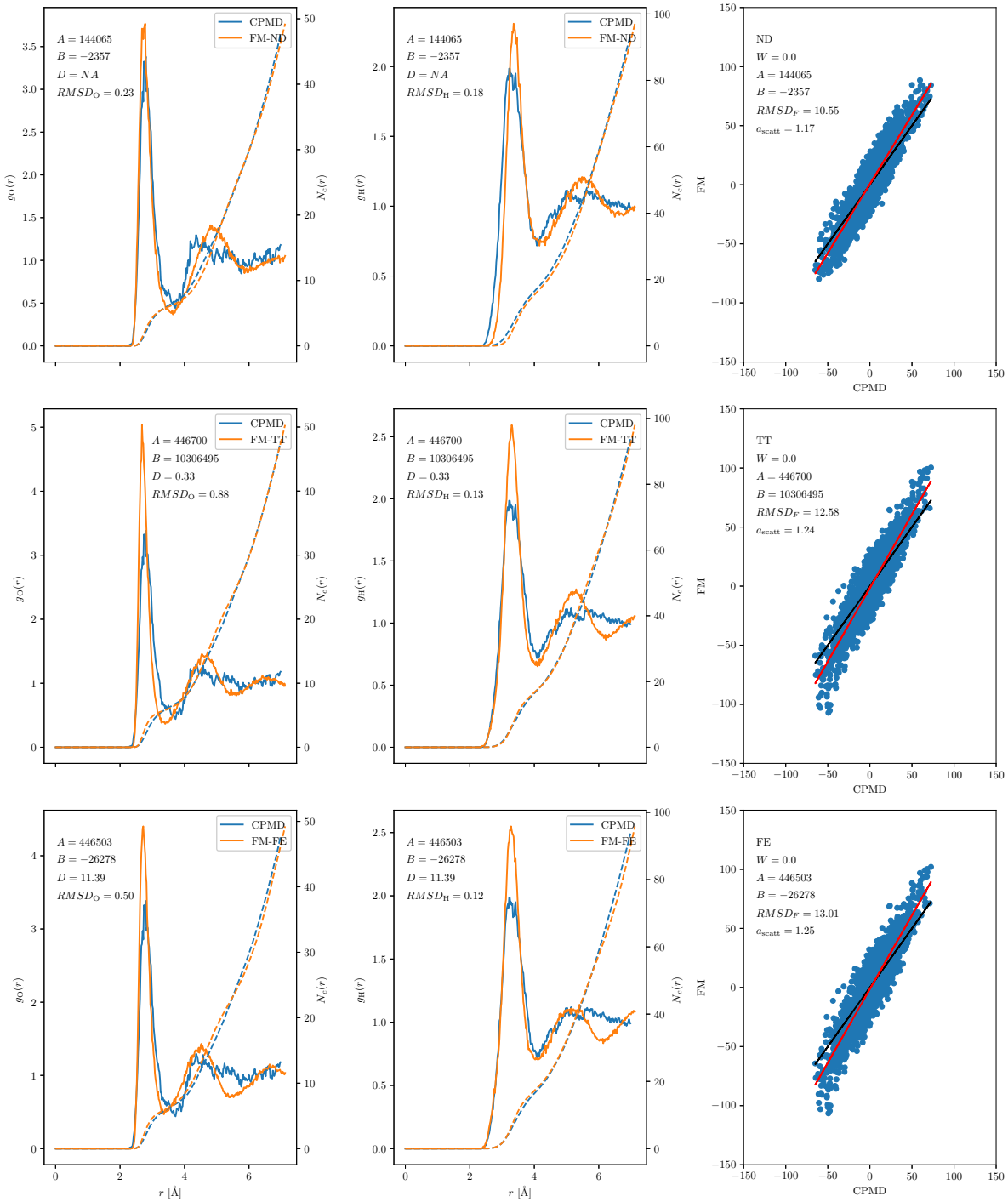

Fig. A.16 Comparison between the ion-oxygen (left) and ion-hydrogen (center) RDFs and the forces (right) for the undamped (top), Tang-Toennies (middle) and Fermi (bottom) dampings of the SPC-FM water models at temperature $T = 300\,\mathrm{K}$ with scaled charges and weight $W = 0$ against the CPMD reference for the potassium ion.

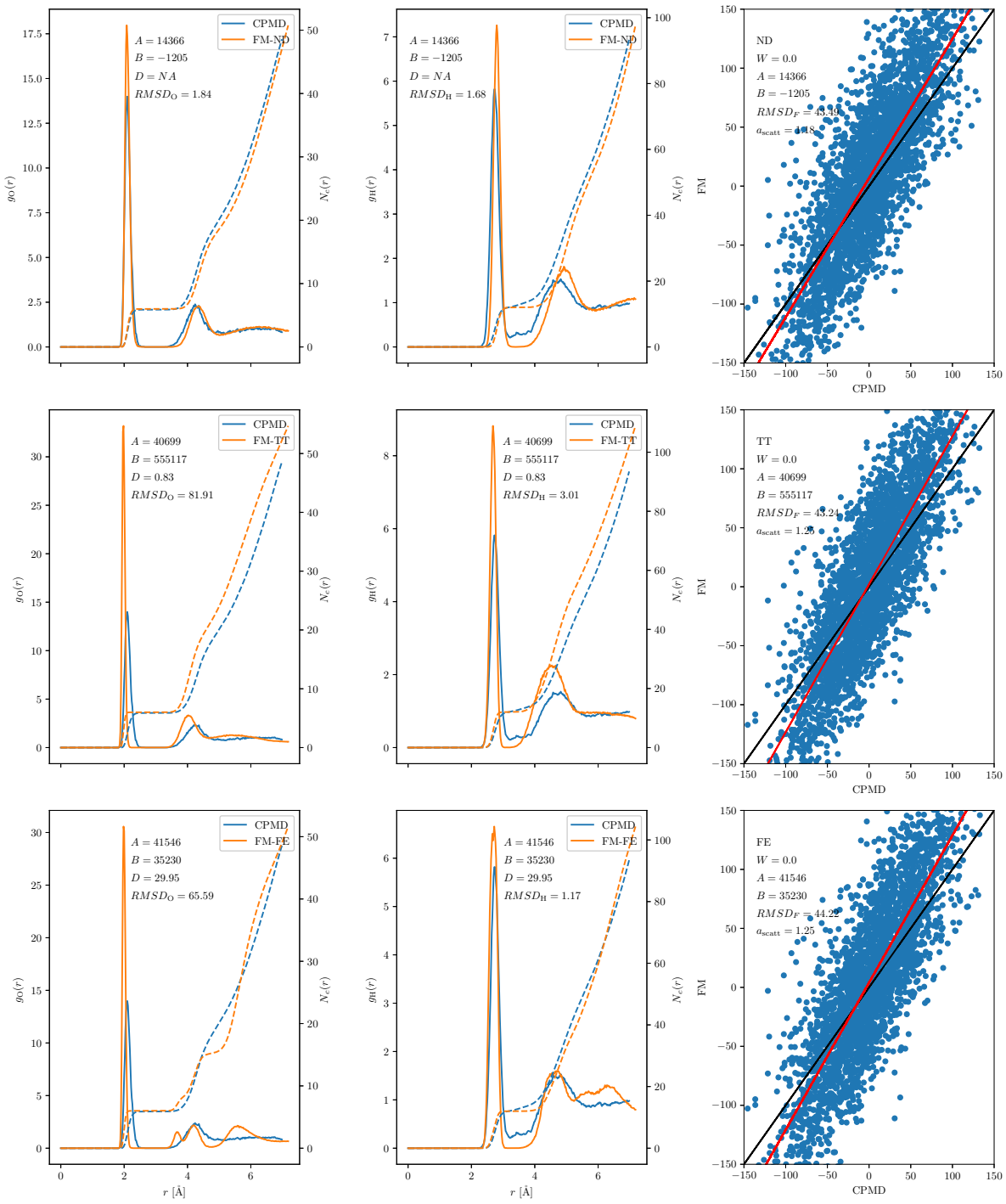

Fig. A.17 Comparison between the ion-oxygen (left) and ion-hydrogen (center) RDFs and the forces (right) for the undamped (top), Tang-Toennies (middle) and Fermi (bottom) dampings of the SPC-FM water models at temperature $T = 300\,\mathrm{K}$ with scaled charges and weight $W = 0$ against the CPMD reference for the magnesium ion.

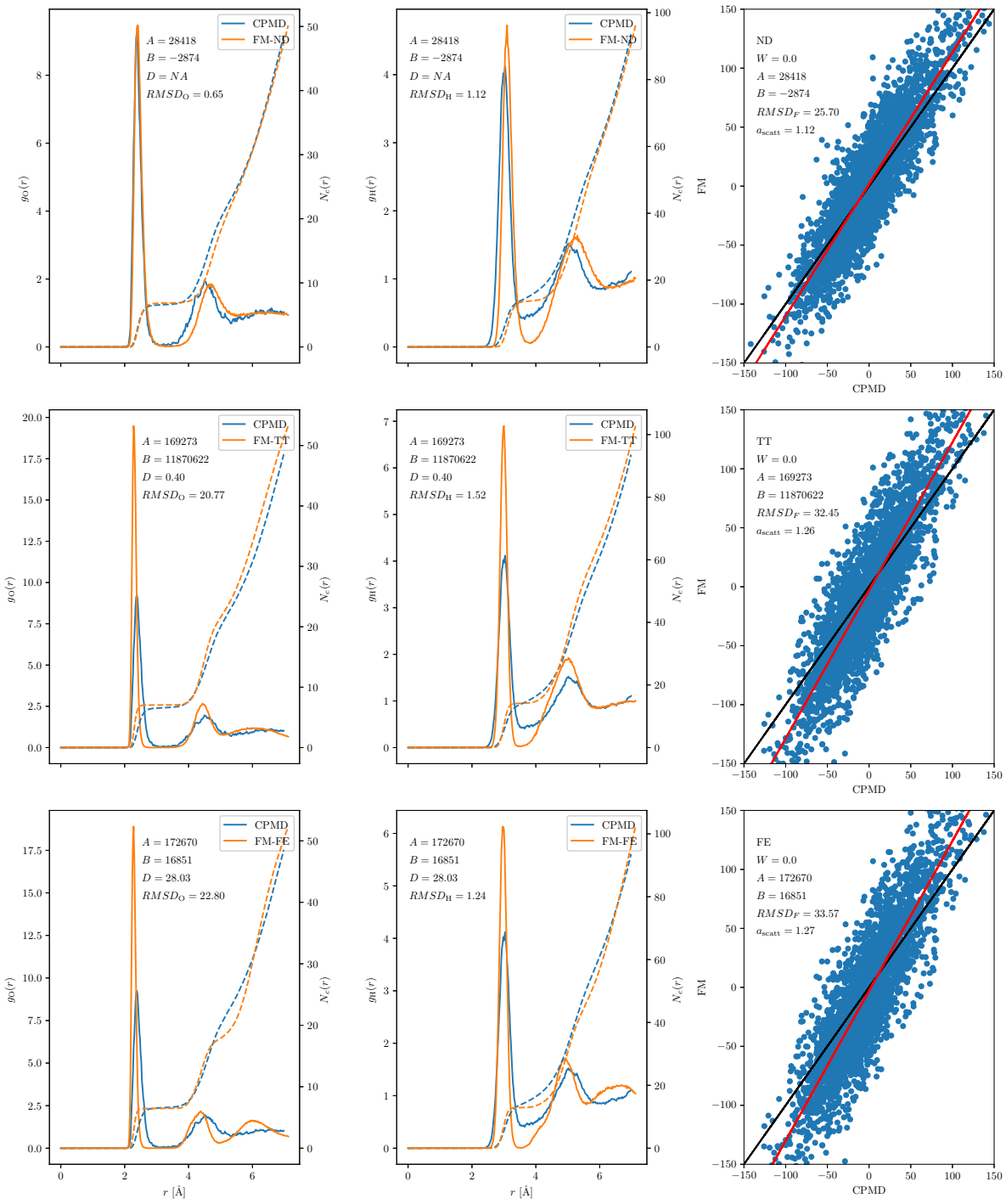

Fig. A.18 Comparison between the ion-oxygen (left) and ion-hydrogen (center) RDFs and the forces (right) for the undamped (top), Tang-Toennies (middle) and Fermi (bottom) dampings of the SPC-FM water models at temperature $T = 300\,\mathrm{K}$ with scaled charges and weight $W = 0$ against the CPMD reference for the calcium ion.

Appendix B

Force matching for the SPC-FM water models at T=330 K with charge scaling

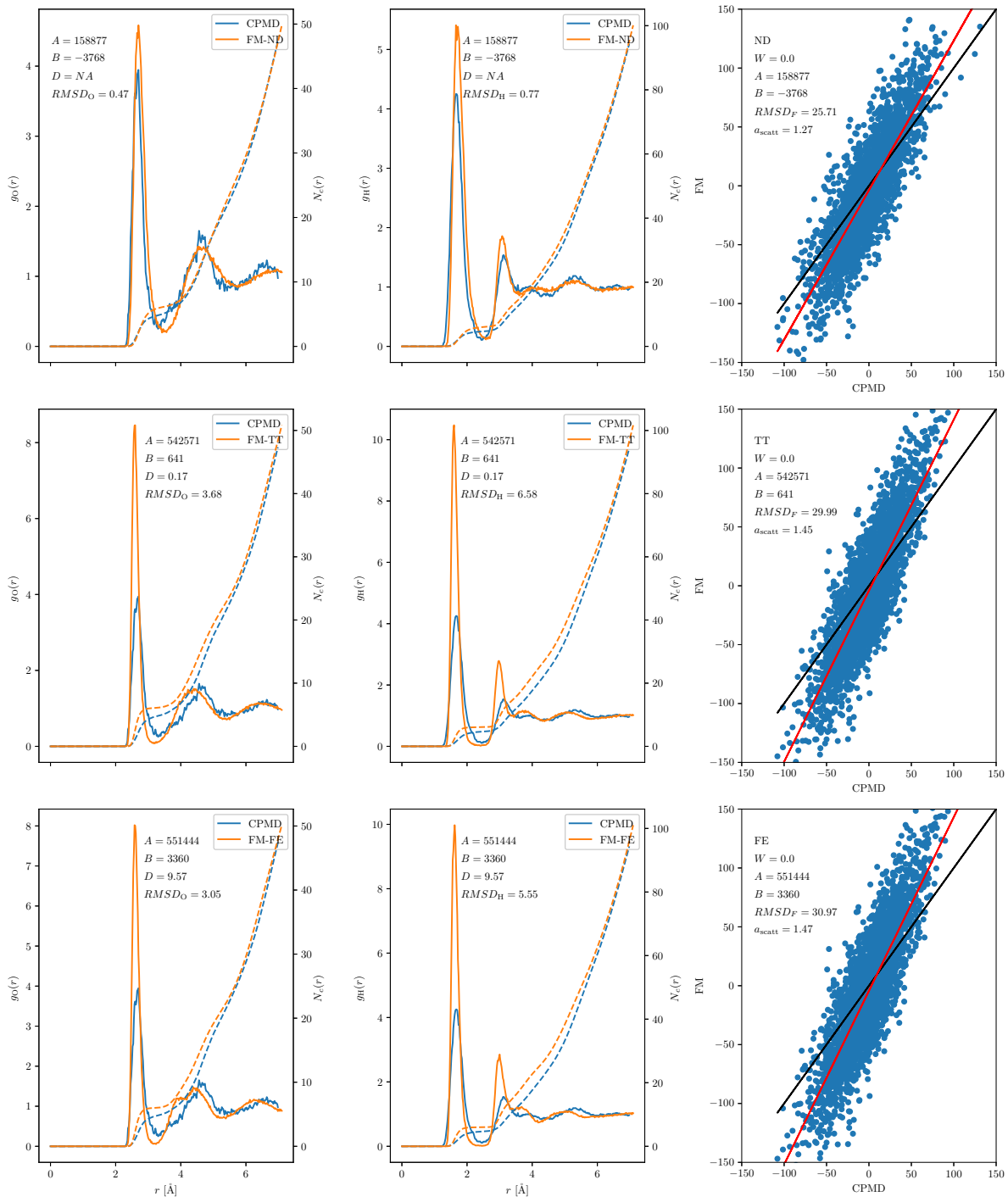

Fig. B.1 Comparison between the ion-oxygen (left) and ion-hydrogen (center) RDFs and the forces (right) for the undamped (top), Tang-Toennies (middle) and Fermi (bottom) dampings of the SPC-FM water models at temperature $T = 330\,\mathrm{K}$ with scaled charges and weight $W = 0$ against the CPMD reference for the fluoride ion.

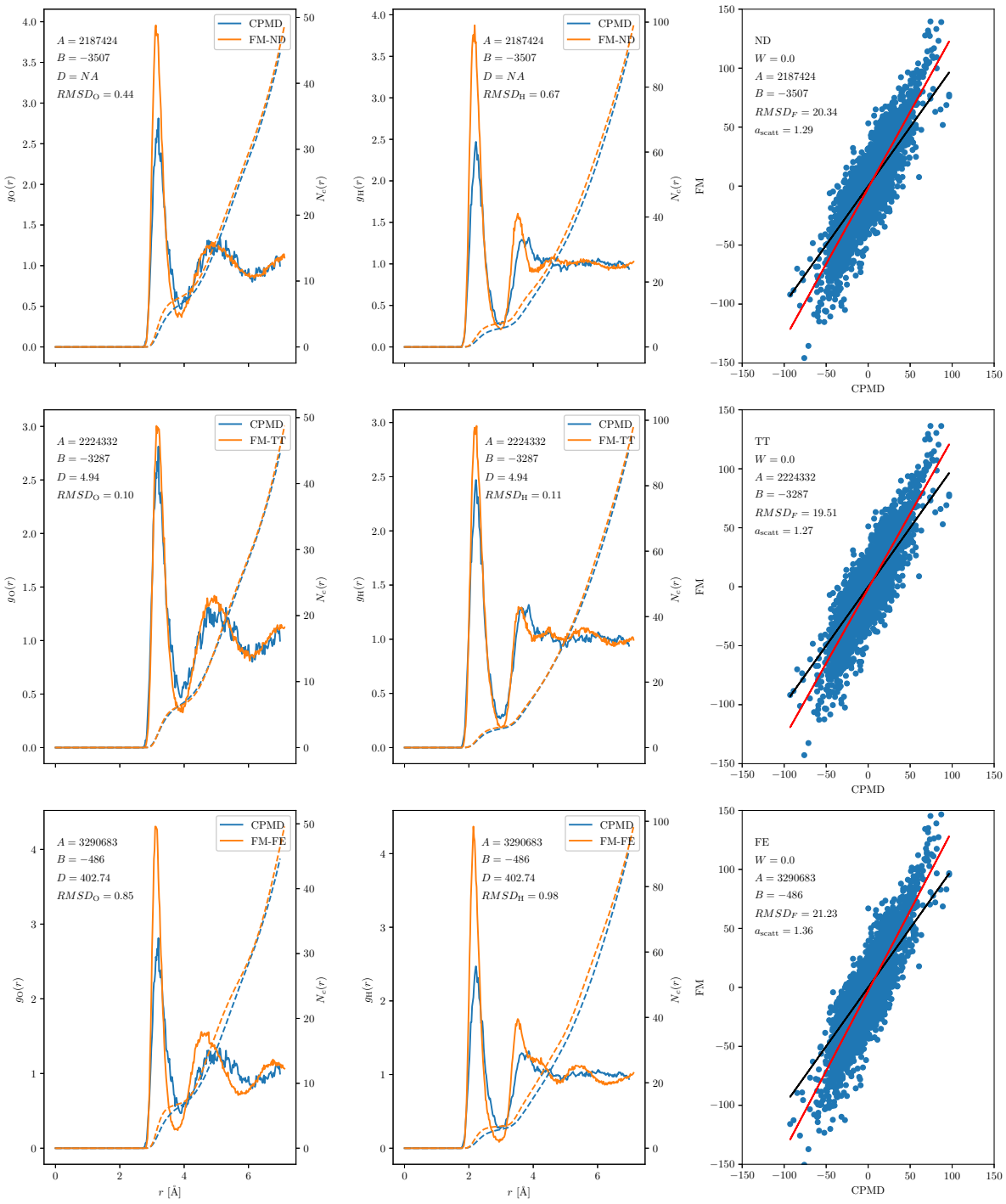

Fig. B.2 Comparison between the ion-oxygen (left) and ion-hydrogen (center) RDFs and the forces (right) for the undamped (top), Tang-Toennies (middle) and Fermi (bottom) dampings of the SPC-FM water models at temperature $T = 330\,\mathrm{K}$ with scaled charges and weight $W = 0$ against the CPMD reference for the chloride ion.

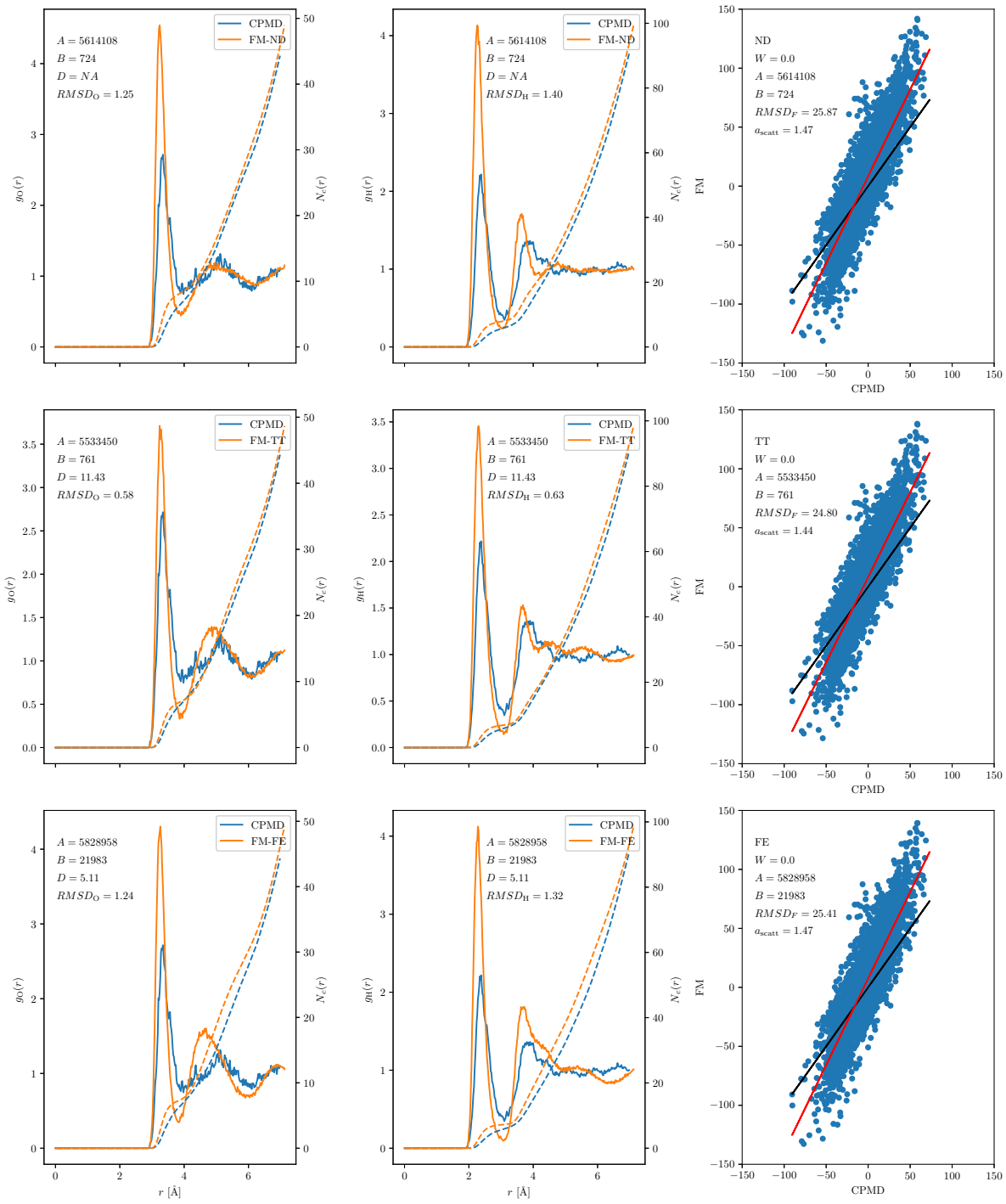

Fig. B.3 Comparison between the ion-oxygen (left) and ion-hydrogen (center) RDFs and the forces (right) for the undamped (top), Tang-Toennies (middle) and Fermi (bottom) dampings of the SPC-FM water models at temperature $T = 330\,\mathrm{K}$ with scaled charges and weight $W = 0$ against the CPMD reference for the bromide ion.

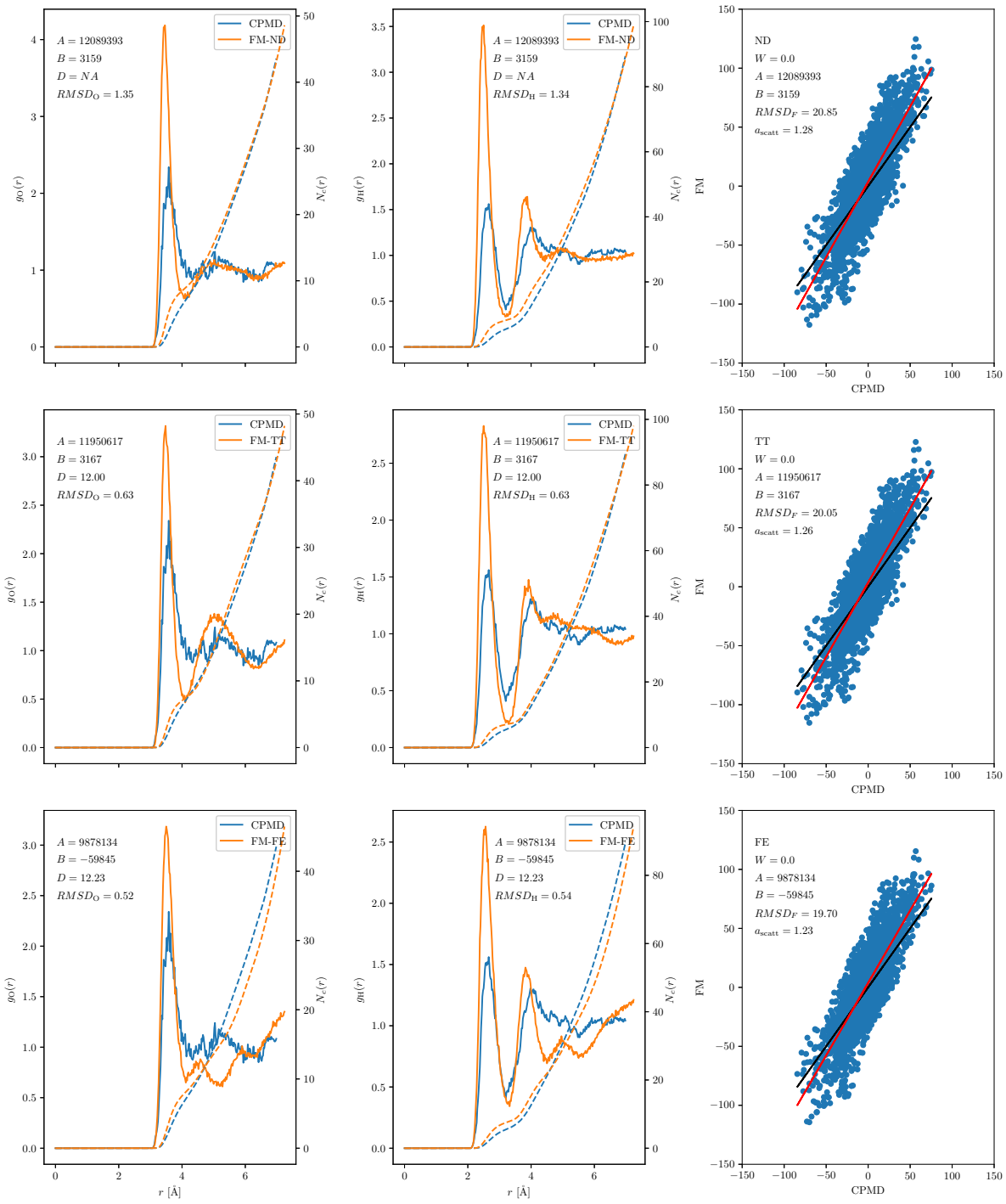

Fig. B.4 Comparison between the ion-oxygen (left) and ion-hydrogen (center) RDFs and the forces (right) for the undamped (top), Tang-Toennies (middle) and Fermi (bottom) dampings of the SPC-FM water models at temperature $T = 330\,\mathrm{K}$ with scaled charges and weight $W = 0$ against the CPMD reference for the iodide ion.

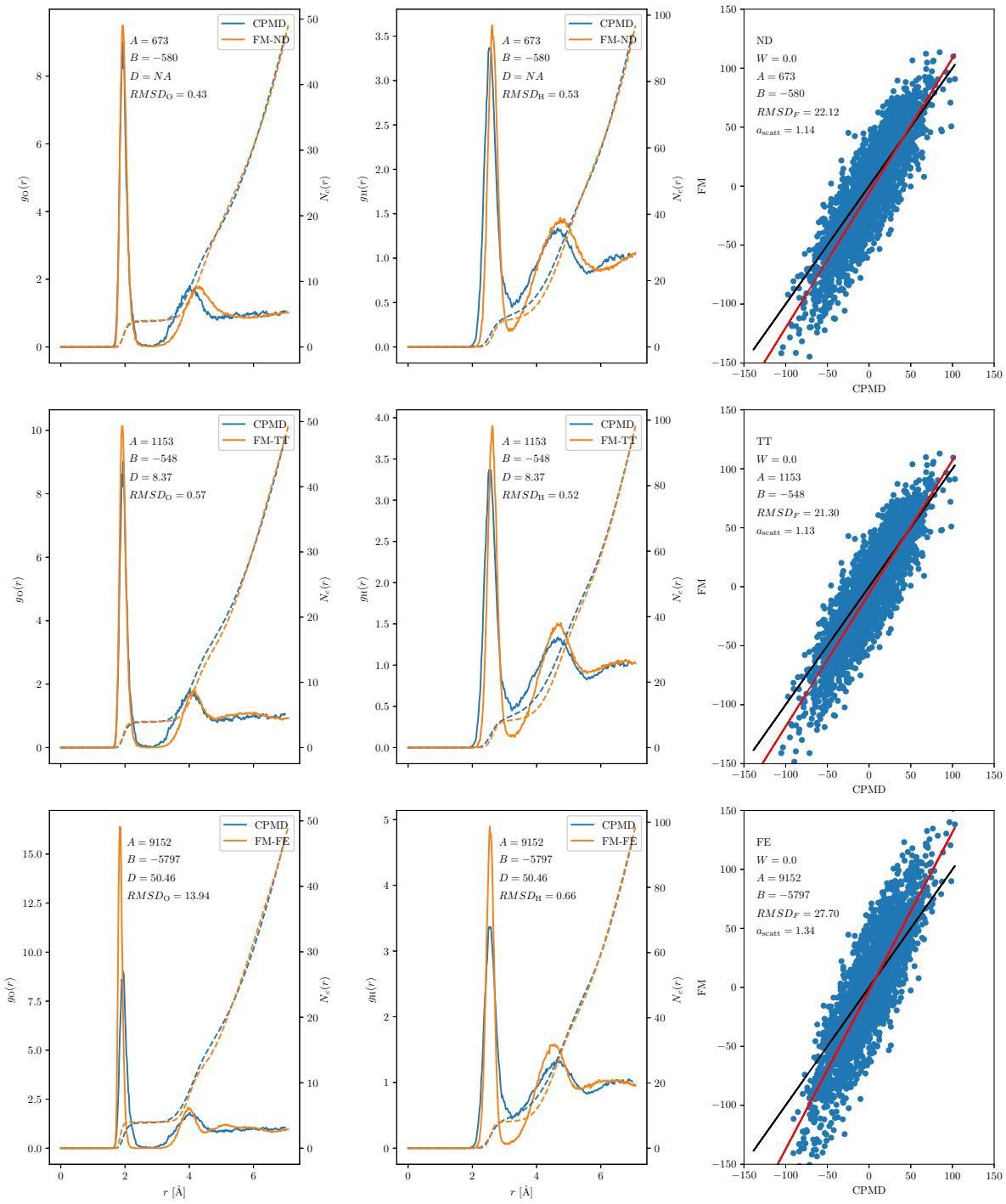

Fig. B.5 Comparison between the ion-oxygen (left) and ion-hydrogen (center) RDFs and the forces (right) for the undamped (top), Tang-Toennies (middle) and Fermi (bottom) dampings of the SPC-FM water models at temperature $T = 330\,\mathrm{K}$ with scaled charges and weight $W = 0$ against the CPMD reference for the lithium ion.

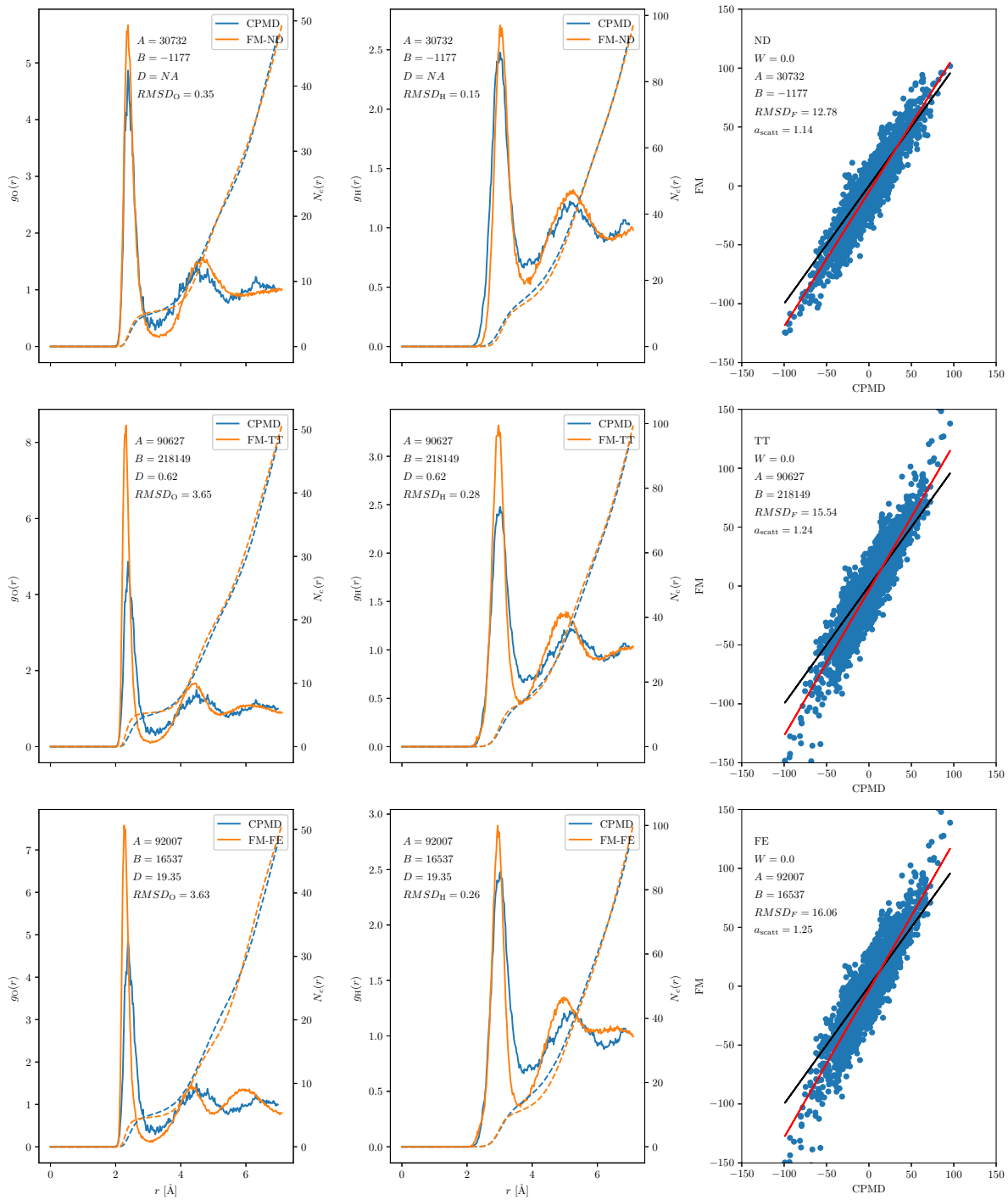

Fig. B.6 Comparison between the ion-oxygen (left) and ion-hydrogen (center) RDFs and the forces (right) for the undamped (top), Tang-Toennies (middle) and Fermi (bottom) dampings of the SPC-FM water models at temperature $T = 330\,\mathrm{K}$ with scaled charges and weight $W = 0$ against the CPMD reference for the sodium ion.

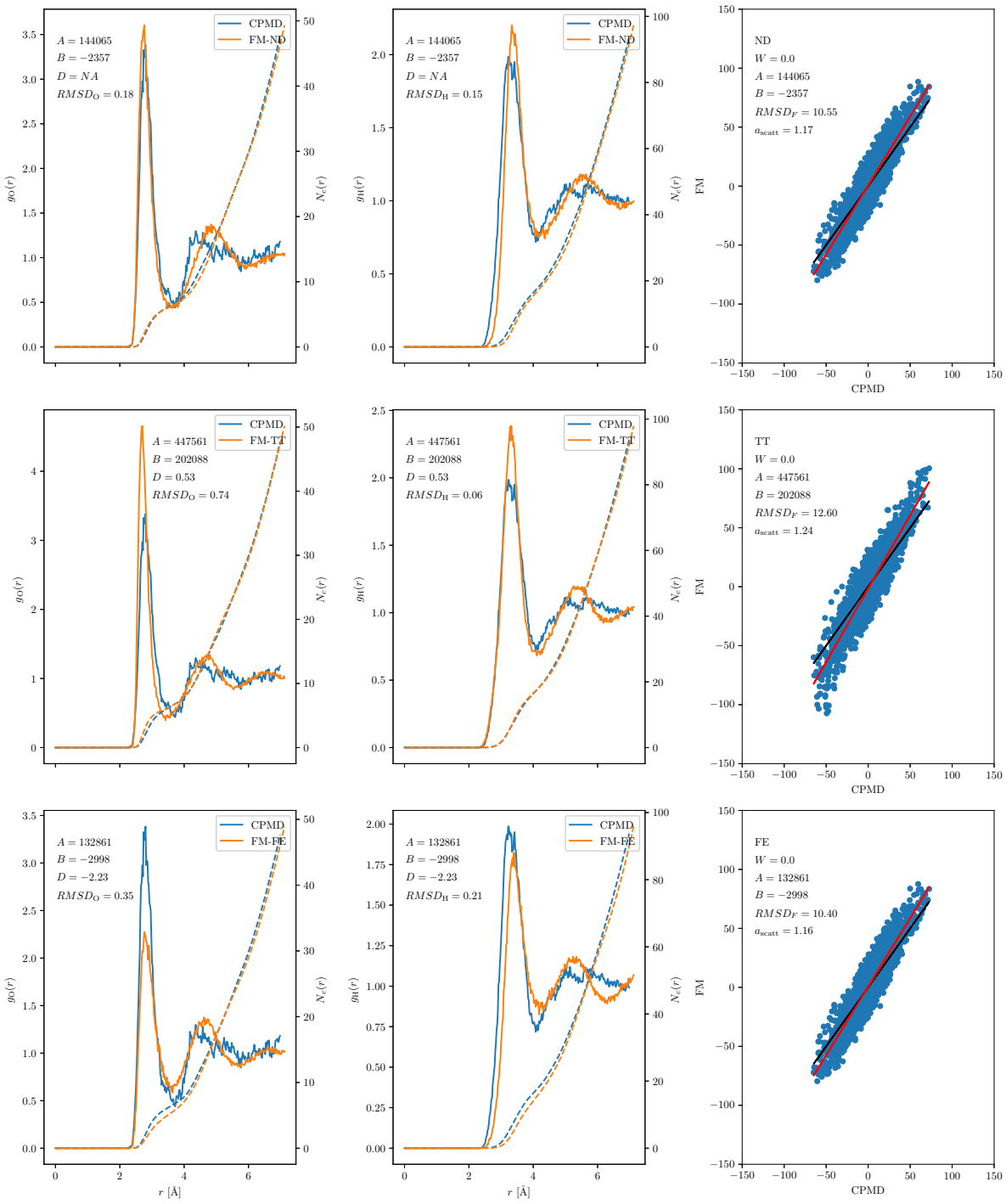

Fig. B.7 Comparison between the ion-oxygen (left) and ion-hydrogen (center) RDFs and the forces (right) for the undamped (top), Tang-Toennies (middle) and Fermi (bottom) dampings of the SPC-FM water models at temperature $T = 330\,\mathrm{K}$ with scaled charges and weight $W = 0$ against the CPMD reference for the potassium ion.

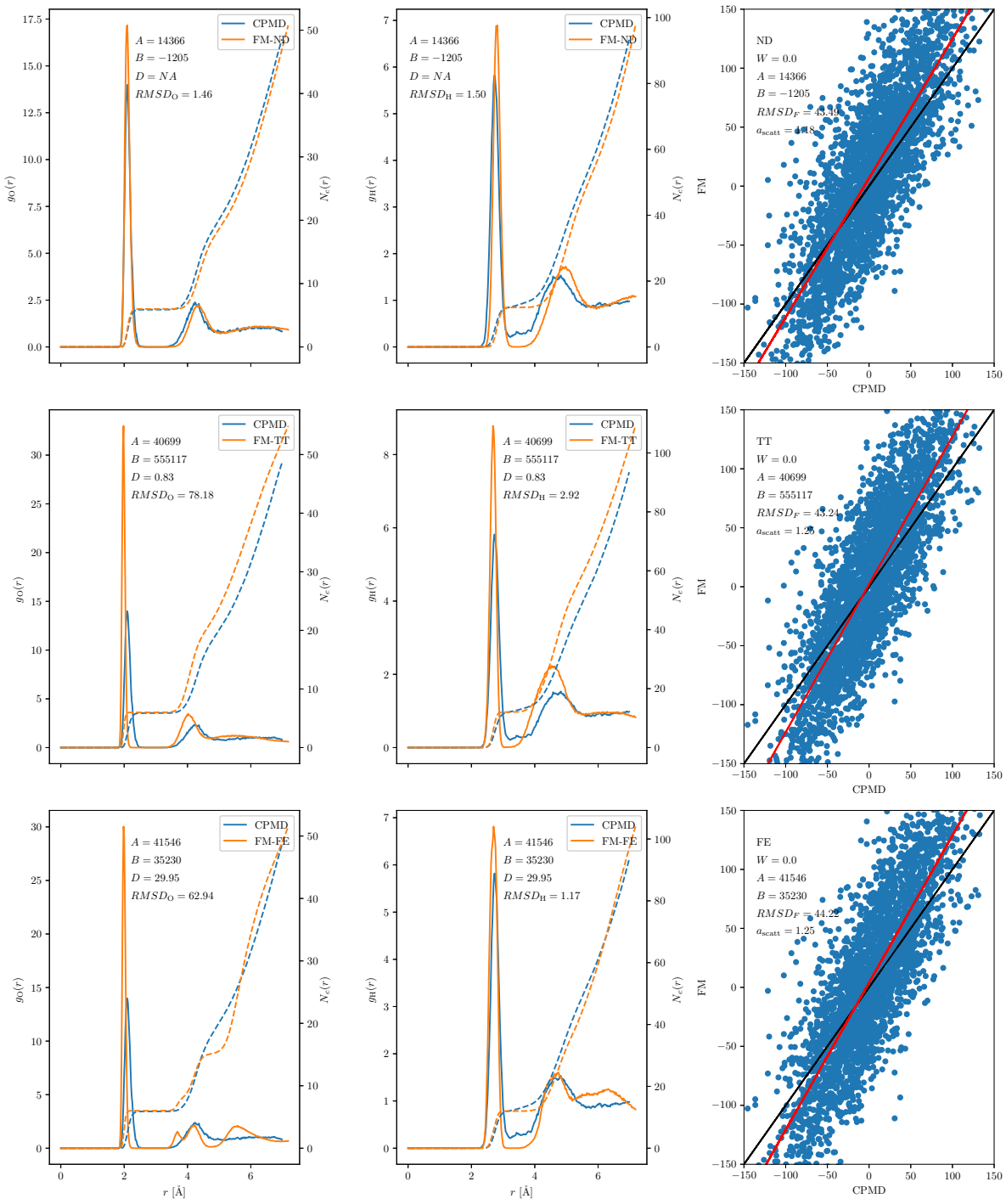

Fig. B.8 Comparison between the ion-oxygen (left) and ion-hydrogen (center) RDFs and the forces (right) for the undamped (top), Tang-Toennies (middle) and Fermi (bottom) dampings of the SPC-FM water models at temperature $T = 330\,\mathrm{K}$ with scaled charges and weight $W = 0$ against the CPMD reference for the magnesium ion.

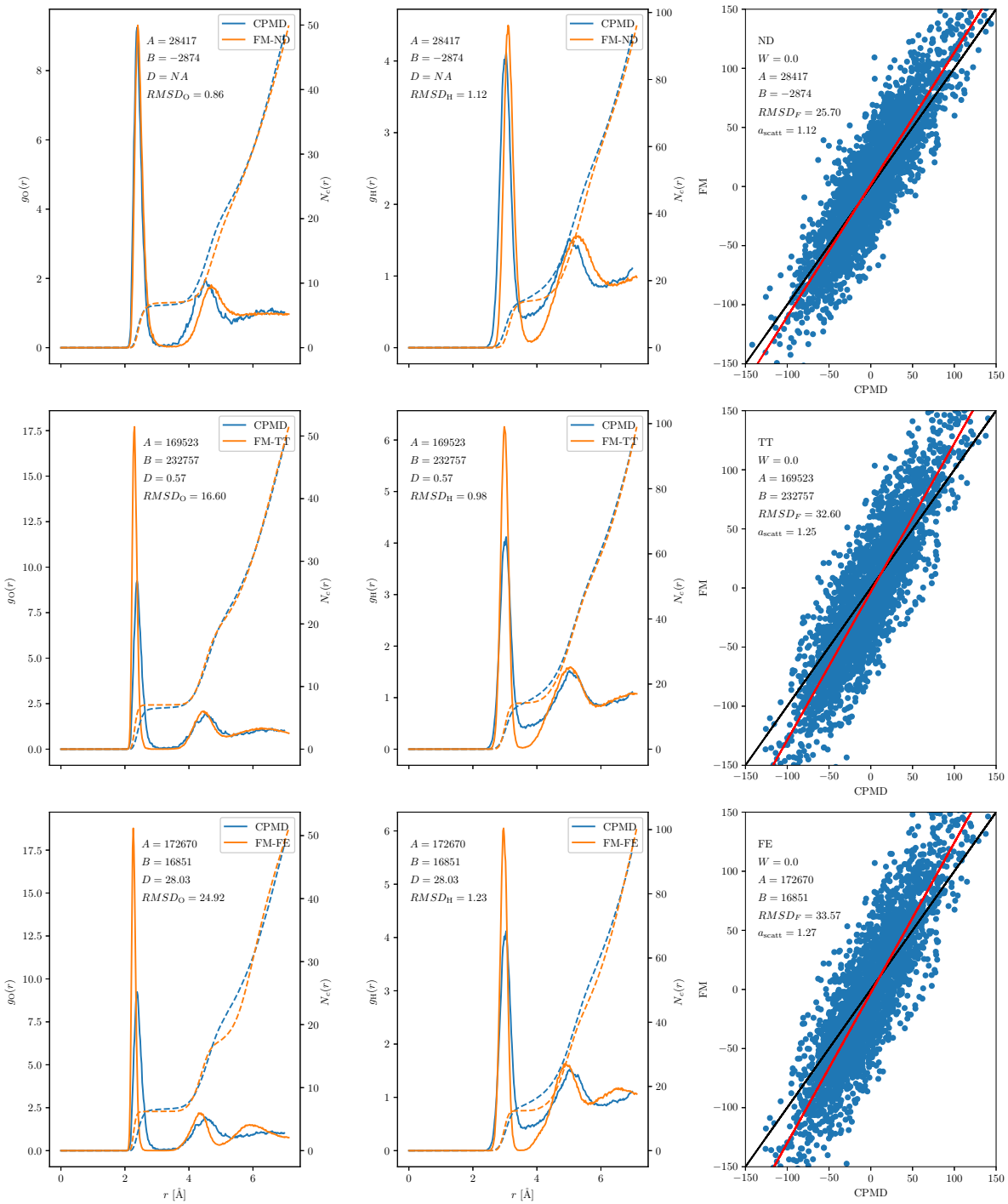

Fig. B.9 Comparison between the ion-oxygen (left) and ion-hydrogen (center) RDFs and the forces (right) for the undamped (top), Tang-Toennies (middle) and Fermi (bottom) dampings of the SPC-FM water models at temperature $T = 330\,\mathrm{K}$ with scaled charges and weight $W = 0$ against the CPMD reference for the calcium ion.